NATIONAL AERONAUTICS AND SPACE ADMINISTRATION

Technical Report 32-1526

Volume V

The Deep Space Network

Progress Report
For July and August 1971

JET PROPULSION LABORATORY
CALIFORNIA INSTITUTE OF TECHNOLOGY
PASADENA, CALIFORNIA

October 15, 1971

NATIONAL AERONAUTICS AND SPACE ADMINISTRATION

Technical Report 32-1526

Volume V

The Deep Space Network

Progress Report
For July and August 1971

JET PROPULSION LABORATORY
CALIFORNIA INSTITUTE OF TECHNOLOGY
PASADENA, CALIFORNIA

October 15, 1971

Prepared Under Contract No. NAS 7-100
National Aeronautics and Space Administration

Preface

This report series presents progress on DSN supporting research and technology, advanced development and engineering, and implementation, and DSN operations which pertain to mission-independent or multiple-mission development as well as to support of flight projects. Each issue presents material in some, but not all, of the following categories in the order indicated.

Description of the DSN

Mission Support
- Interplanetary Flight Projects
- Planetary Flight Projects
- Manned Space Flight Project
- Radio Science Experiments
- Advanced Flight Projects

Advanced Engineering
- Tracking and Navigational Accuracy Analysis
- Communications Systems Research
- Communications Elements Research
- Supporting Research and Technology

Development and Implementation
- Space Flight Operations Facility Development
- Ground Communications Facility Development
- Deep Space Instrumentation Facility Development
- DSN Projects and Systems Development

Operations and Facilities
- DSN Operations
- Space Flight Operations Facility Operations
- Ground Communications Facility Operations
- Deep Space Instrumentation Facility Operations
- Facility Engineering

In each issue, the part entitled "Description of the DSN" describes the functions and facilities of the DSN and may report the current configuration of one of the six DSN systems (tracking, telemetry, command, monitoring, simulation, and operations control).

The work described in this report series is either performed or managed by the Tracking and Data Acquisition organization of JPL for NASA.

Contents

DESCRIPTION OF THE DSN

DSN Functions and Facilities 1
N. A. Renzetti

MISSION SUPPORT

Interplanetary Flight Projects

***Pioneer* Mission Support** 4
A. J. Siegmeth

***Helios* Mission Support** 17
P. S. Goodwin

Planetary Flight Projects

***Mariner* Mars 1971 Mission Support** 22
R. P. Laeser

***Viking* Mission Support** 24
E. K. Davis

Manned Space Flight Project

***Apollo* Mission Support** 29
R. B. Hartley

Radio Science Experiments

Radio Science Support 42
K. W. Linnes

ADVANCED ENGINEERING

Tracking and Navigational Accuracy Analysis

The Goldstone Interferometer for Earth Physics 45
J. L. Fanselow, P. F. MacDoran, J. B. Thomas, J. G. Williams, C. J. Finnie, T. Sato, L. Skjerve, and D. J. Spitzmesser

Contents (contd)

Comparison of Faraday Rotation Measurements of the Ionosphere 58
L. F. Miller and B. D. Mulhall

A Worldwide Organization to Secure Earth-Related Parameters for Deep Space Missions 66
H. F. Fliegel

A Comparison of Cowell's Method and a Variation-of-Parameters Method for the Computation of Precision Satellite Orbits 74
S. S. Dallas and E. A. Rinderle

Communications Systems Research

Combinational Complexity Measures as a Function of Fan-out 79
D. L. Johnson, J. E. Savage, and L. Welch

Sequential Tests for Exponential Distributions 82
G. Lorden

Contributions to a Mathematical Theory of Complexity 91
L. H. Harper and J. E. Savage

Some Results on the Matrix Multiplication Problem 99
L. H. Harper and J. E. Savage

Communications Elements Research

Tracking and Data Acquisition Elements Research: Low Noise Receivers: Microwave Maser Development 102
R. Clauss and R. Quinn

Superconducting Magnet for a Ku-Band Maser 109
R. Berwin, E. Wiebe, and P. Dachel

Antenna Noise Temperature Contributions Due to Ohmic and Leakage Losses of the DSS 14 64-m Antenna Reflector Surface 115
T. Y. Otoshi

Supporting Research and Technology

DSN Research and Technology Support 120
E. B. Jackson

Contents (contd)

Load Distribution on the Surface of Paraboloidal Reflector Antennas 122
M. Kron

DEVELOPMENT AND IMPLEMENTATION

SFOF Development

CPS Sustaining Engineering 129
C. L. Zandell

GCF Development

DSS Communications Equipment Subsystem Simulation Center High-Speed Data Assembly 132
D. S. Bremner

OPERATIONS AND FACILITIES

SFOF Operations

***Pioneer F* and *G* Mission Support Area** 136
A. H. Hofmann

Bibliography 141

DSN Functions and Facilities

N. A. Renzetti
Mission Support Office

The objectives, functions, and organization of the Deep Space Network are summarized. The Deep Space Instrumentation Facility, the Ground Communications Facility, and the Space Flight Operations Facility are described.

The Deep Space Network (DSN), established by the NASA Office of Tracking and Data Acquisition under the system management and technical direction of JPL, is designed for two-way communications with unmanned spacecraft traveling approximately 16,000 km (10,000 mi) from earth to planetary distances. It supports, or has supported, the following NASA deep space exploration projects: *Ranger, Surveyor, Mariner* Venus 1962, *Mariner* Mars 1964, *Mariner* Venus 67, *Mariner* Mars 1969, *Mariner* Mars 1971 (JPL); *Lunar Orbiter* and *Viking* (Langley Research Center); *Pioneer* (Ames Research Center); *Helios* (West Germany); and *Apollo* (Manned Spacecraft Center), to supplement the Manned Space Flight Network (MSFN).

The DSN is distinct from other NASA networks such as the MSFN, which has primary responsibility for tracking the manned spacecraft of the *Apollo* Project, and the Space Tracking and Data Acquisition Network (STADAN), which tracks earth-orbiting scientific and communications satellites. With no future unmanned lunar spacecraft presently planned, the primary objective of the DSN is to continue its support of planetary and interplanetary flight projects.

To support flight projects, the DSN simultaneously performs advanced engineering on components and systems, integrates proven equipment and methods into the network,[1] and provides direct support of each project through that project's Tracking and Data System. This management element and the project's Mission Operations personnel are responsible for the design and operation of the data, software, and operations systems required for the conduct of flight operations. The organization and procedures necessary to carry out these activities are described in Ref. 1.

[1]When a new piece of equipment or new method has been accepted for integration into the network, it is classed as Goldstone duplicate standard (GSDS), thus standardizing the design and operation of identical items throughout the network.

By tracking the spacecraft, the DSN is involved in the following data types:

(1) *Radio Metric:* generate angles, one- and two-way doppler, and range.

(2) *Telemetry:* receive, record, and retransmit engineering and scientific data.

(3) *Command:* send coded signals to the spacecraft to activate equipment to initiate spacecraft functions.

The DSN operation is characterized by six DSN systems: (1) tracking, (2) telemetry, (3) command, (4) monitoring, (5) simulation, and (6) operations control.

The DSN can be characterized as being comprised of three facilities: the Deep Space Instrumentation Facility (DSIF), the Ground Communications Facility (GCF), and the Space Flight Operations Facility (SFOF).

I. Deep Space Instrumentation Facility

A. Tracking and Data Acquisition Facilities

A world-wide set of deep space stations (DSSs) with large antennas, low-noise phase-lock receiving systems, and high-power transmitters provide radio communications with spacecraft. The DSSs and the deep space communications complexes (DSCCs) they comprise are given in Table 1.

Radio contact with a spacecraft usually begins when the spacecraft is on the launch vehicle at Cape Kennedy, and it is maintained throughout the mission. The early part of the trajectory is covered by selected network stations of the Air Force Eastern Test Range (AFETR) and the MSFN of the Goddard Space Flight Center.[2] Normally, two-way communications are established between the spacecraft and the DSN within 30 min after the spacecraft has been injected into lunar, planetary, or interplanetary flight. A compatibility test station at Cape Kennedy (discussed later) monitors the spacecraft continuously during the launch phase until it passes over the local horizon. The deep space phase begins with acquisition by either DSS 51, 41, or 42. These and the remaining DSSs given in Table 1 provide radio communications to the end of the flight.

To enable continuous radio contact with spacecraft, the DSSs are located approximately 120 deg apart in longitude; thus, a spacecraft in deep space flight is always

[2]The 9-m (30-ft) diam antenna station established by the DSN on Ascension Island during 1965 to act in conjunction with the MSFN orbital support 9-m (30-ft) diam antenna station was transferred to the MSFN in July 1968.

Table 1. Tracking and data acquisition stations of the DSN

DSCC	Location	DSS	DSS serial designation	Antenna		Year of initial operation
				Diameter, m (ft)	Type of mounting	
Goldstone	California	Pioneer	11	26 (85)	Polar	1958
		Echo	12	26 (85)	Polar	1962
		(Venus)[a]	13	26 (85)	Az–El	1962
		Mars	14	64 (210)	Az–El	1966
—	Australia	Woomera[b]	41	26 (85)	Polar	1960
Tidbinbilla	Australia	Weemala (formerly Tidbinbilla)[b]	42	26 (85)	Polar	1965
		Ballima[b] (formerly Booroomba)	43	64 (210)	Az–El	Under construction
—	South Africa	Johannesburg[b]	51	26 (85)	Polar	1961
Madrid	Spain	Robledo[b]	61	26 (85)	Polar	1965
		Cebreros[b]	62	26 (85)	Polar	1967
		Robledo	63	64 (210)	Az–El	Under construction

[a]A research-and-development facility used to demonstrate the feasibility of new equipment and methods to be integrated into the operational network. Besides the 26-m (85-ft) diam az–el-mounted antenna, DSS 13 has a 9-m (30-ft) diam az–el-mounted antenna that is used for testing the design of new equipment and support of ground-based radio science.

[b]Normally staffed and operated by government agencies of the respective countries (except for a temporary staff of the Madrid DSCC), with some assistance of U.S. support personnel.

within the field-of-view of at least one DSS, and for several hours each day may be seen by two DSSs. Furthermore, since most spacecraft on deep space missions travel within 30 deg of the equatorial plane, the DSSs are located within latitudes of 45 deg north or south of the equator. All DSSs operate at S-band frequencies: 2110–2120 MHz for earth-to-spacecraft transmission and 2290–2300 MHz for spacecraft-to-earth transmission.

To provide sufficient tracking capability to enable useful data returns from around the planets and from the edge of the solar system, a 64-m (210-ft) diam antenna network will be required. Two additional 64-m (210-ft) diam antenna DSSs are under construction at Madrid and Canberra, which will operate in conjunction with DSS 14 to provide this capability. These stations are scheduled to be operational by the middle of 1973.

B. Compatibility Test Facilities

In 1959, a mobile L-band compatibility test station was established at Cape Kennedy to verify flight–spacecraft–DSN compatibility prior to the launch of the *Ranger* and *Mariner* Venus 1962 spacecraft. Experience revealed the need for a permanent facility at Cape Kennedy for this function. An S-band compatibility test station with a 1.2-m (4-ft) diam antenna became operational in 1965. In addition to supporting the preflight compatibility tests, this station monitors the spacecraft continuously during the launch phase until it passes over the local horizon.

Spacecraft telecommunications compatibility in the design and prototype development phases was formerly verified by tests at the Goldstone DSCC. To provide a more economical means for conducting such work and because of the increasing use of multiple-mission telemetry and command equipment by the DSN, a compatibility test area (CTA) was established at JPL in 1968. In all essential characteristics, the configuration of this facility is identical to that of the 26-m (85-ft) and 64-m (210-ft) diam antenna stations.

The JPL CTA is used during spacecraft system tests to establish the compatibility with the DSN of the proof test model and development models of spacecraft, and the Cape Kennedy compatibility test station is used for final flight spacecraft compatibility validation testing prior to launch.

II. Ground Communications Facility

The GCF provides voice, high-speed data, wideband data, and teletype communications between the SFOF and the DSSs. In providing these capabilities, the GCF uses the facilities of the worldwide NASA Communications Network (NASCOM)[3] for all long distance circuits, except those between the SFOF and the Goldstone DSCC. Communications between the Goldstone DSCC and the SFOF are provided by a microwave link directly leased by the DSN from a common carrier.

Early missions were supported by voice and teletype circuits only, but increased data rates necessitated the use of high-speed circuits for all DSSs, plus wideband circuits for some stations.

III. Space Flight Operations Facility

Network and mission control functions are performed at the SFOF at JPL. The SFOF receives data from all DSSs and processes that information required by the flight project to conduct mission operations. The following functions are carried out: (1) real-time processing and display of radio metric data; (2) real-time and non-real-time processing and display of telemetry data; (3) simulation of flight operations; (4) near-real-time evaluation of DSN performance; (5) operations control, and status and operational data display; and (6) general support such as internal communications by telephone, intercom, public address, closed-circuit TV, documentation, and reproduction of data packages. Master data records of science data received from spacecraft are generated. Technical areas are provided for flight project personnel who analyze spacecraft performance, trajectories, and generation of commands.

[3]Managed and directed by the Goddard Space Flight Center.

Reference

1. *The Deep Space Network*, Space Programs Summary 37-50, Vol. II, pp. 15–17. Jet Propulsion Laboratory, Pasadena, Calif., Mar. 31, 1968.

Pioneer Mission Support

A. J. Siegmeth
Mission Support Office

A description of the planned configuration and data flow methodology of the Mark III Deep Space Network System is given. This system will support the Pioneer F and G missions and the successive projects of the NASA mission set of the 1970s. Block diagrams graphically illustrate the planned functions of the DSN Telemetry, Tracking, and Command Systems including their capabilities of being compatible with the forthcoming project requirements. The basic interfaces between subsystems of the three DSN facilities are defined.

I. Introduction

The description of the *Pioneer F* and *G* mission profile, the spacecraft with its major subsystems, the Conical Scanning System (CONSCAN), and the specific objectives of the scientific instruments was presented in previous issues of the DSN Progress Report (Refs. 1, 2, and 3). Special emphasis was given on the elaborations of mission characteristics which interface with the tracking and data acquisition functions.

This article provides a description of the ground-based equipment necessary to maintain a two-way telecommunications link with the spacecraft and obtain a precision two-way doppler frequency for radio metric data and orbit determination. The configuration, data flow, and interfaces of the Telemetry, Command, and Tracking Systems of the Mark III Deep Space Network are given.

II. Objectives of the DSN Mark III System

During the 1960 decade, the evolution of the tracking and data acquisition technology of deep space missions extended our human senses beyond all previous imagination. The DSN accommodated various flight project requirements in all areas to furnish the best data return for each mission. Because of changes in the state-of-the-art of deep space telecommunications, flight projects developed their own demodulation and command equipment during the sixties, and the stations of the DSN were constrained by the installation and operation of mission-dependent equipment at all deep space stations (DSSs). Since the network was configured specifically for each project, the standardization and efficient utilization of the network's resources were not possible.

After extensive experience in supporting more than 20 deep space missions within 10 years, the DSN came

to the conclusion that if more than one project required an identical or similar functional capability, that function should be considered to be multiple-mission in nature and should be provided by the tracking and data system common to these projects. It was felt that economic considerations were paramount in deciding whether a specific function should be developed and implemented by a flight project or by the DSN. It was also understood that when a multiple-mission capability was implemented by the DSN, proper flexibility must be provided to accommodate specific project requirements; therefore, in such cases, the DSN provides a simple and easily controlled interface.

The DSN Mark I system, operating in L-band, supported the flight projects during the first half of the 1960 decade. During the second half, the DSN introduced the Mark II system, operating in the S-band frequency range. The Mark I and II systems were especially designed to meet the requirements of each particular flight project. A sizable number of mission-dependent equipments and resources were used, and the number of the project independent/dependent interfaces was extensive. The DSN Mark III system is configured in accordance with the latest state-of-the-art in systems management and systems engineering. The basic objective of the Mark III DSN is to provide effective and reliable tracking and data acquisition support for the more complex planetary and interplanetary space flight missions in the 1970 decade. The DSN Mark III system was designed to serve the mission set of the seventies, and it will have sufficient flexibility to meet specific project requirements.

The DSN Mark III system will provide the following functions:

(1) *Acquisition of spacecraft telemetry data using standardized techniques.* The network will operate at higher and more valuable telemetry rates, for longer periods of time, covering longer distances and supporting multiple spacecraft simultaneously. The capability will also exist to interact efficiently with larger and more complex spacecraft and science packages.

(2) *Positive control of spacecraft using standardized commanding techniques.* The new capabilities will accommodate higher command bit rates covering longer deep space distances when operating directly from the control center by the flight project mission operations team. The advanced command capabilities will make possible simultaneous control of multiple spacecraft and the control of a variety of spacecraft types and scientific experiments.

(3) *Highly accurate radio navigation from Earth-based stations.* The improved radio metric tracking system will furnish precise range and range rate data at longer distances and will make simultaneous tracking and guidance of multiple spacecraft possible. A more accurate orbit computation capability will permit the accommodation of more precise planetary ephemerides and astrodynamical constants.

(4) *Support of complex mission operations requirements.* It will be possible to operate independently and simultaneously multiple-flight missions with some mission support areas at remote locations. The real-time evaluation capability to monitor the network's qualitative and quantitative performance will be an assurance to minimize loss of data and permit the identification of ground versus spacecraft failures.

(5) *Simulation of complex space flight operations.* An extensive simulation capability will permit spacecraft and ground network failure mode testing for flight operations training, and can also be used as a diagnostic tool for ground network testing and fault isolation.

The DSN started the detailed system design of the Mark III system in 1968, and implementation of this third generation system started in 1969. The phase-over between the Mark II and Mark III systems is taking place during the calendar year 1971. The tracking and data acquisition support configuration of the *Mariner 9* mission, which was launched in May 1971, represents the early version of the Mark III system. The network's configuration for the *Pioneer F* mission, to be launched in the latter part of February 1972, will resemble the major features of the Mark III system.

Figure 1 depicts the functional relationship between the six DSN systems and the three DSN facilities. The Tracking, Telemetry, and Command Systems perform the basic functions of the mission support. The Simulation, Monitoring, and Operations Control Systems are necessary to test the facilities, to train the operations teams, to monitor all DSN systems, and to control the operations of the DSN systems.

The DSN facilities can be grouped in three categories: (1) the Deep Space Instrumentation Facility (DSIF), with tracking stations located in California, Australia, Spain,

and South Africa (Table 1); (2) the Ground Communications Facility (GCF), with a centrally located Control Center in the Space Flight Operations Facility (SFOF) located at JPL, Pasadena, California; and (3) the SFOF, which also houses the mission support areas, where the project's mission operations teams carry out the following system functions: project control, flight path analysis, spacecraft analysis, and space science analysis. All facilities have the capability within each DSN system to operate in a bidirectional mode.

A detailed description of the DSN Telemetry, Tracking, and Command Systems is given below. The configuration and data flow of each system is defined as planned to support the *Pioneer F* and *G* missions. Additional interfaces with the flight project between the DSN subsystems of each DSN facility and DSN system are also shown.

The block diagrams of the DSN systems illustrate graphically the planned functions of each DSN system. Each diagram, as viewed from left to right, is divided into the three DSN facilities: DSIF, GCF, and SFOF. Each facility is shown as a group of component subsystems connected with data flow paths.

III. DSN Telemetry System

The DSN Telemetry System is depicted in Fig. 2 and its equipment/subsystem and software capabilities are described in Tables 2 and 3, respectively. The figure describes the 26-m deep space stations configured to support the *Pioneer F* and *G* missions during their cruise phase. The basic telemetry system capabilities of the 64-m deep space stations are similar to the 26-m stations.

The DSN Telemetry System provides the capability for acquisition, conversion, handling, display, distribution, processing, and selection of telemetry data. Telemetry data are defined as the engineering and science information, including video, received from flight spacecraft via the telecommunications links.

The basic characteristics of the DSN Telemetry System will be as follows:

(1) Centralized control from the SFOF of the DSN Telemetry System configuration. This will include the automatic execution by the deep space stations of configuration and telemetry standards and limits messages compiled by the DSN Telemetry Analysis Group, centrally located in the SFOF.

(2) Real-time reporting of DSN Telemetry System status to DSN Operations Control with digital television (DTV) displays through the Monitor System.

(3) Ability to handle a wide range of spacecraft data rates while simultaneously supporting multiple-project and multiple-data streams.

(4) Capability in the SFOF to process data in real time from one or more deep space stations and missions simultaneously without interference. There will be a capability to support missions in both test and flight operations phases.

(5) Capability at each deep space station for subcarrier demodulation, bit detection, and data decoding; preparation of a digital Original Data Record (ODR); and formatting for a high-speed transmission to the SFOF.

IV. DSN Command System

The DSN Command System is shown in Fig. 3 and its equipment/subsystem capabilities are given in Table 4. The DSN Command System provides the means to generate and transmit commands to appropriate spacecraft-related verification, display, and control functions which are incorporated within the system to ensure that these command operations are successful. The DSN Command System provides a project with the means to command the spacecraft from the SFOF. The project may enter commands by input/output (I/O) devices in the SFOF, or by high-speed data (HSD) lines into SFOF from a remote location.

V. DSN Tracking System

A functional block diagram showing the DSN Tracking System configured for 26-m stations is given in Fig. 4 and that for 64-m stations is given in Fig. 5. Equipment/subsystem capabilities for each are described in Tables 5 and 6, respectively.

The DSN Tracking System provides validated, precision radio metric data to flight project users by performing the tasks of data acquisition, handling, editing, calibration, display, distribution, validation, and prediction. In addition, a tracking data selection process is made available to the project users.

DSN metric data are defined as angle and doppler data generated by the DSIF and associated data such as lock

status, time, frequency, data condition, and calibration. Detailed interface design is contained in Ref. 5.

The key characteristics of the DSN Tracking System are as follows:

(1) Processing of DSN metric data in any standard DSN Tracking System format.

(2) Multimission capability to perform:

(a) Simultaneous tracking and data acquisition of several spacecraft within the DSIF by the use of multiple DSSs.

(b) Data handling at DSSs and transmission of data to the SFOF.

References

1. Siegmeth, A. J., "*Pioneer* Mission Support," in *The Deep Space Network Progress Report*, Technical Report 32-1526, Vol. II, pp. 6–17. Jet Propulsion Laboratory, Pasadena, Calif., Apr. 15, 1971.
2. Siegmeth, A. J., "*Pioneer* Mission Support," in *The Deep Space Network Progress Report*, Technical Report 32-1526, Vol. III, pp. 7–19. Jet Propulsion Laboratory, Pasadena, Calif., June 15, 1971.
3. Siegmeth, A. J., "*Pioneer* Mission Support," in *The Deep Space Network Progress Report*, Technical Report 32-1526, Vol. IV, pp. 13–21. Jet Propulsion Laboratory, Pasadena, Calif., Aug. 15, 1971.
4. *DSN Standard Practice, DSN/Flight Project Interface Design Handbook*, Document 810-5, Rev. A, Change 3, Aug. 1971 (JPL internal document).
5. *Deep Space Network System Requirements, Detailed Interface Design*, Document 820-13, Rev. A, Change 11, Aug. 1971 (JPL internal document).

Table 1. Deep Space Instrumentation Facilities

Deep Space Station	Location	Subnet	*Pioneer F and G* support function
DSS 11	Goldstone, California	26-m antennas	Cruise
DSS 12	Goldstone, California	26-m antenna	Cruise
DSS 14	Goldstone, California	64-m antenna	Mission enhancement and Jupiter encounter
DSS 41	Woomera, Australia	26-m antenna	Cruise
DSS 42	Weemala, Australia	26-m antenna	Cruise
DSS 51	Johannesburg, South Africa	26-m antenna	Launch and cruise
DSS 61	Robledo, Spain	26-m antenna	Cruise
DSS 62	Cebreros, Spain	26-m antenna	Cruise
DSS 71	Cape Kennedy, Florida		Spacecraft/DSN compatibility verification
CTA 21	JPL, Pasadena, California		Spacecraft/DSN compatibility testing
DSS 43[a]	Ballima, Australia	64-m antenna	Mission enhancement and Jupiter encounter
DSS 63[a]	Robledo, Spain	64-m antenna	Mission enhancement and Jupiter encounter

[a]After July 1973.

Table 2. DSN Telemetry System equipment/subsystem capabilities for 26-m stations (Fig. 2)

Ⓐ Output time to tag ground receiver data to 1 ms.

Ⓑ System temperature as described in Ref. 4.

Ⓒ The High-Speed Data Assembly receives data from different DSIF systems. Priorities must be assigned by the Project/DSN for transmission of data to the SFOF.

Table 3. DSN Telemetry System software capabilities for 26-m stations (Fig. 2)

ⓐ DSIF Telemetry and Command Subsystem

a. Input processing

(1) Accept one bit stream of combined engineering and science telemetry data varying between 16 and 2048 bps uncoded, or between 32 and 4096 sps coded.

(2) Also accept associated input messages:

(a) Ground receiver automatic gain control (AGC).

(b) Time reference.

(c) Hardware lock status.

(d) Operator message through the computer console.

(e) Nonreal-time playback from digital and post-SDA analog records.

b. Internal processing

(1) Control bit synchronization and detection.

(2) Control decoding.

(3) Calculate signal-to-noise ratio (SNR) and ground AGC in dB.

c. Output processing

(1) Format and output for transmission to the SFOF via HSD circuits.

(2) Subsystem status to Monitor System.

(3) Data to digital ODR.

ⓑ Central Processing System—360/75

a. Input processing

(1) Accept data simultaneously from up to three HSD circuits, separate telemetry and partial status data, route data for internal processing, input process log tapes, and route telemetry HSD messages to Ames Research Center (ARC).

(2) Frame synchronization, pseudo-noise sync error calculation.

(3) Telemetry validation and selection on the basis of TCP signal-to-noise, GCF error, timing, and frame sync quality.

(4) Alarm limits, range suppression, suppression tolerances, data number to engineering unit conversion, data averaging, logic tests, continuity tests.

(5) Interface with SFOF Internal Communications Subsystem, drive hard copy, and volatile displays.

b. Internal processing

(1) Decommutate, and format telemetry data streams.

(2) Process and analyze DSN status and alarm data.

(3) Compare DSN standards (SNR ground AGC, frame sync quality) to predicts.

(4) Generate system log tapes, SDR and MDR files.

c. Output processing

(1) Hard copy and volatile display data to UTDS.

(2) Master Data Record (MDR) tapes.

(3) DSN status and alarms to Telemetry Analysis Group, Monitor System, and Mission Support Area (MSA).

(4) System configuration and replay request messages to the DSIF.

(5) Telemetry data to Remote Information Center via HSDL.

(6) Data to the 1108.

Table 4. DSN Command System equipment/subsystem capabilities for 26- and 64-m stations (Fig. 3)

Ⓐ DSS 14 will have capability for redundant exciters and dual carriers. All other stations shall have a single exciter and single carrier capability.

DSS 14 will have capability to transmit at 400 kW; the 26-m subnet stations will have 10-kW transmit capability; the 26-m mutual stations will have 20-kW transmit capability.

Ⓑ SDS 920 telemetry and command processor program capabilities for command: The following functions shall be available for one spacecraft, sharing the TCP with Telemetry System programs that are not to exceed 2 kbps uncoded.

a. *Input processing*

(1) HSD command, configuration, standards and limits, recall request, disable messages SFOF.

(2) Command messages, enables/disables, and recall messages via local DSS manual input (backup).

b. *Output processing*

(1) Output process and format, for HSD transmission, the following data:

(a) HSD verify messages to inform the SFOF that command HSD messages were received by the 920 with or without errors.

(b) Command recall response messages to inform the SFOF of either:

(i) The status of equipment and software of the multimission command system.

(ii) The current command messages stored within the TCP, but not yet processed.

(c) *Confirm/abort* messages to inform the SFOF that proper command was either transmitted by the DSS, or that an abort occurred while in process of transmitting. Transmitted bits are identified.

(2) Output process and format, for transmission to Digital Instrumentation Subsystem (DIS) computer, via 24-bit parallel register, the following types of monitor data:

(a) All hardware status indicator information from multimission command hardware.

(b) Error indication if bit-by-bit comparison between CMA and TCP shows difference.

(c) Error indicator when received HSD command message or request message blocks indicate HSD error.

(3) Output process and format teletype messages to SMC for local display containing such information as:

(a) Indication of *command* message or *enable/disable* received.

(b) Indication of command *request/response* messages.

(c) Command *confirm/abort* messages.

(d) Indication of command verification message sent.

(4) Output process and format digital magnetic log tape ODR containing all received commands, *enable/disable* messages, command instructions, command confirmation/abort (data combined on tape with telemetry data for the ODR).

(5) Transmit command bits to CMA.

Table 4 (contd)

c. *Internal processing*

(1) Extract spacecraft number from command instruction message and use to obtain parameters with which to initialize multimission command hardware.

(2) Keep time against computer clock reference until stored command is to be processed and sent to the CMA.

(3) Extract required parameters from command instruction message; buffer and store for recall response.

(4) If the command has been *enabled,* transmit command at time given in command message, or immediately, if specified.

(5) Perform verification on command message received over HSD (GCF error detection) and prepare verification message.

(6) Compare data in command instruction message and generate alarm if system is out of tolerance.

(7) If a command is *disabled,* remove it from storage; if command is in process, inhibit transmission of remaining bits.

Ⓒ Located at the station manager's console.

Ⓓ Not used.

Ⓔ The CMD Message Accountability Processor provides automatic interrogation of the DSSs as to status of the commands sent from the SFOF to the DSSs, and provides a continuous accounting of all commands entered into the DSN Command System at the SFOF.

Ⓕ The HSD Message Block Output Processor formats, buffers, and transmits command messages to the appropriate DSS. If no verified response is received, the message is repeated. The time between repeats and the number of repeats before an alarm is raised are controllable.

Ⓖ The HSD Block Return Processor handles verification, alarm, and abort messages received via HSD from DSSs and generates appropriate displays of status and alarms. The data are also presented to the SDR Processor.

Ⓗ The Message Construct Program performs the following functions:

(1) Accepts project generated command messages and prepares them for HSD transmission.

(2) Accepts control messages for command processing and display.

(3) Accepts configuration, standards and limits, and test command messages from Command Analysis Group.

(4) Accepts project generated *enable/disable* messages and transmits to DSS; rejects *enable* if the command message has not yet been verified.

(5) Accepts command recall request messages and prepares for transmission or interrogates CPS buffer and displays command recall response messages.

(6) Compares commands input against critical command table and stops further processing of command until interlock is input from 2260 to release inhibit.

(7) Translates alphanumeric input into binary bit stream for input to the HSD blocks.

Ⓘ The SDR Processor logs and verifies all SFOF–DSS HSD Command System traffic.

Ⓙ The MDR Processor extracts the *confirm* and *abort* message data from the SDR files, generates summaries and labels for the MDR, and writes the MDR data on file or tape.

Table 5. DSN Tracking System equipment/subsystem capabilities for 26-m stations (Fig. 4)

Ⓐ Not used for *Pioneer* Project.

Ⓑ The Tracking Data Processor samples and formats Greenwich Mean Time, doppler, range, angles, and partial status for transmission ⑩ to the Antenna Pointing Subsystem (prime) and/or via TTY ⑯ to the GCF Comm Processor Ⓝ. The reperforated TTY tape is maintained as the low-rate ODR ⑪ (rates 1 per 6 s).

Ⓒ The Antenna Pointing Subsystem receives metric data from the TDP ⑩. The metric data is reformatted to conform to standard National Aeronautics and Space Administration Communications Network (NASCOM) HSD block format and is transmitted via HSD ⑰ to the SFOF. The APS punches a tape for the DSIF ODR ⑫ for rates of 1 per 6 s. The APS also receives predictions via HSD ㉛ or TTY ㉞ (torn paper tape), interpolates these predictions to 1 per second, and provides interpolated angles to the Antenna Pointing Programmer (APP) ⑭. DSIF tracking system partial status is transmitted to the DIS via a 24-bit parallel transfer register ⑬.

Ⓓ The APP receives 1-per-second predicted angular positions from APS and further interpolates these angles to 50 per second; it compares the 50-per-second predictions with the antenna angle readout ⑨ and generates an error signal to the Antenna Servo Subsystem ⑮. The Antenna Servo Subsystem then drives the antenna to null this error signal.

Ⓔ The Digital Instrumentation Subsystem receives the tracking system partial status via the 24-bit parallel transfer register for display to DSS operational control. Predictions are transmitted from the SFOF to the DSS via HSDL ㉛ and are formatted and displayed ㉜ to DSS operational control for spacecraft acquisition.

Ⓕ The SFOF Tracking Data Input Processor provides a data format identification, decommutation, data conversion, and reformatting and displays input data. It also provides a capability of the derivation of the sample rate, line outage detection, and alarm classification.

Ⓖ The Pseudo-Residual Processor computes the difference between observables and predictions, identifies blunder points, computes data "noise" and provides a data quality index to the Master File Program (MFP) that is added to the SDR.

Table 5 (contd)

Ⓗ The MFP creates an SDR on disk or tape, provides a capability of rejecting data, provides a data accountability function, edits tracking data, tags the SDR with the quality indicator computed in Ⓖ, transfers data to the 1108 through the Project Data Selector Ⓙ ⑱, and provides a display capability.

Ⓘ The SDR Accountability Program computes the percentage of data received "good" as compared with the scheduled data availability.

Ⓙ The Project Data Selector Program provides a capability to a project for the data selection ⑱ based on spacecraft, station, data type, and sample rate. The selected data is transferred to the project by tape or the electrical interface. The data selection program is also used to provide a magnetic tape ⑱ by spacecraft identifier for the DSN Master Data Record.

Ⓚ The Tracking System Analytical Calibration (TSAC) Program computes calibrations for time and polar motion variations, transfers station locations, calibrates data for charged particles, and calibrates data for tropospheric corrections. These calibrations are made available to the project via the TSAC SDR ⑲ and Project Data Selector Ⓙ.

Ⓛ The Predict Program computes DSS observables from a project-supplied spacecraft ephemeris ㉘. Also computed are DSS view periods and spacecraft events, such as occultation.

Ⓜ The Operations Control Software formats and transmits to the DSS, via HSDL ㉛ or TTY ㉚ (dependent on availability), the validated predictions that were transferred to the Prediction File ㉙.

Ⓝ Communications Processor which routes TTY data.

Ⓞ The Orbit Data Editor (ODE) Program accepts data from the Project Data Selector Ⓙ. This data is edited, calibrated, and formatted for inclusion on the master file of DPODP Ⓟ.

Ⓟ The Double Precision Orbit Determination Program accepts data from the Orbit Data Editor Ⓞ and determines a "best" state vector for the observables.

Ⓠ The Trajectory Program (DPTRAJ) provides a spacecraft ephemeris tape based on DPODP ㉖ solution, or a state vector provided by other sources ㉗. This spacecraft ephemeris is transferred to the 360/75 via tape or the electrical interface ㉘.

Table 6. DSN Tracking System equipment/subsystem capabilities for 64-m stations (Fig. 5)

Ⓐ The DSIF Tracking Subsystem (DTS), a single multipurpose computer, performs the following functions: tracking data formatting, planetary ranging, error detection, predict generation, and antenna pointing.

Ⓑ The ranging function of the DTS provides ranging information at planetary distances (not used by *Pioneer* Project).

Ⓒ The Tracking Data Processor (TDP) function of the DTS samples and formats GMT, doppler, range, angles, errors, and partial status for transmission via HSD ⑰ to the SFOF. The TDP also generates onsite tracking data predictions for station use and for antenna pointing operations ⑭. Detected alarms are provided the Digital Instrumentation Subsystem ⑬. The DTS also receives predictions and control messages via HSDL ㉞ from the SFOF.

Ⓓ The antenna pointing function of the DTS receives information from the TDP, compares with predictions of antenna angles, and generates an error signal to the Antenna Servo Subsystem ⑮.

Ⓔ The Digital Instrumentation Subsystem receives partial status and error alarms from the TDP ⑬ for monitor and operational control. The DIS also receives predicts via HSDL ㉛ from the SFOF and outputs page prints of the predicts ㉜ for station spacecraft acquisition operations.

Ⓕ The SFOF Tracking Data Input Processor (TYDIP) provides a data format identification, decommutation, data conversion and reformatting, and displays input data. It also provides a capability of the derivation of the sample rate, line outage detection, and alarm classification.

Ⓖ The Pseudo-Residual Processor computes the difference between observables and predictions, identifies blunder points, computes data "noise" and provides a data quality index that is added to the SDR.

Ⓗ The Master File Program (MFP) creates an SDR on disk or tape, provides a capability of rejecting data, provides a data accountability function, edits radio metric data, tags SDR with the quality indicator computed in Pseudo-Residual Program Ⓖ, transfers data to the 1108, and provides a display capability.

Table 6 (contd)

Ⓘ The System Data Record accountability program computes the percentage of data received "good" as compared with the scheduled data availability.

Ⓙ The Project Data Selector Program provides a capability to a project for the data selection ⑱ based on spacecraft, station, data type, and sample rate. The selected data is transferred to the project by tape or electrical interface. The data selection program is also used to provide a magnetic tape ⑱ by spacecraft identifier for the DSN Master Data Record.

Ⓚ The Tracking System Analytical Calibration (TSAC) Program computes calibrations for time and polar motion variations, transfers station locations, calibrates data for charged particles and calibrates data for tropospheric corrections. These calibrations are made available to the project via the TSAC SDR ⑲.

Ⓛ The Predict Program computes DSS observables from a project-supplied spacecraft probe ephemeris ㉘. Also computed are DSS view periods and spacecraft events, such as occultation ㉙.

Ⓜ The DSN Operations Control software accepts the validated predicts from the prediction files and formats and transmits the predicts to the DSS via HSDL ㉛ or teletype ㉚, dependent on availability.

Ⓞ The Orbit Data Editor accepts data from the Project Data Selector ⑱, which is edited, calibrated, and formatted for inclusion on the master file of DPODP Ⓟ.

Ⓟ The Double Precision Orbit Determination Program accepts data from the Orbit Data Editor and determines a "best" state vector for the observables.

Ⓠ The Trajectory Program (DPTRAJ) provides a spacecraft ephemeris tape based on DPODP solution or a state vector provided by other sources ㉗. This spacecraft probe ephemeris is transferred to the 360/75 via tape or the electrical interface ㉘.

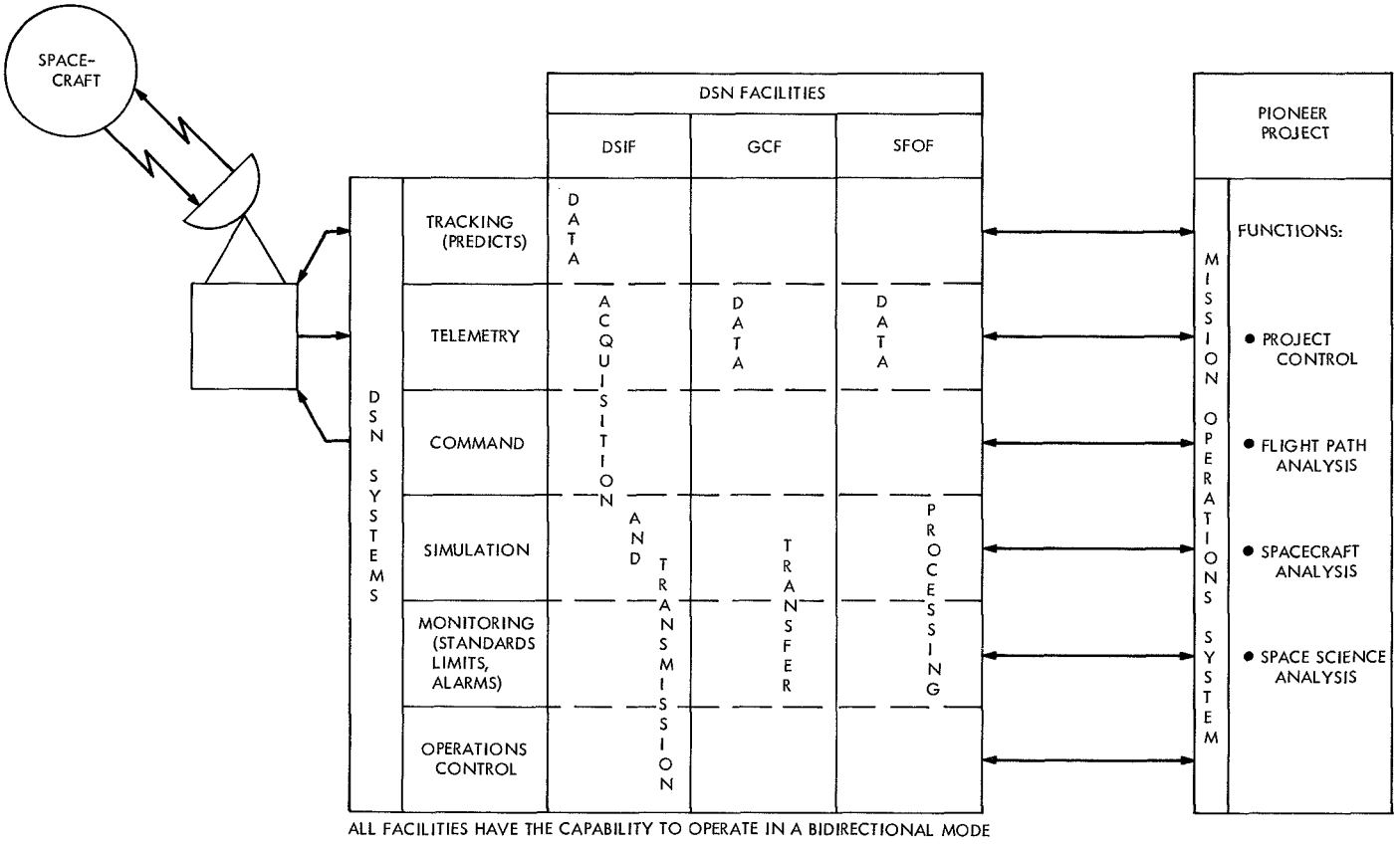

Fig. 1. Deep Space Network Systems

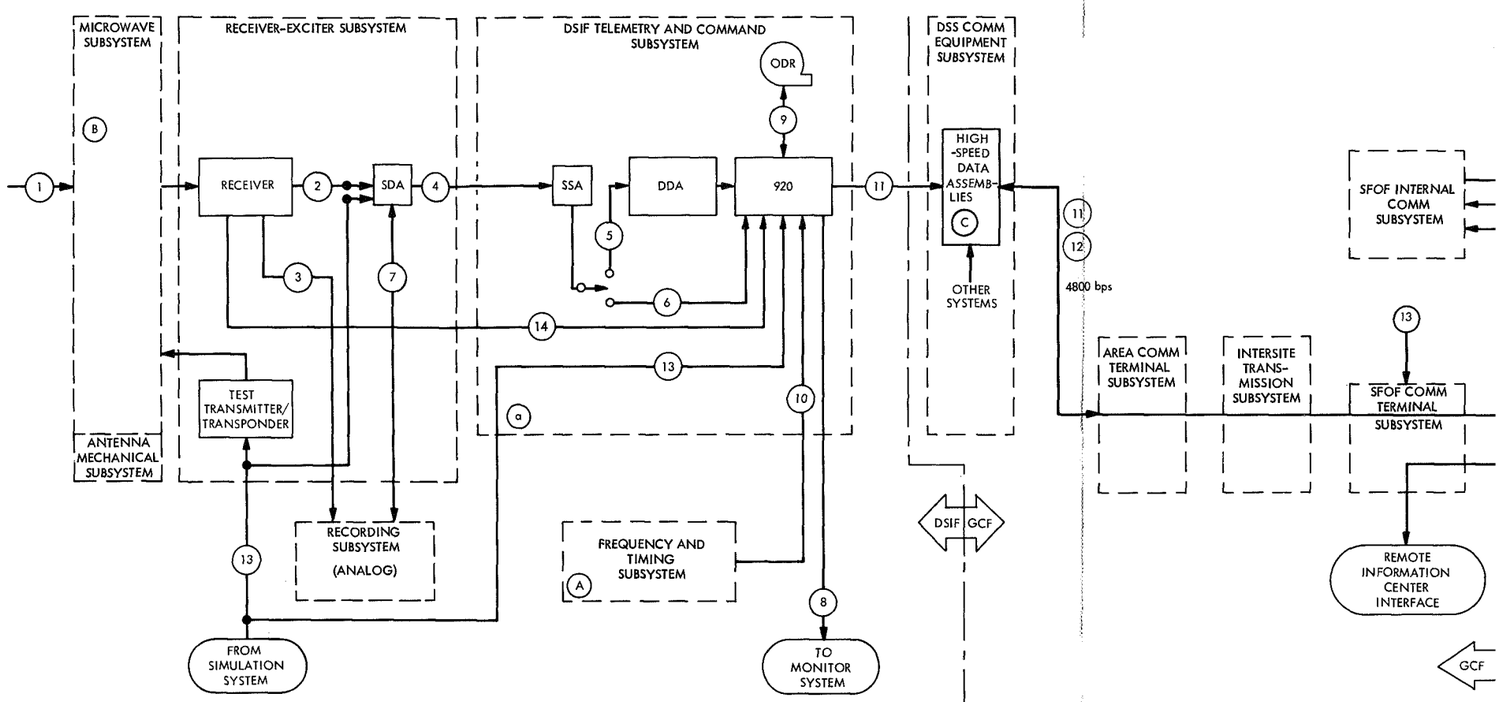

(1) CARRIER FROM ONE SPACECRAFT

(2) 32.768-kHz SUBCARRIER PHASE-MODULATED ON 10-MHz CARRIER

(3) 32.768-kHz SUBCARRIER WITH TELEMETRY DATA (NO PLAYBACK CAPABILITY)

(4) DATA STREAM 16-2048 bps UNCODED OR 32-4096 sps CODED

(5) CODED DATA

(6) UNCODED DATA

(7) SUBCARRIER DEMODULATOR ASSEMBLY (SDA) OUTPUT AND PLAYBACK OF RECORDED SDA OUTPUT

(8) INITIAL CONFIGURATION AND EVENT, TELEMETRY INSTRUMENTATION STATUS

(9) DIGITAL ODR RECORDING AND PLAYBACK (DELETED, CODED FRAMES WILL BE PLAYED BACK THROUGH THE DDA FOR REPLAYED DATA)

(10) TIME FOR GROUND DATA TAGGING

(11) TELEMETRY DATA TO SFOF VIA HIGH-SPEED DATA LINE, INCLUDES:
(a) ENGINEERING AND SCIENCE DATA AT 2048 bps MAXIMUM,
(b) REPLAY OF ODR NOT SIMULTANEOUS WITH (a), AND (c) DSS TELEMETRY SYSTEM PARTIAL STATUS (SNR, LOCK, AND CONFIGURATION INDICATORS) AND SUPPLEMENTARY DATA (GROUND ACG AT 10 samples/s MAXIMUM)

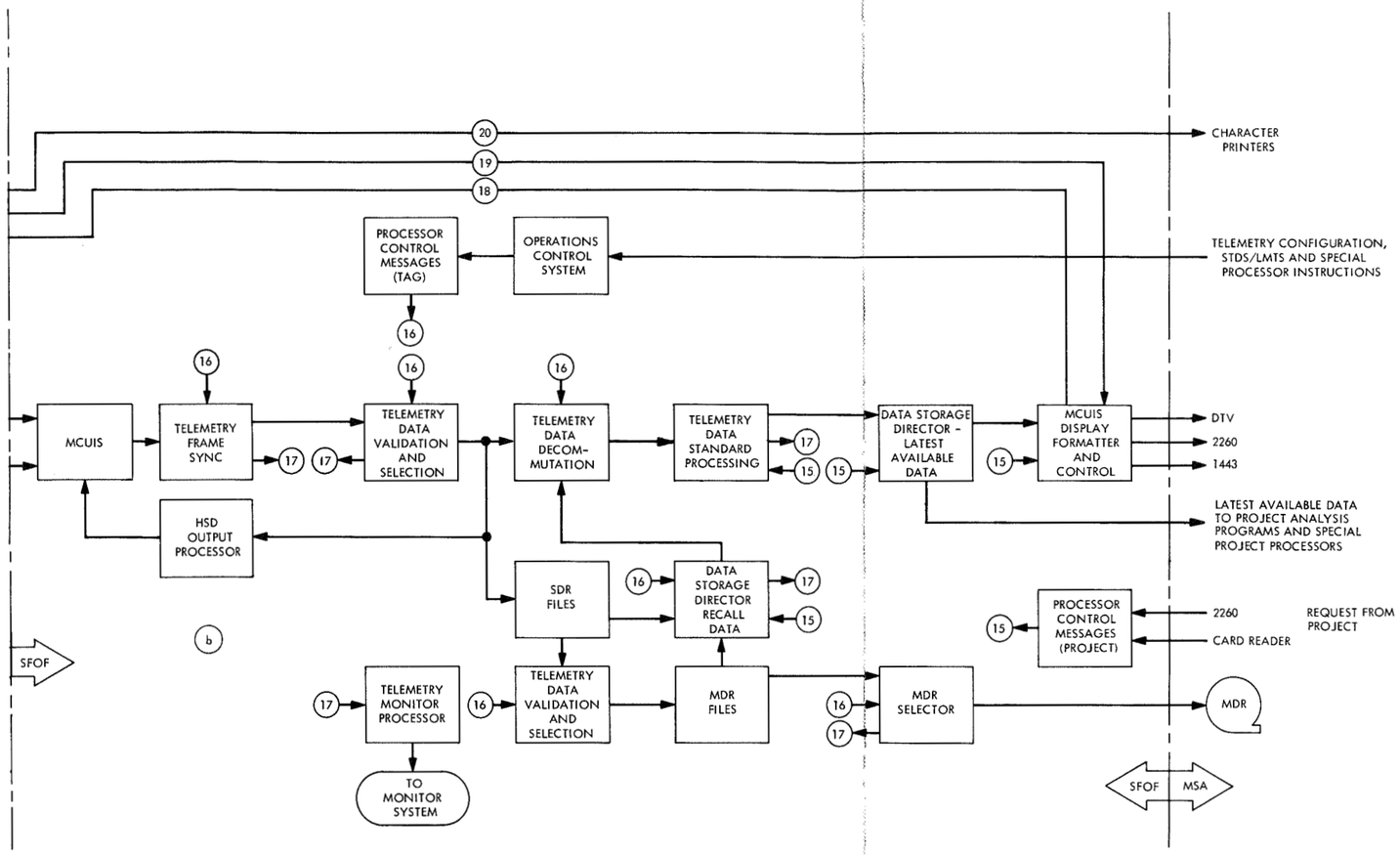

⑫ CONFIGURATION AND REPLAY REQUEST MESSAGES FROM THE SFOF TO THE DSIF VIA HSDL

⑬ SIMULATED TELEMETRY INPUTS

⑭ GROUND RECEIVER AGC

⑮ CONTROL FOR TELEMETRY DATA PROCESSING BY THE PROJECT FROM USER TERMINAL AND DISPLAY SUBSYSTEM (UTDS)

⑯ CONTROL FOR TELEMETRY MDR PROCESSING BY DSN TELEMETRY ANALYSIS GROUP FROM UTDS

⑰ DSN TELEMETRY SYSTEM INSTRUMENTATION STATUS AND SELECTED DECOMMUTATED SPACECRAFT PARAMETERS FOR MONITOR DISPLAY

⑱ CONTROL TO SFOF INTERNAL COMM SUBSYSTEM FOR DIGITAL TV

⑲ DIGITAL TV SIGNALS FOR DISPLAY

⑳ 360/75 CHARACTER PRINTER OUTPUT FROM COMMUNICATIONS PROCESSOR

Ⓐ TO Ⓒ DEFINED IN TABLE 2

ⓐ TO ⓑ DEFINED IN TABLE 3

Fig. 2. DSN Telemetry System 26-m DSS functional block diagram for *Pioneer F* and *G* cruise mode configuration

3

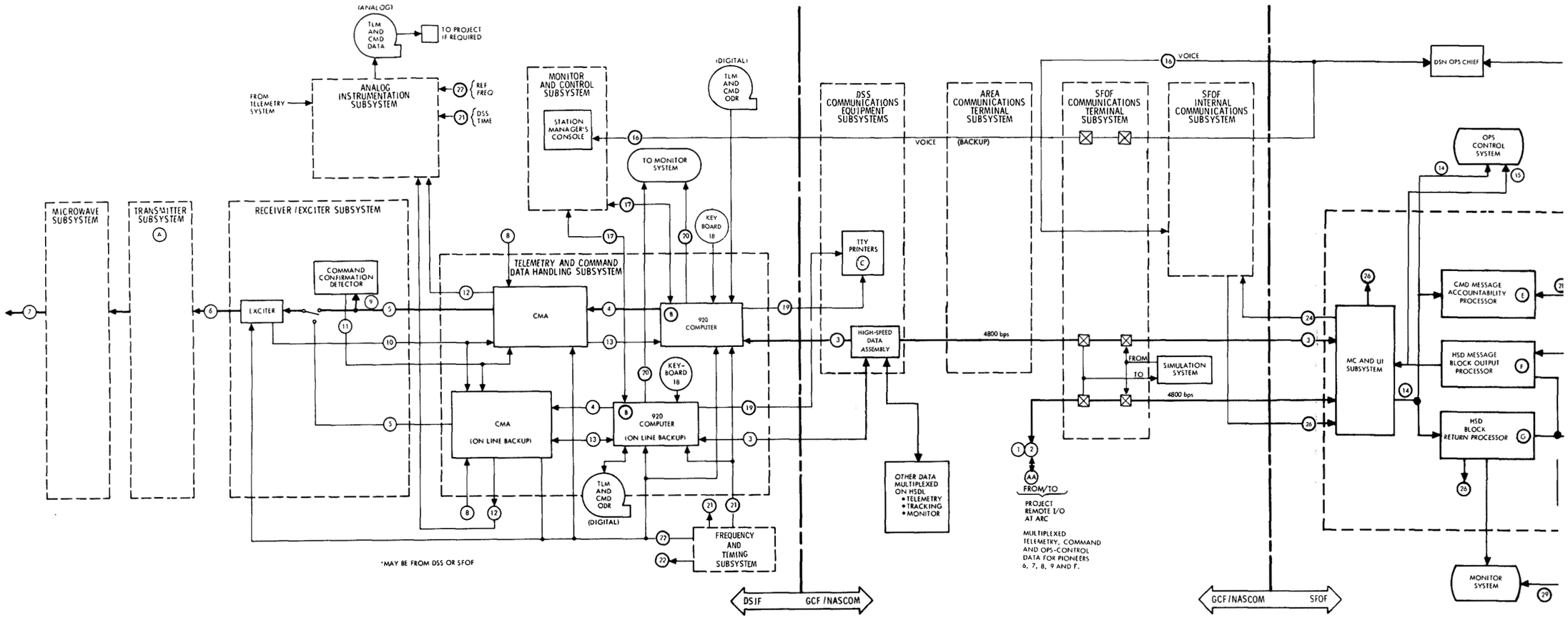

① COMMAND MESSAGE OUTPUTS FROM REMOTE MSA TO SFOF

② SFOF-PROCESSED COMMAND INFORMATION RESPONDING TO ① AND PROVIDING INFORMATION FOR REMOTE MSA DISPLAYS

③ COMMAND MESSAGES, COMMAND INSTRUCTION MESSAGES, AND COMMAND RECALL REQUEST MESSAGES TO DSS; COMMAND VERIFICATION, CONFIRM/ABORT, ALARM, AND RECALL RESPONSE MESSAGES TO SFOF

④ COMMAND WORD BITS

⑤ COMMAND MODULATED SUBCARRIER

⑥ TRANSMITTER DRIVE

⑦ AMPLIFIED, MODULATED S-BAND UPLINK CARRIER

⑧ TRANSMITTER, EXCITER, AND MODULATOR, ON OR OFF INDICATION

⑨ MODULATOR OUTPUT FOR COMMAND CONFIRMATION

⑩ EXCITER FREQUENCY

⑪ DETECTED MODULATOR OUTPUT, ITEM ⑨ FOR ABORT OR CONFIRMATION

⑫ COMMAND MODULATION ASSEMBLY OUTPUT FOR RECORDING ON ANALOG TAPE

⑬ CONTROL INFORMATION, COMMAND BITS, AND CONFIGURATION INFORMATION FED BACK TO THE COMPUTER

⑭ COMMAND SYSTEM MESSAGES SENT FROM DSS TO SFOF

⑮ COMMAND MESSAGES TO BE USED BY OPERATIONS CONTROL SYSTEM TO LIST EXPECTED DSN CONFIGURATION CHANGES RESULTING FROM COMMANDS TRANSMITTED

⑯ VOICE CIRCUITS FOR EMERGENCY MODE COMMAND COORDINATION

⑰ MANUAL MODE ENABLE AND DISPLAY CONTROL SIGNALS

⑱ MANUAL MODE COMMAND INPUT, ENABLED BY STATION MANAGER

⑲ COMMANDS, VERIFICATION, CONFIRMATION, ABORT, AND ALARM INFORMATION FOR LOCAL DISPLAY AT DSS

⑳ COMMAND SYSTEM CONFIGURATION, STATUS, AND ALARMS

㉑ DSS TIME

㉒ REFERENCE FREQUENCIES

㉓ CONTROL MESSAGES FOR COMMAND PROCESSING AND DISPLAY, RECALL RESPONSE MESSAGES, AND DATA DISPLAY

Fig. 3. DSN Command System 26- and 64-m DSS functional block diagram for Pioneer F and G cruise mode configuration

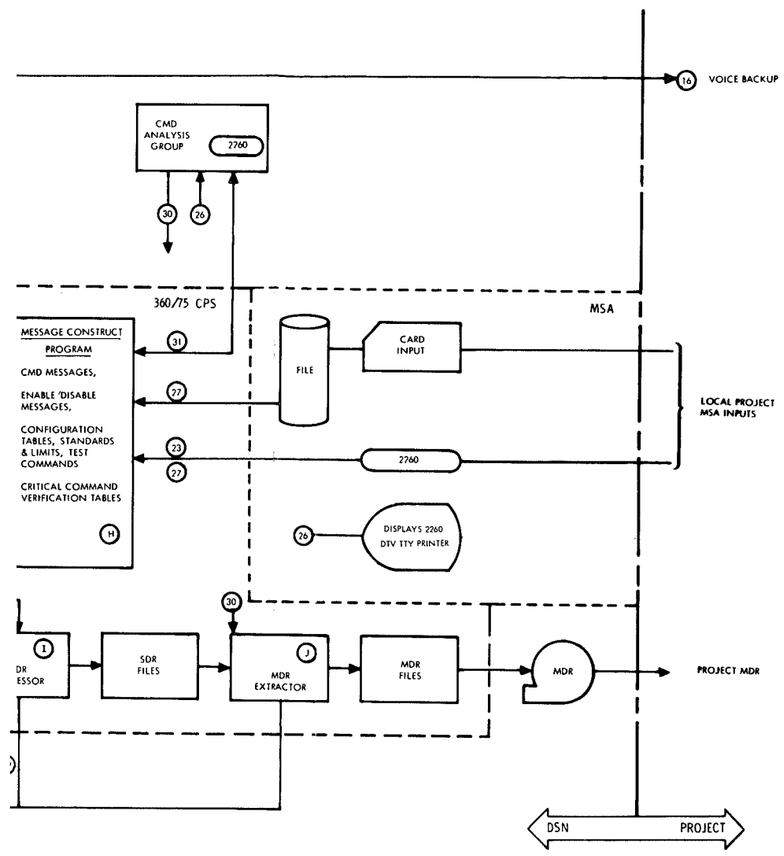

(24) CONTROL TO SFOF INTERNAL COMMUNICATIONS SUBSYSTEM FOR CHARACTER PRINTER AND CLOSED-CIRCUIT TELEVISION (CCTV) DISPLAY

(25) NOT USED

(26) DATA FOR CHARACTER PRINTER, CCTV DISPLAY, DTV DISPLAYS, AND HIGH-SPEED PRINTERS

(27) COMMAND MESSAGE INPUTS

(28) COMMAND MESSAGES FOR ACCOUNTABILITY PROCESSOR

(29) DATA SUMMARIES AND ALARMS

(30) INPUTS, RECALL REQUESTS TO MDR PROCESSOR FROM COMMAND ANALYSIS GROUP

(31) CONFIGURATION, STANDARDS AND LIMITS, TEST COMMANDS, RECALL REQUEST INPUTS

(A) TO (J) DEFINED IN TABLE 4

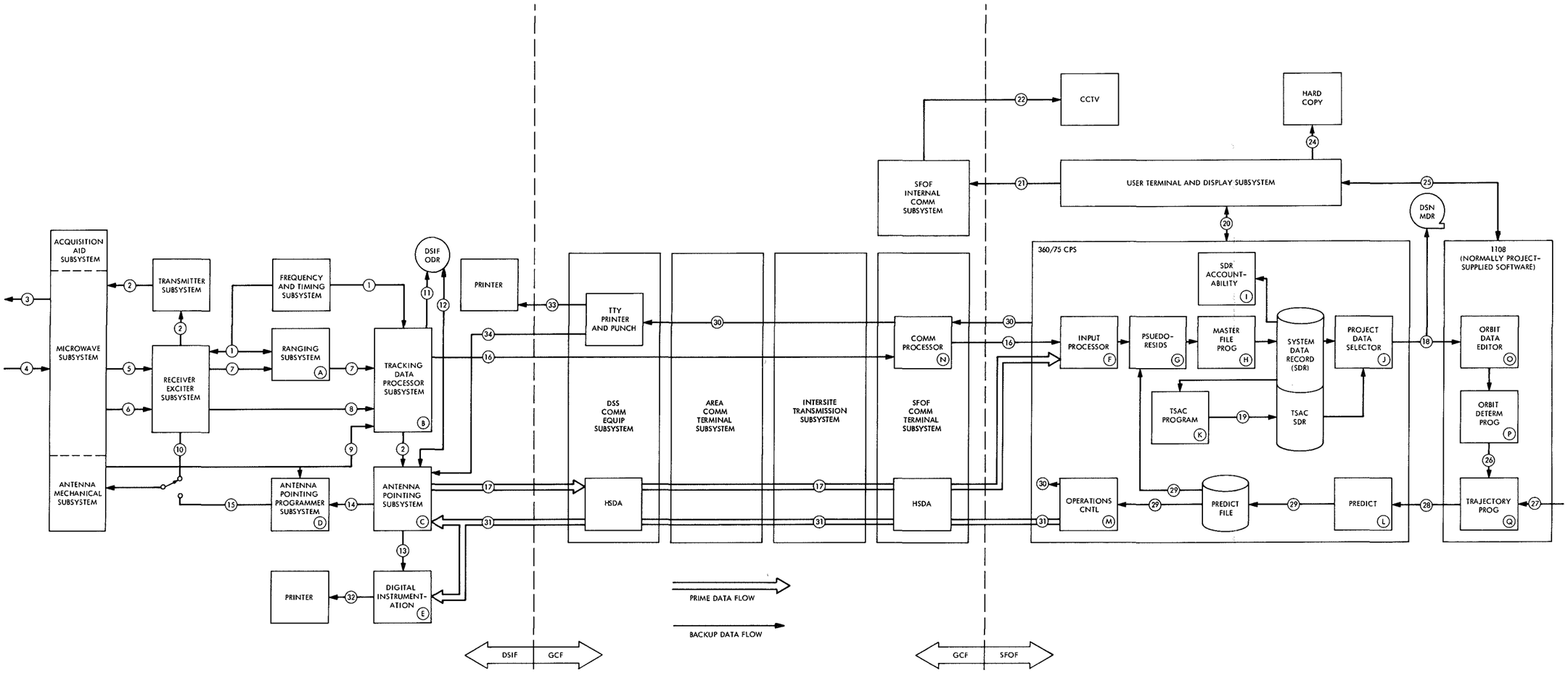

① REFERENCE FREQUENCY/TIME
② TRANSMITTER DRIVE
③ AMPLIFIED, MODULATED S-BAND CARRIER
④ S-BAND DOWNLINK
⑤ RECEIVER 1 INPUT
⑥ RECEIVER 2 INPUT
⑦ RANGE DATA AND RANGE PARTIAL STATUS (NOT USED BY PIONEER PROJECT)
⑧ DOPPLER DATA, TRANSMITTER VCO FREQUENCY, AND DOPPLER PARTIAL STATUS
⑨ ANGLE DATA AND ANGLE PARTIAL STATUS
⑩ AUTOTRACK FEEDBACK
⑪ LOW-RATE ODR (RATES EQUAL TO OR LESS THAN 1 PER 6 s)
⑫ HIGH-RATE ODR (RATES GREATER THAN 1 PER 6 s)
⑬ TRACKING SYSTEM PARTIAL STATUS TO MONITOR
⑭ ANGLE PREDICTIONS INTERPOLATED TO 1 PER SECOND
⑮ ANTENNA SERVO-DRIVE SIGNALS
⑯ LOW-RATE FORMATTED METRIC DATA VIA TTY (BACKUP)
⑰ LOW- AND HIGH-RATE FORMATTED METRIC DATA VIA HSD (PRIME)
⑱ METRIC DATA FROM SYSTEM DATA RECORD TO PROJECT AND DSN MDR
⑲ CALIBRATIONS FOR METRIC DATA
⑳ SFOF TRACKING SYSTEM I/O INSTRUCTIONS
㉑ DATA AND STATUS FOR DISPLAY VIA CCTV
㉒ CCTV DISPLAYS OF ㉑
㉓ NOT USED
㉔ HARD COPY DISPLAY OF REQUESTED DATA
㉕ PROJECT I/O INSTRUCTIONS TO ORBIT SOFTWARE
㉖ STATE VECTOR FROM DOUBLE PRECISION ORBIT DETERMINATION PROGRAM
㉗ STATE VECTOR FROM EXTERNAL SOURCE
㉘ SPACECRAFT EPHEMERIS
㉙ DSS PREDICTED OBSERVABLES
㉚ DSS PREDICTIONS TRANSMITTED VIA TTY BY OPERATIONS CONTROL SOFTWARE
㉛ DSS PREDICTIONS TRANSMITTED VIA HSDL BY OPERATIONS CONTROL SOFTWARE
㉜ PAGE PRINT OF ㉛ FOR DSS ACQUISITION OF SPACECRAFT (PRIME)
㉝ PAGE PRINT OF ㉚ FOR DSS ACQUISITION OF SPACECRAFT (BACKUP)
㉞ PAPER TAPE OF PREDICTIONS FOR ANTENNA POINTING SUBSYSTEM (BACKUP)

Ⓐ TO Ⓠ DEFINED IN TABLE 5

Fig. 4. DSN Tracking System 26-m DSS functional block diagram for *Pioneer F* and *G* cruise mode configuration

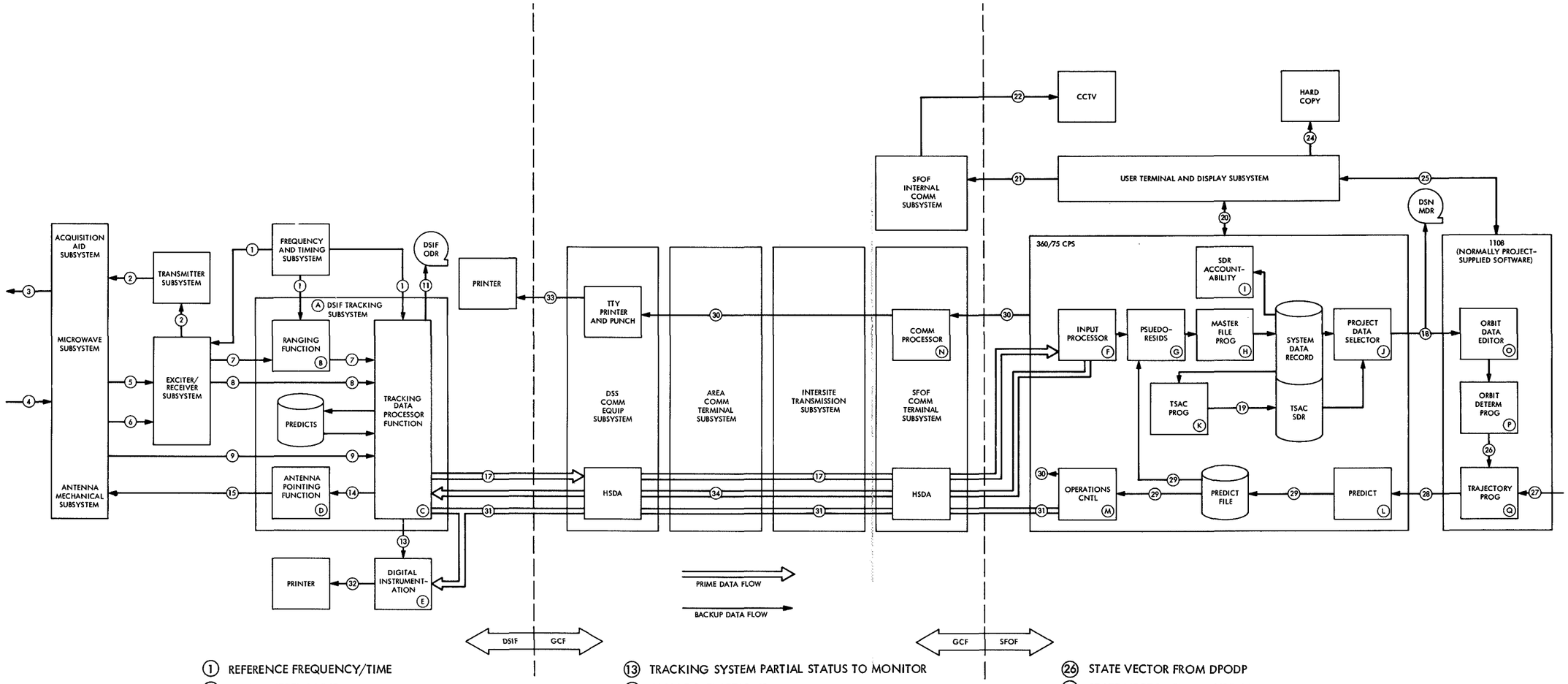

(1) REFERENCE FREQUENCY/TIME
(2) TRANSMITTER DRIVE
(3) AMPLIFIED, MODULATED S-BAND CARRIER
(4) S-BAND DOWNLINK
(5) RECEIVER 1 INPUT
(6) RECEIVER 2 INPUT
(7) RANGE DATA AND RANGE PARTIAL STATUS (NOT USED BY PIONEER PROJECT)
(8) DOPPLER DATA, TRANSMITTER VCO FREQUENCY, AND DOPPLER PARTIAL STATUS
(9) ANGLE DATA AND ANGLE PARTIAL STATUS
(10) NOT USED
(11) DSIF ODR
(12) NOT USED
(13) TRACKING SYSTEM PARTIAL STATUS TO MONITOR
(14) ANGLE PREDICTIONS
(15) ANTENNA SERVO-DRIVE SIGNALS
(16) NOT USED
(17) FORMATTED METRIC DATA VIA HSDA
(18) METRIC DATA FROM SDR TO PROJECT AND DSN MDR
(19) CALIBRATIONS FOR METRIC DATA
(20) I/O INSTRUCTIONS TO SFOF TRACKING SOFTWARE
(21) DATA AND STATUS FOR DISPLAY ON CCTV
(22) CCTV DISPLAYS OF (21)
(23) NOT USED
(24) HARD COPY DISPLAY OF REQUESTED DATA
(25) PROJECT I/O INSTRUCTIONS TO ORBIT SOFTWARE
(26) STATE VECTOR FROM DPODP
(27) STATE VECTOR FROM EXTERNAL SOURCE
(28) SPACECRAFT EPHEMERIS
(29) DSS PREDICTED OBSERVABLES
(30) DSS PREDICTIONS TRANSMITTED VIA TTY BY OPERATIONS CONTROL SOFTWARE
(31) DSS PREDICTIONS TRANSMITTED VIA HSDL BY OPERATIONS CONTROL SOFTWARE
(32) PAGE PRINT OF (31) FOR DSS ACQUISITION OF SPACECRAFT (PRIME)
(33) PAGE PRINT OF (30) FOR DSS ACQUISITION OF SPACECRAFT (BACKUP)
(34) PAPER TAPE OF PREDICTIONS FOR ANTENNA POINTING SUBSYSTEM (BACKUP)

(A) TO (Q) DEFINED IN TABLE 6

Fig. 5. DSN Tracking System 64-m DSS functional block diagram for *Pioneer F* and *G* cruise mode configuration

Helios Mission Support

P. S. Goodwin
Mission Support Office

Project Helios is the first NASA international deep space project—although there have been prior NASA international sub-orbital and earth-orbiting cooperative space projects. Helios is a joint undertaking by the Federal Republic of West Germany and the United States of America, who divide the project responsibilities. Two unmanned scientific satellites are planned for heliocentric orbits—the first to be launched in mid-1974, and the second in late 1975. Prior volumes of this series describe the history and objectives of this program, the contemplated spacecraft configuration, and its telecommunications and telemetry systems. This article deals with the spacecraft's command system, its requirements, and conceptual block diagrams.

I. Introduction

This is the fourth of a series of articles pertaining to Project *Helios*. A detailed description of the *Helios* spacecraft radio system was given in Ref. 1. Specifically, the transponder's coherent versus noncoherent modes of operation and the telemetry portion of the spacecraft's data handling system were described. This article will complete the discussion of the data handling system by describing the command system.

II. The *Helios* Telecommand System

A. Redundancy

The *Helios* spacecraft is designed with two actively redundant *receiver/command detector* chains. These are shown in Fig. 1. The first chain is fixed-wired to the low-gain (omni) antenna system, while the second chain is fixed-wired to the medium-gain antenna system. (As discussed in previous articles, the spacecraft's high-gain antenna provides a transmit-only function.) Since both *receiver/command detector* chains are continuously active, there are redundant means to enter commands into the spacecraft in case of a failure in one of the chains. Since both receivers operate on the same S-band carrier frequency, means are provided whereby ground control can select the desired chain through which to enter the command. They are described in the following.

First, there is a desired path due to the gain differential between the low- and medium-gain antennas. During the near-earth and cislunar portions of the mission, the preferred path will be via the low-gain antenna system, since the spacecraft will not yet have been oriented such that the medium-gain antenna pattern impinges upon Earth (Refs. 2, 3). However, after the step II orientation maneuver, the situation will be reversed, with the medium-gain antenna having a 6- to 8-dB advantage over the low-gain antenna system.

Second, each *receiver/command detector* chain has a separate command subcarrier frequency—i.e., 448 versus 512 Hz—thereby permitting ground control to select the chain they desire regardless of spacecraft orientation, even though the 8 symbols/s command rate is coherent with both subcarrier frequencies.

Third, as further protection, each chain's command verifier has a unique address in the command word structure. This will preclude commands accidentally appearing in the wrong chain from entering the decoding matrix.

The combination of the above features provides a truly redundant, fixed-wired active command system that can be operated in either the non-coherent or coherent transponder mode, while at the same time providing ample insurance against a double command entry.

B. *Helios* Command Requirements

The performance requirements for the *Helios* command system are shown in Table 1. It is interesting to note that, while the performance of the command system is dependent upon having sufficient uplink signal strength, the redundant *receiver/command detector* chains previously described do not otherwise significantly contribute to achieving the requirements listed in Table 1. This is because the commands are entered through only one chain or path at a time. The redundancy does, however, provide hardware reliability. Command bit or word error reliability must be coded into the command symbol structure itself.

C. *Helios* Command Code

1. General. To achieve the low error probabilities listed in Table 1, *Helios* commands are Manchester-coded, which translates each command bit into two symbols (the original bit followed by its complement) for transmission to the spacecraft. The coded 8 symbols/sec command symbol stream is phase-shift-keyed (PSK) modulated onto one of the two (i.e., 448 or 512 Hz) command subcarrier frequencies which is, in turn, phase-modulated onto the S-band uplink carrier. (Ranging modulation may or may not be also present on the S-band uplink carrier — depending upon the mission mode at the time.) Upon receipt at the spacecraft, the command signal follows one of the paths described in the foregoing *Paragraph A* and is routed through the appropriate command verifier to the decoding matrix. The decoding matrix has 256 separate hard-wire outputs which are routed to the individual items to be controlled aboard the spacecraft. These 256 outputs represent the total (i.e., maximum) list of commands that can be sent to the *Helios* spacecraft.

2. Idle sequence. Due to both the relatively low frequency of the command subcarriers and the stringent requirements for low bit or word error probability, the spacecraft command detector loop will have a fairly narrow bandwidth. On the other hand, narrow bandwidths do not respond well to square-shaped pulses. The latter problem can be minimized if the spacecraft command detector is kept in synchronism with the incoming command symbol stream. For *Helios*, this is accomplished by sending an uncoded *idle stream* of bits/symbols to the spacecraft during the intervals between commands. The *idle stream* has the following pattern:

$$\ldots 001001001 \ldots$$

This *idle stream*, which is sent at a rate of 8 bits/symbols per second, is also coherent with the two command subcarrier frequencies — i.e., 448 or 512 Hz. As mentioned in Ref. 1, it is necessary for the spacecraft to receive the *idle stream* for a few minutes prior to receiving a command or series of commands in order to ensure that the bit synchronizer (Fig. 1) is in lock. However, once the bit synchronizer is in lock, the *idle stream* may be interrupted on either a "0" or a "1" to start the actual command sequence.

3. Command symbol sequence. Each *Helios* command consists of a sequence of 68 symbols sent at a rate of 8 symbols/sec. The 68 symbols compose one command word. One command word must be sent for every command desired to be executed. The allocation of symbols within any one command word is shown in Fig. 2. From Fig. 2 it is noted that each command word repeats the command address twice and also contains three synchronizing subwords. In addition, each command word of 68 symbols also contains flag, verification, and parity bits which are similarly repeated twice within the total command word. The flag bit symbols are used to determine if the address is to be processed by the command decoder to generate one of the 256 command outputs or if the address bit is to be delivered directly to the data handling system to prepare it for the next mode of operation. The verification bit symbols are used to determine which *receiver/command detector* is permitted access to the decoding matrix (see Fig. 1). The parity bit symbols are used in a conventional manner to validate the address

and verification portions of the command message. The foregoing structure plus the benefits of Manchester coding, are designed to fulfill the requirements set forth in Table 1.

On occasion, it may be desirable to send a series or chain of commands in one sequence, i.e., without interruption. In such a situation, the final 8 sync bits of the preceding command in the chain are eliminated because they duplicate the leading 8 sync bits of the next command to be sent. In other words, sync words are only eliminated when they: (1) appear adjacent to one another, and (2) when commands are chained together and sent without interruption. At present, there is no spacecraft limitation regarding the number of commands in a chain; however, the high-speed data line between the SFOF and the DSSs does have a *data block size* limitation that, for practical purposes, will probably limit the number of commands in any one chain to approximately ten.

4. Impact on the DSN. A pre-coded command table of 256 potential commands does not present a difficult problem to the SFOF. Neither does the transmission of a selected pre-coded command or series (up to ten) of commands from the SFOF to the DSS over the high-speed data lines present a significant problem. Upon receipt at the station, the DSS telemetry and command processor (TCP) will both log the total command message and repeat it back to the SFOF for verification and subsequent enabling prior to transmission. At the time of transmission (either immediate upon enabling or at a specified time) the precoded command symbols stored in the TCP will be synchronously and coherently modulated onto the appropriate command subcarrier for transmission to the *Helios* spacecraft. To accomplish the latter requires that the station:

(1) Derive the command subcarrier frequency, the *idle stream* frequency, and the timing for the command symbols themselves from one coherent source, and

(2) Receive prior instructions as to which *Helios* command subcarrier frequency to employ for a given command.

Both of these requirements can be met by the Mark III command system presently being implemented into the DSN. Therefore, as long as the proper operational procedures are followed, there does not appear to be a problem for the DSN to execute the *Helios* commands as presently conceived.

III. Conclusion

This article concludes the present series of descriptions of the *Helios* Spacecraft radio system and its associated data handling subsystem. The discussion to date has been intentionally restricted to conceptual block diagrams because at this stage of the spacecraft's development many of the design details have not yet been finalized. Therefore, the reader should consider this and preceding articles to be only conceptually correct and subject to change as experience with specific design details dictates modification.

References

1. Goodwin, P. S., "*Helios* Mission Support," in *The Deep Space Network Progress Report,* Technical Report 32-1526, Vol. IV, pp. 22–27. Jet Propulsion Laboratory, Pasadena, Calif., Aug. 15, 1971.

2. Goodwin, P. S., "*Helios* Mission Support," in *The Deep Space Network Progress Report,* Technical Report 32-1526, Vol. II, pp. 18–27. Jet Propulsion Laboratory, Pasadena, Calif., April 15, 1971.

3. Goodwin, P. S., "*Helios* Mission Support," in *The Deep Space Network Progress Report,* Technical Report 32-1526, Vol. III, pp. 20–25. Jet Propulsion Laboratory, Pasadena, Calif., June 15, 1971.

Table 1. *Helios* command requirements

Requirement	Value
Bit error probability	$\leqslant 10^{-5}$
Detected word error probability	$\leqslant 10^{-3}$
Undetected word error probability	$\leqslant 10^{-10}$

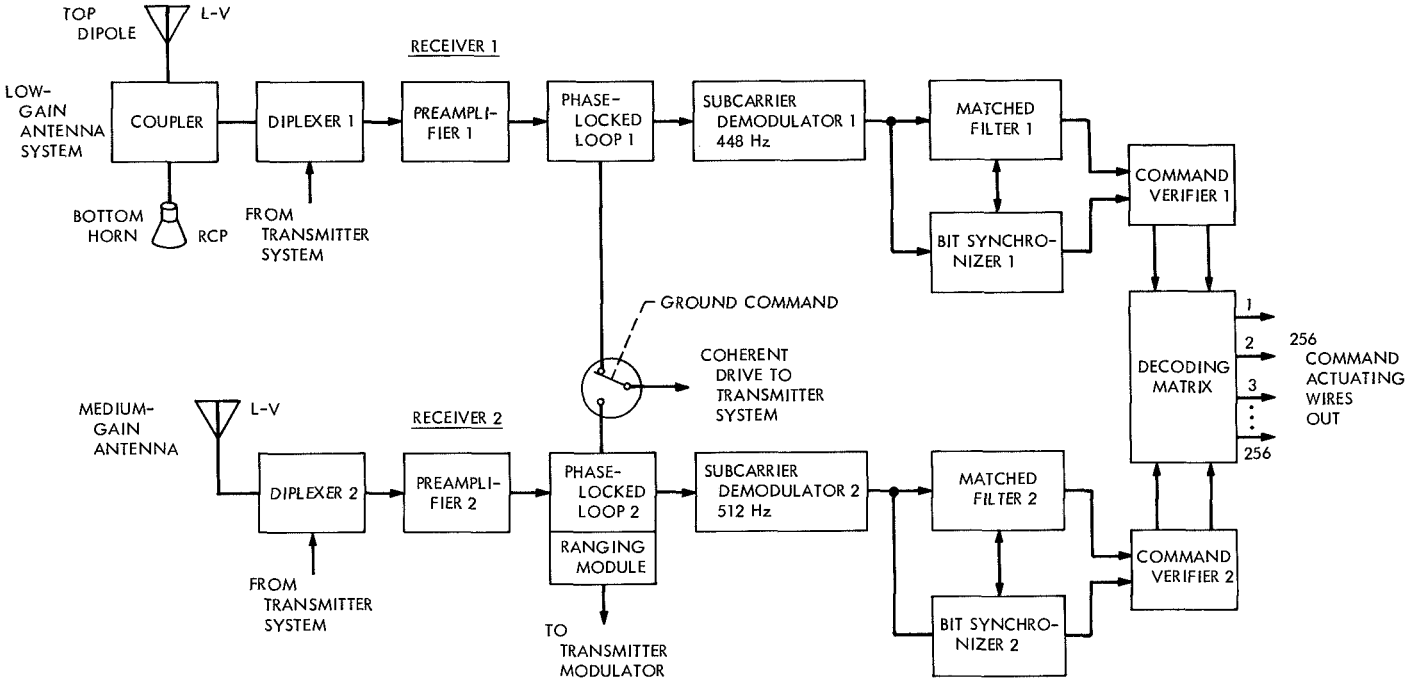

Fig. 1. *Helios* command detection system block diagram

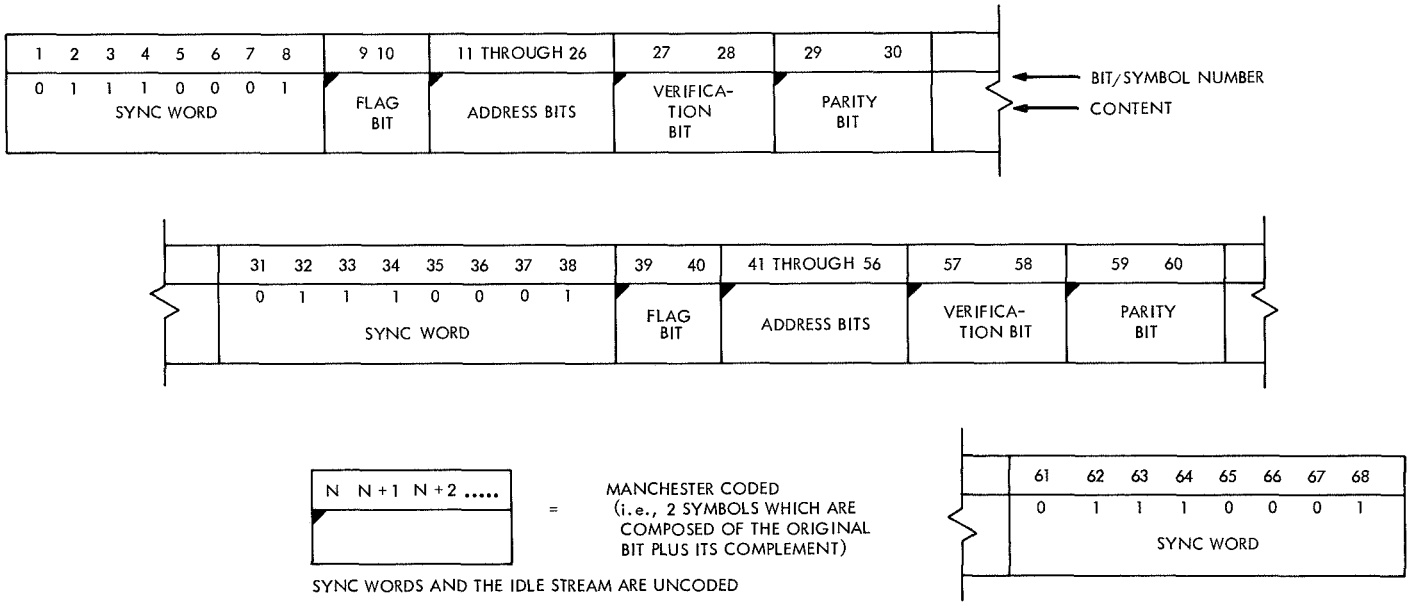

Fig. 2. *Helios* command bit/symbol sequence

Mariner Mars 1971 Mission Support

R. P. Laeser
Mission Support Office

While continuing to provide the tracking and data acquisition function for Mariner 9 on its journey to Mars, the DSN is planning and practicing for the orbital operations. The final steps of implementation and the test plans for orbital operations are outlined in this article.

I. Introduction

Previous articles have described the complex plans and configurations of the DSN for supporting the operations of the *Mariner* Mars 1971 mission. The time has finally arrived when we can describe the application of some of these plans and configurations; but the implementation, planning, testing, and training continues, because of the all-important Mars orbit operations beginning in November.

II. Cruise Support

After the loss of *Mariner 8* in the Atlantic Ocean off Puerto Rico, *Mariner 9* was successfully launched on Memorial Day, May 30, 1971. DSN coverage, starting with initial acquisition by DSS 51, has been continuous and nearly flawless. The continuous coverage was not initially a Project requirement, but with only one remaining spacecraft, the Project requested the DSN to apply to *Mariner 9* all resources that it had planned to apply to the dual mission. This has been done by the DSN, except in the area of 360/75 computer support, where, because of pressing development needs, the originally planned continuous support has been cut first to 14 h/day and then to 8 h/day. It is expected to be restored to 24 h/day before Mars orbit insertion.

The sacrifice of 10 to 16 h/day of 360/75 computer support has not been painless. Command activity has had to be limited, except for cases where manual commanding is acceptable, to the up-time of the 360/75 computers. Analysis of metric data has come to a standstill because the full 8 h is required to recall and process the data which has been piling up in the 490 communications processor. Monitor activity has been halted for 16 h of the day. DSN telemetry system analysis and Project data analysis is now heavily dependent on the mission and test computers (MTCs). And finally, pre-pass data flow tests cannot always be completely performed. Operations have been difficult under these conditions, but due to resourcefulness the result has been a smoother cruise operation than many expected.

There have been three notable spacecraft problems during cruise: excess usage of attitude-control gas, occasional loss of some telemetry measurements because of a commutator problem, and a decreased spacecraft transmitted signal level. Only the last problem has had any

effect on the DSN; several DSS 14 tracks have been scheduled where special spectrum analysis equipment is used in an attempt to isolate the problem.

III. Changes In Plan

In some cases, pre-mission generated plans have been modified for one of two reasons: a one rather than two-spacecraft mission, or late deliveries from implementation. The DSS 14 telemetry and command configuration was modified from a unique three-computer configuration to a standard two-computer configuration because of the need to process for only one spacecraft. In addition, the dual-engineering program was eliminated.

The 360/75 computer implementation schedule problems caused the deletion of many planned capabilities, including all master data record (MDR) and experiment data record (EDR) generation, all high-rate telemetry processing, and the interface with the high-speed data line to Boulder, Colorado. These processing loads were shifted to the MTCs; the MTC is also providing the DSN Telemetry Analysis Group a rudimentary network analysis capability.

IV. Implementation Progress

Implementation progress has not been as fast as originally planned, especially with the SFOF computers. 360/75 Model 3 was made available for operations in early August, and Model 4 will first be available after the start of Mission Operations System (MOS) orbital training. These problems and possibility of worse problems resulted in the deletion of many earlier planned capabilities. However, none of the deletions were critical or without an alternate. The Model 4 system is based upon the Manned-Spacecraft-Center-produced real-time operating system (RTOS) 15, rather than RTOS 13 as in earlier models and is expected to provide significant capability improvements.

The telemetry and command processor assembly (TCP) software also had its problems. It was discovered that the 16.2-kbps telemetry could not be processed properly, and several weeks of schedule time were lost before the problem was isolated and rectified.

V. Planning for Test and Training

The DSN plans the following activities prior to the beginning of support of orbital operations:

(1) Integration of facility elements

(2) Network system tests

(3) Combined system/combined station tests

(4) Facility training

(5) Network training

Because of late delivery of some equipment, these functions will not be able to be performed linearly with Project training; there will be some overlap. Therefore, both MOS and DSN personnel are working closely together to assure a test and training schedule with both maximum checkout of the ground systems and minimum impact on operations activities and training plans.

Viking Mission Support

E. K. Davis
DSN Engineering and Operations Office

Since the redirection of the Viking Project in January 1970, the DSN interface organization has been heavily involved with project organizational elements in advanced planning, exchanges of technical information, identification of requirements, capabilities, problems, and their resolution. This article is a general summary of the accomplishments in these areas of long-range planning including pertinent open questions to be resolved in the detailed planning phase.

I. Introduction

In Ref. 1, the author states that subsequent articles would describe significant *Viking*-related achievements in certain specific areas as the DSN interface organization progresses through the planning, implementation, testing, and operational stages of the mission. This shift in reporting emphasis is in keeping with the current activities of the DSN interface organization. The long-range, functional planning phase nears completion, while detailed planning will constitute the major activity during the next year.

This article summarizes the achievements during the long-range planning phase which have established a readiness for accomplishing detailed plans. As a general progress report, it will serve as a baseline for future detailed reports. Items discussed are primarily those which are prerequisite to the detailed definition of interfaces and plans, such as: (1) Project Tracking and Data System management agreements regarding organizational interfaces and procedures for planning, coordination, control, and documentation; (2) approved Project-/System-level schedules; (3) validated tracking and data acquisition requirements which are based on an approved mission design; (4) Tracking and Data System Functional Specifications for *Viking* 1975; (5) DSN System Requirements and Plans which consider *Viking* 1975 requirements; (6) exchange of preliminary technical design and interface information to avoid subsequent incompatibilities at the interfaces between the Project and Deep Space Network; (7) general correlation of Deep Space Network planned capabilities and Project requirements identifying areas requiring detailed attention; (8) Deep Space Network commitments; and (9) budget guidelines and approved financial plans which provide resources required to support *Viking*-related activities.

The information herein generally covers the period subsequent to the redirection of the *Viking* Project from the

1973 to the 1975 opportunity—January 1970 to August 30, 1971.

II. Management Agreements

Following is a brief summary of Project, Tracking and Data System, and Deep Space Network management agreements which are pertinent to on-going activities.

A. Organizational Interfaces for Planning

To facilitate planning and coordination, the Project has organized a number of Working Groups, Sub-Working Groups, and Teams. Personnel of the DSN interface organization are assigned as members of the appropriate groups and teams. Those of primary importance are: Telecommunications Working Group, Mission Analysis and Design Team, Integrated Test Working Group, Flight Operations Working Group, and its Test/Training and Software Sub-Working Groups. As the titles imply, these groups represent the major areas wherein interfaces exist between the DSN and Project.

Likewise, the DSN has planning teams in which Project personnel participate. Prior to the redirection of the *Viking* Project, the DSN Capabilities Planning Team for *Viking* was well into its task of developing baseline configurations for each of the DSN systems for *Viking* support. After the redirection, the DSN Capability Planning Team was terminated until the effect on requirements was evaluated. The telemetry, command, and tracking systems diagrams which were completed will serve as a starting point when Capability Planning Team activities resume in September 1971. DSN-detailed planning will be accomplished by the DSN Interface Team.

B. Project Control

The Project has implemented a number of techniques to exercise control over schedules and configurations. The DSN has agreed to participate in the employment of these techniques to the extent outlined below.

1. Schedules. Various levels of schedules are the essential elements in the control function. The *Viking*-Tracking and Data System Schedule, level 3, supports the Project Master Schedule and includes a relatively small number of DSN major milestones. This schedule, along with a narrative analysis, is submitted monthly for inclusion in the Project Management Report.

DSN Milestone Schedule, level 5, has been published and is the controlling schedule for DSN activities. Detailed activities in this schedule have been set to meet TDS Schedule commitments. On a trial basis in October 1970, the DSN agreed to participate in the *Viking* Integrated Program Evaluation and Review Technique (PERT). The level 5 schedule served as the basis for inputs to PERT. This has been a useful tool for accomplishing detailed schedule coordination between the DSN and elements of the Project. Therefore, DSN participation shall continue.

2. Configuration management. The *Viking* Project Configuration Management Plan sets forth detailed requirements and procedures to be used by Project systems. However, the multiple-mission nature of the DSN precludes internal application of Project control procedures. Commitments to the *Viking* Project are generally based upon or take the form of interface agreements. Therefore, the DSN position regarding Project configuration management is that Project procedures shall be applicable to but not beyond the established interfaces. DSN procedures will be employed to guarantee the continued compatibility of the interfaces until the end of the *Viking* mission. DSN changes which alter the interfaces will be subjected to Project approval through the *Viking* Integrated Change procedure. The Project has concurred with this approach as documented in Appendix B to the *Viking* Project Configuration Management Plan.

C. Documentation

The *Viking* Project Data Management Plan sets forth policies and procedures for standardizing and controlling documentation in the Project systems. The plan establishes that the existing documentation system may be employed. However, the TDS and DSN have agreed to alter certain standard documentation practices where desirable to meet joint Project/DSN documentation objectives.

1. TDS Data Management Plan. The Project Data Management Plan required each system to produce a corresponding implementing plan. Although the existing TDS and DSN Standard Practices met many of the Project Plan requests, it was necessary to produce a TDS Data Management Plan for *Viking* to cover Project-peculiar requests and to obtain approval for exceptions to the Project Plan. The TDS Data Management Plan for *Viking* 1975 Project (614-4) was approved by the Project in April 1971 and published in May 1971.

2. Interface documents. Interfaces between the DSN and Project are normally documented in DSN Operations Plan, Volume II, requiring DSN and Project approval. Also, plans indicated that Project documents would be

produced which accomplished essentially the same purpose. In November 1970, agreements which eliminated this duplication were reached between the Flight Operations, Orbiter, Lander Systems and the Tracking and Data System. An Orbiter System, Lander System, and Launch and Flight Operations System to Tracking and Data System Interface Requirements Document will be produced. This is considered a Project-level document and will consist of four volumes: (1) General Requirements, (2) Orbiter System to DSN, (3) Lander System to DSN, and (4) Launch and Flight Operations to DSN. Consequently, DSN Operations Plan for *Viking* 1975, Volume II, will not be produced.

3. Compatibility Test Plans. Negotiations between the DSN and Project have established that the scope and objectives of DSN/Spacecraft RF compatibility tests will be included in the *Viking* 1975 Project Master Integrated Test Plan, Summary Volume. The Project published this document, with TDS Manager concurrence, in September 1970. It has further been agreed that the *Viking* TDS Compatibility Test Plan will be a Project document published as a sub-tier volume of the Master Integrated Test Plan and replacing DSN Test Plan for *Viking*, Volume I, Part A, DSN/Spacecraft Telecommunications Compatibility Test Plan. Test procedures required to execute this plan will be developed and published by the DSN as a part of the DSN Test Plan for *Viking*, Volume II, DSN Test Procedures. The *Viking* TDS Compatibility Test Plan has been published in Coordination Copy form and is now under review.

4. TDS Functional Specifications. The Project documentation plan and tree established the requirement for system specifications in response to the Project specification. Initially the TDS was excluded since this requirement was foreign to standard documentation practices. It was later determined that a TDS Functional Specification for *Viking* would be produced. This specification defines the DSN functional performance requirements and provides a basis for developing the formal commitments to the *Viking* 1975 Project. As such, this document supersedes JPL document 611-1, Rev. A, Change 1, "TDS Estimated Capabilities for *Viking* 75 Project," dated December 1, 1970. The TDS Functional Specification, 614-3, was released on August 19, 1971 in review copy form for comments prior to publication of the final copy.

III. Tracking and Data Acquisition Requirements

Work done prior to the redirection of the *Viking* Project and the subsequent redirection provided the basis for Project publication of the SIRD much earlier than normally experienced on prior projects. Coordination copies of the SIRD were distributed in April 1971, and a review copy in June 1971. The approval copy is scheduled for distribution in September 1971. The receipt of tracking and data acquisition requirements at these dates fits well with the DSN capability planning, design, and budget cycles. The DSN interface organization worked closely with the Project in developing the SIRD and the proper statement of requirements. This interaction in conjunction with the exchange of technical information (*Section V*) has given a first-level evaluation of requirements and capabilities.

IV. DSN System Requirements and Plans

Knowledge of *Viking* requirements permitted the DSN System Engineering Group to give detailed consideration to *Viking* needs in CY 71 updates of the DSN System Requirements Documents covering the 1972–1975 time period. Consequently, support for *Viking* has received early attention in on-going System Design Reviews. This has resulted in early determination of additional DSN resources required to provide *Viking* support. In turn, these have been factored into the current budget guidelines and FY 72–74 Financial Plan.

At the present time, the DSN interface organization is giving priority attention to the development of a preliminary version of the NASA Support Plan (NSP), in response to the SIRD. Open areas and requirements which cannot be met are being identified and will be subjected to resolution in the detailed planning phase.

V. Technical Exchanges

Working groups discussed in *Section II-A* provide the forum for technical exchanges between the DSN, orbiter, lander, and flight operations organizations. Technical exchanges have led to the identification of problems and recommendations for their resolution. These activities have required a high level of support by the DSN interface organization since January 1970. The primary areas wherein technical exchanges have occurred naturally identify with the DSN–Project interfaces: telecommunications and data processing. Following is a summary of the major accomplishments.

A. Interface Documentation

To facilitate the communication of technical information from the DSN to Project, the DSN/Flight Project Interface Design Handbook (DSN document 810-5) was developed and distributed in January 1970. Revisions pro-

duced in March 1970, October 1970, May 1971, and August 1971 have increased the level of detail and kept interface design data current with DSN plans. The handbook deals with DSN interface parameters and performance for telecommunication, data processing, and simulation. Reference 2 describes the purpose and content of the handbook in more detail.

Tracking and Data System documents 815-2, "Flight Project Standard Technical Interfaces"; 815-4, "TDS/Project Standard Compatibility Management Plan"; and Deep Space Network document 810-8, "DSN/Flight Project Interface Compatibility Test Design Handbook," were published in 1970 to facilitate Project understanding of DSN interface identification and compatibility verification requirements and plans.

B. Telecommunications

DSN multi-mission command performance information pertinent to the decision on the single-channel versus dual-channel design for the spacecraft was provided through the Telecommunications Working Group. Subsequent adoption of the single-channel design was in keeping with the DSN Command System development plans. Frequency selection studies resulted in the assignment of channels 10, 13, 16, and 19. Dual-uplink power requirements/capability represented a major area of study in 1970. The resulting requirements for dual 40-kW uplink at DSS 14 and dual 10-kW uplink at DSS 43 and DSS 63 appear consistent with planned capabilities. Close coordination with the Mission Design and Navigation Groups verified that planned capabilities would meet mission navigation accuracy requirements.

C. Data Processing

In addition to the information provided by the DSN/Flight Project Interface Design Handbook, an extensive effort has been made to provide the Project with detailed data regarding design and operational interfaces with the DSN Central Processing System. User manuals and procedures were distributed. After analysis of the Project's planned software programs, it was decided in April 1971 that all nonreal-time programs would be developed to run on the 1108 computers. Therefore, in May 1971, efforts were directed toward determining the feasibility of converting Project contractor-developed programs to run on the 1108. As a part of this activity, a presentation was made to Project personnel on the 1108 organization and capabilities. The presentation included an actual demonstration wherein a contractor-developed converted lander entry program was run on the 1108 without difficulty. Additional tests of this nature were run in May–June 1971. A final report stated the following conclusions:

(1) Development of Flight Operations software on the contractor's baseline computer (CDC 6500) is a feasible concept. The technical problems in conversion are considered minimal.

(2) Conversion of programs written in minimal language (Fortran IV using no CDC-, IBM-, or Univac-peculiar features) is a relatively easy task, with clerical errors being the most frequent problem.

(3) In some programs having very sensitive numerical techniques, differences in results due to machine accuracies are the most difficult to resolve.

(4) Magnetic tapes can be interchanged between the CDC 6500 and Univac 1108.

Presentations and data exchanges were accomplished through the Flight Operations Working Group regarding spacecraft and DSN command and telemetry characteristics. Lander telemetry formats were found to be incompatible with DSN decommutation capabilities. Subsequent revisions to the lander telemetry design have significantly reduced the problem. Still, not all data processing requirements can be met by planned central processor capabilities. Additional recommendations are under consideration at this time. Therefore, resolution of telemetry processing interface problems will be a subject for future reports.

Similarly, it was found that command idle sequence characteristics of the orbiter and lander were different from each other and that neither was compatible with the DSN Command System. A series of technical exchanges resolved the problem by agreement to include the Project-unique portions of both idle sequences as a part of the Project-generated command message.

D. Test Support

Progress in compatibility test planning has been significant as indicated by the earlier discussion on Compatibility Test Plans. The essential elements of radio-frequency (RF) interface tests have been resolved. The DSN Milestone Schedule has been revised to provide support for Flight Operations/Spacecraft Compatibility Tests which will be conducted during the RF compatibility test period.

However, a serious incompatibility continues unresolved at this time between Project requirements for verification/demonstration tests and DSN test requirements for achieving operational readiness. The current schedule establishes May 1, 1975 as the DSN operational readiness date. The Project has levied a new requirement for a flight opera-

tions demonstration test in March 1975. In preparation for the demonstration, the Flight Operations System requires four months for system verification and crew training. Although partial DSN readiness could be achieved for the March 1975 demonstration test, it is not feasible to reach this state in November 1974 prior to Flight Operations verification tests. Solutions which would have advanced the Project software delivery date were unacceptable to the Project. Solutions which involved concurrent Flight Operations and DSN test activities were unacceptable due to the high risk of interference and of not achieving objectives. Resolution of this problem is being given high-level attention at this time.

E. Station Coverage

Using detailed tracking, telemetry, and command requirements in the SIRD and telecommunications performance information, the DSN Scheduling Group has analyzed DSN capabilities to provide the required coverage. The results show that the three-station, 64-meter subnet cannot meet requirements. The problem arises from extensive coverage requirements for both spacecraft and the tracking geometry. Both spacecraft have essentially the same Deep Space Station view period but both are not in the beamwidth of the antenna until approximately Mars-orbit insertion minus three days on the second spacecraft. Using the baseline design performance tables, the 26-meter subnet would experience threshold conditions in January 1976, about six months prior to orbit insertion. However, recent approval of orbiter design changes (two-degree freedom antenna and receive capability on the high-gain antenna) establishes the possibility of using the 26-meter subnet to solve the coverage problem. The Project is in the process of revising the 26-meter link performance analysis based on the new spacecraft parameters.

References

1. Mudgway, D. J., "*Viking* Mission Support," in *The Deep Space Network Progress Report*, Technical Report 32-1526, Vol. IV, pp. 40–46. Jet Propulsion Laboratory, Pasadena, Calif., Aug. 15, 1971.
2. Mudgway, D. J., "DSN Support for *Viking*," in *The Deep Space Network*, Space Programs Summary 37-63, Vol. II, p. 14. Jet Propulsion Laboratory, Pasadena, Calif., May 31, 1970.

Apollo Mission Support

R. B. Hartley
DSN Engineering and Operations Office

The support provided by the DSN to the Manned Space Flight Network during the Apollo 15 mission is described. Support was provided from four 26-m (85-ft) DSN stations, the Goldstone 64-m (210-ft) antenna, the Ground Communications Facility, and the Space Flight Operations Facility. Premission and mission activities are discussed and a brief mission description is included.

I. Introduction

The DSN support provided to the MSFN for past *Apollo* lunar missions has been described in Refs. 1 and 2 and earlier issues of the Space Programs Summary Volume II series. This article describes the support provided for the *Apollo 15* (AS-510) mission, the fourth successful manned lunar landing and the first of the new "J" type missions devoted almost exclusively to scientific objectives as opposed to the engineering emphasis of the earlier "H" missions.

II. Mission Description

Apollo 15, the eighth manned *Apollo* mission flown above the three-stage *Saturn V* launch vehicle, carried astronauts David R. Scott (Commander), Alfred M. Worden (Command Module Pilot), and James B. Irwin (Lunar Module Pilot). The mission goal was exploration of the canyon-like Hadley Rille and the Apennine foothills. A second goal was the collection of scientific data while in an extended lunar orbit phase.

Launch from Cape Kennedy Pad 39A occurred at 13:34:00.79 GMT on July 26, 1971, at a launch azimuth of 80.088 deg. Injection into translunar trajectory over the Pacific Ocean occurred midway through the second revolution in Earth parking orbit with a 5-min 47-s burn of the S-IVB stage engine. Translunar injection (TLI) put the spacecraft on a direct trajectory toward the Moon, making *Apollo 15* the first mission to abandon entirely the "free-return" trajectory which requires no propulsion to return to Earth. This direct trajectory conserves fuel for the critical landing sequence.

Following TLI the Command Service Module (CSM) separated from the booster, docked with the unattended Lunar Module (LM), and extracted the LM from the S-IVB. The S-IVB was directed by ground command toward a crash on the Moon as an additional calibration of the seismometers left there by the *Apollo 12* and *14* missions. The impact occurred at 20:58:41.75 GMT on July 29 at lunar coordinates 1.0°S and 11.87°W, about 185 km (100 nmi) from the *Apollo 14* landing site.

Midcourse Correction 1 was deleted due to the accuracy of the TLI maneuver. During the translunar cruise a short was noted in the CSM Service Propulsion System thrust indicator circuit. This short would have caused problems during maneuvers, and a set of workaround procedures set developed. Midcourse Correction 2 was not needed, but was scheduled as a test of these new procedures. Midcourse Correction 3 was deleted, and Midcourse Correction 4 was a short 0.92-s burn.

Other anomalies occurring during translunar cruise were a broken cover glass on the LM range/range rate meter (no impact), a chlorinator valve leak (tightened), and one strong voltage dip on the spacecraft ac and dc power busses. The latter problem occurred only two seconds after loss of uplink caused by a DSS 11 transmitter tripoff, prompting some concern that the two events were related. Later investigation showed that a CSM circuit breaker feeding some lighted pushbuttons on the spacecraft computer console had tripped. A short large enough to trip the circuit breaker would also have caused the voltage dips. The circuit breaker was never reset.

Shortly before entering lunar orbit, the astronauts blew off a door covering the Scientific Instruments Module (SIM) of the Service Module (see Fig. 1). The SIM bay, a first for *Apollo 15*, carries scientific instruments for observation of the Moon from lunar orbit. The instruments include a gamma ray spectrometer developed at JPL, an X-ray spectrometer, an alpha particle spectrometer, a mass spectrometer, a laser altimeter, a 7.62-cm (3-in.) mapping camera, and a 60.96-cm (24-in.) panoramic camera.

A successful lunar orbit insertion (LOI) burn of 400.7 s put the spacecraft into a 315- by 108-km (170- by 58-nmi) orbit. Two orbits later a descent orbit insertion (DOI) burn lowered the spacecraft to a 109- by 17.1-km (58.5- by 9.2-nmi) orbit. A DOI trim maneuver later raised this perilune to 17.8 km (9.6 nmi).

During lunar orbit 12 the CSM and LM separated with astronauts Scott and Irwin in the LM preparing for descent to the lunar surface on orbit 14. The undocking was delayed approximately 26 min due to a poor connection on the umbilical wire to the CSM docking probe. Shortly after undocking the CSM maneuvered into a near-circular orbit 121 by 102 km (65.2 by 54.8 nmi).

The approach to landing was steeper (25 deg) than any Moon lander before, providing extra clearance from the 3.66-km (12,000 ft) Apennine peaks. The LM made a normal landing about 121.92 m (400 ft) northeast of the target. The actual landed location is 26.0835°N and 3.665°E. Soon after landing the astronauts conducted a standup extravehicular activity (SEVA), which involved depressurizing the cabin, opening the top (docking) hatch, and making a photographic and visual survey of the landing site from the top hatch. This activity was partly to acquire visual reference points for subsequent navigation chores. A sleep period followed, during which one of the two bistatic radar experiments was conducted with the orbiting CSM.

During the first extravehicular activity (EVA) period the astronauts deployed the lunar rover (Fig. 2), used for the first time on *Apollo 15*. Although the front steering was inoperative, the rear steering was sufficient, and the crew drove to several small craters where scientific exploration, surface sampling, and photographic documentation were completed. Observers on Earth were able to watch the activities at each stopping point, thanks to the new Lunar Communications Relay Unit (LCRU) (Fig. 3). On previous missions the astronauts' VHF transmissions were relayed to Earth by the LM, but with the rover the men would travel beyond VHF range from the LM. Hence, the LCRU was designed as a portable S-band/VHF transceiver, normally resting on the rover, to keep the astronauts in contact with mission control. In addition to voice and telemetry on the downlink, the video output of the LM camera could be transmitted. The uplink carried capcom voice plus television commands (pan, tilt, zoom). A special assembly on the rover provided a mounting platform for the LM TV camera and actuated the camera according to the received commands.

At the end of EVA number 1, the crew deployed the *Apollo* Lunar Surface Experiments Package (ALSEP), which contains a seismometer and several fields and particles experiments. The crew then re-entered the LM for an eating and sleeping period during which the second bistatic radar experiment was conducted with the CSM.

At the start of the second EVA, the steering problem in the rover was cleared by resetting a circuit breaker. It was with a fully functioning rover that the astronauts drove to another series of craters for sample collection and scientific investigation, and returned to complete the deployment of the ALSEP package.

After a third eating and sleeping period, the crew made their third and last lunar excursion. This time the route took them along Hadley Rille for some spectacular vistas and a chance to collect samples from what is believed to be lunar bedrock. The total distance traveled during all three EVAs was 28 km, and the rover was driven at a maximum speed of 12 km/h. A total of 83 kg (183 lb) of Moon rock was collected and nearly 3.2 km (2 mi) of film was exposed.

It was less than four hours after the third EVA when the Lunar Module blasted off the lunar surface to rejoin the orbiting CSM. The liftoff was witnessed on Earth via the LCRU and its associated TV camera. Rendezvous and docking were normal and all lunar samples were transferred to the CSM. During a pressure check prior to LM jettison, a leak was detected in the LM/CSM tunnel. Removal and inspection of the hatch disclosed no reason for the leak, and on reinstallation the leak was gone. The pressure check was continued for over an hour, and the LM was finally jettisoned on revolution 52, one orbit later than planned. The LM was maneuvered to a crash on the Moon for another calibration of the three seismometers. Crash occurred at coordinates 26.36197°N and 0.25345°E, 92.6 km (50 nmi) from the *Apollo 15* site.

The CSM remained in lunar orbit almost two days longer conducting orbital science experiments with emphasis on the SIM bay experiments. This extended lunar orbit stay is another *Apollo* "first" in keeping with the science goals of the "J" type mission. The film packages from the SIM bay cameras were retrieved by the Command Module Pilot who took a "spacewalk" during transearth cruise. Shortly before transearth injection, the crew released a Particle and Fields Subsatellite (P&FS) (Fig. 4) into an orbit of 139 by 100 km (75.1 by 57.3 nmi) at an inclination of 151.3 deg. The subsatellite has a coherent S-band transponder for lunar mass concentration (mascon) studies at JPL.[1]

The accuracy of transearth injection (TEI) was such that only one short midcourse burn was required shortly before Earth atmosphere entry. *Apollo 15* landed at approximately 26°4′N and 158°4.5′W some 480 km (300 mi) north of Hawaii.

Table 1 shows the mission event times and Table 2 gives a summary of television coverage.

[1]W. L. Sjogren, principal investigator.

III. Requirements for DSN Support of *Apollo 15*

A. DSN 26-m Antenna Stations

As was done with previous *Apollo* lunar missions, DSSs 11, 42, and 61 were committed to support *Apollo 15* under direct MSFN/MSC control. The responsibilities at these stations have changed, however.

Previously, the stations had two control rooms or "wings," one MSFN and one DSN, and a set of common equipment, including antenna, servo, microwave, masers, and power amplifiers, with a complicated switch to select the control room to be connected to the common equipment. To avoid needless construction, the DSN wing was designated to be the control room for the new 64-m antennas now being built adjoining DSSs 42 and 61. All equipment to operate the 26-m antenna in either DSN or MSFN mode was moved into what had been called the MSFN wing, and the DSN, with MSFN concurrence, assumed responsibility for maintenance and operations of the entire station. DSS 11 was similarly configured to maintain network standardization.

In order to support the increased DSN responsibilities at these stations, the DSIF insisted on a dedicated voice line to each station during its tracking period. The line was for use only if the station had a problem and needed immediate assistance from the SFOF. No routine traffic was to appear on this line. In addition, the existing voice line from the DSN Operations Chief to the MSFN Operations Chief was extended at each end to allow the DSIF Operations Advisor to talk directly to the MSFN Network Support Team.

A new requirement on the 26-m stations was for the reception of the LCRU downlink at 2265.5 MHz, lower in frequency than any previously received *Apollo* signals. The uplink was on the same frequency as the LM uplink. The P&FS was also to be tracked, but this presented no problem since the uplink and downlink frequencies are the same as the LM.

In view of past problems with transmitter tripoffs, the DSN was required to modify its battleshort function at DSSs 11, 42, and 61. The modification left only one interlock, the arc detector, in operation. No other personnel safety or equipment interlocks will function when the battleshort is engaged. The battleshort is used during brief, mission-critical events, such as LM touchdown, when loss of uplink is very undesirable. In the event of a false interlock, there would be no interruption of the

uplink. If the interlock is genuine, however, the power amplifier or its power supply would probably be destroyed and be unavailable for the remainder of the mission. Without the battleshort, interlock tripoffs are usually cleared rapidly, losing only a few seconds of uplink lock. Thus, an agonizing tradeoff must be made over use of the battleshort.

B. DSS 14

The Mars station, DSS 14, was required to receive voice, telemetry, biomedical, and TV, and relay the data to the Goldstone Prime MSFN station (GDS). Specific requirements existed for low lunar orbits, touchdown, EVA television, and LM crash. Coverage was also desired for television during translunar coast.

C. Precision Doppler Data

As part of a continuing study of lunar potential anomalies (mascons), DSS 14 was required to provide precision high-speed doppler recordings of the CSM and LM during low lunar orbits and of the LM during the descent phase and later during the crash. In cooperation with the principal experimenter for this JPL study, a set of internal DSN requirements was developed to make use of the high-resolution doppler data available from DSN stations equipped with doppler resolvers. Four passes at DSS 51 were scheduled for this purpose. DSS 51 was made available by tracking *Mariner* Mars 1971 from DSS 62. This was fortunate because the Moon was at a low declination, and DSS 51 had long view periods. Additionally, the desired doppler was recorded at DSS 14 during the passes that had previously been scheduled for official *Apollo* support. Preliminary results from the same experiment on *Apollo 14* are given in Ref. 3.

A related *Apollo* requirement was for high-speed strip-chart recordings of DSS 14 received signal level during orbit 3 of the CSM and the crash of the LM.

D. Bistatic Radar Experiment

DSS 14 was required to conduct another bistatic radar experiment as had been done during *Apollo 14* (see Ref. 2). The requirements had been expanded to encompass two orbits, 17 and 28, in place of the one orbit on *Apollo 14*. The experiment consists of receiving the CSM downlink signal, which has been reflected from the lunar surface, at DSS 14 in two orthogonal polarizations simultaneously. From the recorded signal characteristics deductions can be made as to the nature of the lunar soil.

E. ALSEP Support

The ALSEP transmissions are usually supported by the 9-m (30-ft) antennas of the MSFN. DSN support was requested during *Apollo 14* because the ALSEP on that mission occasionally transmitted at a high bit rate (10.6 kilobits per second) and the 26-m stations provided the necessary signal-to-noise ratio. During testing for that mission, it was found that the ALSEP uplink frequency of 2119 MHz was so far removed from the normal DSN and *Apollo* uplink frequencies as to require retuning of the klystron tubes in the ground transmitters. This retuning significantly increases the chances for internal klystron failure and caused some concern. Accordingly, before *Apollo 15* (whose ALSEP had no high bit rate), the DSN voiced its concern to the MSFN. After consultation with NASA Headquarters, it was decided that the DSN would continue with ALSEP uplink testing and operations regardless of the mission risks.

F. LCRU

Shortly before the mission the *Apollo* Project requested short tracks of the LCRU from DSS 14 on August 4, 5, 7, and 8. The plan was to conduct television surveys of the landing site after the astronauts had departed. The LCRU batteries were expected to last approximately one week. Since this activity is not intimately related to manned flight support, a ruling was requested from NASA Headquarters on the relationship between the LCRU after LM liftoff and the other unmanned mission support of the DSN. The approval was received and the requested tracking was scheduled by cancelling some DSS 14 support of other projects.

IV. Premission Preparations and Testing

A. DSN 26-m Stations

Although the requirement to support LCRU transmissions has been known for some time, final testing of the support capability took place in early 1971 and continued until shortly before launch. The concern centered around reception of the LCRU frequency of 2265.5 MHz, below the normal *Apollo* band. Wideband masers had been installed at DSS 42 and LCRU reception there proved to be no problem. DSSs 11 and 61 had not yet received the new masers, and the bandwidth of the old maser was not sufficient to cover both *Apollo* and the LCRU. The final procedure developed through this testing was to tune one maser at each site to the lower half of the band and the other maser to the upper half. There was no redundancy in this configuration as retuning required

30 min. In addition, the output of only one maser at a time could be selected, though this selection could be changed rapidly. A similar configuration was used at DSS 14 where the masers are different but have a similar bandwidth problem. As the LCRU link is marginal from a signal strength standpoint and is critically affected by a steep gain slope, several tests were necessary to demonstrate compatibility. Before *Apollo 16,* the new wideband masers will be installed at DSSs 11, 14, and 61.

Soon after the DSS 11 reconfiguration was completed (see *Section III-A,* above) in early June 1971, power amplifier (PA) number 3 began to experience interlock tripoffs. Repeated testing and extensive component replacement (even replacement of the entire power supply) failed to improve the reliability. During the two weeks before launch, DSS 11 was reported "Red" due to the intermittent faults. This unreliability continued through the mission period, and, as of this writing, is still unsolved despite considerable efforts at diagnosis.

DSSs 11, 42, and 61 were placed under configuration control for the *Apollo 15* mission as of 00:01 GMT on July 16, 1971, and were placed on mission status by the MSFN as of 00:01 GMT on July 15, 1971. On previous missions, scheduling control of these stations reverted to the MSFN during the mission status period. In view of the increased DSN responsibilities at these stations for *Apollo 15* and beyond, the DSN planned to retain scheduling control, and the DSN/MSFN Operating Interface Procedures document (Ref. 4) reflected this plan. The MSFN, based on alleged verbal agreements, assumed that scheduling would be done by the MSFN as in the past. Accordingly, on July 15, the stations began to receive conflicting scheduling messages from both the DSN and MSFN. After several days of negotiation, MSFN scheduling was assigned control as a temporary expedient. It is felt that on *Apollo 16* these stations must be scheduled by the DSN since they will be tracking the *Pioneer F* spacecraft between *Apollo* passes.

B. DSS 14

DSS 14 conducted the normal premission tests including installation and tests of the bistatic radar experiment equipment as shown in Table 3. No scheduling problems were experienced with DSS 14 as scheduling control for the station has always been retained by the DSN.

C. DSN Predicts

Antenna pointing information for DSSs 11, 42, and 61 comes directly from Houston in the form of a 29-point acquisition message. This message also serves DSS 14 but has been considered a backup to SFOF-generated predicts. On *Apollo 15* the 29-point message was declared the prime source of predicts for DSS 14. The SFOF continued to supply predicts, but as a backup source only. Both predict systems were tested before the mission. The 29-point system worked perfectly, but the SFOF had some minor software problems. The predicts are generated by entering a Houston-supplied state vector into the 1108 computer where the Double Precision Trajectory Program outputs a probe ephemeris tape. The tape is carried to the IBM 360/75 for processing by the predicts program. The predicts are transmitted directly by the 360. Unfortunately, both computers are undergoing a series of software updates, and with each update the interface compatibility can break down. Only a few days before launch the trajectory program in the 1108 was modified and it was necessary to add a small reformatting program to the 360 to make the data from the probe ephemeris tape compatible with the predicts program. With this last-minute modification the predicts procedure was tested and declared "Green" for launch.

V. *Apollo 15* Operations

A. DSN 26-m Stations

DSSs 11, 42, and 61 successfully supported all phases of the *Apollo 15* mission. The problems experienced are noted in Table 4. As can be seen, the problems with DSS 11 transmitter number 3 continued. Three tripoffs of this transmitter were experienced during actual uplinking to the spacecraft. After the third tripoff, mission control in Houston finally acquiesced to DSN pleas (which began before launch) and declared DSS 11 transmitter number 4 as prime. After that decision there were no further uplink losses at DSS 11.

During the first pass at Goldstone shortly after TLI, the spacecraft view angles were beyond the antenna gimbal limits at the Goldstone Prime MSFN stations. Therefore, DSS 11 was required to transmit simultaneously on separate frequencies to the CSM and the instrument unit of the S-IVB booster. Although this capability has existed for the entire *Apollo* program, this is the first time that the capability has actually been used at a DSN station.

The 26-m stations tracked ALSEP several times but were never called upon to transmit the ALSEP uplink signal.

B. DSS 14

Seven *Apollo* passes were tracked as shown in Table 4. The station also tracked the LCRU twice. The station had originally been scheduled for four LCRU tracks, but after failure of the LCRU at the end of the first pass and a futile attempt at revival on the second pass, DSS 14 was released from further support.

DSS 14 supported the bistatic radar experiment as planned. The experiment was somewhat degraded during lunar revolution 17 because the spacecraft had been pitched the wrong direction, making the radiation toward the lunar surface elliptical rather than circular. Revolution 28 efforts produced good data, and was not noticeably degraded by the operator error which resulted in a brief mispointing of the antenna.

DSS 14 failed to switch to high doppler sampling rate upon LM jettison as required. LM jettison occurred at a nonstandard time, and 16 min passed before the station was advised of the event. A verbal mark will be requested from the MSFN if future missions have event-related requirements such as this.

C. DSS 51

DSS 51 tracked *Apollo* on four days as shown in Table 4. Apparently the station was not familiar with the *Apollo* requirements and took doppler samples at a one-minute rate instead of a one-second rate during part of the first pass. Unfortunately, the one-second samples were of high priority, since the spacecraft was in a very low lunar orbit at the time. The remainder of the doppler data on pass number 1 and subsequent passes was successfully recorded as required.

D. Predict Operations

The 29-point acquisition message, which was the prime source of predicts for DSS 14, was used with no problems. The messages occasionally arrived later than desired, but the station was never completely without predicts.

In the SFOF, eight sets of predicts were generated during the mission and transmitted to DSS 14. One set of preflight nominal landing site predicts was generated and transmitted before the mission to DSSs 14 and 51. No problems occurred in supplying the scheduled stations with predicts.

E. GCF Participation

The DSN GCF provided voice, teletype, and high-speed data circuits to support the DSN *Apollo* operations. In addition, JPL acts as West Coast Switching Center for the NASA Communications Network and handles many non-DSN circuits in support of *Apollo*. There were no known GCF anomalies and GCF support was considered excellent. The voice lines that were scheduled to each 26-m station (*Section III-A*, above) were used only once, and deletion of this requirement is being considered.

F. SFOF Participation

The SFOF areas and equipment used for *Apollo 15* included the Operations Area, the Network Analysis Area, the *Mariner* Mars 1971 computer terminal area, the Univac 1108, and IBM 360/75 computers. The SFOF support is limited to predict generation, tracking data reception, and some off-line monitoring. The only SFOF problems were in the software area. In addition to the predict software problems mentioned in *Section V-C*, the 360 computer was unable to receive *Apollo* tracking data when tracking data from *Mariner* Mars 1971 was also being received. Therefore, the *Apollo* data had to be manually recalled from the GCF Communications Processor during inactive periods of *Mariner* Mars 1971. Other than these software problems, SFOF support was excellent.

References

1. Hartley, R. B., "*Apollo* Mission Support," in *The Deep Space Network*, Space Programs Summary 37-64, Vol. II, pp. 7–11. Jet Propulsion Laboratory, Pasadena, Calif., Aug. 31, 1970.

2. Hartley, R. B., "*Apollo* Mission Support," in *The Deep Space Network Progress Report*, Technical Report 32-1526, Vol. II, pp. 33–41. Jet Propulsion Laboratory, Pasadena, Calif., Apr. 15, 1971.

3. Sjogren, W. L., et al., "S-Band Transponder Experiment," in *The Apollo 14 Preliminary Science Report*, NASA document SP-272. National Aeronautics and Space Administration, Washington, 1971.

4. *MSFN/DSN Station Operating Interface Procedures for Support of Manned Apollo Missions*, MSFN document 508.3. Goddard Space Flight Center, Greenbelt, Md., May 1971.

Table 1. *Apollo 15* sequence of major events

Event	Ground elapsed time, h:min:s	Greenwich Mean Time, h:min:s	Event	Ground elapsed time, h:min:s	Greenwich Mean Time, h:min:s
Launch	00:00:00	Jul 26/13:34:01	End EVA 1	126:14:00	Jul 31/19:48:01
TLI ignition	02:49:48	Jul 26/16:23:49	Bistatic radar begin (Rev 28)	131:42:37	Aug 01/01:16:38
TLI cutoff	02:55:35	Jul 26/16:29:36	Bistatic radar end	132:54:40	Aug 01/02:28:41
First midcourse (TLI + 9 h)	Deleted		Begin EVA 2	142:14:17	Aug 01/11:48:18
Second midcourse (TLI + 27 h)	28:40:00	Jul 27/18:14:01	End EVA 2	149:27:09	Aug 01/19:01:10
Third midcourse (LOI − 22 h)	Deleted		Begin EVA 3	163:18:00	Aug 02/08:52:01
Begin bistatic frequency measurement	60:36:00	Jul 29/02:10:01	CSM plane change	165:12:50	Aug 02/10:46:51
End bistatic frequency measurement	60:43:00	Jul 29/02:17:01	End EVA 3	168:08:00	Aug 02/13:42:01
Fourth midcourse (LOI − 5 h)	73:31:14	Jul 29/15:05:15	LM ascent	171:37:22	Aug 02/17:11:23
SIM door jettison	74:06:14	Jul 29/15:40:15	CSM/LM docking	173:36:00	Aug 02/19:10:01
LOI	78:31:46	Jul 29/20:05:47	LM jettison	179:30:00	Aug 03/01:04:01
S-IVB impact	79:24:41	Jul 29/20:58:42	LM separation	179:50:00	Aug 03/01:24:01
DOI	82:39:48	Jul 30/00:13:49	LM deorbit burn	181:04:19	Aug 03/02:38:20
DOI trim	95:56:43	Jul 30/13:30:44	LM crash	181:29:35	Aug 03/03:03:36
Undock	100:13:30	Jul 30/17:47:31	CSM shaping burn	221:20:47	Aug 04/18:54:48
CSM circularization	101:38:50	Jul 30/19:12:51	P&FS deploy	222:39:36	Aug 04/20:13:37
Powered descent initiation	104:30:09	Jul 30/22:04:10	P&FS signal received	222:55:00	Aug 04/20:29:01
Touchdown	104:42:29	Jul 30/22:16:30	TEI	223:48:45	Aug 04/21:22:46
Begin SEVA	106:42:00	Jul 31/00:16:01	Fifth midcourse (TEI + 15 h)	Deleted	
End SEVA	107:16:00	Jul 31/00:50:01	Begin CSM EVA	241:56:58	Aug 05/15:30:59
Bistatic radar begin (Rev 17)	110:02:45	Jul 31/03:36:46	End CSM EVA	242:36:15	Aug 05/16:10:16
Bistatic radar end	111:15:21	Jul 31/04:49:22	Sixth midcourse (Entry − 22 h)	Deleted	
Begin EVA 1	119:39:40	Jul 31/13:13:41	Seventh midcourse (Entry − 3 h)	291:58:00	Aug 07/17:32:01
ALSEP transmitter activated	125:03:00	Jul 31/18:37:01	Splashdown	295:11:53	Aug 07/20:45:54

Table 2. *Apollo 15* television

GMT, h:min	GET, h:min	Duration, h:min	Subject	Vehicle	Station
Jul 26/17:01	03:27	00:08	Transposition and docking	CSM	GDS
Jul 28/00:29	34:55	00:51	Interior and transfer to LM	CSM	GDS
Jul 30/12:28	94:54	00:15	Landing site	CSM	MAD
Jul 31/13:34[a]	120:00[a]	06:00[b]	EVA-1	LM/LCRU	HSK/MAD
Aug 01/11:54[a]	142:20[a]	06:30[b]	EVA-2	LCRU	PKS/HSK/MAD
Aug 02/09:04[a]	163:30[a]	04:30[b]	EVA-3	LCRU	PKS/HSK/MAD
Aug 02/17:04	171:30	00:15	LM liftoff	LCRU	PKS/HSK/MAD
Aug 02/19:00	173:26	00:13	Rendezvous and docking	CSM	MAD
Aug 04/08:57	211:23	00:07	Surface TV	LCRU	MARS
Aug 05/15:24	241:50	01:00	Transearth EVA	CSM	HSK
Aug 06/19:56	270:22	00:52	Press conference and eclipse	CSM	MAD

[a]Approximate times.

[b]Intermittent coverage.

Table 3. DSS 14 tests

Date, 1971	GMT, h:min	Test
Jul 07	14:00–22:00	Bistatic cable installation
Jul 14		Configuration verification test
Jul 18	01:00–01:00	DSS 14/GDS prime data flow test
Jul 22	09:00–13:00	Bistatic countdown
Jul 22	13:00–20:00	Bistatic test

Table 4. *Apollo 15* tracking

DSS	GMT, h:min	Problems
11	Jul 26/16:35–05:38	None.
	Jul 27/19:55–02:50	PA 3 fault at 23:21. One way for 48 s due to erroneous instructions from Prime. Released from track early for troubleshooting.
	Jul 28/20:17–05:50	PA 3 fault at 03:26. Uplink lost for 14 s. High-voltage power supply from DSS 14 installed after pass.
	Jul 29/20:22–05:39	PA 3 fault at 03:21. Uplink lost for 20 s.
	Jul 30/21:39–06:45	PA 3 fault at 02:42 (was in standby).
	Jul 31/22:22–06:19	None.
	Aug 01/23:31–07:55	None.
	Aug 03/00:30–08:44	PA 3 fault at 12:30 on Aug 2 (station inactive).
	Aug 04/02:06–09:10	PA 3 fault at 03:30 (was in standby).
	Aug 05/02:02–10:17	Glitches on HA error voltages. No impact because station autotracking. Problem not repeatable.
	Aug 06/02:21–09:59	None.
	Aug 07/03:04–09:59	PA 3 fault at 04:36. Wrong TLM bandwidth while tracking subsatellite.
14	Jul 27/02:17–05:14	None.
	Jul 28/01:24–05:35	None.
	Jul 28/23:02–05:40	None.
	Jul 29/20:29–05:39	None.
	Jul 30/21:39–06:19	None.

Table 4 (contd)

DSS	GMT, h:min	Problems
14 (contd)	Jul 31/22:29–06:19	Antenna pointing 0.2 deg off boresight for first 10 min of lunar revolution 28.
	Aug 03/00:30–03:35	Failed to switch to high doppler sample rate until 16 min after LM jettison.
	Aug 04/08:51–09:40	None (LCRU track).
	Aug 05/04:00–06:30	None (LCRU search).
42	Jul 27/01:00–13:00	None.
	Jul 28/01:08–13:31	None.
	Jul 29/01:22–13:41	None.
	Jul 30/01:18–14:23	None.
	Jul 31/01:54–14:41	None.
	Aug 01/03:14–16:16	None.
	Aug 02/03:18–17:14	None.
	Aug 03/04:26–17:28	None.
	Aug 04/06:02–19:06	None.
	Aug 05/05:29–19:14	Heat exchanger problem on standby PA.
	Aug 06/05:50–19:25	None.
	Aug 07/06:11–20:26	None.
51	Jul 30/10:17–22:18	Failed to take required doppler data for four of six lunar orbits.
	Jul 31/11:30–22:34	None.
	Aug 03/13:20–01:16	None.
	Aug 04/14:18–21:04	None.
61	Jul 26/09:32–21:19	Bad ranging readouts on System 3; replaced faulty cord.
	Jul 27/12:21–21:56	None.
	Jul 28/12:51–22:06	None.
	Jul 29/13:01–21:55	None.
	Jul 30/14:04–22:38	None.
	Jul 31/15:26–22:33	Pretrack ranging problem; repaired before track.
	Aug 01/15:53–23:43	None.
	Aug 02/16:53–23:45	Wrong character in Tracking Data Processor header.
	Aug 03/18:16–01:21	None.
	Aug 04/18:34–02:22	None.
	Aug 05/18:58–02:23	None.
	Aug 06/19:28–02:30	None.

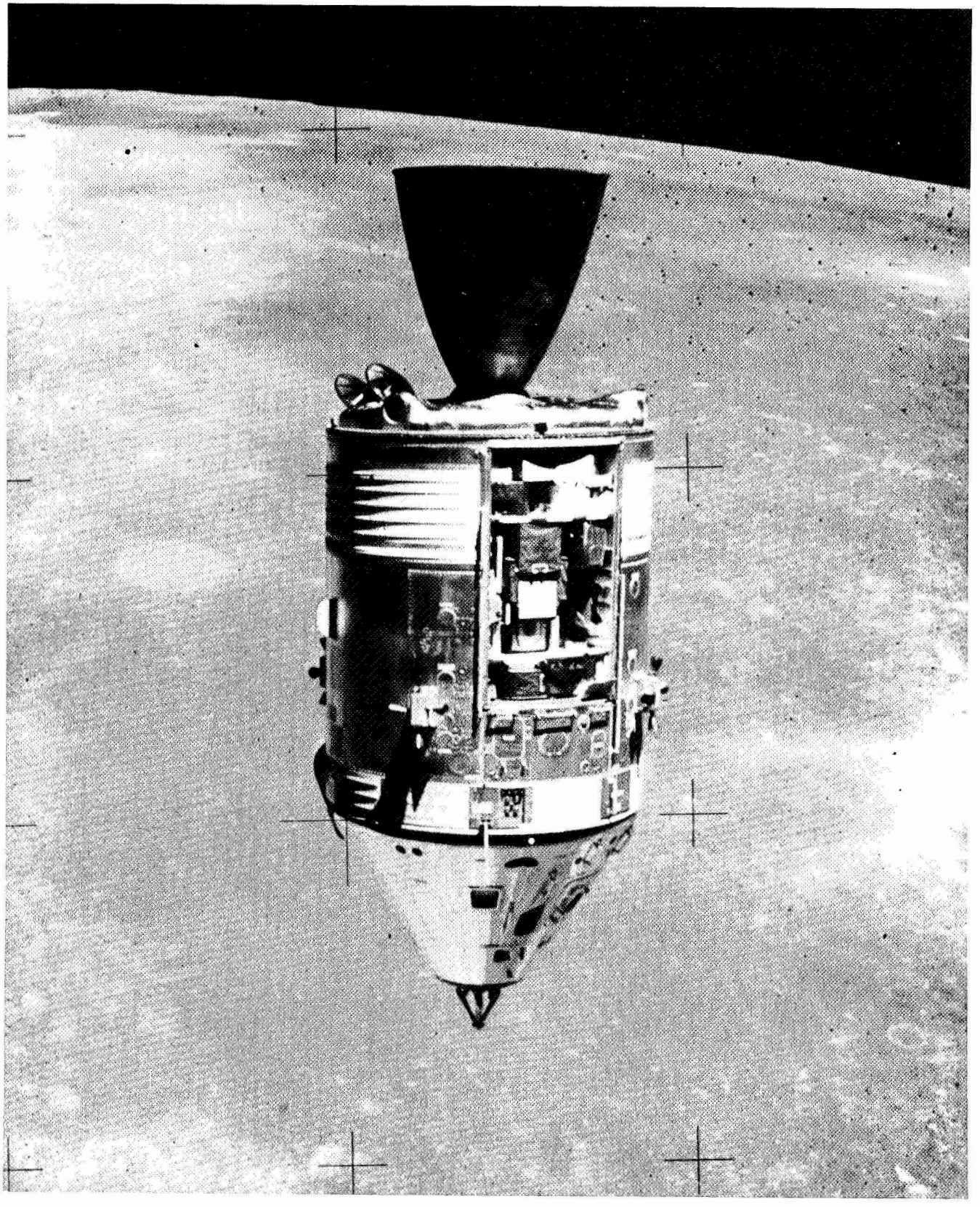

Fig. 1. Scientific Instrument Module Bay of Service Module

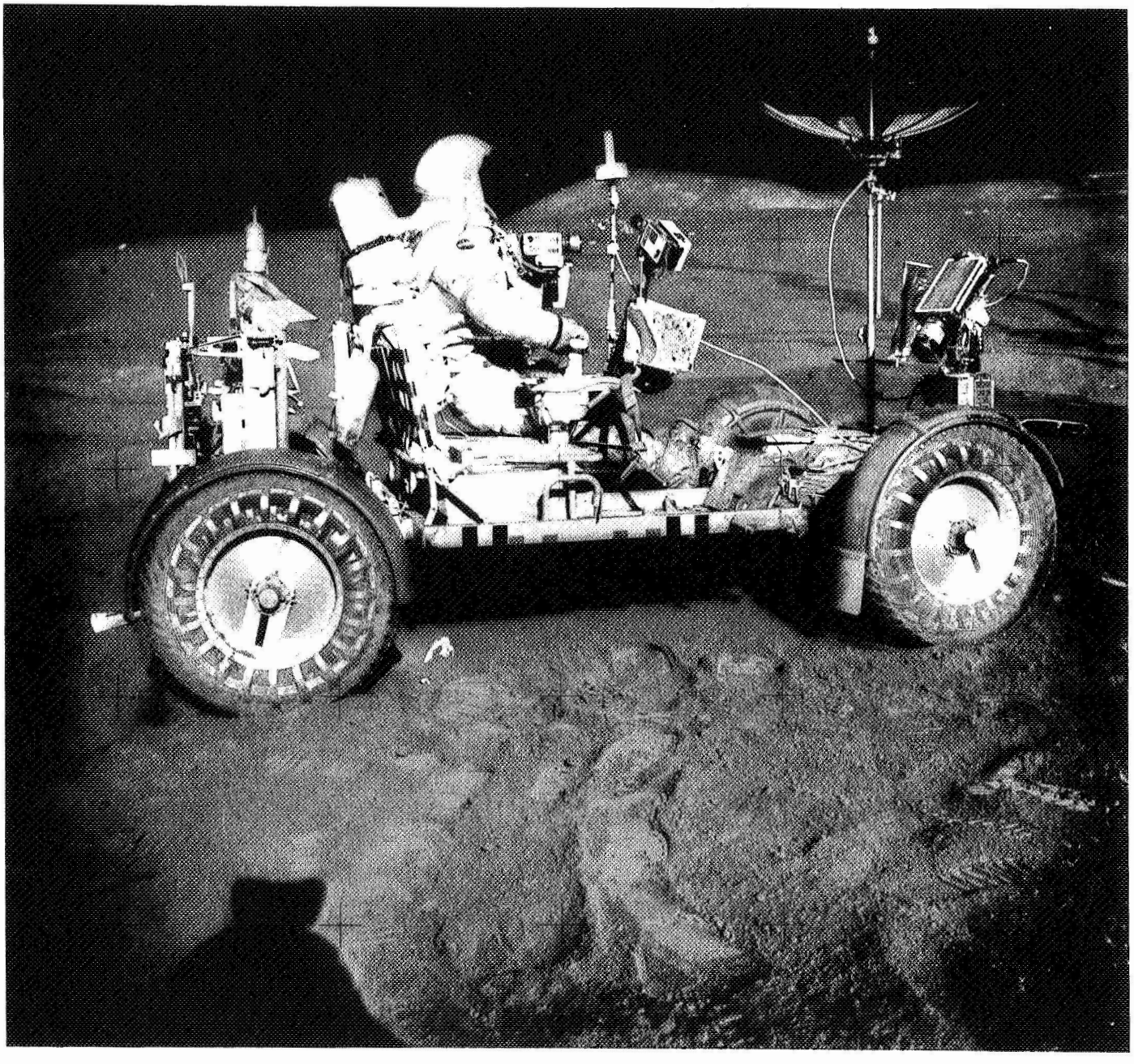

Fig. 2. *Apollo 15* Lunar Rover

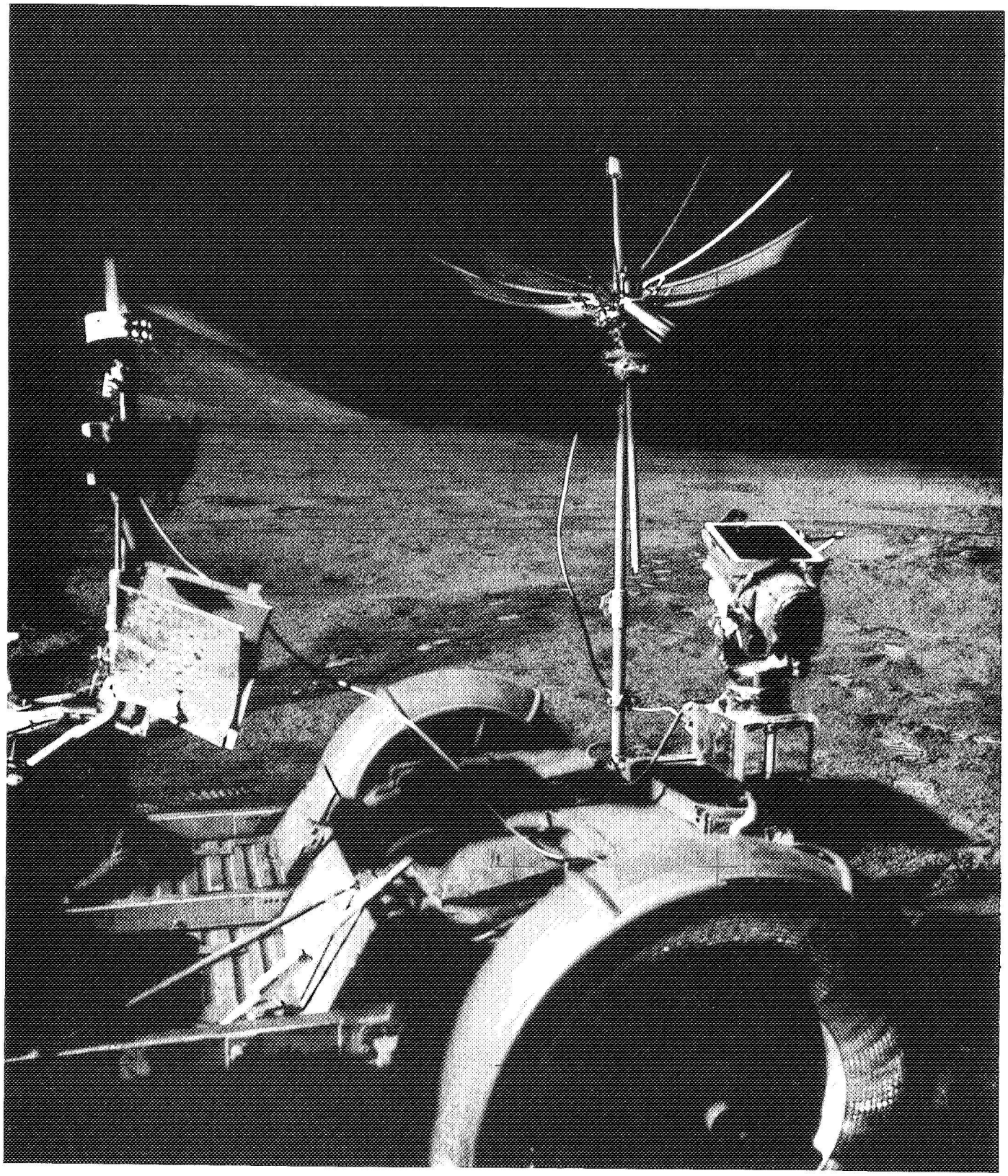

Fig. 3. View of rover showing ground commanded television camera, lunar communications relay unit, and high- and low-gain antennas

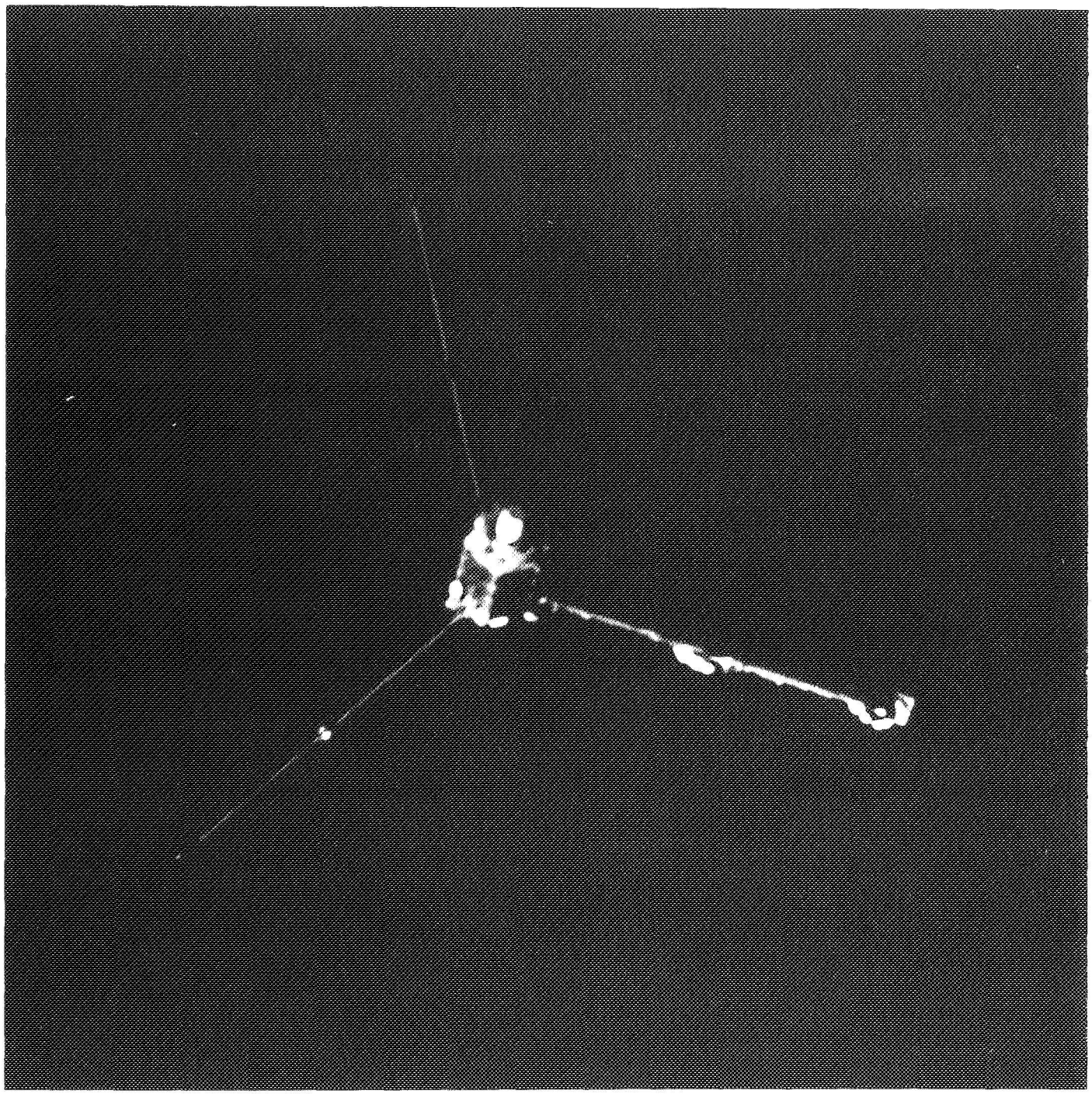

Fig. 4. Particle and fields subsatellite upon release from *Apollo 15* Command and Service Modules

Radio Science Support

K. W. Linnes
Mission Support Office

Since 1967 radio scientists have used the DSN 26- and 64-m antenna stations to investigate pulsars, to study the effects of solar corona on radio signals, and to observe radio emissions of X-ray sources. More recently, very long baseline interferometry (VLBI) techniques have been used for high resolution studies of quasars. During the reporting period, several proposals were received for extension of VLBI observations which had reported the startling expansion of quasar 3C279.

I. Introduction

The 26- and 64-m antenna stations of the DSN have been used for several years to support radio science experiments. NASA, JPL, and university scientists have used key DSN facilities whose particular and unique capabilities were required for the performance of the experiments. In order to formalize the method of selecting experiments and experimenters, a Radio Astronomy Experiment Selection (RAES) panel was formed in 1969. Notice of availability of these facilities was placed in professional journals to inform the scientific community that they were available for limited use by qualified radio scientists (Ref. 1). No charge is made for use of the standard DSN facilities and equipment; special equipment, however, must be provided by the experimenters. A summary of all experiments conducted through April 1971 was reported in Ref. 2.

II. Radio Science Operations

Table 1 summarizes the experiments supported since April 1971. The observations at X-band by Clark, Shapiro, and others in June are an extension of the General Relativity VLBI experiment performed in October 1970 and February 1971 between the 64-m antenna at Goldstone DSCC and the MIT Haystack antenna. Additional published findings appeared during this reporting period (Ref. 3).

III. RAES Panel Activities

The RAES Panel received and approved the proposals for experiments shown in Table 2.

References

1. *Bull. Amer. Astronom. Soc.,* Vol. 2, No. 1, p. 177, 1970.
2. Linnes, K. W., Sato, T., and Spitzmesser, D., "Radio Science Support," in *The Deep Space Network Progress Report,* Technical Report 32-1526, Vol. III, pp. 46–51. Jet Propulsion Laboratory, Pasadena, Calif., June 15, 1971.
3. Whitney, A. R., et al., "Quasars Revisited: Rapid Time Variations Observed Via Very Long Baseline Interferometry," *Science,* Vol. 173, p. 225, July 16, 1971.

Table 1. Radio science experiments involving 64- and 26-m antenna facilities

Experiment	Purpose	Experimenter	DSN Facility	Date
Very long baseline interferometry, X-band	To conduct VLBI survey of radio sources using baseline between Crimean Astrophysical Observatory in the USSR and the NRAO and Goldstone DSCC	J. Broderick, (NRAO) B. Clark (NRAO) M. Cohen (Caltech) D. Jauncey (Cornell University) K. Kellermann (NRAO) L. Matveyenko (Institute for Cosmic Research, USSR) I. Moiseyev (CAO, USSR) V. Vitkevitch (Institute for Cosmic Research, USSR)	DSS 14 (with 43-m antenna at NRAO and 22-m antenna at CAO)	30 May 1971 25 June 1971
Very long baseline interferometry (medium data bandwidth, S-band)	To determine angular size of radio sources	J. Gubbay (University of Adelaide) A. Legg (Space Research Group, WRE) D. Robertson (Space Research Group, WRE) A. Moffet (Caltech) B. Seidel (JPL)	DSS 14 and DSS 41	12 June 1971
Very long baseline interferometry (2295 MHz, NRAO recording terminals)	High resolution studies of extra galactic radio sources	J. Broderick (NRAO) B. Clark (NRAO) M. Cohen (Caltech) D. Jauncey (Cornell University) K. Kellermann (NRAO)	DSS 13 (and NRAO 43-m antenna)	7 August 1971
Quasar structure by X-band VLBI	To monitor time variations and fine structure and apparent position of quasars	T. Clark (GSFC) R. Goldstein (JPL) H. Hinteregger (MIT) C. Knight (MIT) G. Marandino, (University of Maryland) A. Rogers (MIT Haystack Observatory) I. Shapiro (MIT) D. Spitzmesser (JPL) A. Whitney (MIT)	DSS 14 (and MIT Haystack Antenna)	9,19 June 1971

Table 2. Recent experiments approved by the RAES panel

Experiment	Purpose	Experimenter	DSN facility
Spiral galaxy mapping	To study galaxies with anomalous red shifts and their possible association with radio sources	H. Arp (Caltech)	DSS 14
Quasar structure by X-band VLBI	To monitor time variations and fine structure and apparent position of quasars	T. Clark (GSFC) R. Goldstein (JPL) H. Hinteregger (MIT) C. Knight (MIT) G. Marandino (University of Maryland) A. Rogers (MIT Haystack Observatory) I. Shapiro (MIT) D. Spitzmesser (JPL) A. Whitney (MIT)	DSS 14 (and MIT Haystack antenna)
X-band VLBI	Repeat of earlier observations to search for changes in 33 or more sources	J. Broderick (NRAO) B. Clark (NRAO) K. Kellermann (NRAO) D. Jauncey (Cornell University) M. Cohen (Caltech) D. Shaffer (Caltech)	DSS 14 (and MIT Haystack antenna)

The Goldstone Interferometer for Earth Physics

J. L. Fanselow, P. F. MacDoran, J. B. Thomas, and J. G. Williams
Tracking and Orbit Determination Section

C. J. Finnie and T. Sato
Communications Elements Research Section

L. Skjerve
Philco-Ford Corporation

D. J. Spitzmesser
DSIF Operations Section

The first in a series of very long baseline interferometry feasibility demonstrations for applications to Earth Physics was conducted on January 29, 1971. In this demonstration two Goldstone tracking stations, the 26-m Echo station and the 64-m Mars station, were equipped with JPL hydrogen maser frequency systems and operated in electrically independent, although coordinated, observing modes. S-band (2.3 GHz) radio signals from 14 celestial radio sources were recorded at each station on digital magnetic tape. Later, these tapes were brought together for computer cross-correlation to produce an interferometric observable. Using the interferometer fringe frequency, a measurement of the two equatorial baseline components was made. The discrepancy between these measurements and the inter-station geodetic survey was less than 30 cm in each of these two components.

I. Introduction

In very long baseline interferometry (VLBI) measurements, the radio signal produced by a distant source is recorded simultaneously at two radio antennas. Because of a difference in raypaths, the signal will be delayed in time at one antenna relative to the other. By cross-correlating the two signals, the time delay and/or its time derivative may be determined. When narrow band recording equipment is used, as in the present work, only the time derivative of the time delay may be measured with adequate precision to be useful. If the radio signal is generated by an extragalactic object, the radio source may be regarded as a fixed object because of its great distance.

In this case, the time variation of the time delay is due entirely to the Earth's motion, but depends, of course, on the source location and the baseline vector between the two antennas. In general, measurement of the derivative of the time delay for many natural sources can lead, by means of a least-squares analysis, to the determination of source locations, the baseline vector, and Earth motion parameters, such as UT1 (Universal Time), and polar motion.

The VLBI Earth Physics Program at JPL has established among its goals the measurement of UT1, polar motion, and baseline vectors with submeter accuracy. The first experiment in this program was a feasibility demonstration conducted on January 29, 1971, between the 26-m Echo station and the 64-m Mars station of the Goldstone Deep Space Communications Complex (see Fig. 1). Although the stations were separated by only 16 km, the instrumentation of each station was electrically independent from that of the other. Such independence is of primary importance to the technique of VLBI and therefore makes this experiment a meaningful precursor to future VLBI Earth Physics experiments with overseas Deep Space Network (DSN) stations. The shortness of the Goldstone baseline afforded several advantages for a first experiment. Specifically, the reduced sensitivity to transmission media effects, source position errors, universal time, polar motion, and logistical support simplified the perfection of observing techniques and the development of data reduction software.

This article outlines narrowband interferometer theory, summarizes these short baseline experiments, and presents the results of these measurements.

II. Experiment Description

One of the main considerations in the design of this first feasibility demonstration was to make maximum use of existing DSN station resources. D. S. Robertson and A. H. Legg of the Weapons Research Establishment, Australia, had previously developed a VLBI recording method using the Digital Instrumentation Subsystem (DIS), which is a part of every DSN station. The recorded bandwidth was 24 kHz, dictated primarily by the DIS tape recorders. A discussion of this recording method may be found in Ref. 1, although Fig. 2 of this article contains the most salient features of the configuration used.

In this configuration each station was electrically independent of the other except for a voice circuit used for observing coordination. In effect, the separation of the stations could have been arbitrarily large, specifically intercontinental. The use of hydrogen maser frequency systems to control the receiver local oscillators at these isolated stations provided a level of precision previously unattainable by more conventional frequency standards.

Radio noise from 14 celestial sources was observed at S-band (2298 MHz). Forty pairs of magnetic tapes, each of 12 minutes duration, were recorded in a series of observations spanning ± 60 deg of local hour angle and $+67$ to -43 deg of declination between 20:00 GMT, January 29, 1971, and 07:00 GMT, January 30, 1971. Table 1 summarizes the specific sources used for this experiment.

III. Interferometry Theory (Narrow Band)

Figure 3 shows a schematic diagram of a radio interferometer station pair, while Fig. 4 gives the geometry of the situation. Since these two antennas are separated by a distance $|\mathbf{D}|$, there will be a difference in the time of reception of the signal at the two antennas. This delay, τ_g, is given by

$$\tau_g = \frac{\mathbf{D}}{c} \cdot \hat{\mathbf{s}} \tag{1}$$

where c is the speed of light, and $\hat{\mathbf{s}}$ is a unit vector opposite the direction of propagation of the wave front (assumed plane for simplicity only). This time delay has a maximum possible value of the Earth's radius/c, or 0.021 s. The quantity

$$\nu_F = \omega_0 \frac{\partial \tau_g}{\partial t} \tag{2}$$

is known as the fringe rate, where ω_0 is the received frequency, and is just the negative of the doppler shift between the two stations. In general, cross-correlation of the two data streams allows the time delay τ_g and the fringe rate ν_F to be measured.

The dot product in Eq. (1) is most usefully expanded in terms of the equatorial coordinate system of date. In this system, the right ascension and declination of the source are given by α_s, δ_s while the equivalent quantities for the baseline vector $\mathbf{D}$ are α_b, δ_b.

Explicitly writing out the dot product in Eq. (1),

$$\begin{aligned}\tau_g &= \frac{|\mathbf{D}|}{c}[\cos\delta_b \cos\alpha_b \cos\delta_s \cos\alpha_s \\ &\quad + \cos\delta_b \sin\alpha_b \cos\delta_s \sin\alpha_s + \sin\delta_b \sin\delta_s] \\ &= \frac{|\mathbf{D}|}{c}[\sin\delta_b \sin\delta_s + \cos\delta_b \cos\delta_s \cos(\alpha_b - \alpha_s)]\end{aligned} \tag{3}$$

The fringe rate (2) is then

$$v_F = -\frac{|\mathbf{D}|\,\omega_0}{c}\left[\cos\delta_b \cos\delta_s \sin(\alpha_b - \alpha_s)\right]\frac{\partial}{\partial t}(\alpha_b - \alpha_s) \tag{4}$$

If the equatorial projection of $|\mathbf{D}|$ is called r_b,

$$r_b = |\mathbf{D}| \cos\delta_b \tag{5}$$

Since

$$\frac{\partial}{\partial t}(\alpha_b - \alpha_s) = \omega_e \tag{6}$$

where ω_e is the angular velocity of rotation of the Earth (0.73×10^{-4} rad/s),

$$v_F = \frac{\omega_0 r_b}{c}\,\omega_e \cos\delta_s \sin(\alpha_b - \alpha_s) \tag{7}$$

Equation (3) emphasizes that cylindrical coordinates are the natural units for this problem. However, the problem is also conveniently expressed in terms of a right-handed cartesian coordinate system fastened to the Earth with the x axis through Greenwich and the z axis along the instantaneous rotation axis. If $\alpha_G(t)$ is the right ascension of Greenwich, and λ_b is the longitude of the baseline in the Earth-fixed system, then

$$\lambda_b = \tan^{-1}\left(\frac{y_2 - y_1}{x_2 - x_1}\right) \tag{8}$$

where x_i, y_i, z_i refer to the Earth-fixed, geocentric coordinates of the ith station, and the right ascension of the baseline vector becomes

$$\alpha_b(t) = \lambda_b + \alpha_G(t) \tag{9}$$

In a system fixed to the Earth,

$$X = |\mathbf{D}| \cos\delta_b \cos\lambda_b \tag{10}$$

$$Y = |\mathbf{D}| \cos\delta_b \sin\lambda_b \tag{11}$$

$$Z = |\mathbf{D}| \sin\delta_b$$

where X, Y, Z are the projections of the baseline on the x, y, z axes. The geometry of the Goldstone baseline is illustrated in Fig. 5.

Substituting Eq. (9) into Eq. (3), one can obtain

$$\tau_g = \frac{1}{c}\left(Z \sin\delta_s + \cos\delta_s \{X \cos[\alpha_G(t) - \alpha_s] - Y \sin[\alpha_G(t) - \alpha_s]\}\right) \tag{12}$$

and

$$v_F = -\frac{\omega_e \omega_0}{c}\left(\cos\delta_s \{X \sin[\alpha_G(t) - \alpha_s] + Y \cos[\alpha_G(t) - \alpha_s]\}\right) \tag{13}$$

Because of the narrow recorded bandwidth (24 kHz) of this experiment, the time delay observable (τ_g) was restricted in precision to a few microseconds (1 μs = 300 m). This experiment was aimed at making baseline measurements with submeter accuracy. Therefore, the time delay was ignored in favor of the fringe frequency observable which could provide the required precision. Since the fringe frequency is independent of z as indicated by Eq. (13), these measurements could precisely determine only the equatorial projection of the baseline.

Because we are interested in only the phase and frequency of the cross-correlation function, it is necessary only to analyze the interferometer response to monochromatic illumination.

Although the video signals at each station are infinitely clipped and digitally recorded, an analog derivation of the signal recording and processing contains the essential features of the technique.

Suppose that the electric field detected at antenna 1 is given by the expression

$$E_1(t) = E_0 \cos[\omega_0 t + \phi_{T1}(t)] \tag{14}$$

where ω_0 is the frequency at S-band, and ϕ_{T1} represents the phase drift due to transmission media. The retarded field detected at station 2 will then become

$$E_2(t) = E_0 \cos[\omega_0 (t - \tau_g) + \phi_{T2}(t)] \tag{15}$$

where τ_g represents the differential time of arrival due to the geometry and ϕ_{T2} represents the transmission media effects along the raypath to station 2. The voltage signal recorded at antenna 1 may be represented by the expression

$$V_1(t) = A \cos[(\omega_0 - \omega_1)t + \phi_{T1}(t) + \phi_{I1}(t)] \tag{16}$$

where ω_1 is the effective mixing frequency and ϕ_{I1} represents instrumental phase shifts. Similarly, the recorded signal at antenna 2 is given by the expression

$$V_2(t) = A\cos[(\omega_0 - \omega_2)t - \omega_0\tau_g + \phi_{T2}(t) + \phi_{I2}(t)] \quad (17)$$

IV. Data Reduction

In the cross-correlation process, the signal from station 2 is offset by a model time delay τ_m, and the two signals are multiplied together in order to produce a beat signal of the form

$$\begin{aligned} F(t) &= V_1(t)\,V_2(t+\tau_m) \\ &= A\cos[(\omega_2 - \omega_1)t + \omega_2\tau_m \\ &\quad + \omega_0(\tau_g - \tau_m) + \phi_I(t) + \phi_T(t)] \end{aligned} \quad (18)$$

where

$$\phi_I = \phi_{I1} - \phi_{I2}$$

$$\phi_T = \phi_{T1} - \phi_{T2}$$

The model time delay τ_m is calculated on the basis of an assumed baseline and source location.

For efficiency in data handling, the beat signal $F(t)$ (fast fringes) is digitally processed to remove the known higher frequency components of the phase. This procedure, which is called fringe stopping, is analogous to the heterodyne function of a receiver using a heterodyne frequency of $(\omega_2 - \omega_1) + \omega_2\dot{\tau}_m$. The stopped fringes G_S are given by

$$G_S(t) = A\cos[\omega_0(\tau_g - \tau_m) + \phi_T(t) + \phi_I(t)] \quad (19)$$

An example of stopped fringes is shown in Fig. 6 along with a cosine curve fit to them by least squares. Because of the $2\pi n$ ambiguity involved in inversion of trigonometric functions, only the time dependence of the phase may be obtained from the stopped fringes. That is, the phase may be determined except for an unknown additive constant. Two methods are presently used to extract this time dependence: Fourier analysis and phase tracking.

The first method, Fourier analysis, is useful when the stopped fringe frequency is effectively constant over the integration period. The choice of integration period T depends on the instrumental stability, transmission media stability, and time delay modelling accuracy. A Fourier transform of the stopped fringes yields the stopped fringe frequency ν_S, which is given by

$$\nu_S = \text{stopped fringe frequency} = \nu_R + \nu_N \quad (20)$$

where

$$\nu_N = \text{frequency offset} = \dot{\phi}_I + \dot{\phi}_T \quad (21)$$

$$\nu_R = \text{residual fringe frequency} = \omega_0(\dot{\tau}_g - \dot{\tau}_m) \quad (22)$$

The term ν_R is called the *residual fringe frequency*, whereas the quantity ν_N is called the *frequency offset* and is intended as a general term. As indicated above, it results from the combined effects of instrumental and transmission media phase shifts. For this experiment, the simplest model for ν_N assumes $\dot{\phi}_T = 0$ and $\dot{\phi}_I =$ constant, the latter accounting for an offset between the two first local oscillator frequencies. As will be discussed later, ν_N actually was not constant during certain portions of the experiment.

Figure 7 displays the Fourier transform of one of the short baseline runs with an integration time T of approximately 700 s. The transform of a single frequency is proportional to $[\sin(T\Delta\nu/2)]/(T\Delta\nu/2)$, where $\Delta\nu$ is the frequency difference from ν_S and has a half-width to the first null of $1/T$. Since Fig. 7 exhibits this expected shape, a narrow range of frequencies (< 0.2 mHz) is present in the fringe rate. The upper limit is consistent with expected hydrogen maser performance and expected modelling accuracy.

Although the Fourier transform technique can efficiently extract the stopped fringe frequency and reveal spectral distributions that are comparable to the natural $1/T$ width of the Fourier transform, it cannot reveal the time history of phase excursions which could be useful in data interpretation. Therefore, a least-squares technique was used to count cycles in order to determine the time dependence of the phase. The initial phase of individual 33-s segments is obtained by the data fitting technique illustrated in Fig. 6. In this manner, 21 initial phase values were calculated for each 700-s run, thereby giving the time dependence of the phase. These 21 phase values were then fit by a least-squares linear time function over the tape length (700 s). The slope of this fit function is equal to the (average) stopped fringe frequency for that run. Phase residuals are obtained by subtracting from each individual phase value the corresponding linear fit value. Figures 8a and 8b show phase residuals for runs 15 and 20. Phase residuals produced by the linear fit will be random if no systematic nonlinear trends are present in the phase because of modelling error, instrumental instability or transmission media. For the present short baseline experiment, a model time delay can be constructed that is accurate enough to make the residual fringe frequency

change undetectable over a 700-s interval. Thus, in this particular experiment, nonlinear phase excursions indicate instrumental or transmission media phase drifts. Figure 8a consists mainly of random noise and indicates a frequency stability better than 50 μHz at S-band or $\Delta f/f \lesssim 2 \times 10^{-14}$. Figure 8b, however, seems to contain systematic phase deviations of the order of 0.1 cycle and indicates that the frequency (instantaneous slope) wanders by about 1 mHz. Further investigation is required to determine whether these short-term excursions are produced by instrumental instability or by the transmission media.

Random residuals that appear in the residual phase plots appear to be due primarily to receiver noise and lead to frequency measurement errors in the 20- to 200-μHz range for correlated source strengths of 1 to 10 flux units[1] and integration times of 700 s. H-maser flicker noise can contribute an additional uncertainty between 15 to 30 μHz at S-band. Thus, the inherent accuracy of the narrow-band system should fall in the 20- to 200-μHz range for S-band measurements for sources with 1–10 flux units of unresolved power. Such frequency accuracy in principle would allow baseline measurements with an uncertainty between 5 and 30 cm. However, instrumental and transmission media phase excursions often prohibit measurements of this accuracy. For example, calibration or control of the 1-mHz frequency variations revealed in the NRAO 190 plot (Fig. 8b) will be necessary in order to exploit the inherent accuracy of the interferometer.

V. Stopped Fringe Frequency Model

After cross-correlation and fringe analysis, the reduced data consist of a stopped fringe frequency for each run. Since the model for the time delay was only approximate, the fringe rate after stopping is not zero. Therefore, an additional model must be constructed for the stopped fringe frequency in order to extract the actual baseline. As seen in Eq. (20), the stopped fringe frequency is given by

$$\nu_S = \omega_0 (\dot{\tau}_g - \dot{\tau}_m) + \dot{\phi}_T + \dot{\phi}_I \tag{23}$$

where the first term represents the residual fringe frequency and $\dot{\phi}_T$ and $\dot{\phi}_I$ are the time derivatives of the transmission media and instrumental phase drifts.

In general, the residual fringe frequency can be due to several errors in the model time delay. However, in the short baseline experiment, model errors due to source locations, UT1, precession, nutation, aberration, and polar motion make contributions to the residual fringe frequency which are below the measurement uncertainty of 50 μHz. Since all of these errors can be represented by an equivalent source position error, their importance may be demonstrated by evaluating the partial derivatives of the fringe frequency, Eq. (7), with respect to the source angles α_s and δ_s:

$$\frac{\partial \nu_F}{\partial \alpha_s} = \frac{\omega_0 \omega_e \mathbf{r}_b}{c} \cos \delta_s \cos (\alpha_b - \alpha_s) \tag{24}$$

$$\frac{\partial \nu_F}{\partial \delta_s} = -\frac{\omega_0 \omega_e \mathbf{r}_b}{c} \sin \delta_s \sin (\alpha_b - \alpha_s) \tag{25}$$

For both derivatives, the maximum sensitivity for the Goldstone baseline is 30 μHz/arc sec. Since the aggregate effect of all the above error sources was equivalent to less than one arc sec in source position, their combined contribution to the residual fringe frequency was less than 30 μHz. Thus, the residual fringe frequency model must only account for baseline error and is given by

$$\omega_0 (\dot{\tau}_g - \dot{\tau}_m) = \frac{\partial \nu_F}{\partial X} \Delta X + \frac{\partial \nu_F}{\partial Y} \Delta Y \tag{26}$$

where ΔX, ΔY are the corrections to the equatorial components of the baseline and where

$$\frac{\partial \nu_F}{\partial X} = \frac{\omega_0 \omega_e}{c} \cos \delta_s \sin [\alpha_G (t) - \alpha_s] \tag{27}$$

$$\frac{\partial \nu_F}{\partial Y} = -\frac{\omega_0 \omega_e}{c} \cos \delta_s \cos [\alpha_G (t) - \alpha_s] \tag{28}$$

as indicated by Eq. (13).

Because of the proximity of the raypaths in a short baseline measurement, the transmission media phase shifts along the two paths should be nearly identical so that the difference found in the interferometer phase shift ϕ_T should be nearly zero. If the instrumentation at both stations were perfectly stable but a small offset existed between the two local oscillators, the instrumental term $\dot{\phi}_I$ would be constant. Under these conditions, the frequency offset ν_N could be represented by a constant.

Under all of these assumptions, the fitting equations become

[1]One flux unit = 10^{-26} watts/m^2/Hz. Table 1 lists flux measurements on 10 sources using the DSS 14 total power radiometer.

$$\left.\begin{aligned} \nu_1 &= \left.\frac{\partial \nu_F}{\partial X}\right|_1 \Delta X + \left.\frac{\partial \nu_F}{\partial Y}\right|_1 \Delta Y + \nu_N \\ \nu_2 &= \left.\frac{\partial \nu_F}{\partial X}\right|_2 \Delta X + \left.\frac{\partial \nu_F}{\partial Y}\right|_2 \Delta Y + \nu_N \\ &\vdots \\ \nu_i &= \left.\frac{\partial \nu_F}{\partial X}\right|_i \Delta X + \left.\frac{\partial \nu_F}{\partial Y}\right|_i \Delta Y + \nu_N \end{aligned}\right\} \quad (29)$$

where ν_i is the stopped fringe frequency for the ith run, ν_N is a constant frequency offset, and ΔX, ΔY are corrections to the assumed equatorial components of the baseline. The partials are evaluated at the middle of the run interval.

VI. Results

From a total set of 40 runs, 33 tape pairs were readily processed. Seven pairs were deleted primarily because of tape writing problems. When the stopped fringe frequencies for these 33 runs were simultaneously fit by least-squares using the model of the previous section, the rms residual for the total set was 500 μHz. These fit residuals were obtained by subtracting the right-hand side of Eq. (29) (using the fit values for ΔX, ΔY, and ν_N) from the observed stopped fringe frequency for each run. Such large residuals were in sharp contrast with the typical measurement uncertainty of 50 μHz for individual runs.

This disagreement forced a reappraisal of all the assumptions used in the data reduction. One of the assumptions involved the constancy of the frequency offset ν_N. To test the possibility of temporal variations in ν_N, we assumed that the frequency offset experienced long-term variations but was constant during certain unknown time intervals. The advantage of this hypothesis was that the above model could be applied during any time interval suspected of constant offset. The 33 runs were separated into various sequences and each segment was fit separately using the constant offset model. Most sequences produced large residuals ($\approx 500\,\mu$Hz) and baseline corrections that disagreed between sequences by as much as 5 meters. However, we were able to locate two time intervals for which the fit residuals were small ($< 100\,\mu$Hz) and for which the baseline corrections were in agreement.

Table 2 summarizes these results in terms of the baseline corrections (ΔX, ΔY), frequency offset ν_N, and fit residuals. The errors in the table are one standard deviation formal statistical errors. Figure 9 illustrates the stopped fringe frequency values obtained for runs 26–40 and the fit residuals for these runs. Both the small residuals and the baseline agreement between the two sequences indicate that the assumption of a constant frequency offset during each of these two sequences is valid.

When the results for these two sequences are combined, they yield the following baseline corrections:

$$\Delta X = 1.2 \pm 0.2\,\text{m}$$

$$\Delta Y = 0.3 \pm 0.3\,\text{m}$$

The final adopted errors have been made larger than the formal statistical errors in an attempt to account for systematic trends in the residuals.

The full corrected equatorial baseline components are obtained by applying the above composite baseline corrections to the assumed baseline as shown in Table 3. Geodetic survey values (Ref. 2) have also been included in this table and are in excellent agreement with the interferometer results.

If we assume that the measured baseline corrections are valid, the frequency offset for each run may be obtained by subtracting the residual frequency due to this baseline error from the stopped fringe frequency. This has the same effect as repeating the cross-correlation and fringe stopping procedures using the corrected baseline. The resulting frequency offsets are plotted versus run number and time in Fig. 10. The plot indicates that the offset exhibited 1-mHz excursions relative to the nighttime value.

VII. Discussion

Unexplained frequency and phase excursions were present with both short-term (minutes) and long-term (hours) variations. The source of the variations could conceivably be either transmission media or instrumentation.

Consider first the short-term variations of which Fig. 8b is an example. In that case, a 0.2 S-band cycle drift occurs, implying a 2.6-cm phase change. It is not possible to uniquely identify the source of these excursions; however, some physical mechanisms can be hypothesized which produce similar effects. For example, the troposphere represents a 2.2-m phase delay at the zenith. Thus, only about a 1% difference is needed in the raypaths to cause a 2.6-cm phase shift. A similar argument applies for the effects on the ionosphere. While the transmission media is a possible cause, instrumental phase shifts of 2.6 cm are also possible.

The long-term variations are seen in Fig. 10. One of the most obvious features of Fig. 10 is the apparent frequency offset dependence on time of day. A day versus night dependence connotes a thermal heating or transmission media effect, particularly the ionosphere.

In order for the transmission media to be the cause of the Fig. 10 excursions, the observations must exhibit some particular properties. For example, there should be some dependence on the elevation angle of the antennas and the magnitude of the effects must be consistent with likely dissimilarities in the two raypaths, since an interferometer is inherently a differential device.

Figure 11 shows the tropospheric frequency error for a single raypath versus run number, given a 2.2-m zenith phase delay. This figure accounts for no transmission media cancellation due to the similarity of the raypaths and is therefore the worst-case error. With regard to the magnitude of the frequency excursions in Fig. 10, it seems unlikely that 2-mHz tropospheric effects could be introduced differentially in the interferometer raypaths. In addition, a comparison of Figs. 10 and 11 shows virtually no correlation. For these reasons, the troposphere may be rejected as a cause of the long-term offset variations.

By an argument similar to the one given above, the ionosphere also becomes a doubtful source of these long-term variations.

If the frequency offset variations are due solely to instrumental instability, a time integration of the frequency offset (Fig. 10) will yield the long-term instrumental phase excursions. By taking the nighttime offset as base frequency and arbitrarily making the phase zero at 12:00 local time, one can integrate the offset to obtain the phase excursions shown in Fig. 12. The phase increased to about 7 cycles by 15:00 local time and then decreased to -5 cycles at 20:00 and remained essentially constant until the end of the experiment, 23:00.

The major instrumental elements to be suspected are the frequency synthesizers, traveling-wave S-band maser, hydrogen maser frequency system, and antenna cabling. Preliminary investigations conducted at the Goldstone DSCC[2] have shown cable electrical length stabilities of 0.01 cycle of S-band except during periods of rapid thermal changes, such as sunrise. The sunrise heating has been observed to result in 0.1-cycle shift within about one-half hour. Thus, the largest phase rates expected would be 50 μHz and then only in a transient manner. Frequency offsetting mechanisms to explain Fig. 10 must be sustainable at the millihertz level over hours.

[2]Personal communications with F. Borncamp, DSIF Operations Section, JPL.

Frequency variations originating in the H-maser output are highly unlikely at the part in 10^{12} level that would be required for millihertz variations at S-band, making the H-masers an unlikely source of the excursions.

The traveling-wave maser (TWM) operates at S-band and provides the first stage of amplification for each station. A TWM is constructed in such a way that hundreds of wavelengths are present within its slow wave structure. Since changes in the observed frequency offset of Fig. 10 could have been caused by changes in electrical path, the TWM was a suspect component. The effects of temperature, magnetic field strength, and magnetic field shape have been examined and reported in Ref. 3. The electrical path length changes (<18 deg) measured in that work were far from the 12-cycle shifts required by Fig. 12. TWM phase shifts have been observed due to the Earth's magnetic field. However, R. C. Clauss[3] reports that tests conducted at DSS 14 showed 30-deg phase shifts with an azimuthal dependence. Thus, the TWM does not appear to be the cause of the frequency offset variations.

The last major instrumental suspect is the Hewlett Packard model 5100B frequency synthesizers. As seen in Fig. 2, four synthesizers were used in each station's configuration. The interferometer is sensitive to the performance of all the synthesizers but is particularly sensitive to the synthesizer used to generate the first local oscillator signal since instabilities in this first local oscillator synthesizer are multiplied by 96. Table 2 and Fig. 11 show that the baseline solution for runs 26–40 generated an rms residual of 74 μHz, indicating a fractional frequency deviation of not greater than $\Delta f/f = 3 \times 10^{-14}$ over time spans of 10 minutes to 4 hours during these last 13 runs.

Performance specifications for the synthesizer are not stated by Hewlett Packard for averaging times greater than 1 second, where it is $\Delta f/f = 1 \times 10^{-11}$. Under the most ideal circumstances (white phase noise), the synthesizer's fractional frequency deviation could improve only by the square root of the averaging time. Therefore, at 10 minutes, the performance should be about $\Delta f/f = 4 \times 10^{-13}$. The frequency system performance achieved on runs 26–40 was an order of magnitude better than could be inferred from the manufacturer's specified performance. Thus, the data indicates that the synthesizers did outperform inferred specifications during certain periods; however, it is also possible that the long-term performance was at the part in 10^{12} level, giving rise to the observed frequency offset variations of Fig. 10.

[3]Communications Elements Research Section, JPL.

VIII. Summary

Independent station radio interferometry has been used to measure the baseline between two stations of the Goldstone Deep Space Communications Complex with an accuracy of 30 cm. This short baseline experiment has revealed long-term (hours) and short-term (minutes) frequency instabilities that require either calibration or control before the inherent accuracy of less than 10 cm can be achieved. The experience of this interferometer demonstration has allowed the development of observing techniques, data reduction software, and results which could be independently verified with high precision.

References

1. Sato, T., Skjerve, L., and Spitzmesser, D., "Radio Science Support," in *The Deep Space Network,* Space Programs Summary 37-62, Vol. II, pp. 125–127. Jet Propulsion Laboratory, Pasadena, Calif., Mar. 31, 1970.
2. Mulhall, B. D., et al., *Tracking System Analytic Calibration Activities for the Mariner Mars 1969 Mission,* Technical Report 32-1499. Jet Propulsion Laboratory, Pasadena, Calif., Nov. 15, 1970.
3. Clauss, R. C., "Low-Noise Receivers, Microwave Maser Development, Second Generation Maser," in *The Deep Space Network,* Space Programs Summary 37-51, Vol. II, pp. 73–77. Jet Propulsion Laboratory, Pasadena, Calif., May 31, 1968.

Table 1. Summary of radio sources used in short baseline experiment

Source	Position						Number of runs	Observed total flux density[a] (Jan. 29, 1971), flux units
	Right ascension (1950.0)			Declination (1950.0)				
	Hour	Min	Second	Degree	Min	Second		
P 0106 + 01[b]	01	06	04.54	01	19	00.3	4	1.8 (2)[c]
DW 0224 + 67	02	24	43.	67	07	35.	1	
P 0237 − 23[b]	02	37	52.75	−23	22	05.9	4	5.6 (2)
3C 84[b]	03	16	29.526	41	19	52.78	4	12.0 (1)
NRAO 140[b]	03	33	22.38	32	08	36.8	3	3.0 (1)
3C 120[b]	04	30	31.63	05	14	59.5	4	5.8 (2)
P 0438 − 43[b]	04	38	44.	−43	38	51.	1	9.2 (1)
NRAO 190[b]	04	40	05.29	−00	23	20.1	6	3.0 (3)
P 0521 − 36	05	21	13.00	−36	30	15.	1	13.1 (1)
3C 345	16	41	17.56	39	54	10.6	3	
P 1741 − 038	17	41	20.60	−03	48	49.0	1	
P 2134 + 004	21	34	05.29	00	28	25.8	1	
CTA 102[b]	22	30	07.80	11	28	22.8	3	5.2 (1)
3C 454.3[b]	22	51	29.52	15	52	53.7	4	11.5 (2)

[a]20% uncertainty.
[b]Denotes sources used for baseline solution.
[c]Number of measurements in parentheses.

Table 2. Interferometer-derived corrections to assumed baseline

Runs	ΔX, m	ΔY, m	ν_N, mHz	Rms residual, μHz
15–23	0.9 ± 0.35	−0.23 ± 0.2	2.56 ± 0.1	95
26–40	1.4 ± 0.15	−0.47 ± 0.3	3.6 ± 0.2	74

Table 3. Equatorial baseline components

Baseline	X, m	Y, m	r_b, m	λ_b, deg
Assumed	−3179.6	10637.2	11102.2	163.3578
Corrected	−3178.4 ± 0.2	10636.9 ± 0.3	11101.6 ± 0.3	163.3633 ± 0.0011
Surveyed	−3178.42 ± 0.15	10636.60 ± 0.15	11101.3 ± 0.16	163.3628 ± 0.0007

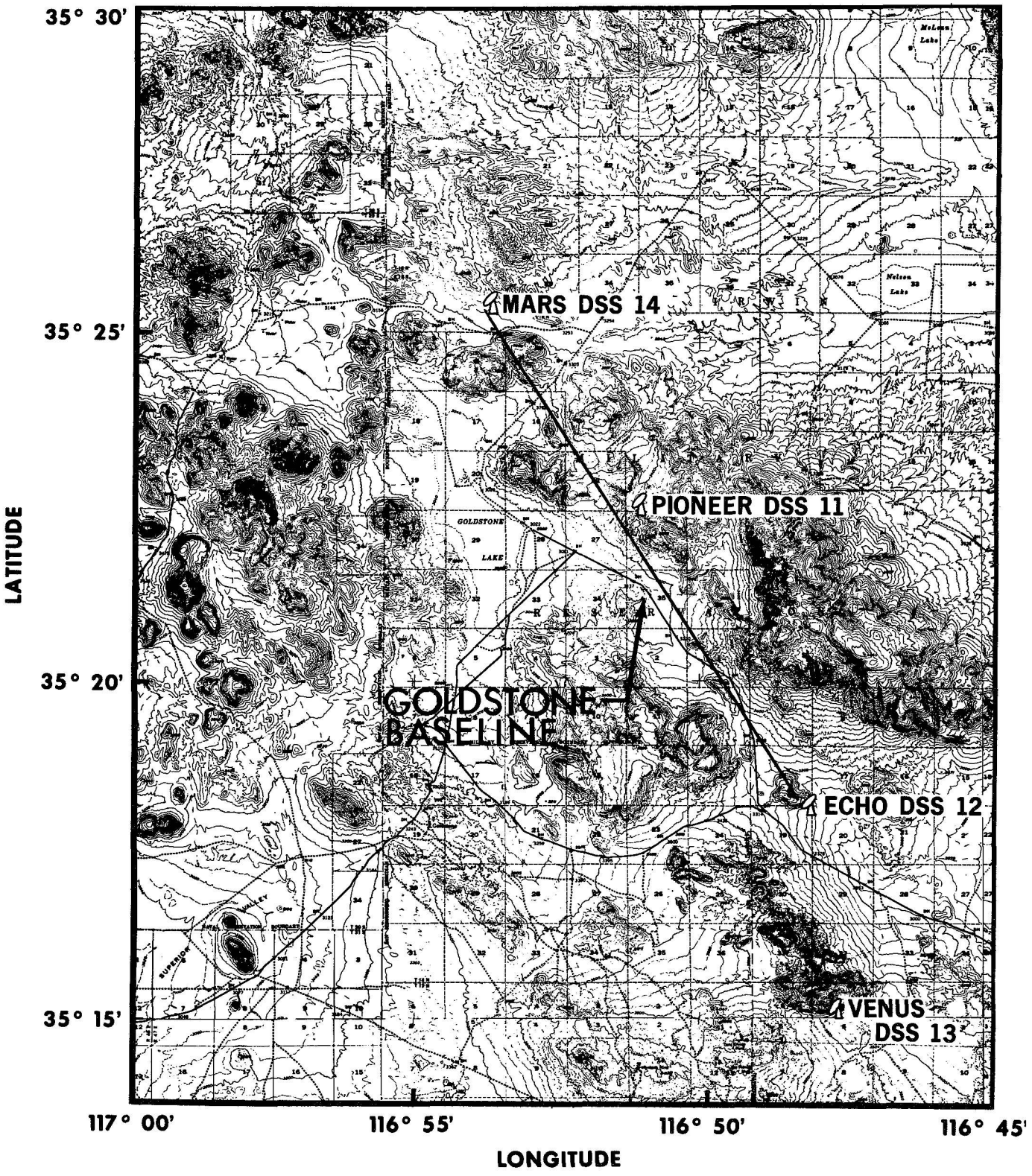

Fig. 1. Goldstone Deep Space Communications Complex

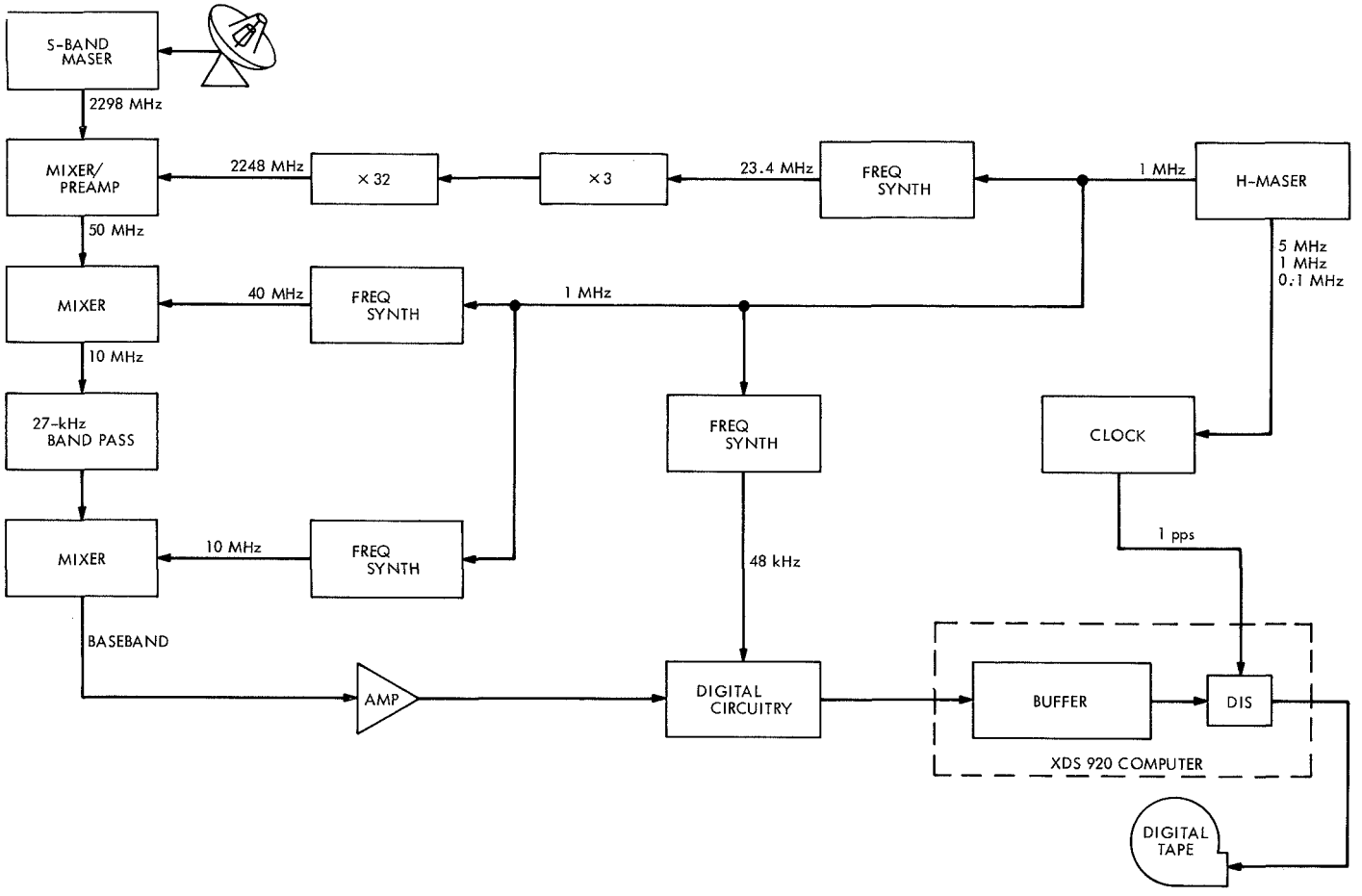

Fig. 2. Interferometry station configurations

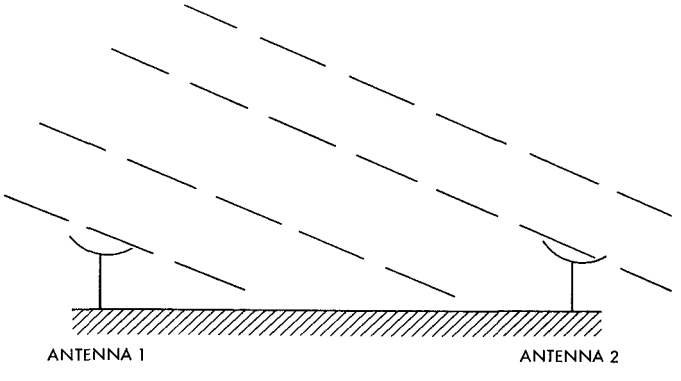

Fig. 3. Interferometer pair

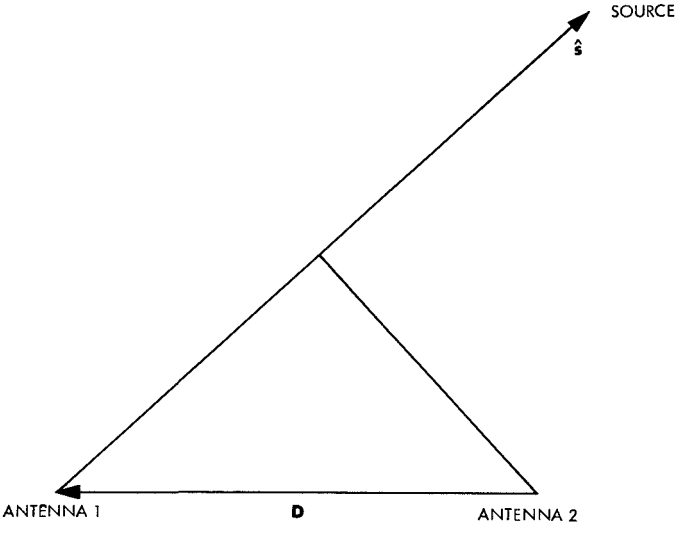

Fig. 4. Interferometer geometry

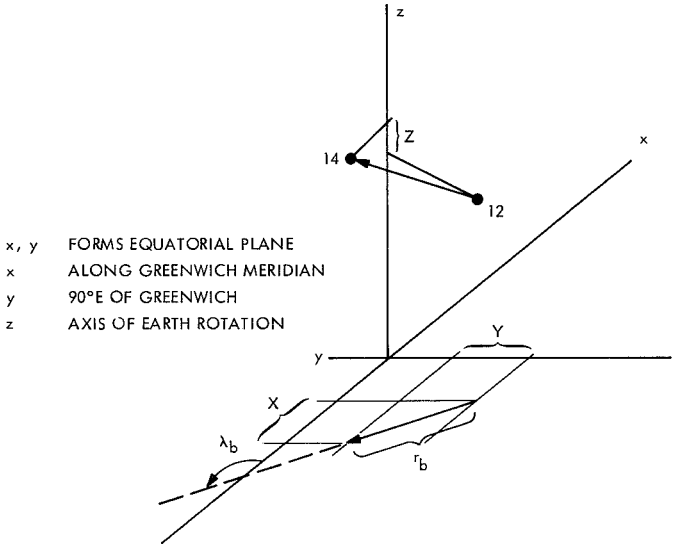

Fig. 5. Goldstone (DSS 12, 14) baseline

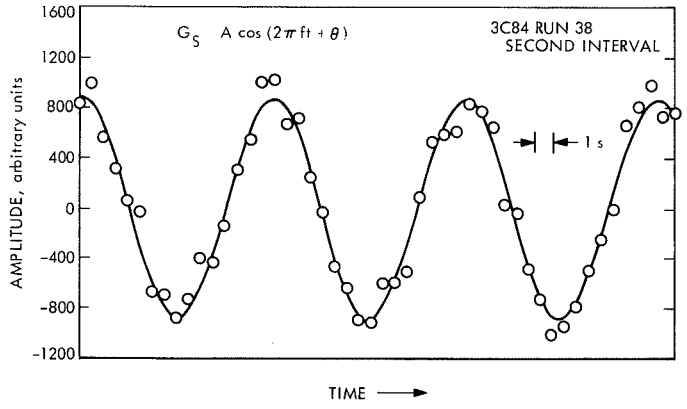

Fig. 6. Stopped fringes

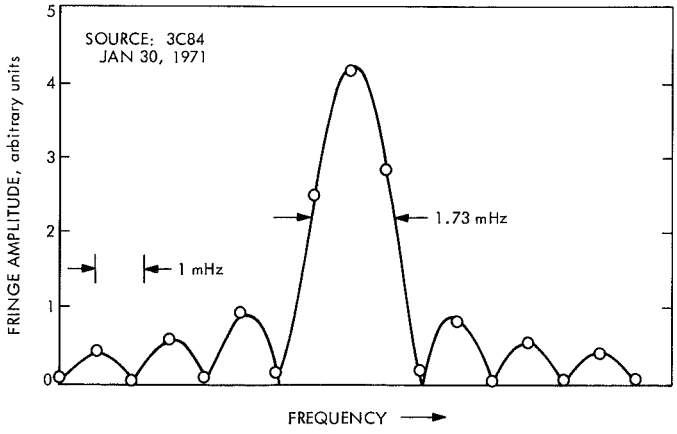

Fig. 7. Fourier transform of residual fringes

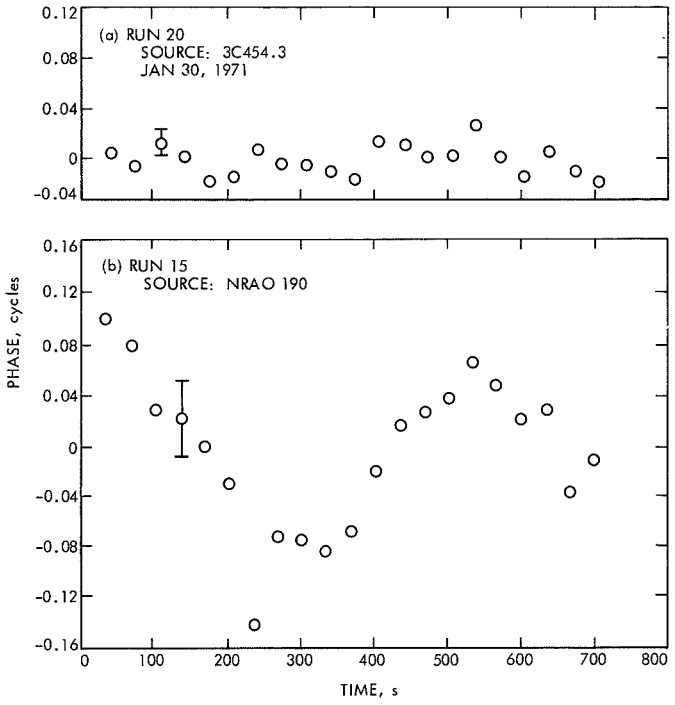

Fig. 8. Fringe phase residuals

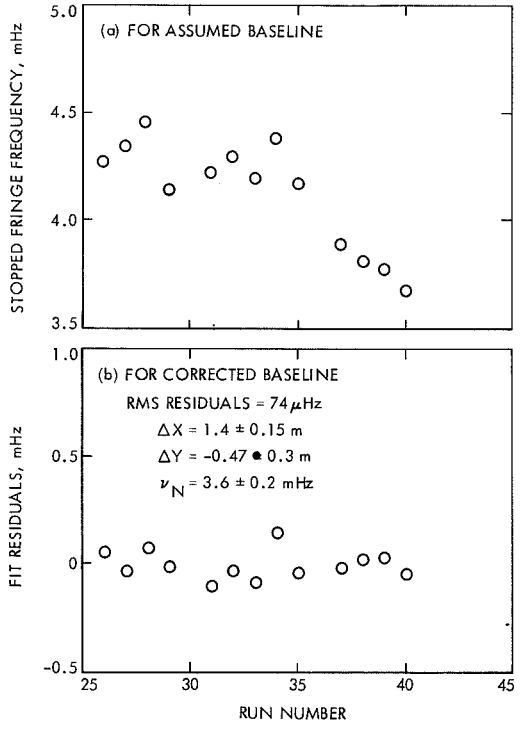

Fig. 9. Stopped fringe frequency values and fit residuals for runs 26–40

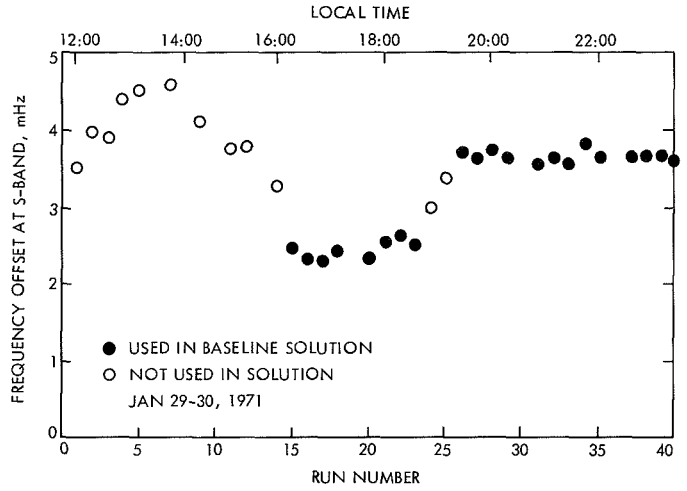

Fig. 10. Interferometer frequency offset for corrected baseline

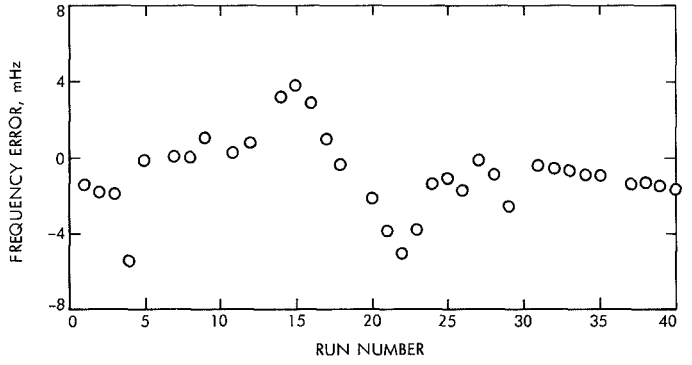

Fig. 11. Tropospheric frequency error for a single raypath

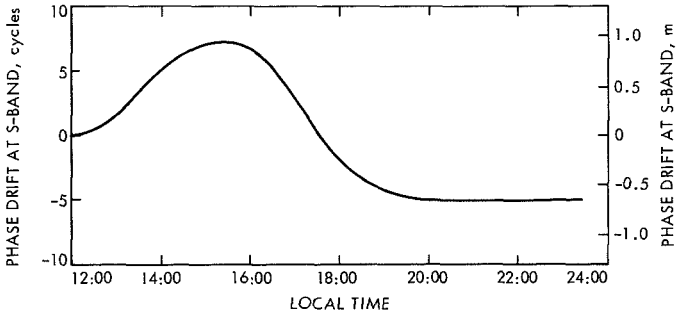

Fig. 12. Interferometer phase drift

Comparison of Faraday Rotation Measurements of the Ionosphere

L. F. Miller and B. D. Mulhall
Tracking and Orbit Determination Section

An evaluation of the mapping techniques employed to provide ionospheric charged particle calibration for post-flight analysis and for Mariner Mars 1971 tracking system analytical calibration operations was performed. Comparisons based on Faraday rotation data from geostationary satellites were made between various satellites as recorded at the Venus Deep Space Station and by Stanford Center for radar astronomy.

I. Introduction

Continual efforts are being made as part of the tracking system analytic calibration (TSAC) effort to improve the accuracy of the ionospheric calibration. One approach to this calibration is the use of Faraday rotation measurements, principally from geostationary satellites. A description of the technique for employing a stationary measurement as a calibration for a moving line of sight can be found in Ref. 1. To evaluate these mapping techniques, a computer program ICARIS (Ionispheric CompARISon), with the capacity to compare charged particle measurements over two different lines of sight, has been written. ICARIS can compare measurements made to stationary satellites or to space probes and can use various types of charged particle measurements, i.e., Faraday rotation, differenced range versus integrated doppler, dual frequency, or ionosonde.

This article describes several comparisons which have been made using ICARIS, concentrating on a comparison of Faraday rotation measurements made from Goldstone DSCC to ATS-1[1] and to ATS-5 (two geostationary satellites) during the period December 1970 to February 1971.

These comparisons were to evaluate the mapping of measurements from one line of sight to another and thereby establish the quality of calibrations calculated from data. The comparisons indicate that the mapping is generally better than 0.5 m of radio path change at S-band. The comparisons were made by mapping (adjusting in time and space) the ATS-1 data to the ATS-5 line of sight and comparing the mapped ATS-1 data to the unmapped ATS-5 data. The process was then reversed. A successful mapping is one for which the mapped and unmapped data are nearly identical. If the mapping is good, space probe data may be calibrated

[1]ATS = *Applications Technology Satellite.*

for charged particles by a measurement to zenith (in the case of ionosonde data) or to some arbitrary fixed position (in the case of Faraday rotation measurements to a geostationary satellite). The mapping used in ICARIS is not always expected to be good over the range of all possible elevation angles and longitude differences between mapped and unmapped data. The assumption of spherical symmetry of the ionosphere (at a given sun–earth–probe angle) can be expected to fail at low elevation angles, and may fail elsewhere as well. The comparisons described in this article indicate some of these limitations.

II. ATS-1 and ATS-5 Faraday Rotation Comparison

A. Background

Faraday rotation measurements were available for 26 days during the period December 1970 to February 1971 for the geostationary satellites ATS-1 and ATS-5. The days of comparison were chosen under the criterion that sufficient data were available to provide a significant test.

The data was originally recorded at DSS 13 on a paper tape or on a strip chart recorder. The ATS satellites transmit a beacon at 137-MHz for which the Faraday rotation of an electromagnetic wave may be as great as 900 deg or as little as 90 deg at zenith during a typical day. It is necessary to "refasten" the data, which has been recorded modulo 180 deg. The technique for refastening the data has been described in Ref. 1.

Two problems accompanied the reduction of data. They were revealed only upon comparison of the ATS-1 and ATS-5 data sets. First, the ATS-5 data still had several ambiguities which had not been detected. If the data record was quite smooth at that point, the ambiguities were prominent, and identifiable by the fact that they left a vertical gap in the data of 180 deg. If the record was jogged or there were only a few time points in the area, repeated attempts were necessary to get a best fit to the ATS-1 data.

The second problem was the determination of the magnitude of the conversion factor. Calculations of the geomagnetic field suggested that 180 deg of Faraday rotation corresponded to an electron content of 0.479×10^{17} electrons/m^2. This value introduced two characteristic irregularities into the ATS-5 data: the ATS-5 peak-to-trough amplitude was always larger (by fixed factor) than the ATS-1 data; and at each point where a modulo was inserted a small discontinuity ($\sim 0.05 \times 10^{17}$ electrons/m^2) was introduced into the ATS-5 trace. After considerable experimentation with five days worth of data (2/1/71 to 2/6/71), it developed that a conversion factor for 180 deg of 0.430×10^{17} electrons/m^2 eliminated these errors. The fact that these systematic anomalies did not recur when the complete data set was compared gives one some confidence in the *a posteriori* experimental value for the conversion factor. The cause of this descrepancy between the computed and empirical values for the conversion should be explored further.

B. Results

The average standard deviation of the difference between ATS-1 and ATS-5 was 0.11×10^{17} electrons/m^2 (~ 0.1 m of radio path change at S-band). ICARIS was reciprocal. That is, the results obtained did not depend on which satellite data was mapped. There was a very small systematic difference between the two sets of measurements: $<\text{ATS-5} - \text{ATS-1}> = 0.02 \times 10^{17}$ electron/m^2. This could be due to a small error in the conversion factor, but the absence of any of the small discontinuities produced by an inaccurate conversion constant weighs against this explanation. More likely, it is caused by an error in the mapping technique. Figure 1 shows a day on which the comparison was very good—February 3, 1971. Notice that the deviation between mapped (ATS-1) and (ATS-5) averages 0.056×10^{17} electrons/m^2 ($\sim$ 6-cm range error). Careful examination of the figure shows that the ATS-5 data may lag the ATS-1 data during the day–night and night–day transitions by $\sim$10 min. This has yet to be explained. It may be an error in recording or reading the strip chart, a mapping error, software error, or a reflection of actual conditions.

Figure 2 (12/24/70) shows that same lagging tendency, greatly magnified, which is believed to be an error in strip chart recording or reading. ATS-5 is located at 105°W (Table 1) on the celestial equator, while ATS-1 is located at 150°W. Thus, ATS-5 is in the sun about 3 h earlier than ATS-1. The ICARIS mapping corrects for this by comparing measurements made at the same sidereal time, not at the same clock time. Perhaps this is too simple a correction, and the earth's polar inclination or the differing elevation angles of the probes (ATS-1 $\sim$ 36 deg; ATS-5 $\sim$ 48 deg) modify this time translation slightly. Other speculations are possible. Stricter tests of ICARIS mapping would be low elevation angle comparisons and data over a much greater

longitude range (useful for multiple-station tracking calibration).

III. Other Comparisons Using ICARIS

For July 2 and 3, 1971, a comparison of Stanford to ATS-1 and ATS-3 Faraday rotation data has been made. This data (Fig. 3) is somewhat more erratic than the DSS 13 to ATS-1–ATS-5 comparison. It is tempting to ascribe this irregularity to the summer season, since the summer ionosphere is much more irregular than at other seasons and nothing else has changed significantly. (ATS-3 is at 47°W). More data is required to make any firmer statement.

A comparison of Stanford ATS-1 data measured in 1967 and Goldstone DSCC ATS-1 data taken in 1969. with Spanish ionosonde data for the same period was also done. This data exists for 23 days in 1967 and 17 days in 1969 from August through November. The data is quite sparse. Often the mutual pass period consists of as few as 10 points (see Fig. 4). The ionosonde data, probably because only the content up to the F2 layer is measured while the portion above F2 is estimated, is systematically less than the Faraday rotation measurement. In some cases, the nighttime ionosonde reading is equal to the nighttime Faraday rotation measurement, but this is not consistent. To draw meaningful conclusions about the longitude mapping ability of ICARIS, Faraday rotation data from Spain is required.

Acknowledgment

The authors wish to express their appreciation to M. Davis and Dr. T. Howard of the Center for Radar Astronomy, Stanford University, who have provided a Faraday rotation polarimeter and portions of the data employed in this work.

Reference

1. Mulhall, B. D., et al., *Tracking System Analytic Calibration Activities for the Mariner Mars 1969 Mission,* Technical Report 32-1499. Jet Propulsion Laboratory, Pasadena, Calif., Nov. 15, 1970.

Table 1. Geostationary satellite view angles

Satellite	Longitude	Elevation, deg	Azimuth, deg
ATS-1	150°W	36	230 (from DSS-13)
		37	222 (from Stanford)
ATS-3	47°W	28	122 (from Stanford)
ATS-5	105°W	48	160 (from DSS-13)

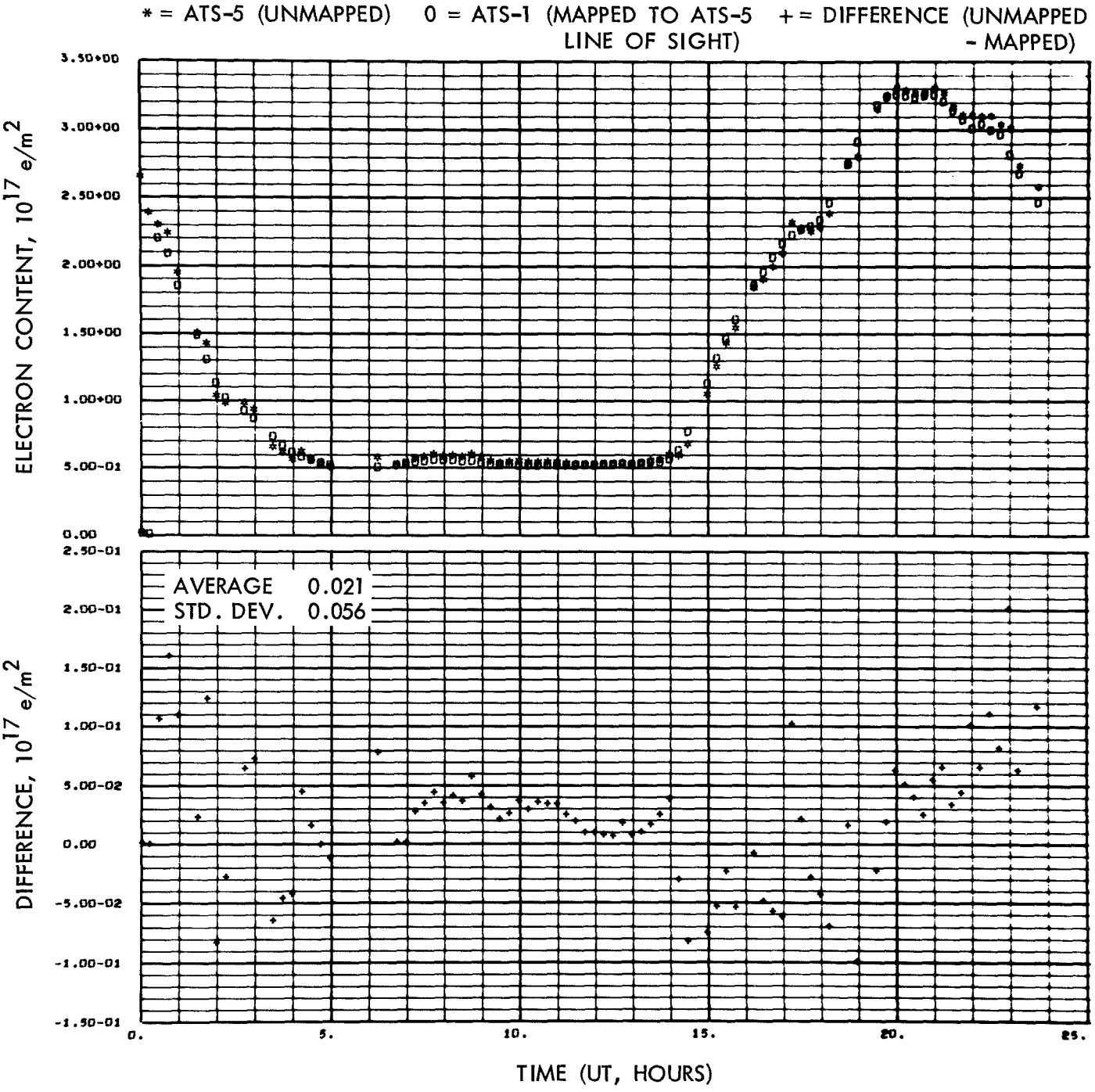

Fig. 1. Comparison of ATS-5 and ATS-1 Faraday rotation measurements of 2-3-71

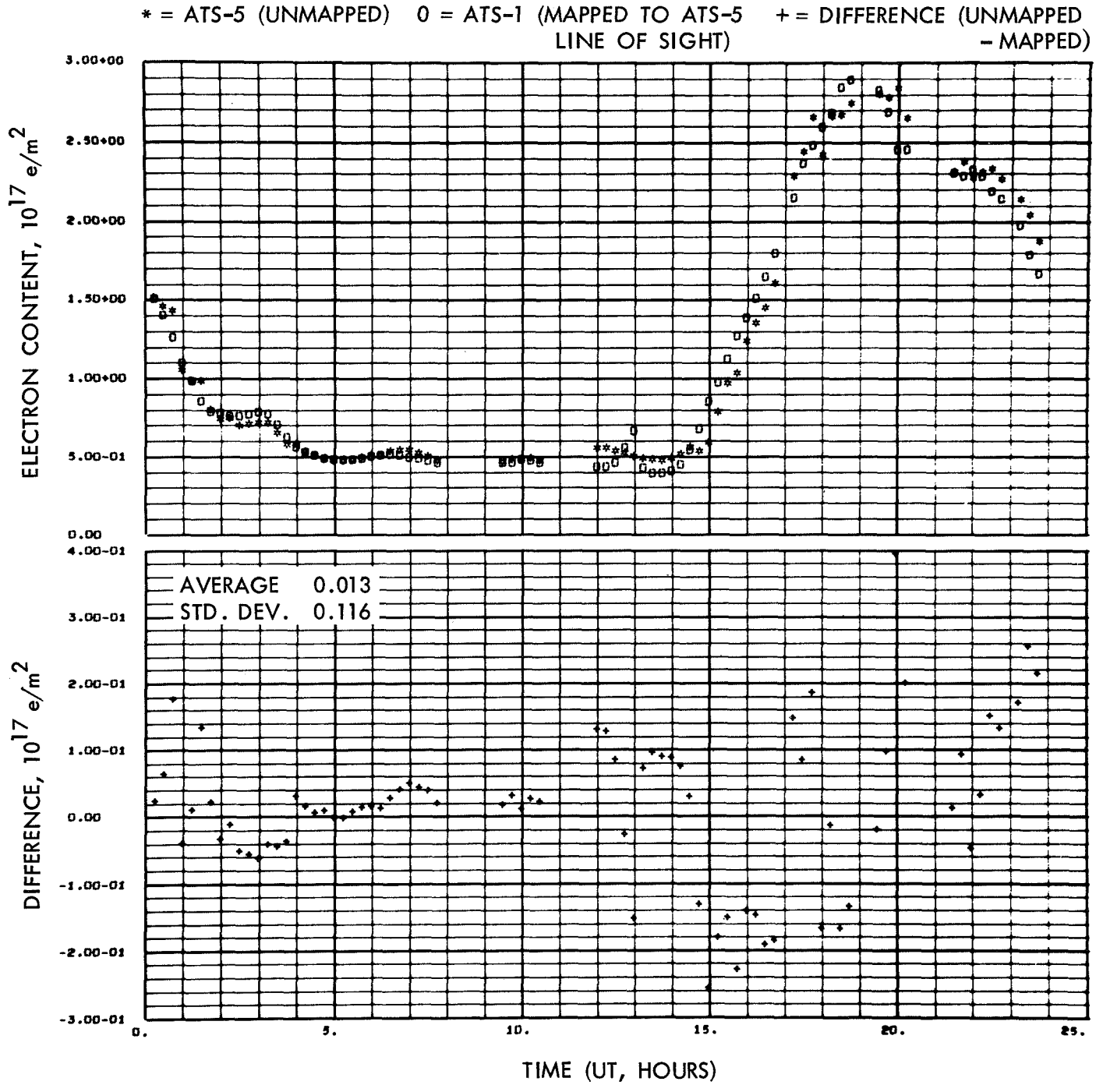

Fig. 2. Comparison of ATS-5 and ATS-1 Faraday rotation measurements of 12-24-70

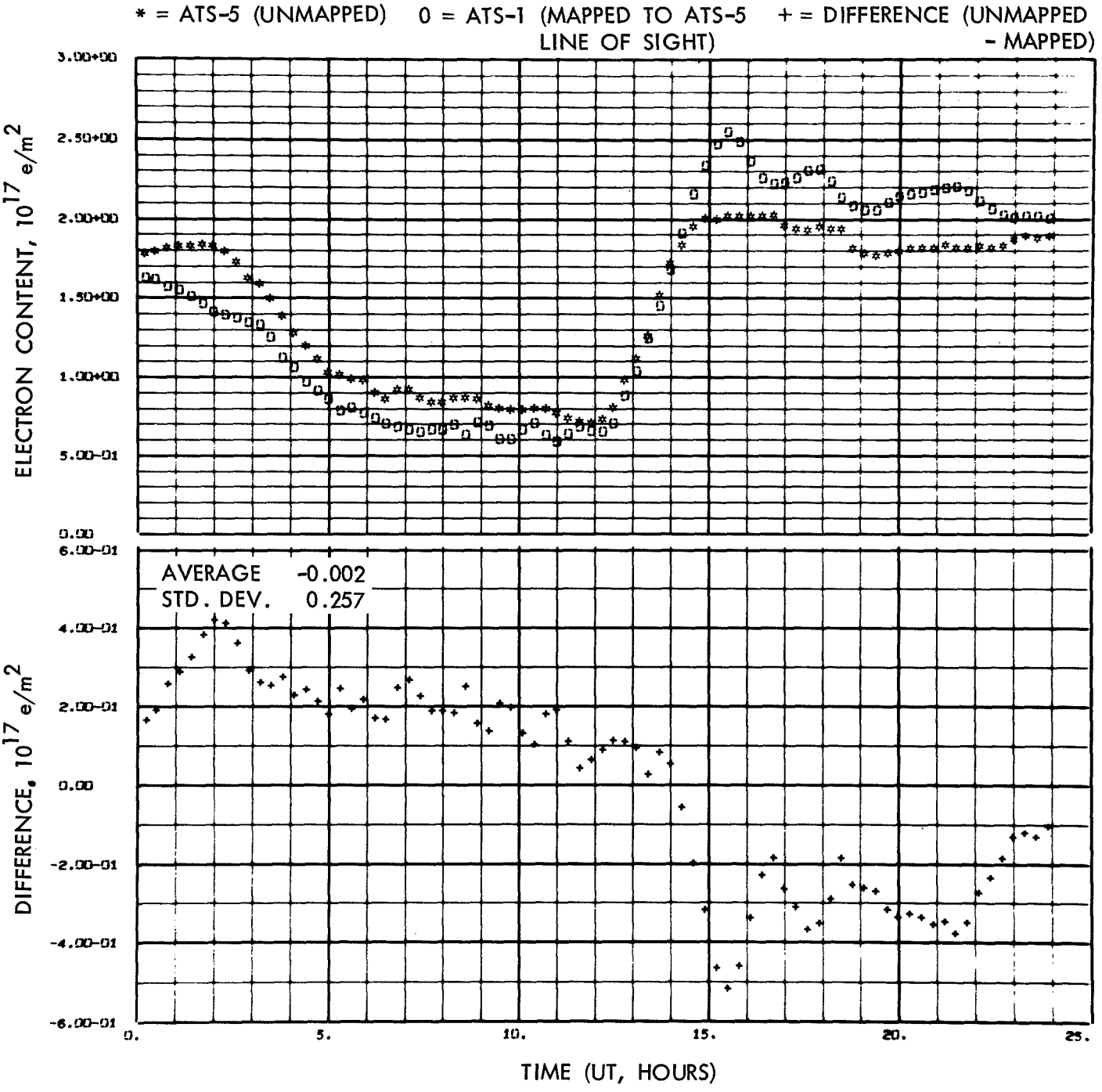

Fig. 3. Comparison of ATS-3 and ATS-1 Faraday rotation measurements of 7-3-71

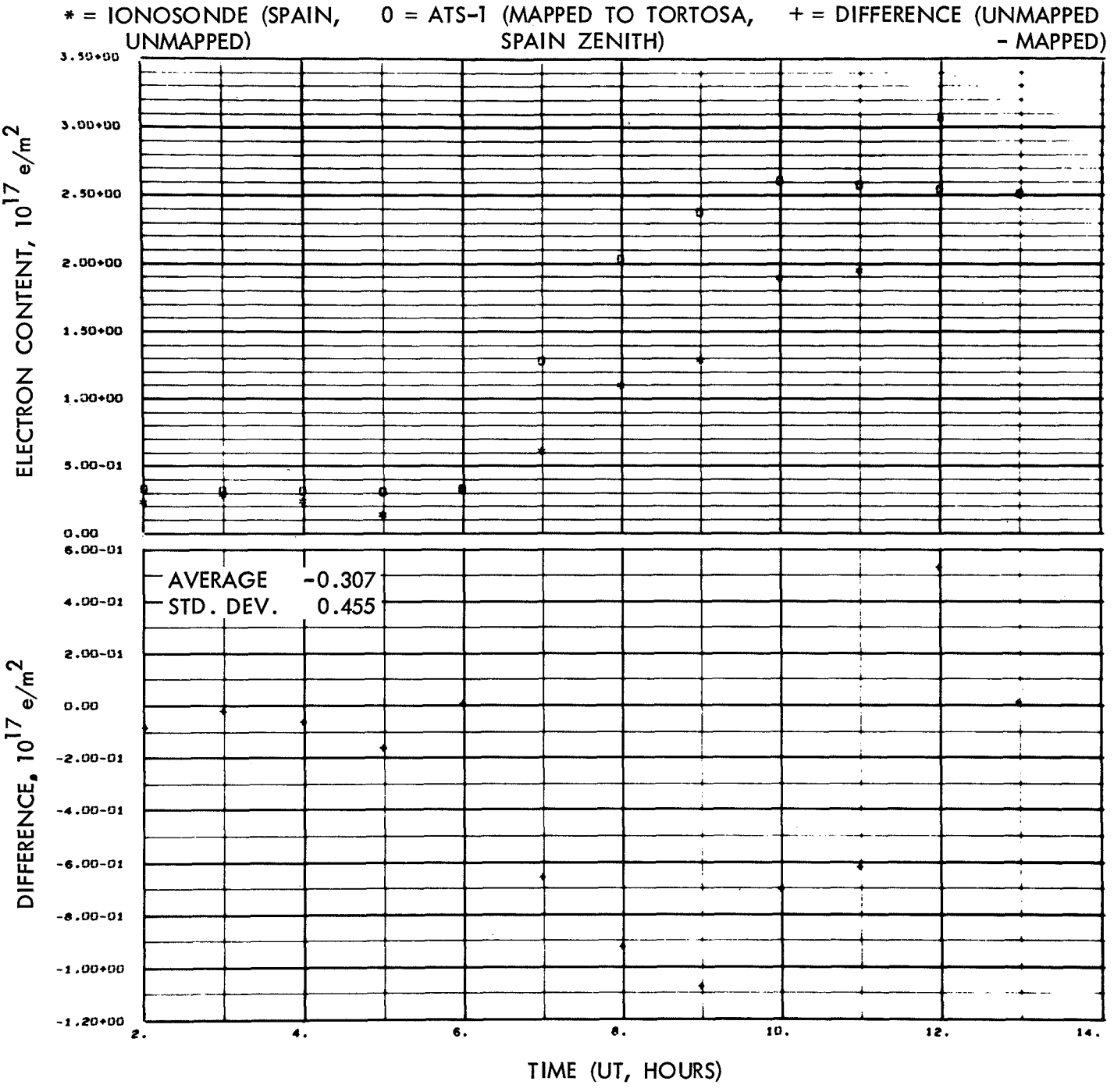

Fig. 4. Comparison of ionosonde (Observatorio de Ebro, Tortosa, Spain) and ATS-1 Faraday rotation (California) 11-7-67

A Worldwide Organization to Secure Earth-Related Parameters for Deep Space Missions

H. F. Fliegel
Tracking and Orbit Determination Section

A global express service to obtain timing and polar motion parameters for deep space mission support has been organized through the Bureau International de l'Heure. The results are incorporated into a daily operation. This article outlines what the new sources of data are, what procedures are used to reduce the data, and what software is available to the user.

I. Introduction

The need for increased accuracy in determining DSN coordinates to support *Mariner* Mars 1971 and future missions has made two major changes necessary at JPL to obtain timing and polar motion parameters. This article outlines what the new sources of data are, what procedures are used to reduce them, and what software is available to the user. The timing parameters and their importance were explained by Trask and Muller (Ref. 1). An introduction to the whole subject of timing and its use in spacecraft orbit determination was given by Moyer (Ref. 2). A similar introduction to polar motion was given by Muller (Ref. 3).

The first major change from the procedure used to support *Mariner* Mars 1969 is in securing astronomical data from a worldwide network of observatories rather than from the US Naval Observatory alone. The primary reason for this change was to obtain polar motion values with standard deviation not exceeding 0.7 meters, according to our committed error budget. Polar position cannot be obtained by US observatories alone. The Bureau International de l'Heure (BIH) has for many years collected, reduced, and published polar motion and timing data from cooperating national time services throughout the world. However, the most recent published data is from 40 to 70 days old, and errors due to extrapolating such data are often 1 to 3 meters. Beginning in 1971, JPL has sponsored

a contract for BIH to obtain time and latitude data from at least 12 cooperating observatories by teletype, as soon as obtained, to provide the world's first rapid time and polar motion service. A secondary, but quite important, benefit of this service is to reduce the random error in UT1 to less than 5 ms. Systematic errors of any one observatory tend to average out, bad weather in any one part of the world does not seriously affect the service, and real-time measurements of polar motion improve the accuracy of UT1 which is computed therefrom.

The second major change in JPL procedure has been to replace the former TPOLY computer program with the THALES–PLATO systems and a variety of smaller supporting programs. (For a description of the TPOLY program, see Ref. 4.) With measurements arriving from 12 or more observatories and not from 2 only, a great deal more is required in preliminary error analysis and screening of the data than formerly. Furthermore, since timing parameter decks are being generated for the mission virtually on a real-time basis and not long in advance, an error-free system, coupling a flexible output format with numerous internal and external checks for accuracy, becomes essential.

This article discusses the organization of the rapid time and polar motion service of the BIH and describes the types of information BIH supplies, the schedule of delivery, and the format of data transmission. The concluding section of this article gives a preliminary sketch of how well the service seems to perform. A more complete analysis will appear after the *Mariner* Mars 1971 mission.

II. The BIH Rapid Time and Polar Motion Service

The Bureau International de l'Heure (BIH) is the agency sponsored by the International Astronomical Union (IAU) and the International Union of Geodesy and Geophysics (IUGG) to collate, reduce, and publish timing data from all cooperating national time services throughout the world, and by means of such data to secure scientifically accurate and internationally accepted standards of time. BIH is supported by UNESCO. By resolution of the IAU, BIH uses its astronomical data to solve both for UT1 and for the instantaneous coordinates X and Y of the terrestrial pole, which three quantities specify the orientation of the Earth in space. Published final values of these quantities appear in BIH Circular D about one month after observation. However, since the causes of the variation of the Earth's rotation are many and are not completely known, the parameters of that rotation, UT1, X, Y, cannot be predicted accurately in advance, and the time-lag between observation and publication was a vexing source of error to many users. In particular, JPL could not use Circular D information for real-time mission operations. Therefore, Dr. Bernard Guinot, the director of BIH, decided to enlist the cooperation of a limited number of highly accurate time and latitude observatories to form the world's first rapid time and polar motion service. (The strategy is somewhat similar to that of an earlier effort called the Rapid Latitude Service, but the present service embraces time and polar motion in a single solution.)

One must distinguish between the astronomical service itself, which is exclusively a BIH function currently financed by JPL, and the use of the service to provide machine-readable timing and polar motion parameter decks suitable for space missions, which is a joint effort between BIH and JPL. We will speak of the former as the BIH Rapid Service, and of the latter as the JPL–BIH Operation.

The BIH Rapid Service hinges on the cooperation of a select list of observatories. Data from 76 observatories were included in the BIH Circular D solutions for time and/or latitude in 1969 (the year of the *Mariner 6* and 7 missions), but the observatories were far from equal in weight. Weights in the BIH system are chosen to be the squares of integers, and, in the timing solutions for the year 1969, 10 stations had weight 49, 10 had weight 25, 6 had weight 16, and the sum of the weights of all the rest was only 114. These weights, of course, are inversely proportional to the squares of the measured standard deviations of the data; they are far higher for modern instruments observing stars of well-determined positions than for either the older types of visual instruments or for new observatories just beginning to establish their catalogs. Thus, the 10 observatories of weight 49 contribute more than half the total weight of the final solution for time, and a similar situation obtains for latitude. Therefore, an efficient and reasonably accurate rapid service can be organized by obtaining data by teletype from only those observatories of high weight. Furthermore, since the systematic errors of these observatories persist from year to year, they can be measured from the final solution for previous months and corrected in advance. Thus, the accuracy of the BIH Rapid Service can be made even greater than the weights of the contributing observatories alone would indicate. Such, then, is the strategy of the Service: first, to select for participation well-established observatories; and, second, to apply systematic corrections based on past performance. Note carefully that even observatories which do not contribute directly to the Rapid Service are important to it, for they help determine the systematic corrections to those which do.

The list of observatories participating in the BIH Rapid Service as of August 1971 is given in Table 1.

BIH reduces the data from the observatories contributing to its Rapid Service by the same procedures it uses to prepare Circular D or the *Rapport Annuel*; thus, all BIH publications are on the same system. Rapid Service reductions are made at 3.5-day intervals, rather than at the 5-day intervals used for Circular D. Following the most recent data as closely as possible, BIH computes each week straight line segments—initial values and rates—which characterize the behavior of X, Y, and UT1 during that week, and teletypes them to its Rapid Service subscribers (currently, JPL). It is not practical for BIH to force the values at the beginning of one week to agree with the values at the end of the previous week, since raw time and latitude data are notoriously noisy, and frequently an apparent upward trend one week is shown by the following week's data to have been an illusion. Thus, the sequence of straight line segments are not joined at the ends; they constitute a discontinuous function. JPL requires timing and polar motion functions more amenable to extensive machine calculation, and JPL procedures are described in the following section.

III. The JPL–BIH Operation: The THALES–PLATO Systems

The special requirements on timing and polar motion for deep space mission support are as follows:

(1) The quantities UT1, X, and Y should be specified in the form of functions, readily computable, continuous in the first derivative.

(2) For the *Mariner* Mars 1971 mission, the standard deviation of the computed X and Y of polar position should not exceed 0.7 meters, and that of timing should not exceed 4 ms.

(3) Parameters should be predicted and supplied as far in advance as possible, but it is especially important that unexpected changes in the Earth's rotation be reported as rapidly as possible.

(4) Since the timing and polar motion routines form only a tiny part of the orbit determination program, and since no one person can have an intuitive feel for all the factors entering into a given day's solution for spacecraft position, it is essential that operations be fully automatic, with high redundancy and numerous safeguards to avoid error.

Practically, the data processing required divides conveniently into two major tasks. First, one must form the best real-time estimates of X, Y, and UT1 and their rates of change, the rates being especially important because of the need to predict ahead for at least a few days. In this first task one must also estimate the accuracy of the real-time solutions, evaluating the quality of the optical observations as it changes with weather, season, and unknown factors. Second, one must represent the sequence of such estimates formed week after week by some mathematical function, and supply parameters in machine-readable form which define that function for such programs as SATODP (Satellite Orbit Determination Program). Other minor tasks—minor in the sense of requiring less software, but important to guaranteeing mission success—are checking final output decks for mathematical consistency and against punch errors, and providing contingency procedures for use against systems failures, loss of one computer due to power failure, earthquake, or other causes. The first major task is performed by program THALES, and the second by PLATO. Between those two programs stands the cognizant engineer, who must examine the residuals of the optical observations supplied by BIH and certify THALES output before passing it on to PLATO. The relationship of THALES to PLATO, and of both to the BIH Rapid Service and to other programs, is diagrammed in Fig. 1. We now describe the programs.

THALES (Time Handling And Latitude Evaluation System) reduces raw astronomical measurements of time and latitude to X, Y, and UT1. For this purpose, BIH sends JPL copies of the data sheets submitted by each observatory contributing to the Rapid Service. THALES computes the check sums which verify that the data has been teletyped properly, computes X, Y, and UT1 for each batch of data corrected to whatever epoch the operator supplies by NAMELIST (a Fortran term) input, and lists the residuals of each observation from the mean solution, computing the largest residual, the mean residual, and the standard deviation for each observatory.

PLATO (PLATform Observables) accepts X, Y, and UT1 input from any source (currently, from THALES), fits through the data any of a variety of orthonormal function series (Fourier, Chebyshev) or splined cubics, at the operator's discretion, and produces the final output deck which is used by TIMPOL (see below) in the SATODP and other programs for mission support.

CYNIC (Checklisting Yes–No Indicator of Consistency) is used in the certification of PLATO output decks. CYNIC checks the format of the PLATO deck against

missing parentheses, cards out of order, and the like; it also checks seconds past 1950, A.1 − UT1, and A.1 − UTC against the civil date of the label. Such seeming redundancy was found necessary to screen out operator error and possible system errors in the running of the fairly intricate program PLATO.

STOIC (Standby Timing Operation In Contingencies) is a backup program that can generate an output deck in the PLATO format directly from THALES output in case the PLATO system through some accident becomes inoperative. It is currently under development.

TIMPOL (TIMe and POLe) is the subroutine actually called in the orbital determination programs SATODP and DPTRAJ and other programs which makes use of the data read in from the PLATO output deck to compute parameters at the instant specified by the user.

IV. Level of Performance—A Preliminary Sketch

Since predictions must be made a few days in advance even when using the Rapid Service, and in order to average out the random errors in the data for each given week, THALES fits a smooth curve each week through the data for the past eight weeks and extrapolates it forward. For polar motion, an Archimedean spiral arc is fit, centered on the point $X = 0.00$, $Y = 0.25$, which is the approximate center of polar wandering in recent years. To timing data, a straight line is fit to UT2. This procedure gives two measures of the consistency of the reduced data. One may calculate the mean standard deviation of a given week's data from the eight-week curve. Averaging since the inception of the service, we obtain

$$\sigma_X = 0.021 \text{ arc sec} = 0.65 \text{ meters}$$

$$\sigma_Y = 0.019 \text{ arc sec} = 0.58 \text{ meters}$$

$$\sigma_T = 2.7 \text{ milliseconds}$$

We may also compare different eight-week curves, and compute the standard deviations of the values of X, Y, and UT1 calculated for a given date. For a typical date, we obtain

$$\sigma_X = 0.0064 \text{ arc sec} = 0.20 \text{ meters}$$

$$\sigma_Y = 0.0086 \text{ arc sec} = 0.27 \text{ meters}$$

$$\sigma_T = 1.4 \text{ milliseconds}$$

The first set of figures measures how well the model fits the data, and the second set measures how well X, Y, and UT1 can be obtained if one believes the model. Clearly, THALES reduces the data consistently and uses a model that fits the data well over eight-week intervals. Furthermore, the model is useful for prediction. The error in predicting UT1 35 days in advance of the *Apollo 15* launch was 6 milliseconds, and declined linearly as the awaited day approached.

However, "if all men went mad after the same fashion, they might agree one with another well enough.[1]" Three facts remind us that the measures of consistency given above are perhaps a factor of 3 more optimistic than the true accuracy of the operation:

(1) The X-coordinate of polar motion from THALES agrees rather well with that from BIH, but the Y-coordinate has been consistently 2 meters too small. Similar discrepancies exist between International Latitude Service (ILS), BIH, and the US Naval Weapons Laboratory solutions (see Ref. 5). We are currently using an empirical correction to make PLATO agree with BIH.

(2) Various observatories contributing to the BIH Rapid Service display short-term errors consistent over eight weeks but different from previous years. For example, Richmond has consistently reported UT1 from 10 to 20 milliseconds higher than Washington during the spring and summer of this year.

(3) In past years, BIH UT2 has remained nearly linear with constant slope for weeks or months at a time, only to change its slope suddenly to a new value. Roughly 10 such events have occurred in the past six years, most recently in mid-March of 1971. The UT2 fit over eight weeks, described above, will display high precision only until the next such event, during which a much shorter averaging span must be used.

We believe, therefore, that the Tracking System Analytical Calibration (TSAC) figures of merit adopted for *Mariner* Mars 1971 ($\sigma = 0.7$ meters in X and Y and $\sigma =$ 4 milliseconds in UT1) are a realistic estimate of the quality of the present JPL–BIH Operation.

V. Summary

(1) The BIH Rapid Service is now supplying by teletype time and polar motion values obtained from

[1]Francis Bacon, *Novum Organum*, Aphorism XXVII.

not less than 12 observatories distributed around the globe, virtually on a real-time basis.

(2) JPL is making its own reduction of raw astronomical data, which BIH supplies in addition to its own Rapid Service. The data processing is divided into two major programs: THALES, to solve for X, Y, and UT1 from the raw data; and PLATO, to represent X, Y, and UT1 in machine-readable form.

(3) The existing service satisfies the TSAC requirements for *Mariner* Mars 1971, but probably could not satisfy requirements much more stringent. We believe that we are close to reaching the ultimate accuracy obtainable from conventional astronomical measurements.

References

1. Trask, D. W., and Muller, P. M., "Timing: DSIF Two-Way Doppler Inherent Accuracy Limitations," in *The Deep Space Network*, Space Programs Summary 37-39, Vol. III, pp. 7–16. Jet Propulsion Laboratory, Pasadena, Calif., May 31, 1966.
2. Moyer, T. D., *Mathematical Formulation of the Double-Precision Orbit Determination Program (DPODP)*, Technical Report 32-1527. Jet Propulsion Laboratory, Pasadena, Calif., May 15, 1971.
3. Muller, P. M., "Polar Motion and DSN Station Locations," in *The Deep Space Network*, Space Programs Summary 37-45, Vol. III, pp. 10–14. Jet Propulsion Laboratory, Pasadena, Calif., May 31, 1967.
4. Muller, P. M., and Chao, C. C., "New Timing Polynomial Program and Data," in *The Deep Space Network*, Space Programs Summary 37-57, Vol. II, pp. 42–51. Jet Propulsion Laboratory, Pasadena, Calif., May 31, 1969.
5. Chao, C. C., and Fliegel, H. F., "Polar Motion: Doppler Determination Using Satellites Compared to Optical Results," in *The Deep Space Network*, Space Programs Summary 37-66, Vol. II, pp. 23–26. Jet Propulsion Laboratory, Pasadena, Calif., Nov. 30, 1970.

Table 1. Observatories participating in BIH Rapid Service

Observatory	Location	BIH code	Instrument
Besançon	France	BS	Astrolabe
Calgary	Alberta, Canada	CL	PZT[a]
Herstmonceux	Sussex, England	G	PZT
Hamburg	Germany	H	PZT
Mount Stromlo	Canberra, Australia	MS	PZT
Mizusawa	Japan	MZP	PZT
Ottawa	Ontario, Canada	O	PZT
Paris	France	PA	Astrolabe
Paris North	France	PAN	Astrolabe
Richmond	Florida, USA	RCP	PZT
Santiago	Chile	SC	Astrolabe
San Fernando	Spain	SFA	Astrolabe
Tokyo	Japan	TO	PZT
Washington	DC, USA	W	PZT

[a]PZT = photographic zenith tube.

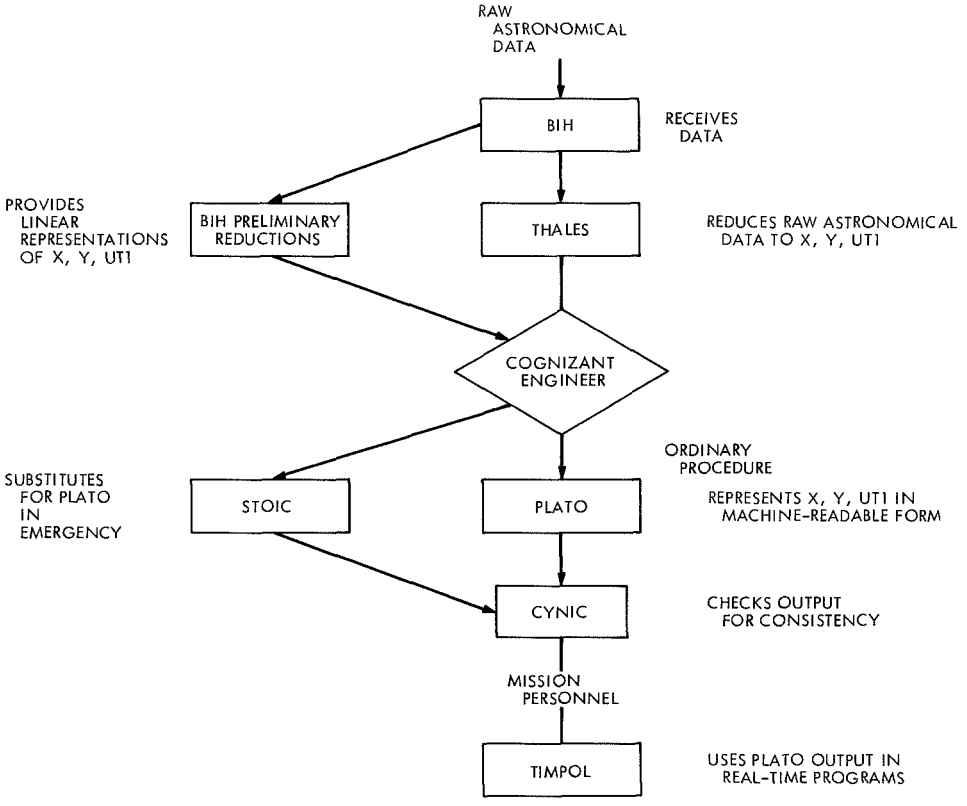

Fig. 1. Interrelationships between JPL–BIH operations

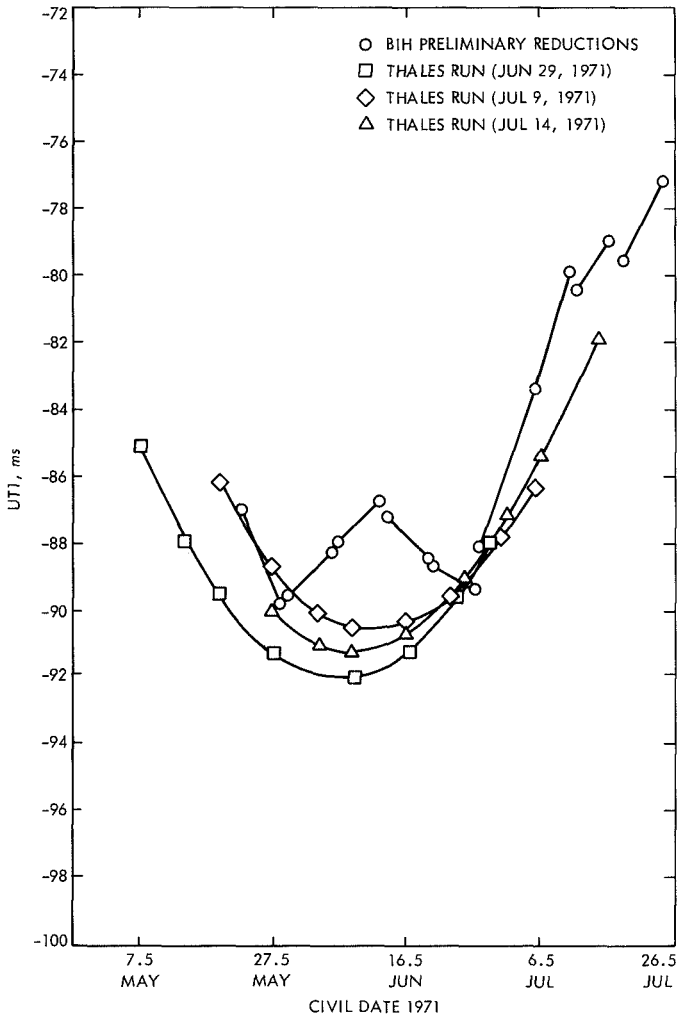

Fig. 2. THALES and BIH representations of UT1

A Comparison of Cowell's Method and a Variation-of-Parameters Method for the Computation of Precision Satellite Orbits

S. S. Dallas
Navigation and Mission Design Section
E. A. Rinderle
Flight Operations and DSN Programming Section

A precision special perturbations program that uses either Cowell's method or a variation-of-parameters method to compute an elliptical orbit is analyzed to determine which mode is more efficient when computing satellite orbits. The results obtained indicate that the variation-of-parameters mode is significantly more efficient if the numerical integrator being used is optimized in that mode by varying the integration order and local error control and by using either a predictor or predictor-corrector algorithm.

The objective of this investigation is limited to determining if a variation-of-parameters method is superior to Cowell's method for computing satellite orbits in the environment of a complicated precision trajectory program with various interface complexities (e.g., planetary ephemeris file, sophisticated triggering options, comprehensive input and output options, etc.).

A realistic satellite orbit about the planet Mars (the *Mariner* Mars 1971 Mission A orbit) was chosen for the investigation. The initial state vector with respect to the Mars equator and equinox of date is

$$(a\ e\ i\ \omega\ \Omega\ T) = (12652.618\,\text{km}, 0.63300876, 80.0\,\text{deg},$$
$$328.3937\,\text{deg}, 38.3701\,\text{deg},$$
$$11/19/71\ 14^{h}\ 42^{m}\ \text{UTC})$$

The numerical data in this study was generated using the JPL Univac 1108 digital computer (the executive 8 operating system) and a modified research version of the JPL Double Precision Trajectory Program (DPTRAJ). The modification to DPTRAJ consisted of the inclusion of an option to compute the orbit using a variation-of-

parameters method in addition to the standard Cowell method.

The variation-of-parameters method of orbit computation consists of the numerical integration of perturbative variations in terms of parameters such as the Keplerian elements a, e, i, ω, Ω, T. The parameters characterize an osculating orbit, which is a progressively changing reference orbit, that yields the actual position and velocity at any given instant of time. The particular parameters used for this study are as follows:

$$\mathbf{a} = \text{vector of length } e \text{ in direction of periapsis} = e\mathbf{P} \tag{1}$$

$$\mathbf{h} = \text{angular momentum vector} = |\mathbf{h}|\,\mathbf{W} \tag{2}$$

$$n = \text{mean motion} = \sqrt{\mu}/a^{3/2} \tag{3}$$

$$L_0 = \text{mean longitude} = M_0 + \Omega + \omega \tag{4}$$

where M_0 is the mean anomaly at $t = t_0$.

Note that in the case of retrograde motion ($i_0 > \pi/2$), $L_{r0} = M_0 - \Omega + \omega$ is used in place of L_0. Because of this particular choice of parameters, the variation-of-parameters option is just as flexible as Cowell's option in integrating satellite orbits. That is, any satellite orbit having an eccentricity in the range $0 \leq e < 1$ and an inclination in the range $0 \leq i \leq \pi$ can be integrated equally well by the two methods. This more general variation-of-parameters formulation must be used to obtain a valid comparison with Cowell's method even though its use requires more computation than a formulation using the Keplerian elements. In addition, note that eight first-order differential equations of motion are singly integrated to obtain an over-determined state vector of the satellite. These equations are as follows (see Ref. 1 for their derivations):

$$\frac{d\mathbf{a}}{dt} = \frac{1}{\mu}\left[2(\dot{s}\dot{s}')\mathbf{r} - (r\dot{r}')\dot{\mathbf{r}} - (r\dot{r})\dot{\mathbf{r}}'\right] \tag{5}$$

$$\frac{d\mathbf{h}}{dt} = \frac{1}{\sqrt{\mu}}(\mathbf{r} \times \dot{\mathbf{r}}') \tag{6}$$

$$\frac{dn}{dt} = -\frac{3}{\sqrt{\mu a}}\dot{s}\ddot{s}' \tag{7}$$

$$\frac{dL}{dt} = n + \frac{r\dot{b}'}{\sqrt{\mu p}}\frac{(r\sin u \sin i)}{1+\cos i} - \frac{2(r\dot{r}')}{\sqrt{\mu a}} - \frac{1}{1+\frac{\sqrt{\mu p}}{\sqrt{\mu a}}}\left[\frac{(r\dot{r}')}{\sqrt{\mu p}}\left(\frac{p}{r}\right)(e\cos v) - \frac{(r\dot{v}')}{\sqrt{\mu p}}\left(\frac{p}{r}+1\right)(r\,e\sin v)\right] \tag{8}$$

(or an equivalent expression for dL_r/dt) where

$$r = \sqrt{\mathbf{r}\cdot\mathbf{r}}, \qquad \sqrt{\mu p} = |\mathbf{r}\times\dot{\mathbf{r}}|, \qquad r\dot{r} = \mathbf{r}\cdot\dot{\mathbf{r}} \tag{9}$$

$$\mathbf{U} = \frac{\mathbf{r}}{r}, \qquad \mathbf{W} = \frac{1}{\sqrt{\mu p}}(\mathbf{r}\times\dot{\mathbf{r}}), \qquad \mathbf{V} = \mathbf{W}\times\mathbf{U} \tag{10}$$

$$r\dot{r}' = \mathbf{r}\cdot\dot{\mathbf{r}}', \qquad r\dot{v}' = \mathbf{V}\cdot\dot{\mathbf{r}}', \qquad r\dot{b}' = \mathbf{W}\cdot\dot{\mathbf{r}}', \qquad \dot{s}\dot{s}' = \dot{\mathbf{r}}\cdot\dot{\mathbf{r}}' \tag{11}$$

$$\frac{1}{\sqrt{\mu a}} = \frac{1}{\sqrt{\mu}}\left(\frac{2}{r} - \frac{\dot{\mathbf{r}}\cdot\dot{\mathbf{r}}}{\mu}\right)^{1/2}, \qquad \frac{p}{r} = \frac{(\sqrt{\mu p})^2}{\mu r} \tag{12}$$

$$r\sin u \sin i = \mathbf{K}\cdot\mathbf{r}, \qquad \cos i = \mathbf{K}\cdot\mathbf{W}, \qquad n = \frac{\mu^2}{(\sqrt{\mu a})^3} \tag{13}$$

$$e\cos v = \frac{p}{r} - 1, \qquad r\,e\sin v = \frac{(r\dot{r})}{\mu}\sqrt{\mu p} \tag{14}$$

and where **I**, **J**, **K** is an inertial basis having the Earth mean equatorial plane of 1950.0 as the principal plane and the direction of the mean vernal equinox of 1950.0 as the principal direction. Note that the differential equations of motion are formulated directly in terms of the perturbative accelerations in the reference Cartesian coordinate system rather than in terms of the parameters being integrated. The quantity $\ddot{\mathbf{r}}'$ represents the total perturbative acceleration acting upon the satellite. In this study, $\ddot{\mathbf{r}}'$ consists of the perturbations due to the asphericity of the central body (J_2 only), N bodies other than the central body, and solar radiation pressure. In the course of this study, the best six of the eight parameters integrated will be determined. The intention is eventually to eliminate the integrations of the two less desirable parameters and to replace them with relationships derived from the following equations:

$$\mathbf{a}\cdot\mathbf{h} = 0 \tag{15}$$

$$\mathbf{a}\cdot\mathbf{a} + (n^2/\mu)^{1/3}\mathbf{h}\cdot\mathbf{h} - 1 = 0 \tag{16}$$

Note that in the case of L_0 (or L_{r0}), numerical integration is actually performed on L (or L_r). Then L_0 (or L_{r0}) is obtained by means of the equation

$$L_0 = L_{00} - n(t - t_0) + \int_{t_0}^{t} \frac{dL}{dt} d\tau \qquad (17)$$

(or the equivalent expression for L_{r0}).

The complexity of the differential equations (5) through (8) and the necessity of solving a modified Kepler's equation by iteration at each integration step are clearly disadvantages in the variation-of-parameters method. Both these quantities adversely affect the amount of computer execution time required to advance the solution one step. The principal advantage of the variation-of-parameters method is that the derivatives are small and change slowly with time because of the absence of the central force term. Consequently, the integration tables converge more rapidly than in Cowell's method and therefore allow larger tabular intervals, particularly in the region near periapsis.

When using Cowell's method in the modified DPTRAJ, the numerical integration is performed using the tenth-order variable-step second-sum process that has proven so successful in the case of interplanetary trajectories (Ref. 2). When using the variation-of-parameters method in the modified DPTRAJ, the numerical integration is performed using the same process but with variations on the fixed integration order and local error control and with and without a corrector cycle. Talbot and Rinderle (Ref. 3) have compared the performance of this integrator with the performance of a variable-order polynomial-type integrator and a "Fourier"-type integrator in integrating a Mars orbiter using a classical variation-of-parameters method. They found that the performances of these integrators are similar. For about the same accuracy the runs varied by about 15 to 20% in the number of times the derivatives are evaluated. Note that a 15 to 20% variation in derivative evaluations does not translate into a 15 to 20% variation in cost because evaluating the derivatives is not the principal consumer of execution time in a complex program such as DPTRAJ.

The algorithms used to solve the two sets of equations are quite similar. In both cases, a multi-step process in summed form closely related to an Adams-type process is used. The algorithms consist basically of a starting procedure to compute the solution values at m points backward in time (where m is the number of backward differences used in the integration formulas and is denoted as the order of the process), and a stepping procedure to advance the solution one step in time using information at the previous m points. In Cowell's method, only tenth order was used, and both the predict-correct and predict-partial-correct (Ref. 4) modes were used. In the variation-of-parameters method, orders 4, 6, 8, and 10 were tried, and the predict only and predict-correct modes were used. In most cases, the automatic step size control based upon an estimate of the local truncation error (Ref. 2) was employed.

The standard of comparison for this study was obtained by entering the initial conditions for the *Mariner* orbit given previously into DPTRAJ and numerically integrating the differential equations of motion of the satellite with very tight error control ($ERMX = 10^{-13}$ and $ERMN = 10^{-18}$). Although the solution obtained in this manner is not perfectly accurate, the accuracy is much higher than the accuracy of the test cases, and, therefore, a valid standard of comparison was obtained. A measure of the accuracy of the test cases relative to the standard of comparison was obtained by computing the magnitudes of the position ($|\Delta \mathbf{r}|$) and velocity ($|\Delta \dot{\mathbf{r}}|$) vector errors. A measure of the cost of the test cases was chosen to be the Central Processing Unit (CPU) time corrected for any nonstandard production practices and known improvements in the variation-of-parameters method.[1]

A total of 34 cases was run in this study including the standard of comparison. Each of the cases was run with the same initial conditions (the *Mariner* orbit) using either Cowell's method or the variation-of-parameters method. The majority of the variation-of-parameters cases was predict only, sixth order, and variable step, and differed primarily in the local error control.

A preliminary comparison of the variation-of-parameters cases run to date shows that the best case is the predict-only, sixth-order, variable-step case with the local truncation error bounded by an $ERMX$ and $ERMN$ proportional to r_a/r (where r_a is the apoapsis distance). Table 1 shows a comparison of this case with a case determined by Cowell's method having the same accuracy after 20 revolutions. This comparison shows that the variation-of-parameters method requires approximately 59 seconds less CPU time (about 18%) than does Cowell's method. The test cases indicate that this savings in CPU time results in a significant savings in the total cost. These

[1]The two major corrections made were for the additional costs of special output and an inefficient iterative procedure for solving Kepler's equation.

results are preliminary since this study has not been completed. Consequently, the improvement of 18% in the CPU time should be regarded only as an indication of the improvement to be expected from using the variation-of-parameters method in place of Cowell's method when computing precision satellite orbits.

In conclusion, the significantly more efficient variation-of-parameters method for computing precision satellite orbits offers the potential for reducing the cost of satellite orbit computations and also for reducing the computer execution time during real-time mission operations for future orbiter projects. The final results of this study will include a measure of these reductions in cost and computer execution time and a recommendation as to whether the variation-of-parameters method should be included in the standard production and mission operations versions of DPTRAJ.

References

1. Dallas, S. S., and Rinderle, E. A., *A Special Perturbations Theory Using the Variation of Parameters Formulation*, TM 392-31, Apr. 1970 (JPL internal document).
2. Spier, G. W., *Design and Implementation of Models for the Double Precision Trajectory Program (DPTRAJ)*, Technical Memorandum 33-451. Jet Propulsion Laboratory, Pasadena, Calif., Apr. 15, 1971.
3. Talbot, T. D., and Rinderle, E. A., "Choice of Integrators for Use With a Variation-of-Parameters Formulation," in *The Deep Space Network Progress Report*, Technical Report 32-1526, Vol. I, pp. 117–121. Jet Propulsion Laboratory, Pasadena, Calif., Feb. 15, 1971.
4. Talbot, T. D., "A Predict–Partial Correct Integration Scheme for Integrating Spacecraft Trajectories," in *The Deep Space Network*, Space Programs Summary 37-59, Vol. II, pp. 78–84. Jet Propulsion Laboratory, Pasadena, Calif., Sept. 30, 1969.

Table 1. Comparison of Cowell's method and a variation-of-parameters method

Method	Order	Local error control		Revolution number	Accuracy[a]		Number of steps	Number of derivative evaluations	CPU time, s	
		ERMX	*ERMN*		$\lvert\Delta r\rvert$, m	$\lvert\Delta \dot{r}\rvert$, m/s			Output	Corrected[b]
(1) Cowell (predict-correct, variable step)	10	2×10^{-10}	2×10^{-15}	5 apoapsis	4.62	0.0003	1024	2288	—	—
				5 periapsis	8.46	0.0049				
				20 apoapsis	521.26	0.0577	3608	8126	395	335
				20 periapsis	2261.93	1.1008				
(2) *Variation of parameters* (predict only, variable step)	6	$10^{-8}(r_a/r)$	$10^{-12}(r_a/r)$	5 apoapsis	25.94	0.0027	*745*	*871*	—	—
				5 periapsis	122.99	0.0631				
				20 apoapsis	537.61	0.0606	2844	3330	405	*276*
				20 periapsis	2398.12	1.1662				

[a]These errors occur approximately at apoapsis ($t - t_0 = 54$ and 234 h) and periapsis ($t - t_0 = 60$ and 240 h) of revolutions five and twenty.
[b]Corrected for nonstandard production practices and known improvements.

Combinational Complexity Measures as a Function of Fan-Out

D. L. Johnson
Communications Research Section

J. E. Savage
Engineering Division, Brown University

L. Welch
Electrical Engineering Dept., University of California at Los Angeles

If $C_s(f_1, \cdots, f_L)$ is the fan-out s combinational complexity of the functions $f_1, f_2, \cdots, f_L$ with respect to straight-line algorithms (or combinational machines) of fan-in r, then it is shown that

$$C_\infty(f_1, \cdots, f_L) \leq C_s(f_1, \cdots, f_L) \leq \left(\frac{d(r-1)}{s-1} + 1\right) C_\infty(f_1, \cdots, f_L) + \frac{d}{s-1}(L - N)$$

where N is the number of variables on which $f_1, \cdots, f_L$ depend and $d = C_s(I)$ where I is the identity function in one variable. Thus, a well-designed combinational machine or algorithm will not have a fan-out which is more than several times its fan-in.

I. Introduction

In this paper we develop bounds on the fan-out s combinational complexity of functions. These bounds show that the combinational complexity of functions has a weak dependence on fan-out when $s \geq 2$.

II. Bounds on Combinational Complexity

Before we develop the promised bounds, we state the following definitions which are needed in the sequel.

Definition 1. *Let Ω be a set of functions over the set Σ, such that if $h_i : \in \Omega$, then $h_i : \Sigma^{n_i} \to \Sigma$. Let*

$$\Gamma = \Sigma \cup \{X_1, X_2, \cdots, X_N\}$$

Then, an (Ω, Γ) algorithm (or "straight-line" algorithm) is a K-tuple $\beta = (\beta_1, \beta_2, \cdots, \beta_K)$ where either $\beta_k \in \Gamma$ or $\beta_k = (h_i; k_1, k_2, \cdots, k_{n_i})$, $h_i \in \Omega$, $1 \leq k_l < k$. The set of functions $(\beta_1, \beta_2, \cdots, \beta_K)$ is associated with β where $\beta_k = \beta_k$ if $\beta_k \in \Gamma$ and $\beta_k = h_i(\beta_{k_1}, \cdots, \beta_{k_{n_i}})$ if

$$\beta_k = (h_i; k_1, k_2, \cdots, k_{n_i})$$

An algorithm β is said to compute the functions

$$f_l: \Sigma^{m_l} \to \Sigma, \qquad m_l \leq N, \qquad 1 \leq l \leq L$$

if there exist $\beta_{m_1}, \cdots, \beta_{m_L}$ such that $f_l = \beta_{m_l}$

The *fan-in* of Ω is

$$r = \max_i n_i$$

where $h_i: \epsilon\, \Omega$, $h_i: \Sigma^{n_i} \to \Sigma$. If β computes $f_1, f_2, \cdots, f_L$ where $f_l = \beta_{m_l}$, $1 \leq l \leq L$, let γ_i the number of steps of β which use β_i, if $\beta_i \notin \Sigma$, and $\gamma_i = 0$, $\beta_i \in \Sigma$ and let $\theta_i = \gamma_i$, $i \neq m_1, m_2, \cdots, m_L$ and $\theta_i = \gamma_i + 1$ otherwise. Then, the *fan-out* of β is

$$s = \max_i \theta_i$$

Definition 2. *The combinational complexity with fan-out s of*

$$f_l: \Sigma^{m_l} \to \Sigma, \qquad 1 \leq l \leq L, \qquad C_s(f_1, \cdots, f_L)$$

is the smallest number of steps $\beta_k \notin \Gamma$ of any (Ω, Γ) algorithm which computes these functions, if one such exists; otherwise $C_s(f_1, \cdots, f_L)$ is ∞. Associated with any (Ω, Γ) algorithm is a graph G in which vertices correspond to steps of the algorithm and edges are directed and ordered from vertices corresponding to $\beta_{k_1}, \cdots, \beta_{k_{n_i}}$ to the vertex corresponding to β_k if $\beta_k = (h_i; \beta_{k_1}, \cdots, \beta_{k_{n_i}})$. Vertices corresponding to steps $\beta_k \in \Gamma$ are called source vertices.

Combinational machines are circuits which correspond to the graphs of (Ω, Γ) algorithms in which $\Sigma = \{0, 1\}$ and Ω is a set of Boolean functions; thus, there is an equivalence between combinational machines and straight-line algorithms. These algorithms are called "straight-line" because they do not permit loops or conditional branching. We now state the principal result of this article.

Theorem. *Let $f_1, \cdots, f_L$ be distinct functions over Σ which depend on N variables. Let Ω have fan-in r and let it be such that an (Ω, Γ) algorithm exists for the identity function I in one variable. Then*

$$C_\infty(f_1, \cdots, f_2) \leq C_s(f_1, \cdots, f_L) \leq \left(\frac{d(r-1)}{s-1} + 1\right) \times C_\infty(f_1, \cdots, f_L) + \frac{d}{s-1}(L - N)$$

where $d = C_s(I)$.

Proof. Let β be a straight-line algorithm with fan-out s which computes $f_1, \cdots, f_L$ with $C_s(f_1, \cdots, f_L)$ operations. The directed graph of β has N source vertices and L vertices identified with the distinct functions $f_1, \cdots, f_L$. To the graph G of β add L vertices with edges directed into them from the vertices identified with these functions. The number of edges incident upon vertices in this new graph G' is at most $rC_\infty(f_1, \cdots, f_L) + L$ since each of the original vertices has at most r edges directed into them. Thus, if θ_i edges are directed away from the ith vertex of G' then

$$\sum_i \theta_i \leq rC_\infty(f_1, \cdots, f_L) + L$$

where the sum is over all vertices except those associated with constants.

Since Ω is complete, the identity function on one variable $I(x)$ can be constructed with some number, e.g., d, of elements from it with fan-out s. For each i, if the ith vertex of the graph G' has θ_i edges directed away from it, we can add $h(\theta_i, s)$ copies of the algorithm realizing $I(x)$ to produce a graph G'' which has fan-out s. Here

$$h(\theta_i, s) \leq \frac{\theta_i - 1}{s - 1}$$

so the number of elements in G'' is bounded above by

$$\frac{d}{s-1} \sum_i (\theta_i - 1) + C_\infty$$

where the sum on i is taken over all vertices of G including all source vertices other than those associated with constants. Since $C_s(f_1, \cdots, f_L)$ is the minimum number of operations required to realize $f_1, \cdots, f_L$ with fan-out s, it follows that

$$C_s(f_1, \cdots, f_L) \leq \frac{d}{s-1}(rC_\infty(f_1, \cdots, f_L) + L - C_\infty - N) + C_\infty$$

The left-hand equality of the theorem follows since $C_s(f_1, \cdots, f_L)$ is a non-increasing function of s. QED.

The significance of this result is that all of the complexity measures $C_2, C_3, \cdots, C_\infty$, differ by at most a constant. Also, C_s approaches C_∞ with increasing s when r is fixed. For many sets Ω, $d = 1$; for example, this is true for the set of addition, subtraction, multiplication and divi-

sion over the reals and the set of AND, OR and NOT over the set $\{0, 1\}$. However, $d = 2$ for the set Ω containing only NAND over $\{0, 1\}$.

The combinational complexity of a function with fan-out 1, C_1, can differ substantially from its combinational complexity with unlimited fan-out. Subbotovskaya (Ref. 1) has shown that the Boolean function $f(x_1, \cdots, x_N) = X_1 \bigoplus \cdots \bigoplus X_N$ where $\bigoplus$ denotes the EXCLUSIVE OR has $C_1(f) > a_1 N^{3/2}$ for some constant a_1 when Ω consists of AND, OR and NOT and $C_\infty(f) < a_2 N$ for some other constant a_2.

Reference

1. Subbotovskaya, B. A., "Realizations of Linear Functions by Formulas Using $\wedge$, &, $^-$," *Sov. Math. Dokl.*, Vol. 2, 1961.

Sequential Tests for Exponential Distributions

G. Lorden
California Institute of Technology

The problem is to test whether the frequency of random events (e.g., DSIF equipment failures) is at a nominally prescribed value. When the actual frequency is higher, a determination of this fact is to be made as quickly as possible. A test based on sequential maximum likelihood ratio methods is developed and approximations of its performance characteristics are derived. Results of Monte Carlo sampling demonstrate that these approximations are accurate and that high statistical efficiency is attained over a broad range of possible higher frequencies. Some applications to reliability and inventory policies for the DSIF are indicated.

I. Introduction

If $X_1, X_2, \cdots$ are observed times between random events, then the appropriate model assumes they are independent and identically distributed random variables with a probability density function of the exponential form

$$\lambda e^{-\lambda x}, \qquad x > 0$$

The parameter λ is identified as the (average) frequency of events per unit time. In the DSIF, this model is appropriate for both equipment failures and inventory demands. Reliability and inventory policies must depend heavily upon nominal λ-values estimated from available data. Not only are these values subject to error, but also the underlying λ-values themselves are subject to change. Systematic techniques are required for checking whether nominally prescribed λ-values are exceeded. The following examples of specific applications illustrate the general pattern:

(1) Test inventory demand experience periodically to determine whether minimum stockage levels are sufficient.

(2) Test demand rates of an individual facility to see if they are in line with the rates in other facilities.

(3) Check the performance of repair facilities by testing the frequency of repeated failures of repaired parts.

(4) Compare the reliability performance of an individual supplier's parts against established reliability levels.

The statistical problem arising in such situations is to test the nominal value $\lambda = \lambda_0$ against a range of alternatives, conveniently written $\lambda_0(1 + \theta_1) \leq \lambda \leq \lambda_0(1 + \theta_2)$. Here θ_1 is the smallest fractional increase in λ worth detecting, and θ_2 is the largest fractional increase for which high statistical efficiency is important (could be

taken as $+\infty$). Since the problem is essentially unchanged if $X_1, X_2, \cdots$ are multiplied by a scale factor, it will be assumed without loss of generality that $\lambda_0 = 1$. When $\lambda = 1 + \theta$ the probability density function is

$$f_\theta(x) = \begin{cases} (1+\theta)e^{-(1+\theta)x}, & x > 0 \\ 0, & x \leq 0 \end{cases}$$

The null and alternative hypotheses are, respectively,

$$H{:}\theta = 0 \text{ and } K{:}0 < \theta_1 \leq \theta \leq \theta_2$$

In case $\theta_1 = \theta_2$, it is well-known (Ref. 1) that a sequential probability ratio test (SPRT) is optimal in the sense that it minimizes the expected sample sizes required when $\theta = 0$ and $\theta = \theta_1$ subject to prescribed type I and type II error probabilities, α and β. In applications such as reliability testing, however, it frequently is particularly important to reject H quickly if θ is much larger than θ_1, so that it is appropriate to choose θ_2 much larger than θ_1 and to seek a test which comes reasonably close to minimizing the expected sample sizes for all θ in $[\theta_1, \theta_2]$. In (Refs. 2 and 3) it is shown that sequential likelihood ratio tests asymptotically minimize all expected sample sizes as $\alpha, \beta \to 0$.

The present paper is concerned with the "small sample" properties of likelihood ratio tests for exponential distributions. Specifically, the tests for H versus K above are of the following form. Stop and reject H at the first n such that

$$\max_{\theta_1 \leq \theta \leq \theta_2} \log\left(\frac{f_\theta(X_1)\cdots f_\theta(X_n)}{f_0(X_1)\cdots f_0(X_n)}\right) \geq \log\gamma, \qquad (\gamma > 1) \tag{1}$$

or equivalently

$$n\log(1+\hat{\theta}_n) - \hat{\theta}_n S_n \geq \log\gamma$$

where $S_n = X_1 + \cdots + X_n$ and $\hat{\theta}_n$ is the value of θ which maximizes the likelihood function on $[\theta_1, \theta_2]$ (Eqs. 3 to 5); stop and accept H at the first n such that

$$\log\frac{f_{\theta_1}(X_1)\cdots f_{\theta_1}(X_n)}{f_0(X_1)\cdots f_0(X_n)} \leq \log\xi < 0$$

that is,

$$n\log(1+\theta_1) - \theta_1 S_n \leq \log\xi \tag{2}$$

The main problem is to determine how to choose γ and ξ to attain prescribed bounds, α and β, on type I and type II error probabilities. The principal results in this connection are Eqs. (7) and (25) and Table 2 of Section 3. Several examples were investigated by Monte Carlo methods and the formulas proved to be acceptably accurate in all cases. The results are given in Table 3 of *Subsection III* and examples indicating lower bounds on the efficiency of the likelihood ratio tests are given in Table 4.

A major part of the derivation of the approximate formulas for error probabilities is the approximation in *Subsection II* of the distribution of the "excess over the boundary" or "overshoot" when Eqs. (1) and (2) are first satisfied. In the standard approximations to the error probabilities and expected sample sizes of SPRT's, the effects of this overshoot are ignored; but any reasonably accurate approximation must take it into account, as the results of Ref. 4 indicate. It is well-known that the excess over the boundary in Eq. (2) is exponentially distributed by virtue of the characteristic "memoryless" property of the exponentially distributed X's. The derivation of this result is given in *Subsection II*. The distribution of excess over the boundary in Eq. (1) when $\hat{\theta}_n \equiv \theta_1$ (i.e., $\theta_1 = \theta_2$) is approximated by deriving the limit distribution as $\log\gamma \to \infty$, based on a result of S. C. Port (Ref. 5). This limit distribution also leads to a natural approximation to the excess in Eq. (1) in the general case.

A major simplification is effected in *Subsection III* by studying the probability when $\theta = 0$ that Eq. (1) *ever holds* for any n. This differs from the probability, α, that Eq. (1) occurs before Eq. (2) by *at most* a factor of $(1-\beta)$, by virtue of the argument in the usual derivation of SPRT error approximations (Ref. 6). In typical applications this factor is on the order of 0.95 and may be neglected without serious harm. The approximations to SPRT error probabilities given in Section 2 take into account this small correction, but no attempt is made to do this for likelihood ratio tests because the effect is much more complicated than a simple factor and is difficult to determine.

A convenient description of the likelihood ratio defined by Eqs. (1) and (2) is the following: Perform the SPRT of $\theta = 0$ versus $\theta = \theta_1$ defined by the inequalities

$$\log\xi < n\log(1+\theta_1) - \theta_1 S_n < \log\gamma, \tag{3}$$

stopping to make the appropriate decision as soon as either inequality is violated. In addition, whenever

$S_n/n < (1+\theta_2)^{-1}$ (so that $\hat{\theta}_n = \theta_2$) reject H if

$$n \log (1+\theta_2) - \theta_2 S_n \geq \log \gamma \tag{4}$$

and whenever

$$(1+\theta_2)^{-1} \leq \frac{S_n}{n} < (1+\theta_1)^{-1}$$

so that $1 + \hat{\theta}_n = n/S_n$, reject H if

$$\frac{S_n}{n} - \log\left(\frac{S_n}{n}\right) \geq 1 + \frac{\log \gamma}{n} \tag{5}$$

(Note that Eq. (5) can hold when $S_n/n > 1$, but H is not rejected in this case.) The likelihood ratio test thus modifies the SPRT of $\theta = 0$ versus $\theta = \theta_1$ by rejecting $\theta = 0$ sooner when $\hat{\theta}_n > \theta_1$. For

$$n > \frac{\log \gamma}{\log (1+\theta_1) - \dfrac{\theta_1}{1+\theta_1}}$$

(the approximate expected sample size of the SPRT when $\theta = \theta_1$) it is routinely verified that neither Eqs. (4) nor (5) can hold unless the right-hand inequality of Eq. (3) is violated. Thus for n this large, the statistician goes back to performing an SPRT. Obviously, the usual discussions of truncation apply (e.g., Ref. 6), and the effect of truncation on error probabilities is no greater than for the SPRT. Other uses of likelihood ratio tests, such as for testing composite H or minimizing expected sample sizes over the region between H and K, are discussed in Ref. 2. The results of *Subsection III* can be applied in these cases also.

In the limiting case as $\beta \to 0$, one has what Herbert Robbins has called an "open-ended test" of H: observations are terminated only if Eq. (1) is satisfied (and H is rejected). The type I error probability, α, now represents the probability of ever stopping when $\theta = 0$ (which is approximated in *Subsection III*). Such a test (or a test with very small β) may be called for if observations are inexpensive or mandatory (perhaps for another use), and if, for example, *one is already acting as if the null hypothesis were true.* Examples of this situation are the monitoring of repeated failures of repairable equipment to determine eventual replacement, and the continuous evaluation of failure data or test data on a product to determine whether its acceptance or use should be discontinued (or subjected to more stringent evaluation).

II. Distribution of Excess Over the Boundary

In this section the case $\theta_1 = \theta_2$ (i.e., an SPRT) is considered throughout. Let N be the number of observations required to terminate and consider first the excess over the boundary when (2) occurs; that is, the quantity

$$\log \xi - N \log (1+\theta_1) + \theta_1 S_N$$
$$= [\log \xi - N \log (1+\theta_1) + \theta_1 S_{N-1}] + \theta_1 X_N > 0$$

Now, conditioning on the value, say r, of the bracketed quantity (which must be negative, or else stopping would have occurred before N), and on the event $N = n$, the distribution of the excess (if $\theta = 0$) is that of $r + \theta_1 X_n$ given the latter is positive (X_n being independent of $X_1, \cdots, X_{n-1}$). By the "memoryless" property of the exponential distribution, the conditional distribution of $X_n + r/\theta_1$ given it is positive is exponential, mean 1, for every r and n; hence, when $\theta = 0$ the distribution of the excess is exponential, mean θ_1 (i.e., that of $\theta_1 X_1$).

By Wald's derivation of SPRT error approximations (Ref. 6)

$$\frac{P_{\theta_1}(\text{decide } \theta = 0)}{P_0(\text{decide } \theta = 0)} = \frac{\beta}{1-\alpha} = E_0\left[\frac{f_{\theta_1 N}}{f_{0N}} \,\middle|\, \text{decide } \theta = 0\right] \tag{6}$$

where $f_{\theta_1 N}/f_{0N}$ is the value of the likelihood ratio upon stopping. Let

$$L_n = n \log (1+\theta_1) - \theta_1 S_n$$

Then Eq. (6) can be written

$$\frac{\beta}{1-\alpha} = E_0[\exp(L_N) \mid \text{decide } \theta = 0]$$
$$= \xi E_0[\exp(-(\log \xi - L_N)) \mid \text{decide } \theta = 0]$$
$$= \xi E_0 \exp(-\theta_1 X_1)$$

since the excess over the boundary, $\log \xi - L_N$, is distributed like $\theta_1 X_1$. By routine calculation

$$\frac{\beta}{1-\alpha} = \frac{\xi}{1+\theta_1} \tag{7}$$

The analog of Eq. (6) is

$$\frac{P_0(\text{decide } \theta = \theta_1)}{P_{\theta_1}(\text{decide } \theta = \theta_1)} = \frac{\alpha}{1-\beta} = E_{\theta_1}\left[\frac{f_{0N}}{f_{\theta_1 N}} \,\middle|\, \text{decide } \theta = \theta_1\right] \tag{8}$$

and it follows as above that

$$\frac{\alpha}{1-\beta} = \gamma^{-1} E_{\theta_1} [\exp(-(L_N - \log\gamma)) \,|\, \text{decide } \theta = \theta_1] \tag{9}$$

The approximate formula (11) for $\alpha/(1-\beta)$ will be derived from Eq. (9) by replacing the excess over the boundary, $L_N - \log\gamma$, by R, a random variable whose distribution is the limit distribution of $L_N - \log\gamma$ as $\log\gamma \to \infty$. A routine argument shows that this limit distribution does not depend on $\log\xi$, being always the same as in the case $\log\xi = -\infty$, i.e., the usual one-sided boundary in renewal theory.

By Theorem 3 of Ref. 5 the limit distribution of excess over the boundary for cumulative sums of non-lattice variables (e.g., the sequence $\{L_n\}$) has density $e(-x)/E_{\theta_1}L_1$, where

$$e(-x) = P_{\theta_1}(L_1, L_2, \cdots > x) \qquad \text{for } x \geq 0$$

and is zero for $x < 0$. The density function of $L_1 = \log(1+\theta_1) - \theta_1 X_1$ when $\theta = \theta_1$ is

$$g(t) = \begin{cases} \dfrac{1+\theta_1}{\theta_1} \exp\left(\dfrac{1+\theta}{\theta}[t - \log(1+\theta)]\right), & t \leq \log(1+\theta) \\ 0, & t > \log(1+\theta) \end{cases}$$

Conditioning on the value of L_1, we have

$$e(-x) = \int_x^\infty \left(1 - \frac{e^{x-t}}{1+\theta_1}\right) g(t)\, dt$$

since

$$P_{\theta_1}[L_2, L_3, \cdots > x \,|\, L_1 = t > x] = P_{\theta_1}[L_1, L_2, \cdots > x - t]$$

which is just a limiting case of Eq. (7) with $\log\gamma = +\infty$ (so that $\alpha = 0$) and $x - t = \log\xi$. The integral is easily evaluated, yielding

$$e(-x) = \begin{cases} 1 - \dfrac{e^x}{1+\theta_1}, & 0 \leq x \leq \log(1+\theta_1) \\ 0, & \text{otherwise} \end{cases}$$

Since

$$E_{\theta_1} L_1 = \log(1+\theta_1) - \frac{\theta_1}{(1+\theta_1)}$$

the limiting distribution of the excess over the boundary, $L_N - \log\gamma$, has density

$$h(x) = \begin{cases} \dfrac{1+\theta_1 - e^x}{(1+\theta_1)\log(1+\theta_1) - \theta_1}, & 0 \leq x \leq \log(1+\theta_1) \\ 0, & \text{otherwise} \end{cases} \tag{10}$$

Therefore, the approximation derived from Eq. (9) is

$$\frac{\alpha}{1-\beta} \approx \gamma^{-1} E_{\theta_1} \exp(-R) = \gamma^{-1} \cdot \frac{\theta_1 - \log(1+\theta_1)}{(1+\theta_1)\log(1+\theta_1) - \theta_1} \tag{11}$$

where R has density h.

Combining Eqs. (7) and (11) leads to the approximations

$$\alpha \approx \frac{1+\theta_1-\xi}{\gamma G(\theta_1)(1+\theta_1) - \xi} \tag{12}$$

and

$$1 - \beta \approx \gamma G(\theta_1)\alpha \approx \frac{\gamma G(\theta_1)(1+\theta_1-\xi)}{\gamma G(\theta_1)(1+\theta_1) - \xi} \tag{13}$$

where

$$G(\theta_1) = \frac{(1+\theta_1)\log(1+\theta_1) - \theta_1}{\theta_1 - \log(1+\theta_1)}$$

Relations (7) and (11) also yield approximations for the expected sample sizes, based on Wald's equation, $E\,L_1 \cdot E\,N = EL_N$.

$$\left(\log(1+\theta_1)-\frac{\theta_1}{1+\theta_1}\right)E_{\theta_1}N \approx \beta\,(\log\xi - E_{\theta_1}(\theta_1 X_1)) + (1-\beta)\,(\log\gamma + E_{\theta_1}R)$$

$$= \beta\left(\log\xi - \frac{\theta_1}{1+\theta_1}\right) + (1-\beta)\left(\log\gamma + \frac{\frac{1}{2}(1+\theta_1)[\log(1+\theta_1)]^2}{(1+\theta_1)\log(1+\theta_1)-\theta_1} - 1\right) \tag{14}$$

Similarly,

$$(\log(1+\theta_1)-\theta_1)\,E_0 N \approx (1-\alpha)\,(\log\xi - E_0(\theta_1 X_1)) + \alpha(\log\gamma + E_0 R)$$

The value of $E_0 R$ does not come out of the above derivation. However, its effect is small, since it is multiplied by α and is in any case bounded by zero and $\log(1+\theta_1)$. The latter value gives a smaller approximation (since $\log(1+\theta_1)-\theta_1$ is negative):

$$(\log(1+\theta_1)-\theta_1)\,E_0 N \approx (1-\alpha)\,(\log\xi - \theta_1) + \alpha(\log\gamma + \log(1+\theta_1)) \tag{15}$$

The approximations (12) to (15) are useful in *Subsection III* for deriving similar approximations in the case of likelihood ratio tests. For SPRTs, Refs. 4 and 7 give exact error probabilities and expected sample sizes. However, formulas (11) to (13) together with the values of $G(\theta)^{-1}$ in Table 2 of *Subsection III* are quite useful in obtaining reasonably accurate approximations to the values of γ and ξ needed to get prescribed α and β for SPRTs. The following table gives some examples to illustrate the degree of accuracy of the approximations (11) to (15).

III. Approximate Error Probabilities of Likelihood Ratio Tests

The type II error probabilities of the likelihood ratio tests defined by Eqs. (1) and (2) obviously attain a maximum, β, at $\theta = \theta_1$. To approximate β, note that the derivation of Eqs. (6) and (7) applies, so that Eq. (7) holds with α equal to the type I error probability of the likelihood ratio test. The value of the factor $(1-\alpha)$ in Eq. (7) can be approximated using the principal result (25) of this section, but the effect on the determination of β is small in typical problems, so that $\beta \approx \xi/(1+\theta_1)$.

To approximate α, an approximation to

$$\alpha^* = P_0\left(\max_{\theta_1 \le \theta \le \theta_2}\,[n\log(1+\theta) - \theta S_n] \ge \log\gamma \text{ for some } n\right)$$

will suffice, since the ratio α/α^* is at least $1-\beta$, as discussed in *Subsection I*. The inequality

$$\max_{\theta_1 \le \theta \le \theta_2}\,[n\log(1+\theta) - \theta S_n] \ge \log\gamma$$

is clearly equivalent to

$$S_n \le \max_{\theta_1 \le \theta \le \theta_2}\left[\frac{n\log(1+\theta)}{\theta} - \frac{\log\gamma}{\theta}\right] \tag{16}$$

and differentiation of the bracketed quantity in Eq. (16) shows that the maximum is attained at $\tilde{\theta}_n$, the solution of

$$\frac{\log\gamma}{n} = \log(1+\tilde{\theta}_n) - \frac{\tilde{\theta}_n}{1+\tilde{\theta}_n} = I(\tilde{\theta}_n), \text{ say}$$

if $m \le n \le M$, where m is the largest integer $\le (\log\gamma)/I(\theta_2)$ and M is the smallest integer $\ge (\log\gamma)/I(\theta_1)$. If $n < m$ the maximum is attained at θ_2 and if $n > M$ it is attained at θ_1. Let N be the smallest n for which Eq. (16) is satisfied (or ∞ if there is no n) and let $N(\theta)$ for $\theta > 0$ be the smallest n (or ∞ if there is no n) such that

$$S_n \le \frac{n\log(1+\theta)}{\theta} - \frac{\log\gamma}{\theta} \tag{17}$$

If $N = n$, then since $\tilde{\theta}_n$ maximizes the bracketed quantity in Eq. (16), evidently Eq. (17) holds with $\theta = \tilde{\theta}_n$, so that $N(\tilde{\theta}_n) \le n$ and, in fact, $N(\tilde{\theta}_n) = n$ (N being $\le N(\tilde{\theta}_n)$ by virtue of $\tilde{\theta}_n \in [\theta_1, \theta_2]$). Therefore, for all n

$$P_0(N = n) \le P_0(N(\tilde{\theta}_n) = n) \tag{18}$$

If $m = 0$, then $\theta_2 > \theta_1$ and the values of θ in $[\tilde{\theta}_1, \theta_2]$ play no role in the test since the maximum in Eq. (16) is the same for every n if θ_2 is replaced by $\tilde{\theta}_1$. Thus, there is no loss of generality in assuming that $\theta_2 \le \tilde{\theta}_1$, i.e.,

that $m \geq 1$. Since $\tilde{\theta}_1 = \cdots = \tilde{\theta}_m = \theta_2$ and $\tilde{\theta}_M = \tilde{\theta}_{M+1} = \cdots = \theta_1$, it follows from Eq. (18) that

$$\alpha^* = \sum_{n=1}^{\infty} P_0(N = n) \leq P_0(N(\theta_2) \leq m) + P_0(M \leq N(\theta_2) < \infty) + \sum_{n=m+1}^{M-1} P_0(N(\tilde{\theta}_n) = n) \tag{19}$$

Regarding n as a continuous variable u on the interval from $(\log \gamma)/I(\theta_2) \approx m$ to $(\log \gamma)/I(\theta_1) \approx M$, with $I(\tilde{\theta}_u) \equiv (\log \gamma)/u$, one can approximate the last summation in Eq. (19) by an integral, which yields the approximate upper bound

$$\alpha^* \lessapprox P_0\left(N(\theta_2) \leq \frac{\log \gamma}{I(\theta_2)}\right) + P_0\left(\frac{\log \gamma}{I(\theta_1)} \leq N(\theta_1) < \infty\right) + \int_{\log \gamma / I(\theta_2)}^{\log \gamma / I(\theta_1)} P_0(N(\tilde{\theta}_u) = u)\, du \tag{20}$$

(The event $N(\tilde{\theta}_u) = u$ makes sense only if u is an integer, but a natural interpolation will come from the calculations which follow). A relation similar to Wald's relation (8), derivable by a similar "cancellation of densities" argument (Ref. 6), is the following. For integer u,

$$\frac{P_0(N(\tilde{\theta}_u) = u)}{P_{\tilde{\theta}_u}(N(\tilde{\theta}_u) = u)} = E_{\tilde{\theta}_u}[\exp(-L_u) \mid N(\tilde{\theta}_u) = u] \tag{21}$$

where $L_u = u \log(1 + \tilde{\theta}_u) - \tilde{\theta}_u S_u$.

The random variable $N(\tilde{\theta}_u)$ is by definition the number of observations of a one-sided SPRT of $\theta = 0$ versus $\tilde{\theta} = \theta_u$. This suggests the approximation

$$E_{\tilde{\theta}_u}[\exp(-L_u) \mid N(\tilde{\theta}_u) = u] \approx E_{\tilde{\theta}_u}[\exp(-\log \gamma - R(\tilde{\theta}_u))] = \gamma^{-1} E_{\tilde{\theta}_u} \exp(-R(\tilde{\theta}_u)),$$

where $R(\tilde{\theta}_u)$ has the limit distribution of excess over the boundary derived in *Subsection II* (upon setting $\theta_1 = \tilde{\theta}_u$). Applying this approximation and Eq. (21),

$$\frac{P_0(N(\tilde{\theta}_u) = u)}{P_{\tilde{\theta}_u}(N(\tilde{\theta}_u) = u)} \approx \gamma^{-1} \frac{\tilde{\theta}_u - \log(1 + \tilde{\theta}_u)}{(1 + \tilde{\theta}_u)\log(1 + \tilde{\theta}_u) - \tilde{\theta}_u} \tag{22}$$

An approximation to $P_{\tilde{\theta}_u}(N(\tilde{\theta}_u) = u)$ is suggested by the fact (Ref. 6) that when $\tilde{\theta}_u$ is true and γ is large, $N(\tilde{\theta}_u)$ is approximately normally distributed with mean $(\log \gamma)/I(\tilde{\theta}_u) = u$ and variance

$$\frac{(\log \gamma)\,\mathrm{Var}_{\tilde{\theta}_u}\left(\log\left(\frac{f_{\tilde{\theta}_u}(X)}{f_0(X)}\right)\right)}{\left(E_{\tilde{\theta}_u} \log\left(\frac{f_{\tilde{\theta}_u}(X)}{f_0(X)}\right)\right)^3} = \frac{(\log \gamma)\frac{\tilde{\theta}_u^2}{(1 + \tilde{\theta}_u)^2}}{I(\tilde{\theta}_u)^3}$$

Taking $1/\sqrt{2\pi}$ times the reciprocal of the standard deviation as an approximation to the probability of the unit-length interval centered on u,

$$P_{\tilde{\theta}_u}(N(\tilde{\theta}_u) = u) \approx \frac{I(\theta_u)^{3/2}(1 + \tilde{\theta}_u)}{\sqrt{2\pi}(\log \gamma)^{1/2}\tilde{\theta}_u} = \frac{I(\tilde{\theta}_u)}{\sqrt{2\pi u}} \cdot \frac{1 + \tilde{\theta}_u}{\tilde{\theta}_u}$$

since

$$\frac{I(\tilde{\theta}_u)^{1/2}}{(\log \gamma)^{1/2}} = u^{-1/2}$$

Combining with Eq. (22) yields

$$P_0(N(\tilde{\theta}_u) = u) \approx \frac{\gamma^{-1} I(\tilde{\theta}_u)}{\sqrt{2\pi u}} \cdot \frac{1 - \frac{(\log(1 + \tilde{\theta}_u))}{\tilde{\theta}_u}}{\log(1 + \tilde{\theta}_u) - \frac{\tilde{\theta}_u}{(1 + \tilde{\theta}_u)}} = \frac{\gamma^{-1}}{\sqrt{2\pi u}}\left(1 - \frac{\log(1 + \tilde{\theta}_u)}{\tilde{\theta}_u}\right). \tag{23}$$

Similarly, the distribution of $N(\theta_2)$ when $\theta = \theta_2$ is asymptotically normal with mean $\log \gamma / I(\theta_2)$, which suggests

$$P_0(N(\theta_2) \leq (\log \gamma)/I(\theta_2)) \approx \frac{1}{2}\gamma^{-1} \cdot \frac{\theta_2 - \log(1 + \theta_2)}{(1 + \theta_2)\log(1 + \theta_2) - \theta_2}$$

Using a similar approximation for $P_0(\log \gamma)/I(\theta_1) \leq N(\theta_1) < \infty)$ and plugging Eq. (23) into Eq. (20),

$$\alpha^* \lessapprox \frac{1}{2}\gamma^{-1}\left[\frac{\theta_2 - \log(1 + \theta_2)}{(1 + \theta_2)\log(1 + \theta_2) - \theta_2} + \frac{\theta_1 - \log(1 + \theta_1)}{(1 + \theta_1)\log(1 + \theta_1) - \theta_1}\right] + \frac{\gamma^{-1}}{\sqrt{2\pi}} \int_{(\log \gamma)/I(\theta_2)}^{(\log \gamma)/I(\theta_1)} u^{-1/2}\left(1 - \frac{\log(1 + \tilde{\theta}_u)}{\tilde{\theta}_u}\right) du \tag{24}$$

The change of variable $x = \log(1 + \tilde{\theta}_u)$ leads to

$$\alpha^* \lessapprox \frac{1}{2}\gamma^{-1}\left[\frac{\theta_2 - \log(1+\theta_2)}{(1+\theta_2)\log(1+\theta_2) - \theta_2} + \frac{\theta_1 - \log(1+\theta_1)}{(1+\theta_1)\log(1+\theta_1) - \theta_1}\right] + \frac{\gamma^{-1}\sqrt{\log\gamma}}{\sqrt{2\pi}}\int_{\log(1+\theta_1)}^{\log(1+\theta_2)} \frac{e^{-x}(e^x - 1 - x)}{(x + e^{-x} - 1)^{3/2}}\,dx \tag{25}$$

Let

$$Q(\theta) = \int_{\log(1.01)}^{\log(1+\theta)} \frac{e^{-x}(e^x - 1 - x)}{(x + e^{-x} - 1)^{3/2}}\,dx$$

Given γ,θ_1,θ_2, the approximate upper bound on α^*, Eq. (25), and hence the approximate upper bound on α for the likelihood ratio test determined by γ,θ_1,θ_2, can be written

$$\frac{1}{2}\gamma^{-1}\left(G(\theta_1)^{-1} + G(\theta_2)^{-1}\right) + \frac{\gamma^{-1}\sqrt{\log\gamma}}{\sqrt{2\pi}}\left(Q(\theta_2) - Q(\theta_1)\right) \tag{26}$$

Monte Carlo sampling was performed in five cases to compare the approximate upper bound in Eq. (25) with the observed frequency of type I errors. The results are given in Table 3 with the tolerances in the last column being the standard deviations of the observed frequencies. All probabilities are expressed as percentages.

For obvious reasons, the Monte Carlo experiments could not be used to determine the frequency with which Eq. (16) holds for some $n = 1,2,\cdots$. The experiments were carried out for a likelihood ratio test which could accept the null hypothesis (and thereby terminate the sample sequence) as soon as Eq. (2) was satisfied. Values of ξ were chosen to ensure that the effect of these terminations was small compared to the sampling errors. In all but the second of the five cases in Table 3, the observed frequencies were smaller than the approximate upper bounds, and the agreement between the two would be improved if the sample sequences were not terminated.

An analysis of the efficiencies of the likelihood ratio tests is easy to make using a definition slightly different from the usual definition. The one-sided SPRT of 0 versus θ defined by Eq. (17) has the optimality property of minimizing $E_\theta N$ among all tests with $\alpha \leq \tilde{\alpha}$, its type I error probability. The efficiency of a test with $\alpha = \tilde{\alpha}$ is usually defined as the ratio $E_\theta N/E_\theta N' < 1$, where N' is the number of observations taken by the other test. But Wald's approximation for expected sample sizes (Ref. 6) and Eq. (14) both indicate that $E_\theta N$ is very nearly proportional to $\log \tilde{\alpha}^{-1}$. It is therefore reasonable (and, in the present investigation, convenient) to define the efficiency of a test with given α and $E_\theta N'$ as the ratio $\log \alpha^{-1}/\log \tilde{\alpha}^{-1}$ where $\tilde{\alpha}$ is the type I error probability of a one-sided SPRT of 0 versus θ having $E_\theta N = E_\theta N'$.

For the likelihood ratio tests it is of interest to compute these efficiencies for θ's ranging over $[\theta_1,\theta_2]$. This is an "unfair" comparison in the sense that a single likelihood ratio test, designed to perform well for all θ in $[\theta_1,\theta_2]$ is compared for each θ with the optimal test (an SPRT) *chosen especially for that* θ. Nevertheless, the comparison is interesting as an indication of how great a price is paid in loss of efficiency at one value of θ in order to attain simultaneously "good" performance over a broad range of θ's.

Let α denote the type I error probability of a given likelihood ratio test. When θ_1 is true, the expected number of observations is by Eq. (1) no larger than that of a one-sided SPRT of 0 versus θ_1 with the same boundary, $\log \gamma$. Hence, a lower bound on the efficiency (as defined above) is

$$\frac{\log \alpha^{-1}}{\log \alpha(\theta_1)^{-1}}$$

where $\alpha(\theta_1)$ is the type I error probability of the SPRT of 0 versus θ_1 with boundary $\log \gamma$. Similarly, define for θ in $[\theta_1,\theta_2]$

$$e^*(\theta) = \frac{\log \alpha^{-1}}{\log \alpha(\theta)^{-1}}$$

where $\alpha(\theta)$ is the type I error probability of the one-sided SPRT of 0 versus θ with boundary $\log \gamma$. Table 4 of $e^*(\theta)$'s was computed by using the approximate upper bound (25) as α and approximating $\alpha(\theta)$ from Eq. (13) as $\gamma^{-1}/G(\theta)$ ($\beta = 0$). Since $e^*(\theta)$ was found to be nearly constant over $[\theta_1,\theta_2]$, decreasing slightly over the interval, only the values of $e^*(\theta_1)$ and $e^*(\theta_2)$ are given.

IV. Conclusion

From Table 2 it is easy to determine the critical values γ and ξ needed to achieve prescribed error probabilities with a sequential likelihood ratio test. As the results in Table 4 indicate, a test determined in this way will guarantee high statistical efficiency even if the range $[\theta_1,\theta_2]$ is broad. The application of these tests for DSIF reliability and inventory policies along the lines in *Subsection I* should be both practical and useful.

Acknowledgment

The author is grateful to I. Eisenberger for his help in performing the computations and Monte Carlo experiments.

References

1. Wald, A., and Wolfowitz, J., "Optimum Character of the Sequential Probability Ratio Test," *Ann. Math. Statist.*, Vol. 19, pp. 326–339.
2. Lorden, G., "Likelihood Ratio Tests for Sequential k-Decision Problems," (submitted to *Ann. Math. Statist.*).
3. Lorden, G., "Open-ended Tests for Koopman-Darmois Families" (submitted to *Ann. Math. Statist.*).
4. Kiefer, J., and Wolfowitz, J., (1956). "Sequential Tests of Hypotheses About the Mean Occurrence Time of a Continuous Parameter Poisson Process," *Naval Res. Logist. Quant.*, Vol. 3, pp. 205–219.
5. Port, S. C., "Escape Probability for a Half-Line," *Ann. of Math. Statist.*, Vol. 35 pp. 1351–1355, 1964.
6. Wald, A., *Sequential Analysis*, Wiley & Sons, New York, 1947.
7. Dvoretzky, A., Kiefer, J., and Wolfowitz, J., "Sequential Decision Problems for Processes with Continuous Time Parameter Testing Hypotheses," *Ann. Math. Statist.*, Vol. 24, pp. 254–264, 1953.

Table 1. Comparison of operating characteristics of SPRTs with approximations (11) to (15)

θ	log γ	ξ	α^*, %	β, %	E_0N	E_1N
1.0	2.48	0.005	6.6 (6.6)[a]	0.23 (0.23)	18.5 (18.6)	14.0 (14.0)
0.7	3.73	0.02	2.0 (2.0)	1.2 (1.2)	26.2 (26.2)	32.1 (32.1)
0.4	3.39	0.10	2.8 (2.8)	6.9 (6.9)	39.7 (39.8)	60.7 (60.9)
0.3	2.48	0.10	7.1 (7.0)	7.1 (7.2)	59.0 (59.4)	69.8 (69.8)

[a]Actual values (in parentheses) were computed using the exact formulas in Ref. 7. The agreement is very good and gets better as log γ increases because the limit distribution of excess over the boundary is quickly approached.

Table 2. Values of $G(\theta)\frac{\theta-\log(1+\theta)}{(1+\theta)\log(1+\theta)-\theta}$

and $Q(\theta)=\int_{\log(1.01)}^{\log(1+\theta)}\frac{e^{-x}(e^x-1-x)}{(x+e^{-x}-1)^{3/2}}dx$

θ	$G(\theta_1)^{-1}$	$Q(\theta)$	θ	$G(\theta)^{-1}$	$Q(\theta)$	θ	$G(\theta)^{-1}$	$Q(\theta)$
0.02	0.993	0.971	0.26	0.926	4.396	0.70	0.838	5.501
0.03	0.990	1.535	0.27	0.923	4.442	0.72	0.835	5.529
0.04	0.987	1.933	0.28	0.921	4.486	0.74	0.832	5.556
0.05	0.984	2.239	0.29	0.919	4.528	0.76	0.829	5.583
0.06	0.981	2.488	0.30	0.916	4.568	0.78	0.826	5.608
0.07	0.978	2.697	0.32	0.912	4.644	0.80	0.822	5.632
0.08	0.975	2.877	0.34	0.907	4.715	0.85	0.815	5.690
0.09	0.972	3.035	0.36	0.903	4.782	0.90	0.808	5.744
0.10	0.969	3.175	0.38	0.898	4.844	0.95	0.801	5.794
0.11	0.966	3.301	0.40	0.894	4.902	1.00	0.794	5.841
0.12	0.963	3.416	0.42	0.890	4.958	1.1	0.782	5.926
0.13	0.960	3.521	0.44	0.886	5.010	1.2	0.770	6.001
0.14	0.957	3.617	0.46	0.882	5.059	1.3	0.759	6.068
0.15	0.954	3.706	0.48	0.878	5.106	1.4	0.748	6.129
0.16	0.952	3.789	0.50	0.874	5.150	1.5	0.738	6.184
0.17	0.949	3.867	0.52	0.870	5.192	1.6	0.729	6.234
0.18	0.946	3.939	0.54	0.866	5.233	1.8	0.711	6.323
0.19	0.944	4.008	0.56	0.862	5.271	2.0	0.696	6.399
0.20	0.941	4.072	0.58	0.859	5.308	2.5	0.662	6.549
0.21	0.938	4.133	0.60	0.855	5.344	3.0	0.634	6.662
0.22	0.936	4.191	0.62	0.852	5.378	3.5	0.611	6.751
0.23	0.933	4.246	0.64	0.848	5.410	4.0	0.591	6.823
0.24	0.931	4.298	0.66	0.845	5.442	4.5	0.573	6.884
0.25	0.928	4.348	0.68	0.841	5.472	5.0	0.558	6.935

Table 3. Comparison of error probability approximations with Monte Carlo experiments

θ_1	θ_2	log γ	Approximation, %	Observed frequency, %
0.3	1	2.48	14.0	13.2 ± 1.1
0.2	3	3.39	9.01	9.09 ± 0.91
0.5	4	3.70	4.99	4.33 ± 0.46
0.7	2	3.73	3.50	3.34 ± 0.28
0.3	1	5.31	1.00	0.83 ± 0.14

Table 4. Approximate lower bounds on efficiency, %

θ_1	θ_2	log γ	$e^*(\theta_1)$	$e^*(\theta_2)$
0.3	1	2.48	77	73
0.2	3	3.39	70	63
0.5	4	3.70	78	71
0.7	2	3.73	86	82
0.3	1	5.31	85	83

Contributions to a Mathematical Theory of Complexity

L. H. Harper
University of California at Riverside

J. E. Savage
Brown University

This article is another in a series that attempts to define precisely and investigate the "computational complexity" of a general class of problems which includes many problems that occur in the DSN control center. Specific DSN control center questions that a theory of computational complexity will help define and answer include the problem of the optimum mix of core, disk, and drum storage in the control center, and the intelligent allocation of computational resources to flight projects of differing complexity in such a way that simultaneous real-time computing commitments can be made. This article shows that there exists such a theory which is capable of providing important information about the true complexity of several classes of non-trivial problems.

I. Introduction

The Deep Space Network depends critically upon computation: computation of trajectories, decoding of telemetry, processing of ranging data, etc. For every computation we make, however, we should also ask, "Could this be done more efficiently?" Sometimes we can answer affirmatively by producing a better algorithm; rarely can we assert that no improvement is possible. It is the object of this article to present the elements of a theory of complexity which may lead to a satisfactory answer to this question in many cases. In a previous article (Ref. 1), we began the study of complexity; this article continues the work.

Specific DSN control center questions which a theory of computational complexity will help define and answer include the problem of the optimum mix of core, disk, and drum storage in the control center, and the intelligent allocation of computational resources to flight projects of differing complexity, in such a way that simultaneous real-time computing commitments can be made. This article shows that there exists such a theory which is capable of providing important information about the true complexity of several classes of non-trivial problems.

In *Section II*, we define the *computational complexity* and the *computation time* of any Boolean function of N variables, and contrast a theorem of Lupanov which says that "most" such functions have complexity near 2^N, with a simple lemma which shows that any function which really depends on N variables has complexity at least $\rho(N-1)$ for a certain constant ρ. In *Section III* we present a condition which guarantees that a function is rather complex, sometimes as complex as $N^2/\log N$.

Finally, in *Section IV*, we apply the results of the previous sections to two famous search problems of com-

binatorial mathematics: the "marriage problem" and the "traveling salesman's problem." We establish a lower bound of $0(n^3)$ on the combinational complexity (with logic fan-out one) for the marriage problem. The classical "alternating paths" technique gives an upper bound of $0(n^4)$ for the combinational complexity (with unlimited fan-out) for this problem. Hopefully, more work will eliminate the fan-out restrictions and close the gaps between upper and lower bounds.

II. Algorithms and Complexity Measures

The complexity of various functions will be measured under the assumption that it is computed by a "straight-line" algorithm, which is defined below.

Definition. Let Ω be a finite set of Boolean functions

$$h_i : (\Sigma_2)^{r_i} \to \Sigma_2$$

where $\Sigma_2 = \{0, 1\}$ and $r_i \leq r$, the fan-in of Ω. Let

$$\Gamma = \Sigma_2 \cup \{x_1, x_2, \cdots, x_N\}$$

be the *data set* where x_i is a Boolean variable. Then, a K-step *straight-line algorithm* with data set Γ is a K-tuple $\beta = (\beta_1, \beta_2, \cdots, \beta_K)$, where at the kth step $\beta_k \in \Gamma$ or $\beta_k = (h_i; k_1, \cdots, k_{r_i})$ for some $h_i \in \Omega$, where $1 \leq k_l < k$ for $1 \leq l \leq r_i$. If $\beta_k \in \Gamma$, we associate with it the function $\overline{\beta}_k$, which is either a constant or a variable x_i. If $\beta_k = (h_i; k_1, \cdots, k_{r_i})$, we associate with it the recursively defined function $\overline{\beta}_k = h_i(\overline{\beta}_{k_1}, \overline{\beta}_{k_2}, \cdots, \overline{\beta}_{k_{r_i}})$. The algorithm is said to *compute* the functions $\overline{\beta}_{m_1}, \overline{\beta}_{m_2}, \cdots, \overline{\beta}_{m_q}$ if $\beta_{m_1}, \beta_{m_2}, \cdots, \beta_{m_q}$ are steps of the algorithm. The set of primitives Ω is said to be *complete* if every Boolean function

$$f : (\Sigma_2)^N \to \Sigma_2$$

can be computed by some straight-line algorithm over Γ.

Associated with an algorithm β is a *graph* of the algorithm. This is a set of vertices that are in a 1-1 correspondence with the steps of β and a set of directed edges. A step $\beta_k \in \Gamma$ corresponds to a vertex which has no edges directed into it while a step $\beta_k = (h_i; k_1, \cdots, k_{r_i})$ has a corresponding vertex with ordered edges directed into it from nodes corresponding to $\beta_{k_1}, \cdots, \beta_{k_{r_i}}$. A graph is said to have *fan-out* of s if the maximum number of edges directed away from any vertex is s. This is also said to be the fan-out of the algorithm. If $\beta_k \in \Gamma$, its corresponding node is called a *source vertex*. The graph of an algorithm is also known as the circuit diagram of a *combinational machine*.

A cost, P_i, is associated with the use of each primitive operation $h_i \in \Omega$ and the cost of an algorithm is the sum of the costs of each of its primitive operations. Then, the *combinational complexity* with fan-out s of the Boolean functions $f_1, f_2, \cdots, f_L$ with respect to the set of primitives Ω, $C_s(f_1, f_2, \cdots, f_L)$, is the smallest cost of any straight-line algorithm over Ω which computes these functions and which has fan-out of at most s. Then, it is clearly true that

$$C_\infty(f_1, \cdots, f_L) \leq C_s(f_1, \cdots, f_L) \leq C_{s-1}(f_1, \cdots, f_L) \leq C_1(f_1, \cdots, f_L)$$

The two measures of greatest interest in this article are C_∞, the combinational complexity with unlimited fan-out, and C_1, the combinational complexity with fan-out of 1. It should be noted that an algorithm with fan-out 1 has no memory in the sense that any intermediate functions which are used more than once must be recomputed.

Lupanov (Refs. 2 and 3) has shown that every Boolean function f of N variables can be realized with

$$C_\infty(f) \leq \rho \frac{2^N}{N}(1 + \epsilon)$$

$$C_1(f) \leq \rho \frac{2^N}{\log_2 N}(1 + \epsilon)$$

for $0 < \epsilon$ and $N \geq N^*(\epsilon)$, where

$$\rho = \max_{r_i \geq 2} \frac{P_i}{r_i - 1}$$

These bounds are sharp in the sense that for large N, almost all Boolean functions have $C_\infty(f)$ and $C_1(f)$ which are larger than $\rho(2^N/N)(1 - \epsilon)$ and $\rho(2^N/\log_2 N)(1 - \epsilon)$, respectively.

Let the length of an algorithm be the number of edges on a longest directed path of its graph. Then, another important measure of complexity is the *computation time of Boolean functions* $f_1, \cdots, f_L$ denoted $D(f_1, \cdots, f_L)$, which is defined as the minimal length of a straight-line algorithm over Ω which computes $f_1, \cdots, f_L$. We have immediately that

$$D(f_1, \cdots, f_L) = \max_{1 \leq l \leq L} D(f_l)$$

It can be shown, using the disjunctive normal form decomposition of a Boolean function, that every Boolean function of N variable can be realized with $D(f) \leq N - 1 + \lceil \log_2 N \rceil$. Also, for large N, almost all of these functions has $D(f)$ which is bounded below by a function linear in N.

The following lemma establishes a relation between the measures D and C_1.

LEMMA 1. *Let f be a Boolean function and let f be realized by a straight-line algorithm with fan-in r. Then,*

$$D(f) \geq \left\lceil \log_r \left[(r-1) \frac{C_1(f)}{P_{\max}} + 1 \right] \right\rceil$$

where $P_{\max}$ is the maximum cost P_i for $h_i \in \Omega$.

Proof. Consider an algorithm which realizes f with computation time $D(f)$. Such an algorithm can be assumed to have fan-out of 1 and to have an associated graph which is a tree since only one vertex of the graph corresponds to the function f which is to be computed. Then, the graph of such an algorithm cannot have more than $(r^{D(f)} - 1)/(r-1)$ non-source vertices and this quantity must be at least as large as $C_1(f)/P_{\max}$. The inequality then follows.

Q.E.D.

A test is now developed which when satisfied provides a linear lower bound to combinational complexity.

LEMMA 2. *Let f be a Boolean function which is dependent on N variables. Then,*

$$C_s(f) \geq \rho(N-1), \qquad 1 \leq k \leq \infty$$

where

$$\rho = \min_{r_i \geq 2} \frac{P_i}{r_i - 1}$$

and r_i is the number of inputs on which h_i depends.

Proof. Let β be an optimal algorithm of fan-out s which computes f. Then, the graph of the algorithm has exactly one vertex with no edges directed away from it with all remaining vertices having at least one edge directed away from them. Thus, the number of edges directed away from vertices is at least

$$N - 1 + \sum_i M_i$$

where M_i is the number of occurrences of h_i since each of the N variables on which f depends are associated with source vertices. But there are at most

$$\sum_i M_i r_i$$

edges directed into vertices so

$$N - 1 \leq \sum M_i (r_i - 1)$$

If i_0 minimizes $P_i/(r_i - 1)$, then

$$\rho(N-1) \leq \sum_i M_i \frac{P_{i_0}}{(r_{i_0} - 1)} (r_i - 1)$$

$$\leq \sum_i M_i P_i = C_s(f)$$

which is the desired result.

Q.E.D.

Any function satisfying this test has a combinational complexity which grows at least linearly with the number of variables on which it depends. For $s > 1$, this is the strongest known lower bound. For $s = 1$, Specker's Theorem (Ref. 4) states conditions under which $C_1(f)$ must grow faster than linearly in N, N being the number of variables. In the next section we present a technique which we call Neciporuk's test for generating lower bounds to $C_1(f)$. These bounds can grow as fast as $N^2/\log N$.

A few remarks are in order concerning straight-line algorithms. These algorithms contain no loops nor do they permit conditional branching. For this reason they in general cannot compute functions as quickly as algorithms which have these features. Nevertheless, results of Savage (Ref. 5) show that if A is an autonomous sequential machine which allows loops and conditional branches and computes f, then the inequality $C_\infty(f) \leq (C^*_\infty(A) + 5n_0)\,T$ must be satisfied, where T is the maximum number of cycles executed by A on any point in the domain f, $C^*_\infty(A)$ is the combinational complexity of the next state and output function of A, and n_0 is the number of binary digits required to specify the output of A. We can assert, for example, that if T is much smaller than $C_\infty(f)$, then the complexity of the machine A must be large.

III. Neciporuk's Test

In this section we develop a lower bound to $C_1(f)$ for a Boolean function of N variables. This bound was ab-

stracted from Neciporuk's demonstration (Ref. 6) that for a certain function (actually a sequence of functions) $C_1(f)$ grows as fast as $N^2/\log N$, N being the number of variables on which f depends.

Given a Boolean function f of N variables $x_1, \cdots, x_N$, let

$$f^{x_{i_1}, \cdots, x_{i_{N-m}}}_{a_1, \cdots, a_{N-m}} \Big|_{x_{j_1}, \cdots, x_{j_m}}$$

denote the function of $m \leqq N$ variables derived from f by setting x_{i_K} to the constant a_K. The number of distinct such functions is bounded by 2^{2^m} and 2^{N-m}.

THEOREM. *Suppose f is a Boolean function dependent on N variables, N being divisible by m. If the variables can be partitioned into N/m blocks B_i containing m elements each, in such a way that there are F distinct functions*

$$f^{x_j \notin B_i}_{a_j} \Big|_{x_j \in B_i}$$

for each i, then

$$C_1(f) \gtrsim \frac{\rho}{3(r-1)} (N/m) \log_2 F$$

where $r = \max r_i$.

Proof.

(i) Adding functional elements to the basis Ω cannot increase $C_1(f)$. The element we shall add has three inputs, x, η, and γ, and computes the function $f(x, \eta, \gamma) = \eta x \oplus \gamma$, $\oplus$ denoting EXCLUSIVE OR. Let P_i for this element be 2ρ so that $P_i/(k_i - 1) = \rho$ and this parameter is not lowered for Ω', the enlarged basis. Then $C_1(f) \geqq C_1'(f)$.

(ii) Let β be an optimal straight-line algorithm over Ω', with fan-out one, which computes f. Let t_i be the number of inputs of variables from block B_i and $t = \Sigma t_i$, the total number of inputs. By the linear inequality of Lemma 2,

$$C_1'(f) \geqq \rho(t-1) \simeq \rho t$$

(iii) If i_0 is the index for which

$$t_{i_0} = \min_i t_i$$

then $t \geqq (N/m) t_{i_0}$.

(iv) Consider β as computing the function

$$f^{x_j \notin B_{i_0}}_{a_{i_j}} \Big|_{x_j \in B_{i_0}}$$

by setting the $x_j \notin B_{i_0}$ to constants (call them *free constants*). β may be far from optimal for this task, however, and the following operations might improve it: If any subtree of the graph of β has only constant or free constant inputs, replace that tree by a node representing a new free constant. If any subtree has exactly one variable input, then replace it by the element computing $\eta x \oplus \gamma$, with x being the variable input and η, γ free constants. The desirable property of this element is that

$$f^{\eta\gamma}_{a_1 a_2} \Big|_x$$

can be any function of x, depending on the values of a_1 and a_2. Call the algorithm derived from β by the above transformations β_0. β_0 will still compute any function

$$f^{x_j \notin B_{i_0}}_{a_j} \Big|_{x_j \in B_{i_0}}$$

if the proper values of its free constants are given. Also, it still has t_{i_0} variable inputs.

(v) β_0 has no elements without at least one variable input and no chains of elements with only one variable input to the chain. If we overlook the elements with only one variable input, then all other elements have at least two variable inputs and a simple induction shows that t_{i_0} is at least one more than the number of such elements. If a_1 is the number of elements with one variable input, a_2 is the number of elements with at least two variable inputs, and C_0 is the total number of functional elements, then $C_0 = a_1 + a_2$, and from the above $t_{i_0} \geqq a_2 + 1$. Finally, each element with at least two variable inputs and the inputs of $x_j \in B_{i_0}$ can be followed by at most one element with a single variable input and so $a_2 + t_{i_0} \geqq a_1$. Therefore, $C_0 < 3t_{i_0}$.

(vi) By another application of Lemma 2, this time with $P_i = 1$ for all functional elements,

$$C_0 \geqq \frac{F_0 - 1}{r-1} \simeq \frac{F_0}{r-1}$$

where F_0 is the number of free constants in β_0.

(vii) Recalling that β_0 computes at least F distinct functions depending on the choice of values for free constants, $F_0 \geqq \log_2 F$.

Now, putting all of these inequalities together,

$$\begin{aligned} C_1(f) &\geqq C_1'(f) && \text{(i)}\\ &\gtrsim \rho t && \text{(ii)}\\ &\geqq \rho\,(N/m)\,t_{i_0} && \text{(iii)}\\ &\gtrsim \rho\,(N/m)\,(C_0/3) && \text{(v)}\\ &> (\rho/3)\,(N/m)\,(F_0/r-1) && \text{(vi)}\\ &\geqq [\rho/3\,(r-1)]\,(N/m)\log_2 F && \text{(vii)} \end{aligned}$$

As an example of how Neciporuk's test works, we can exhibit Neciporuk's function: Given a positive integer N, let $m = 2 + \log_2 N$ and let X be an $[N/m] \times m$ matrix of independent Boolean variables, x_{ij}. Also let σ be an $[N/m] \times m$ matrix of distinct m-vectors of 0's and 1's, each containing at least three 1's. Then,

$$\mathcal{N}(X) = \sum_{ij} x_{ij} \sum_{\substack{k \\ (k \neq i)}} \prod_{\sigma_{ijt}=1} x_{kt}$$

where $\sum$ means repeated application of "exclusive or" (sum mod 2). The blocks of the partition in Neciporuk's test will be the rows of X. Fixing i, if $a_{h_0 j_0} \neq a'_{h_0 j_0}$ for some $h_0 \neq i$, then

$$\mathcal{N}^{x_{hj},\,h\neq i}_{a_{hj}}\Big|_{x_{i1},\cdots,x_{i,m}} \neq \mathcal{N}^{x_{hj},\,h\neq i}_{a'_{hj}}\Big|_{x_{i1},\cdots,x_{i,m}}$$

since one of them contains the term

$$\prod_{\sigma_{h_0 j_0 t}=1} x_{it}$$

and the other does not. Therefore,

$$C_1(\mathcal{N}) \gtrsim \frac{\rho}{3}\frac{N^2}{\log_2 N}$$

the strongest lower bound possible from Neciporuk's test.

On the other hand the definition of $\mathcal{N}$, above, gives

$$C_1(\mathcal{N}) \lesssim \frac{N^2}{\log_2 N} P_\oplus + \frac{N^2}{2} P_\cdot \simeq \frac{N^2}{2} P_\cdot$$

showing that Neciporuk's test is fairly accurate.

IV. The Marriage Problem and the Traveling Salesman's Problem

These problems are a familiar part of combinatorial theory [see Berge (Ref. 7), Gomory (Ref. 8), Harper–Rota (Ref. 9), Mirsky–Perfect (Ref. 10), and Lin (Ref. 11)]. However, since some variation is possible, let us begin with precise definitions: Let X be an arbitrary real $n \times n$ matrix and

$$m(X) = \max_P X \cdot P$$

where P ranges over all $n \times n$ permutation matrices and

$$X \cdot P = \sum_{i,j} x_{ij} p_{ij}$$

Then find a P such that $X \cdot P = m(X)$. This is generally called the *marriage problem*, but, for reasons which will become apparent, we shall be more interested in the closely related problem of finding a simple algorithm to compute $m(X)$.

The marriage problem is so called because one may imagine a population of n boys and n girls with x_{ij} being the happiness generated if boy i marries girl j. The problem then is to arrange the n marriages so that the total happiness is maximized.

The value of m at X may always be computed by evaluating $X \cdot P$ for each permutation matrix P and comparing. But this requires $n!$ separate operations which quickly surpasses the capabilities of even our largest and fastest machines. There are more efficient algorithms known, however. As we show in *Section V*, the classical alternating paths algorithm requires on the order of n^4 elementary operations. Hopcroft and Karp have in private communications indicated that this figure may be lowered to $n^{2.5}$ if conditional branch operations are allowed.

The *traveling salesman's problem*, with the same notation, is to find a *cyclic* permutation matrix, P, minimizing $X \cdot P$. As before we shall investigate algorithms for computing

$$t(X) = \min_{P \text{ cyclic}} X \cdot P$$

x_{ij} may now be thought of as the cost of traveling from city i to city j and a traveling salesman of course would wish to make a complete tour at minimal total cost. Again the trivial solution would entail evaluating $X \cdot P$ over all $(n-1)!$ cyclic permutation matrices ($n! \sim \sqrt{2\pi n}\,(n/e)^n$ by Sterling's formula). Bellman [see Gomory (Ref. 5)] has given a dynamic program which reduces this to approximately $n^2 \cdot 2^n$ operations, still exponentially increasing. We shall pass over the clever work on partial solutions and solutions for special cases by saying that no one has yet to

our knowledge found an algorithm for computing $t(X)$ which does a number of computations growing like n^k for fixed k.

In any case the traveling salesman's problem is at least as complex (modulo a small constant) as the marriage problem since the latter can be embedded in the former. If all the entries of X are positive, and we may assume this since adding a constant to all entries of X does not significantly alter the problem, then

$$m(X) = -t\left(\begin{array}{c|c} 0 & -X \\ \hline 0 & 0 \end{array}\right)$$

where the argument of t is $2n \times 2n$. Any lower bound we obtain for the complexity of m then gives a lower bound of the same order for the complexity of t.

In order to apply Neciporuk's test to the marriage problem, we restrict the x_{ij} to values 0 and 1 and let $m_0(X) \equiv m(X) \pmod 2$. Clearly, neither of these transformations would significantly increase the complexity of computing any function, and one may argue that in fact the essential complexity of the marriage problem is retained in the Boolean function $m_0(X)$.

Now X is a matrix of $N = n^2$ Boolean variables, so let $m = n$ and $B_K = \{x_{ij} : 1 \leq i, j \leq n,\ i \equiv j + K \pmod n\}$, $K = 0, 1, \cdots, n-1$. The B_K's partition X and any B_K may be mapped onto any other by row and column permutations which do not effect $m(X)$. F is then the number of distinct functions

$$m_0 \begin{matrix} x_{ij} \notin B_0 \\ a_{ij} \end{matrix} \Big|_{x_{ij} \in B_0}$$

where

$$B_0 = \{x_{ii}, i = 1, \cdots, n\}$$

We wish to find a good lower bound on the number of distinct functions

$$m_0 \begin{matrix} x_{ij},\ i \neq j \\ a_{ij} \end{matrix} \Big|_{x_{11}, \cdots, x_{nn}}$$

There are 2^{n^2-n} such functions and we shall show that at least $2^{n^2/4}$ of them are distinct if n is even. This is established by the following claim: If n is even, then the functions

$$m_0 \begin{matrix} x_{ij},\ i \neq j \\ a_{ij} \end{matrix} \Big|_{x_{11}, \cdots, x_{nn}}$$

for which $a_{ij} = 0$ unless $i \leq n/2 < j$ are all distinct.

Proof of claim. Suppose a_{ij} and a'_{ij} $(i \neq j)$ determine two such functions and that for

$$i_0, j_0, i_0 \leq \frac{n}{2} < j_0$$

$$a_{i_0 j_0} = 0$$

and

$$a'_{i_0 j_0} = 1$$

Then,

$$m \begin{matrix} x_{ij},\ i \neq j \\ a_{ij} \end{matrix} \Big|_{x_{11}, \cdots, x_{nn}} = n - 2$$

at the point

$$x_{ii} = \begin{cases} 1, \text{ if } i \neq i_0, j_0 \\ 0, \text{ if } i = i_0 \text{ or } j_0 \end{cases}$$

and

$$m \begin{matrix} x_{ij},\ i \neq j \\ a'_{ij} \end{matrix} \Big|_{x_{11}, \cdots, x_{nn}} = n - 1$$

at the same point. Therefore,

$$m_0 \begin{matrix} x_{ij},\ i \neq j \\ a_{ij} \end{matrix} \Big|_{x_{11}, \cdots, x_{nn}} \neq m_0 \begin{matrix} x_{ij},\ i \neq j \\ a'_{ij} \end{matrix} \Big|_{x_{11}, \cdots, x_{nn}}$$

Thus, we have:

Theorem. *If X is an $n \times n$ matrix of Boolean variables,*

$$m(X) = \max_P X \cdot P$$

P ranging over all permutation matrices, and $m_0(X) \equiv m(X)$ (mod 2), then

$$C_1(m_0) \gtrsim \frac{\rho\, n^3}{12(r-1)}$$

Since $m_0(X)$ is dependent on all n^2 variables of X, Lemma 2 shows that $C_s(m_0) \geq \rho(n^2 - 1)$. Thus, the Neciporuk test provides a distinct improvement on this bound when $s = 1$. Lemma 1 can be used with either bound to $C_1(m_0)$ to lower bound the computation time $D(m_0)$. The bound provided by Lemma 2 shows that $D(m_0)$ must grow as $2 \log_r n$ while that of the theorem shows that $D(m_0)$ must grow as $3 \log_r n$, which is a small improvement.

To date we have been unsuccessful in generating upper bounds to $C_1(m_0)$ which are algebraic in n or upper bounds to $D_1(m_0)$, which grow less rapidly than n^2. We now state a straight-line algorithm of fan-out $s = n + 1$

which implements the "alternating path" solution to the marriage problem [Berge (Ref. 7)]. This algorithm has fan-in of $r = 2$ and uses the primitive operations of AND, OR, EXCLUSIVE OR (modulo 2 addition), and NEGATION, denoted $\cdot, +, \oplus, \overline{}$, respectively. The variables of X are denoted by x_{ij}, $1 \leq i, j \leq n$ and the intermediate variables $u_i(r,k)$, $u'_i(r,k)$, $u''_i(r,k)$, $1 \leq i \leq n$, $1 \leq r \leq k \leq n$; $v_j(r,k)$, $v'_j(r,k)$, $v''_j(r,k)$, $1 \leq j \leq n$, $1 \leq r \leq k \leq n$; $\gamma_{ij}(k)$, $1 \leq i, j, k \leq n$, and $\theta_j(k)$, $1 \leq j, k \leq n$ are used in the description of the algorithm. If any of these intermediate variables are used with values for their indices which are outside the stated ranges, they are assumed to have value 0.

The intermediate functions computed by the algorithm follow:

$$u_i(1,k) = \begin{cases} 1, & i = k \\ 0, & i \neq k \end{cases}$$

$$v_j(r,k) = \sum_{i=1}^{n} x_{ij} \cdot (u_i(r,k) + u_i(1,k))$$

$$u_i(r,k) = \sum_{j=1}^{n} \gamma_{ij}(k-1) \cdot v_j(r-1,k), \text{ for } r \geq 2$$

$$\theta_j(k) = v_j(k,k) \cdot \left(\overline{\sum_{i=1}^{n} \gamma_{ij}(k-1)}\right) \cdot \left(\overline{\sum_{t=1}^{j-1} \theta_t}\right)$$

$$v'_j(r,k) = \theta_j(k) \cdot (v_j(r,k) \oplus v_j(r-1,k)) + \sum_{i=1}^{n} \gamma_{ij}(k-1) \cdot u'_i(r+1,k)$$

$$u'_i(r,k) = \left(\sum_{j=1}^{n} v'_j(r,k) \cdot x_{ij}\right) \cdot u_i(r,k) \cdot \left(\overline{\sum_{t=1}^{i-1} u'_t(r,k)}\right)$$

$$\gamma_{ij}(k) = \sum_{r=1}^{k} u'_i(r,k) \cdot v'_j(r,k) + \left(\gamma_{ij}(k-1) \oplus \sum_{r=1}^{k} u'_i(r+1,k) \cdot v'_j(r,k)\right)$$

$$m_0(X) = \sum_{i,j} \gamma_{ij}(n)$$

where Σ and $\underset{\oplus}{\Sigma}$ denote the OR and EXCLUSIVE OR, respectively, of more than 2 terms. If P_-, $P_\cdot$, P_+, and $P_\oplus$ are the costs of the NEGATION, AND, OR, and EXCLUSIVE OR operations, then the cost of this algorithm is

$$C = \left(\frac{n^3}{2} + \frac{n^2}{2} + 2n\right) P_- + \left(3n^4 + \frac{5n^3}{2} + 8n^2\right) P_\cdot + \left(\frac{7n^4}{2} - n^3 - 3n^2 + n\right) P_+ + \left(\frac{3n^3}{2} + \frac{n^2}{2} - 1\right) P_\oplus$$

Since this algorithm has fan-out of $s = n + 1$, we have

$$C_\infty(m_0) \leq C_{n+1}(m_0) \leq C_1$$

and this bound grows as n^4 for large n.

V. Conclusion

We have distilled on these pages the main thrust and concrete results which grew out of discussions between the two authors. Side issues and philosophy have been avoided even though they were an integral part of the development of our thoughts. We should like to state here, however, our conviction that combinational complexity (particularly with unlimited fan-out) is a fundamental concept in the study of combinatorial optimization problems. Questions such as those at the beginning of *Section I* assume a precise meaning in these terms and can be treated rationally. The old bugaboos about trade-offs between computing time, memory (random access, tape, multiple tape, etc.), and other machine characteristics are resolved. Definitive statements may even be made about machines capable of looping and conditional branch operations. The key to these applications of combinational complexity is the ability of combinational machines (or equivalently, straight-line algorithms) to model the components and operations of all other digital machines. For details the reader is referred to the papers of Savage (Ref. 5) on combinational complexity (also see Ref. 1).

The results of this article are mainly interesting in that they suggest avenues of further research and we should like to point out those which in our opinion are the most promising: (1) To what other "natural" functions can Neciporuk's test be applied? (2) One of the continuing paradoxes of this subject is that according to Lupanov almost all functions of N variables have

$$C_1(f) \simeq \rho \frac{2^N}{\log N}$$

and yet Neciporuk's function N with

$$C_1(N) \gtrsim \rho \frac{N^2}{\log N}$$

is the world's champion among those explicitly given. Can Neciporuk's technique be generalized to give stronger lower bounds, for instance $C_1(f) \geqq N^K$, for all $K \geqq 1$?

Interesting candidates for large complexity are not lacking. Besides the traveling salesman's function, we have the closely related combinatorial coding function [see Harper (Ref. 12)], and many functions from graph theory such as the chromatic number, χ_G. If G is a graph whose incidence matrix is symmetric $n \times n$ matrix of 0's and 1's (so $N = n(n+1)/2$), then χ_G is the minimum number of colors which can be used to color the vertices of G so that no two neighboring vertices have the same color (see Ref. 7). Another candidate which we cannot resist mentioning is the complexity function itself. For any Boolean function f of n variables, there are 2^n points in the domain. If these points are ordered in their natural binary order, say, then any function of n variables is equivalent to a binary sequence of length 2^n. $C_K(f)$ can then be looked upon as a function of $N = 2^n$ variables (f representing a point in the domain). Thus, we can inquire about the complexity of complexity and it seems reasonable to attribute the paradoxes in our theory to the fact that complexity is most likely a very complex function.

References

1. Savage, J. E., "Digital Telemetry and Command: A Collection of Results on Computational Complexity," in *The Deep Space Network*, Space Programs Summary 37-65, Vol. II, pp. 42–47. Jet Propulsion Laboratory, Pasadena, Calif., Sept. 30, 1970.
2. Lupanov, O. B., "On a Method of Machine Synthesis," *Izvestia B.Y.Z., Radiofizika*, Vol. 1, pp. 120–140, 1959.
3. Lupanov, O. B., "On the Difficulty of Realizing Functions of Logical Algebra with Formulas," *Sb. Problemi Kibernetiki, Fitzmatgiz*, Vol. 3, pp. 61–80, 1960.
4. Hodes, L., and Specker, E., "Lengths of Formulas and Elimination of Quantifiers," in *Contributions to Mathematical Logic*, pp. 175–188. Edited by K. Schutte. North Holland, Amsterdam, 1968.
5. Savage, J. E., *Computational Work and Time on Finite Machines*, 1971 (to be published).
6. Neciporuk, E. E., "A Boolean Function," *Soviet Math-7, Doklady 7*, pp. 999–1000, 1966.
7. Berge, C., *The Theory of Graphs and Its Applications*. John Wiley & Sons, Inc., New York, 1964.
8. Gomory, R. E., "The Traveling Salesman Problem," in *Proceedings of the IBM Scientific Computing Symposium on Combinatorial Problems*, pp. 93–121. IBM, White Plains, New York, 1966.
9. Harper, L. H., and Rota, G-C., "Matching Theory, An Introduction," in *Advances in Probability Theory*, Vol. 1, pp. 172–215. Marcel Dekker, New York, 1971.
10. Mirsky, L., and Perfect, H., "Systems of Representatives," *J. Mathematical Analysis and Applications*, Vol. 15, No. 3, pp. 520–568, Sept. 1966.
11. Lin, S., "Computer Solutions of the Traveling Salesman Problem," *Bell System Tech. J.*, Vol. 44, pp. 2245–2269, 1965.
12. Harper, L. H., "The Combinatorial Coding Problem," in *Proceedings of the Second Chapel Hill Conference on Combinatorial Mathematics and Its Applications*, Chapel Hill, North Carolina, pp. 252–260, 1970.

Some Results on the Matrix Multiplication Problem

L. H. Harper
University of California at Riverside
J. E. Savage
Brown University

Three results on the multiplication of two $n \times n$ matrices are presented. They contribute to our understanding of the complexity of matrix multiplication, and so of code decoding, tracking accuracy computation, antenna structural analysis and other DSN computational tasks.

I. Introduction

Recent results (Refs. 1 and 2) have shown that two $n \times n$ matrices can be multiplied with a number of arithmetic operations which grows as n^a, where $a = \log_2 7 \simeq 2.81$. For large n, this represents a significant reduction from the number of operations which are performed when the defining equations for matrix multiplication are used.

In this article we contribute to the matrix multiplication problem in the following ways: (1) conditions are given under which the conventional method for multiplying two matrices is optimal, (2) an n^2 lower bound on the number of arithmetic operations necessary for the multiplication of two $n \times n$ matrices is derived, and (3) a nearly optimum algorithm for the computation of any one (but arbitrary) element of a product for two matrices is presented.

II. Fan-Out 1 Complexity of Matrix Multiplication

In another article in this volume,[1] "straight-line" algorithms are defined. When restricted to arithmetic operations, these algorithms make repeated use of addition, subtraction, multiplication, and division over the reals. Straight-line algorithms have only these operations, and no loops or conditional branches are permitted. An algorithm is said to compute functions $f_1, \cdots, f_L$ if these

[1]Johnson, D., Savage, J., and Welch, L., "Combinational Complexity Measures as a Function of Fan-Out."

functions are computed at some of the steps of the algorithm. An algorithm is also said to have fan-out s if no computation by the algorithm is used externally or internally more than s times. Then, the *s fan-out combinational complexity* of $f_1, \cdots, f_L$, $C_s(f_1, \cdots, f_L)$ is the smallest number of computation steps in any straight-line algorithm of fan-out s which computes $f_1, \cdots, f_L$.

Let $A = \{a_{ij}\}$, $B = \{b_{ij}\}$ be two $n \times n$ matrices over the reals. Let $D = \{d_{ij}\}$ be the result of multiplying A and B. Then $D = AB$ and

$$d_{ij} = \sum_{k=1}^{n} a_{ik} b_{kj}$$

THEOREM. *Let $C_1(D)$ be the 1 fan-out combinational complexity of the n^2 functions of $D = AB$, where A, B are $n \times n$ arbitrary matrices over the reals. Then, $C_1(D) = n^2(2n-1)$.*

Proof. The standard method for computing D uses n^3 multiplications and $n^2(n-1)$ additions so that

$$C_1(D) \leqq n^2(2n-1)$$

Let β be an optimal straight-line algorithm with fan-out 1 which computes D. Then, the computations used to compute any two elements of D must be different since the algorithm uses the result of a computation only once. Thus, the complexity of D is the sum of complexities of the functions d_{ij}, $1 \leqq i, j \leqq n$. But each of these depends on $2n$ variables and it can be shown[2] that any function dependent on N variable requires at least $N-1$ binary computations. Therefore, we have that $C_1(D) \geqq n^2(2n-1)$ which is exactly the upper bound.

Q.E.D.

III. A Lower Bound on the Combinational Complexity of Matrix Multiplication

In this section we develop a lower bound to $C_s(D)$, $s \geqq 2$, by lower bounding the complexity of the trace of D, $\mathrm{tr}(D)$. We observe that

$$\mathrm{tr}(D) = d_{11} + d_{22} + \cdots + d_{nn}$$

and

$$C_s(\mathrm{tr}(D)) \leqq C_s(d_{11}, d_{22}, \cdots, d_{nn}) + C_s(S(x_1, x_L, \cdots, x_n))$$

where $S(x_1, x_2, \cdots, x_n)$ is the sum of $x_1, x_2, \cdots, x_n$. Since $C_s(S(x_1, x_2, \cdots, x_n)) \leqq n-1$, we have

$$C_s(D) \geqq C_s(d_{11}, d_{22}, \cdots, d_{nn}) \geqq C_s(\mathrm{tr}(D)) - (n-1)$$

However, the function $\mathrm{tr}(D)$ depends on the $2n^2$ variable entries of A and B so, $C_s(\mathrm{tr}(D)) \geqq 2n^2 - 1$. We conclude that:

THEOREM. $C_s(D) \geqq 2n^2 - n + 1, \qquad s \geqq 2$

It has been conjectured (Ref. 3) that $C_s(D)$ must grow as n^2. If so, this bound establishes that this rate of growth cannot be improved.

IV. An Algorithm for Computing the Elements of a Matrix Product

Consider the function $f(i, j, A, B) = d_{ij}$ where $D = \{d_{ij}\} = AB$. This function computes an arbitrary element of AB and we shall show that $C_s(f)$, $s \geqq L$, grows as n^2 and that this rate of growth can be achieved.

Without excessive loss of generality, we restrict attention to matrices with binary elements and to addition and multiplication modulo 2. Then the integers i and j in $f(i,j,A,B)$ must be given a binary encoding. It is easily shown that f depends on all $2n^2$ entries in A and B so that, independently, of the encoding for i and j, $C_s(f) \geqq 2n^2 - 1$.

The following algorithm realizes f with $4n^2 - 1$ computations represent i by $(\alpha_1, \alpha_2, \cdots, \alpha_n)$ and j by $(\beta_1, \beta_2, \cdots, \beta_n)$ where

$$\alpha_e = \begin{cases} 1, & e = i \\ 0, & e \neq i \end{cases}$$

$$\beta_e = \begin{cases} 1, & e = j \\ 0, & e \neq j \end{cases}$$

Then,

$$f(i, j, A, B) = \sum_{m=1}^{n} \left(\sum_{e=1}^{n} \alpha_e a_{em} \right) \left(\sum_{e'=1}^{n} \beta_{e'} b_{me'} \right)$$

$$= d_{ij}$$

and this algorithm has $(2n+1)n$ multiplications and $(2n+1)(n-1)$ additions for a total of $4n^2 - 1$ operations.

It is important to note that the function $f(i,j,A,B)$ pro-

[2] See Harper, L. H., and Savage, J. E., "Contributions to a Mathematical Theory of Complexity" (this volume).

duces an arbitrary element of AB. If some particular element of AB, say d_{12}, is to be computed, the representation

$$d_{12} = \sum_{k=1}^{n} a_{1k} b_{k2}$$

can be used to compute it with $2n - 1$ operations. It is the flexibility implicit in the definition of f that causes its complexity to grow as n^2.

V. Conclusion

Several contributions to the matrix multiplication problem have been given. It still remains to show whether Strassen's algorithm which requires $n^{\log_2 7}$ operations can be improved upon or not.

References

1. Strassen, V., "Gaussian Elimination is Not Optimal," *Numer. Math.*, Vol. 13, pp. 354–356, 1969.
2. Hopcroft, J. E., and Kerr, L. R., "On Minimizing the Number of Multiplications Necessary for Matrix Multiplication," *SIAM J. Appl. Math.*, Vol. 20, No. 1, pp. 35–36, Jan. 1971.
3. Fiduccia, C. L., "Fast Matrix Multiplication," in *Proceedings of the Third ACM Symposium on the Theory of Computing*, Shaker Heights, Ill., May 1971.

Tracking and Data Acquisition Elements Research: Low Noise Receivers: Microwave Maser Development

R. Clauss and R. Quinn
Communications Elements Research Section

A traveling-wave maser, tunable from 14.3 to 16.3 GHz, has been completed and is ready for installation on the 64-m antenna at Goldstone Deep Space Communication Complex. The maser can provide more than 30 dB net gain at any frequency within its tuning range; an equivalent input noise temperature of 8.5 K has been measured in the laboratory. The maser is a ruby-loaded comb structure (C-axis orientation 90 deg) which operates in a closed-cycle helium refrigerator. The 8000-G magnetic field required for maser operation is supplied by a superconducting magnet. The entire package weight is 70 kg, and the unit is capable of operation in any position.

I. Introduction

A traveling-wave maser, tunable from 14.3 to 16.3 GHz, has been completed and is ready for installation on the 64-m antenna at Goldstone DSCC. The maser can provide more than 30 dB net gain at any frequency within its tuning range; an equivalent input noise temperature of 8.5 K has been measured in the laboratory. The maser is a ruby-loaded comb structure (C-axis orientation 90 deg) which operates in a closed-cycle helium refrigerator. The 8000-G magnetic field required for maser operation is supplied by a superconducting magnet. The entire package weight is 70 kg, and the unit is capable of operation in any position.

II. Maser/Refrigerator Package

The traveling-wave maser/closed cycle refrigerator (TWM/CCR) package is shown in Fig. 1. The assembly (with the pump package cover removed) is much smaller than TWM/CCR packages built previously by JPL (Refs. 1–3). The size reduction is made possible by the use of a superconducting magnet at the 4.5 K station of the refrigerator (see "Superconducting Magnet for a Ku-Band Maser," by R. Berwin, et al., in this issue). The maser and superconducting magnet are contained within the vacuum housing bottom cover (Fig. 1). The refrigerator, with vacion pump, vapor pressure gauge, and drive

unit showing, is similar to previously used CCRs. The WR 62 signal waveguide input and output connections are located in the upper part of Fig. 1. The overall package height is 87 cm and the package weight is 70 kg.

III. Pump Package

Two klystrons are used to pump the traveling-wave maser in the push-push mode (Ref. 4). Varian type VA 302 and EM 1138 klystrons each supply 100 mW at 37.35 and 26.45 GHz, respectively, for 15.3-GHz signal frequency operation. The two klystrons with heat sinks, isolators, and a power combining network can be seen in Fig. 1. The pump power combiner uses a low-pass and high-pass filter network (diplexer) so that a minimum of power (less than 1 dB) is lost through the path from the klystrons to the maser pump input connection. Each pair of klystrons can be mechanically tuned to cover maser signal frequency changes of 375 MHz. Electronic tuning of the klystrons permits signal frequency changes of 60 MHz. The entire maser tuning range (14.3 to 16.3 GHz) can be used only by changing klystrons. This limitation is shown by the graph in Fig. 2.

IV. Signal and Pump Waveguides

Input and output signal waveguides (WR 62) are made of 0.064-cm stainless steel. The WR 28 pump waveguide is 0.025-cm stainless steel. All waveguides are electroplated full length on the inside with 0.00013-cm-thick copper. This combination of stainless steel and copper provides low microwave loss and adequate thermal isolation. The input waveguide is thermally connected to the first stage of refrigeration at a distance of 10 cm from the ambient input flange. Cooling the waveguide reduces noise caused by resistive loss.

Mica vacuum windows manufactured by Airtron (Part #110728) provide hard vacuum seals for the waveguides at the CCR top flange. The low window insertion loss (0.012 dB at 15 GHz) contributes less than 1 deg equivalent input noise to the maser.

Transistions from WR 62 waveguide to 0.218-cm-diam coaxial line are mounted at the 4.5-K station. The maser signal input and output transmission lines are coaxial at 4.5 K.

V. Maser Slow-wave Structure and Loading

Figure 3 shows the maser structure on the 4.5-K station of the CCR prior to installation of the superconducting magnet. Alumina strips within the maser are used as dielectric waveguides to transfer pump energy from the pump waveguide at the 4.5-K station to the active maser material.

The maser structure contains two 7.5-cm-long comb type slow-wave structures. Each comb is loaded with ruby (C-axis orientation 90 deg) on one side and an alumina/ferrite isolator on the other side. Yttrium iron garnet pieces (0.0035 cm $\times$ 0.037 cm $\times$ 0.1 cm) are cemented to an alumina piece to form the ferrite strip which gives a signal frequency reverse loss (through the maser) of more than 130 dB.

The isolator and ruby orientation permits changes in magnet rotation (away from the optimum 90-deg angle) of $\pm$0.1 rad (5.7 deg). This insensitivity to orientation allows assembly of the maser and magnet without a need for magnet rotation when the assembly is cold and operating. Ordinary assembly tolerances provide adequate alignment.

The forward loss and slowing characteristics of the TWM are shown in Fig. 4.

VI. Performance

A 47-dB net gain, with 17-MHz instantaneous 3-dB bandwidth, was measured at 15.3 GHz. Other measured gain data between 15.25 and 15.64 GHz are shown on Fig. 5. The measurements covered a range which is limited by the mechanical tuning range of the VA 302 pump klystron.

The measured inversion ratio, together with ruby absorption and forward loss data, have been used to calculate the gain and noise temperature available across the maser tuning range. These predicted performance curves are shown in Fig. 5. Noise caused by losses in the vacuum window, waveguide and coaxial transmission line components are included in the predicted equivalent input noise temperature. A measured value of 8.5 K (using a liquid nitrogen cooled load) agrees well with the predicted 8.6 K temperature at 15.3 GHz.

An overall system temperature measurement, using a copper waveguide horn, also demonstrated very low noise capability. The horn was terminated, alternately, by the "cold" sky or by an ambient temperature piece of microwave absorber. The sky was clear; air temperature was 30°C and relative humidity 46%. The total system temperature measured 18.4 K. The receiver following the maser contributed 0.1 K. The system was sufficiently stable to resolve changes in system temperature of 0.1 K.

References

1. Clauss, R. C., and Quinn, R. B., "Low Noise Receivers: Microwave Maser Development," in *The Deep Space Network*, Space Programs Summary 37-61, Vol. II, pp. 86–89, Jet Propulsion Laboratory, Pasadena, Calif., January 31, 1970.
2. Clauss, R. C., and Quinn, R. B., "Low Noise Receivers: Microwave Maser Development," in *The Deep Space Network*, Space Programs Summary 37-58, Vol. II, pp. 50–52, Jet Propulsion Laboratory, Pasadena, Calif., July 31, 1969.
3. Petty, S. M., and Clauss, R. C., "Low Noise Receivers: Microwave Maser Development," in *The Deep Space Network*, Space Programs Summary 37-42, Vol. III, pp. 42–46, Jet Propulsion Laboratory, Pasadena, Calif., Nov. 1966.
4. Clauss, R., "RF Techniques Research: System Studies for Frequencies above S-band for Space Communications," in *Supporting Research and Advanced Development*, SPS 37-61, Vol. III, pp. 90–93, JPL, Pasadena, Calif., Feb. 1970.

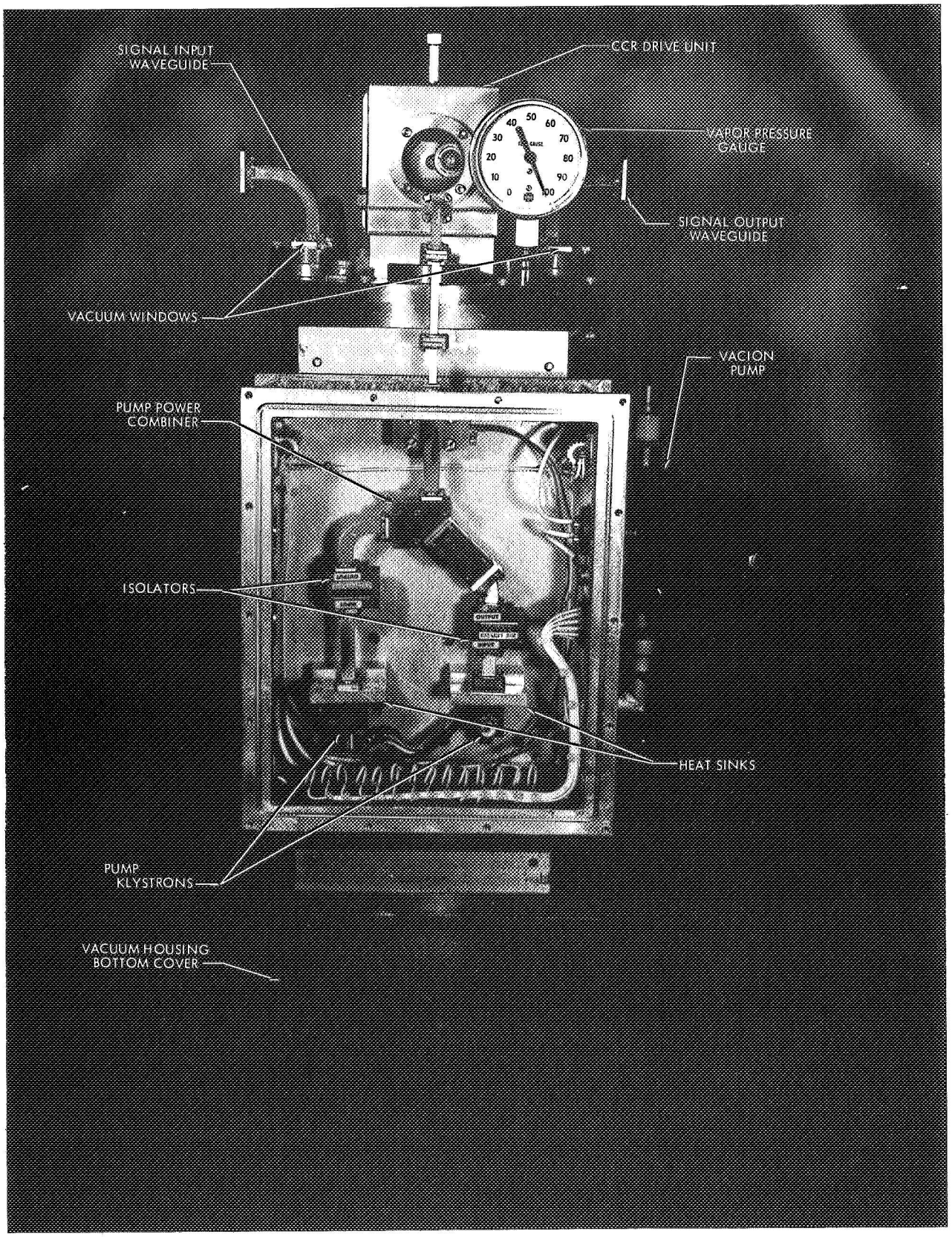

Fig. 1. 15.3-GHz TWM/CCR package

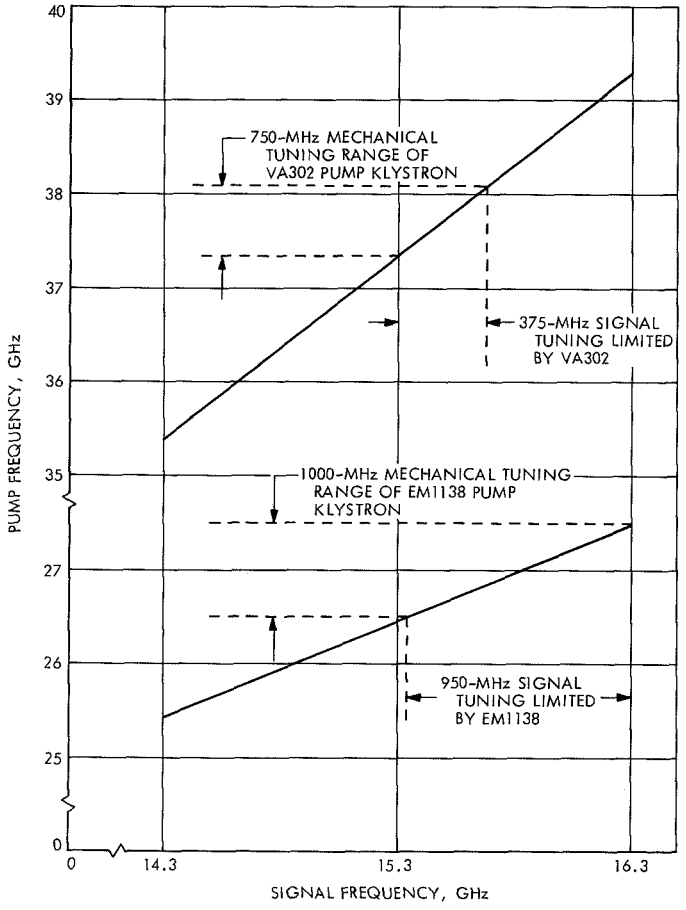

Fig. 2. Signal and pump frequency tuning

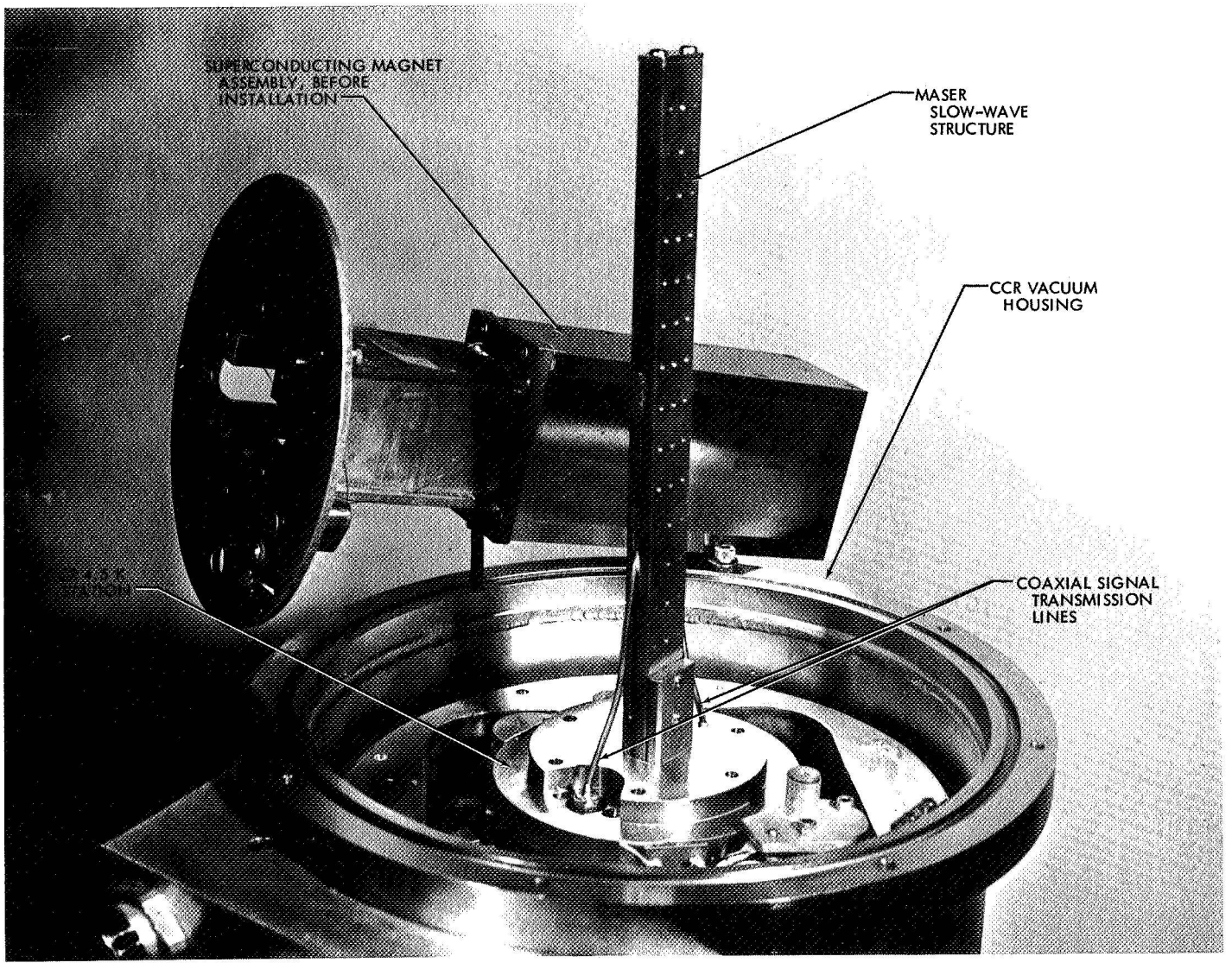

Fig. 3. 15.3-GHz TWM structure

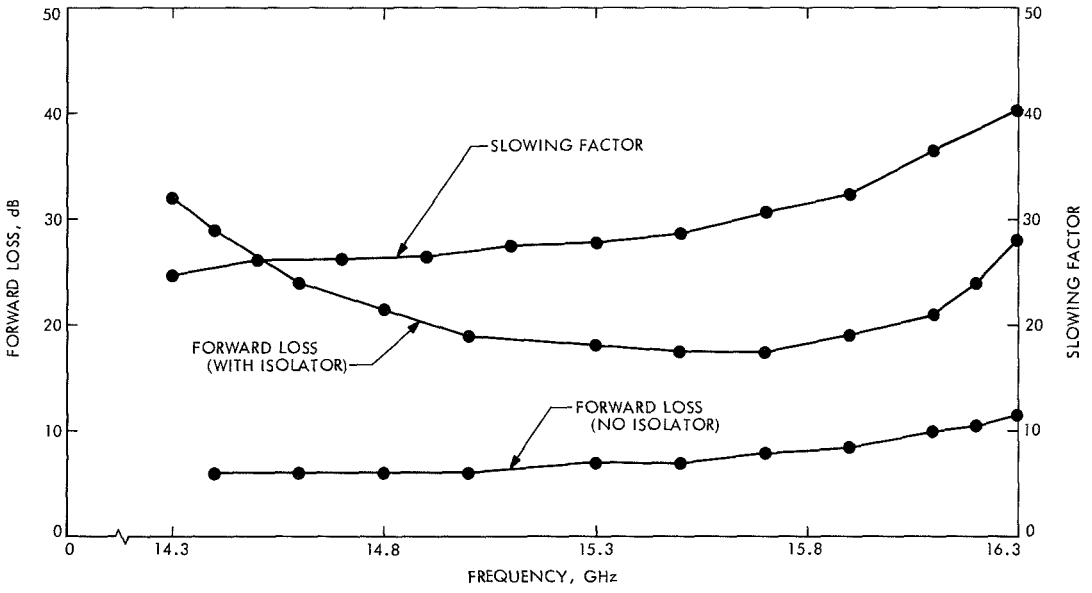

Fig. 4. Slow-wave structure characteristics

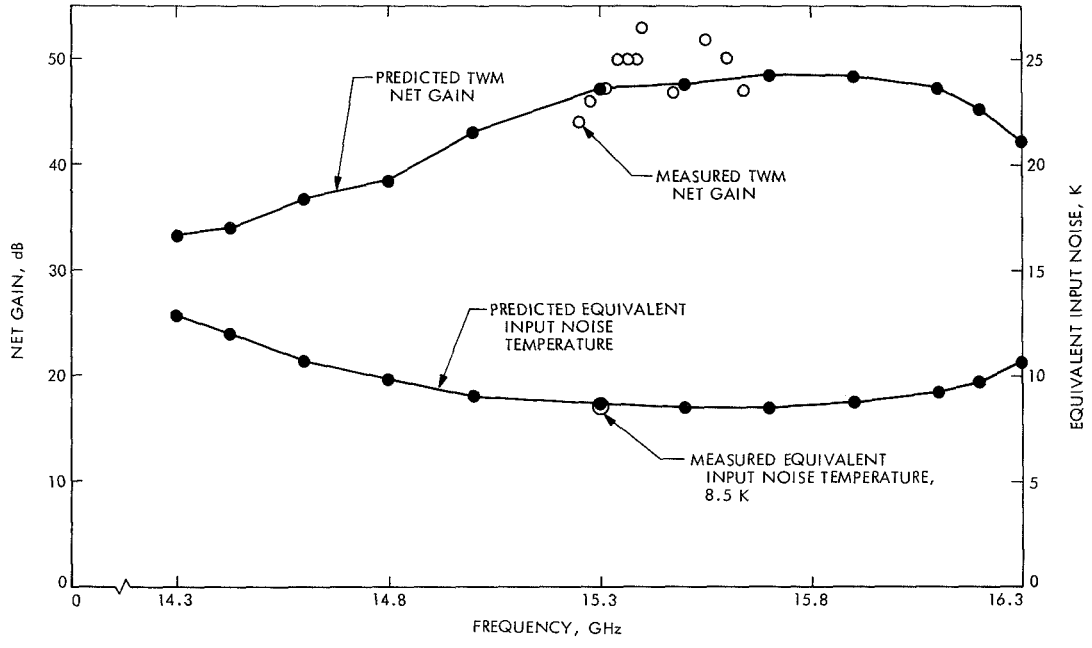

Fig. 5. TWM performance

Superconducting Magnet for a Ku-Band Maser

R. Berwin, E. Wiebe, and P. Dachel
Communications Elements Research Section

A superconducting magnet to provide a uniform magnetic field of up to 8000 G in a 1.14-cm gap for the 15.3-GHz (Ku band) traveling wave maser is described. The magnet operates in a persistent mode in the vacuum environment of a closed-cycle helium refrigerator (4.5 K). The features of a superconducting switch, which has both leads connected to 4.5 K heat stations and thereby does not receive heat generated by the magnet charging leads, is described.

I. Introduction

This paper reports on the development of a superconducting magnet which provides the magnetic field for a Ku-band traveling wave maser. The advantages of using superconducting magnets to assure high phase and gain stability for traveling wave masers are listed, and the configuration of the magnet is described.

II. Discussion

The Ku-band traveling wave maser operates at frequencies between 14.3 and 16.3 GHz.[1] The required operating magnetic field for this maser must be continuously adjustable from 7000 to 8000 G. Present masers in the DSN use permanent magnets to provide 2500 G for S-band and 5000 G for X-band and these magnets weigh 90 kg, or more. In order to increase the magnetic field to 7500 G, while maintaining the spatial uniformity and large gap necessary to enclose the closed-cycle refrigerator shields, the size and weight of the magnet and supporting structure become a limiting design factor. Sensitivity of the permanent magnet to the Earth's magnetic field results in phase variations of the signal through the maser when the antenna is rotated. This sensitivity to external magnetic fields results from the low relative permeability at which the permanent magnet is operating. Additionally, ambient temperature changes produce variations in the permanent magnet field unless temperature compensation is employed. Although good compensation has been obtained, the optimization process is time consuming.

A superconducting magnet has been designed to attain magnetic fields of up to 10,000 G and to provide phase and gain stability of the signal through the maser (of less than ± 5 deg). Due to the high relative permeability of the iron in the superconducting magnet, the iron acts as a shield against external magnetic fields. The superconducting magnet is mounted to the same 4.5 K heat station on the closed-cycle refrigerator (CCR) as is the maser and operates in a persistent mode. The temperature inside the CCR is stable to within 0.001 K and, therefore, temperature compensation of the magnet is unnecessary. Listed below are significant results which have been obtained with the use of superconducting magnets with maser systems:

[1]The Ku band maser is described in "Low Noise Receivers: Microwave Maser Development," by R. Clauss and R. Quinn in this issue.

(1) Allows higher magnetic fields to be attained for higher frequency masers without a significant increase in superconducting magnet weight or refrigerator cooldown time.

(2) Decreases maser/CCR package weight from 180–220 kg (with external magnet) to 63 kg.

(3) Reduces physical size of maser/CCR package.

(4) Eliminates need for temperature compensation process.

(5) Eliminates need for stable power supplies to control magnet trim current.

(6) Reduces sensitivity of superconducting magnet field to external fields by 2 orders of magnitude.

(7) Enables rigid mechanical coupling between maser structure and magnet.

Achievement of items 4, 5, 6, and 7 are expected to reduce the phase variations as compared to present TWMs by approximately 2 orders of magnitude.

III. Description

Figure 1 shows the Cioffi-type (Ref. 1) superconducting magnet used in the Ku-band maser. Figure 1a is a cross-sectional view looking into the magnet gap. The 9 "U" shields are each made of a 50-mm-wide 0.27-mm-thick tape of copper-plated Nb_3Sn material. The Nb_3Sn thickness is 0.03 mm and the copper clad thickness is 0.12 mm on each side. The magnet is wound with 0.127-mm core NbTi wire, which has a 1.5:1 copper-to-superconductor-area ratio and is coated with 0.025-mm Formvar insulation. The pole pieces and return paths are Hiperco 27 (27% cobalt, 73% iron), machined and annealed to specification.

Figure 2 shows the magnet with the side return paths and superconducting shields removed to reveal the maser amplifier situated in the gap. The base plate is at 4.5 K and includes the superconducting junction A, the wire heat sink B, and the shield C for the superconducting switch which contains a light bulb to provide radiant heat to the switch wire passing through the housing. The other wire heat sink D is another 4.5-K heat station which is connected to the base plate with a stainless steel tube.

A. Superconducting Switch Design

Figure 3 shows a schematic of the superconducting switch and magnet coil located in the vacuum of the CCR. The switch consists of a NbTi superconducting wire shunt which passes through a radiation shield containing an incandescent light bulb which provides radiant heat to operate the switch.

When it is desired to change the magnetic field, the light bulb is turned on and the heat radiation drives the switch wire normal. During this time the current in the magnet, which is still superconducting, can be changed by means of an external power supply. As long as there is a changing current dI/dt in the magnet greater than a certain minimum threshold, the light bulb may be turned off and the induced voltage (approximately 2 mV minimum) across the magnet will keep the switch wire normal. When the current in the magnet reaches a stabilized level, the switch wire will become superconducting and the magnet current will operate in a persistent mode, at which time the external power supply can be turned off.

The superconducting switch operates in a vacuum environment with radiant heat to initiate it, and is thermally isolated from ambient loads by two 4.5-K heat stations (Fig. 3). These two heat stations provide electrical isolation between the parallel ends of the magnet leads and switch wire.

In addition, they act as heat sinks for power which is conducted from the switch wire and from the external power leads. The switch wire, where it is heat sunk to the No. 2 4.5-K heat station, (Fig. 2) has about 12-mm bared wire and by varying the length of the bared wire, the wattage to the bulb necessary to create a normal switch wire is varied. There is a compromise, however; the shorter the exposed or bared switch wire, the higher the bulb wattage required to normalize the wire. With 12 mm exposed, the voltage on the bulb is approximately 16 V ($\sim$ 0.6 W power) and the switch operates in less than a second.

B. Other Magnet Considerations

With a persistent-current superconducting magnet it is necessary to have a junction where the winding ends are joined so that the resistance is zero below the critical temperature and at a current necessary to operate the magnet. Many different types of junctions were investigated. The most successful joint was made by stripping the copper cladding off the wire and winding the exposed superconductor into a filament. This filament was then compressed into a matrix of copper with 12 mm of superconducting wire extending through the matrix. The wire

that extended through was welded in a helium gas atmosphere. This type of joint has passed a persistent current of 20 A for 3 wk without any noticeable degradation in magnetic field.

IV. Results

Two magnets were developed for the Ku-band maser: one with a 15.2-mm gap and one with a 11.4-mm gap. These two gaps were obtained with different length pole pieces, and the dimensions of the return paths are the same.

Figure 4 shows a measure of successive charging time for the 11.4-mm gap magnet, obtained in 1.5-A steps. For example, for the first step, the current through the shunt was set at 1.5 A while the magnet was in a persistent mode. The bulb was activated, driving the switch normal, and the voltage across the switch was monitored. The time for the magnet to charge is defined as the time from when the superconducting switch went normal until the switch went superconducting (i.e., in a persistent mode). This time is a sensitive measure of the inductance of the magnet and, therefore, of the permeability of the iron. At approximately 8000 ampere-turns the magnetic material (Hiperco 27) begins to saturate. Below 2000 ampere-turns, the permeability has not yet reached its maximum value.

Figure 5 shows the magnetic field versus ampere-turns for the 15.2-mm-gap magnet. At approximately 11,000 ampere-turns, the effective permeability of the magnet is decreasing due to saturation of the Hiperco 27. Correlation of the saturation region between Figs. 4 and 5 can be seen by multiplying the ampere-turns of Fig. 5 by the ratio of the two magnet gaps ($1.14/1.52 = 0.75$). Thus, 11,000 ampere-turns on the 15.2-mm-gap magnet corresponds with 8500 ampere-turns on the 11.4-mm-gap magnet, and it can be seen from Figs. 4 and 5 that the agreement on the saturation regions is good.

V. Conclusions

The use of superconducting magnets in place of external permanent magnets in maser/CCR systems results in: (1) reduced package size, (2) reduced package weight (⅓ of original weight at Ku-band), and (3) improved phase and gain stability. This type of magnet is especially desirable for masers above X-band where the size and weight of permanent magnets become extreme. After field evaluation of the superconducting magnet in the Ku-band maser, the design will be adapted for use in S- and X-band maser/CCR systems.

Reference

1. Cioffi, P. P., "Approach to the Ideal Magnetic Circuit Concept through Superconductivity," *J. Appl. Phys.*, Vol. 33, No. 1, March, 1962.

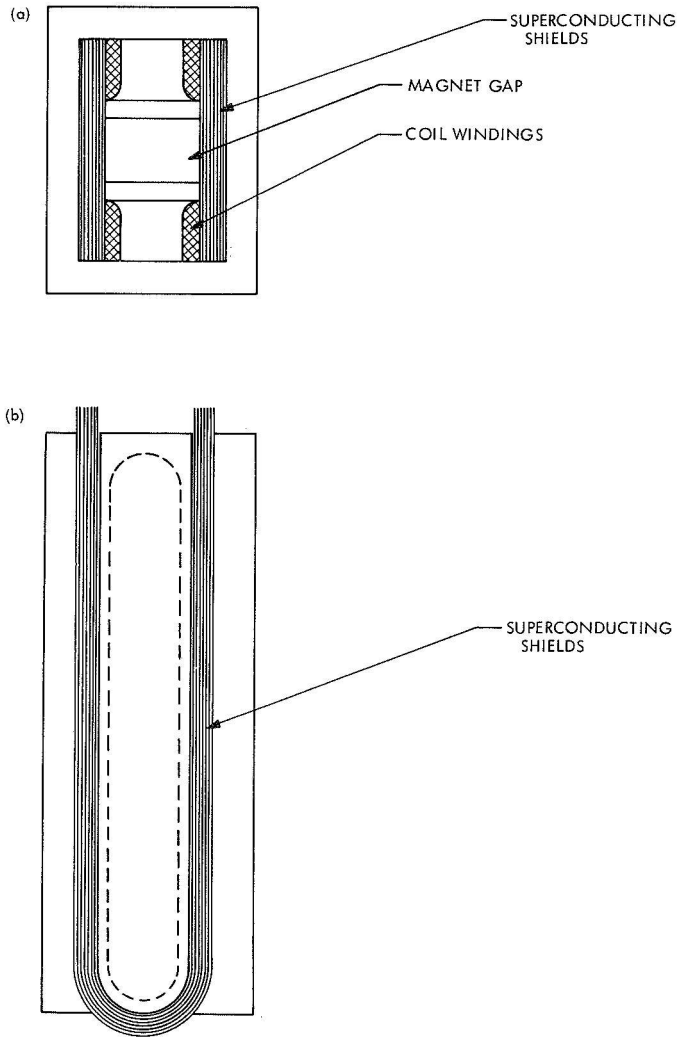

Fig. 1. Cross-sectional and side view of Cioffi-design superconducting magnet

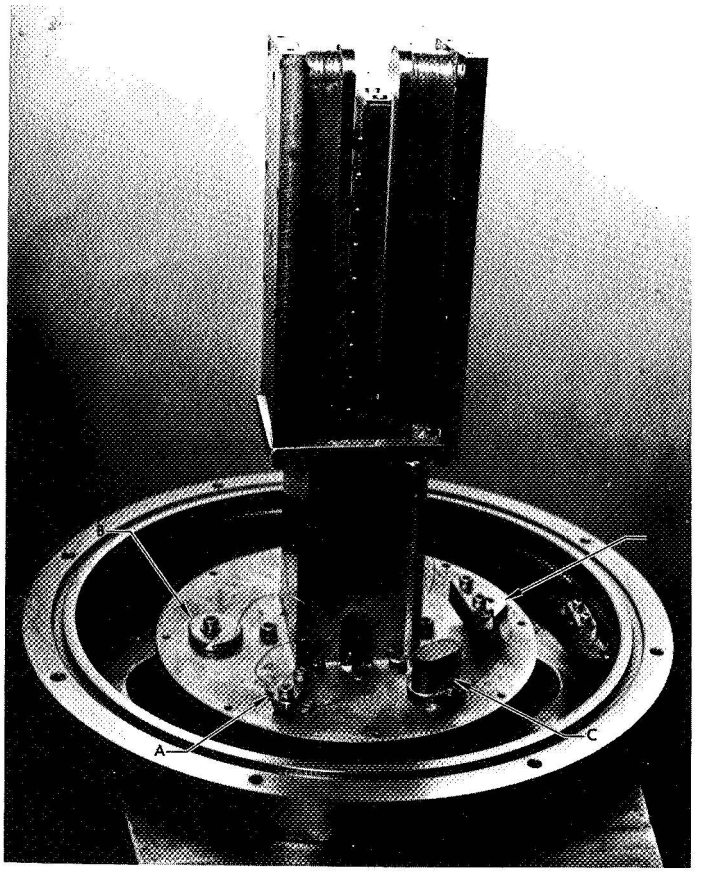

Fig. 2. Superconducting magnet with side return paths and shields removed to show Ku band maser amplifier in gap

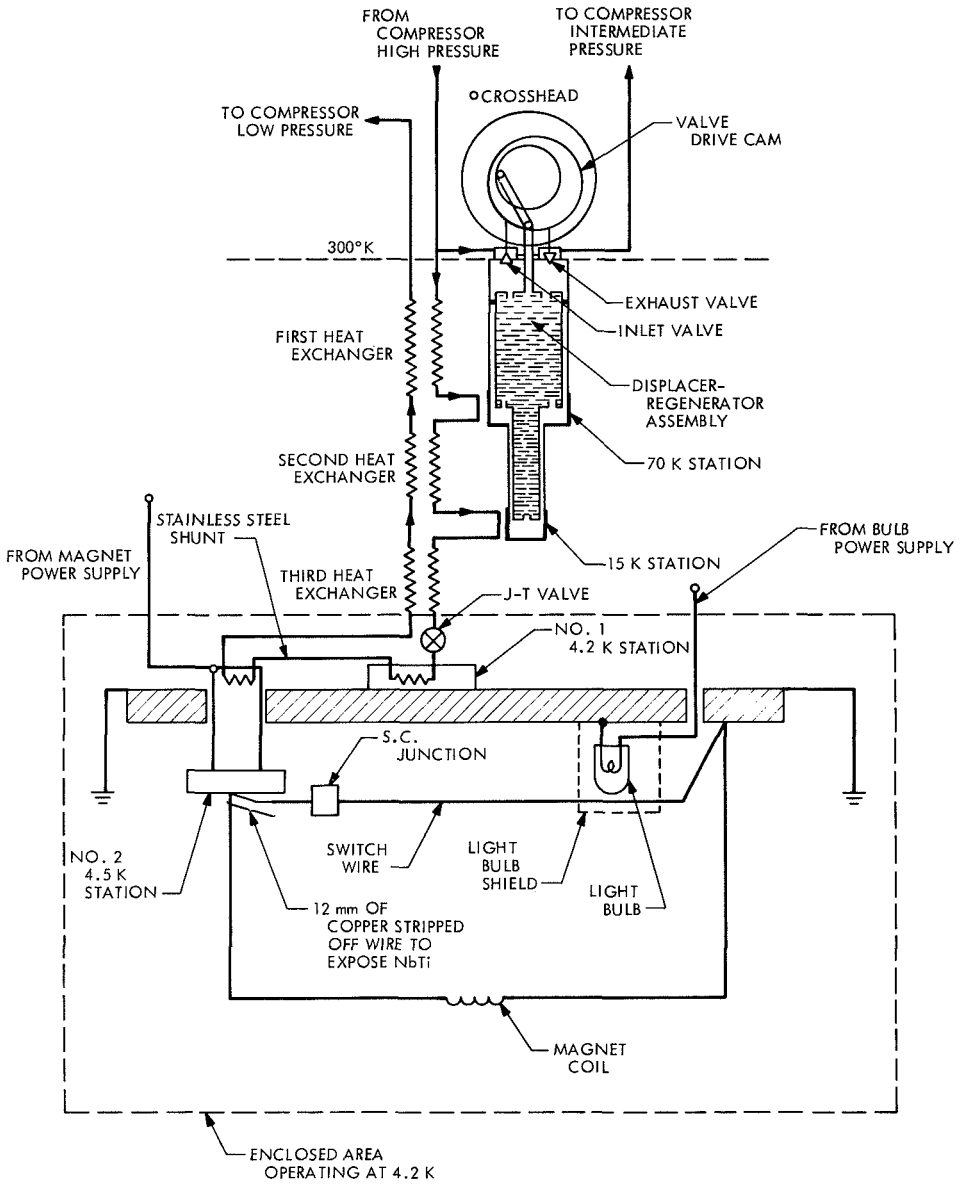

Fig. 3. CCR and schematic of superconducting switch

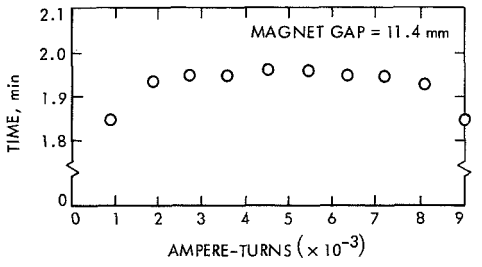

Fig. 4. Charge time of magnet versus ampere-turns in 900 ampere-turn increments

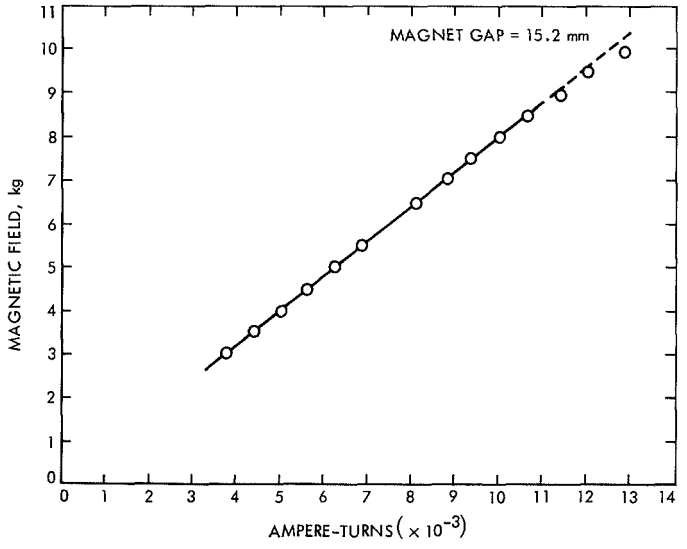

Fig. 5. Magnetic field versus ampere-turns

Antenna Noise Temperature Contributions Due to Ohmic and Leakage Losses of the DSS 14 64-m Antenna Reflector Surface

T. Y. Otoshi
Communications Elements Research Section

This article presents approximate formulas useful for computing antenna noise temperature contributions due to ohmic and leakage losses of a parabolic antenna reflector surface. The total noise temperature contributions due to ohmic and leakage losses for the DSS 14 64-m antenna were calculated to be 0.1, 0.3, and 0.6 K at 2.295, 8.448, and 15.3 GHz, respectively.

I. Introduction

To reduce wind loading on large ground antennas for deep space communications, the reflector surface is usually perforated. A compromise must be made between porosity and acceptable degradation of RF performance because the amount of RF energy that leaks through the reflector surface is a function of porosity. On the outer 47% radius of the 64-m antenna at DSS 14, perforated panels having 51% porosity and 4.76-mm (3/16 in.)-diameter holes are used as the reflective surface material. The panels are painted with white thermal diffusion paint.

Reflector surface losses that increase antenna noise temperature are (1) ohmic losses of the metal and paint used as the reflective surface material, and (2) leakage loss of RF energy passing through the perforated surface. Most of the energy that leaks through the surface is absorbed by the ground environment. To obtain estimates of the noise contributions from these two types of absorptive losses, approximate formulas have been derived. These are presented in the following section.

II. Theoretical Formulas

For a zenith-oriented parabolic antenna with circular symmetry such as that shown in Fig. 1, the antenna noise temperature is

$$T_A = \frac{\int_0^{2\pi}\int_0^{\pi} T_b(\psi,\phi)P(\psi,\phi)\sin\psi d\psi d\phi}{\int_0^{2\pi}\int_0^{\pi} P(\psi,\phi)\sin\psi d\psi d\phi} \quad (1)$$

where

$T_b(\psi,\phi)$ = effective brightness temperature function as defined at the focal point F (Fig. 1), K

$P(\psi,\phi)$ = power per unit solid angle radiated by the feed or apparent feed at focal point F

ψ = polar angle

ϕ = azimuthal angle

For purposes of this study, it is convenient to let Eq. (1) be expressed in terms of contributions from specific sources as

$$T_A = T'_A + (\Delta T_A)_{OL} + (\Delta T_A)_{LL} \tag{2}$$

where

T'_A = total antenna temperature when the reflector surface has no ohmic and leakage losses, K

$(\Delta T_A)_{OL}$ = antenna noise temperature contribution due to reflector surface ohmic losses, K

$(\Delta T_A)_{LL}$ = antenna noise temperature contribution due to reflector surface leakage losses, K

It shall be assumed that the power per unit solid angle as radiated from the focal point is of the form (Ref. 1, Eq. 10, p. 263)

$$P(\psi,\phi) = \frac{1}{2\eta_0}\left[|A_1(\psi)|^2 \sin^2\phi + |B_1(\psi)|^2 \cos^2\phi\right] \tag{3}$$

where

$|A_1(\psi)|$ = E-plane amplitude pattern

$|B_1(\psi)|$ = H-plane amplitude pattern

η_0 = free space wave impedance

After substitutions of Eq. (3) and the appropriate brightness temperature functions into Eq. (1) and integrations with respect to ϕ, it can be shown that

$$(\Delta T_A)_{OL} \simeq \frac{\left(\frac{4R_S}{\eta_0}\right) T_P \int_0^{\psi_E} [1-\alpha(\psi)]\left[p_1(\psi)\sec\frac{\psi}{2} + p_2(\psi)\cos\frac{\psi}{2}\right]\sin\psi d\psi}{\int_0^{\pi} [p_1(\psi)+p_2(\psi)]\sin\psi d\psi} \tag{4}$$

and

$$(\Delta T_A)_{LL} = \frac{\int_{\psi_1}^{\psi_E} T_G(\psi)\,[t_{/\!/}(\psi)\,p_1(\psi) + t_{\perp}(\psi)\,p_2(\psi)]\sin\psi d\psi}{\int_0^{\pi}[p_1(\psi)+p_2(\psi)]\sin\psi d\psi} \tag{5}$$

where $(\Delta T_A)_{OL}$ and $(\Delta T_A)_{LL}$ were defined in Eq. (2) and

$$p_1(\psi) = \left|\frac{A_1(\psi)}{A_1(0)}\right|^2$$

$$p_2(\psi) = \left|\frac{B_1(\psi)}{A_1(0)}\right|^2$$

T_P = physical temperature of the reflector surface, K

R_S = surface resistivity of the reflector surface material, ohms/square. It is a function of frequency and electrical conductivity (Ref. 2).

$\alpha(\psi)$ = porosity of the reflector surface, ratio

$T_G(\psi)$ = effective ground noise temperature function (Ref. 3, Eq. 21, p. 210)

$t_{/\!/}(\psi)$ = leakage power loss ratio for an incident wave polarized with the E-field in the plane of incidence

$t_{\perp}(\psi)$ = leakage power loss ratio for an incident wave polarized with the E-field normal to the plane of incidence

ψ_1, ψ_E = polar angles defining boundaries of the solid and perforated reflector surface regions, respectively (Fig. 1)

For example, $\psi_1 = 34.8°$ and $\psi_E = 61.1°$ for the 64-m antenna and

$\alpha(\psi) = 0$ in the region $0 \leq \psi \leq 34.8°$

$\alpha(\psi) = 0.51$ in the region $34.8° < \psi \leq 61.1°$

Referring to the geometry of Fig. 1, for a parabolic antenna whose surface is perforated periodically with circular holes (Ref. 4),

$$t_{/\!/}(\psi) \approx \left[\frac{8}{3}\frac{d}{\lambda_0}\alpha(\psi)\sec\frac{\psi}{2}\right]^2 \exp\left(-\frac{4\pi t}{1.706d}\right) \tag{6}$$

$$t_{\perp}(\psi) \approx \left[\frac{8}{3}\frac{d}{\lambda_0}\alpha(\psi)\cos\frac{\psi}{2}\right]^2 \exp\left(-\frac{4\pi t}{1.706d}\right) \qquad (7)$$

where d is the hole diameter, λ_0 is the free space wavelength, and t is the thickness of the metallic perforated surface material.

III. Numerical Results

Table 1 is a summary of computations of Eqs. (4) and (5) for the reflector surface of the 64-m antenna at DSS 14. For these computations, it was assumed that $p_1(\psi)$ and $p_2(\psi)$ are identical power patterns. This assumption is valid for the circularly polarized wave case or is approximately valid for the case where a dual-mode horn is the primary Cassegrainian feed operating in a linearly polarized mode. Numerical integrations were performed through the use of a computer program written by T. Cullen. The necessary illumination power pattern data for the 64-m antenna main reflector surface at various microwave frequencies was furnished by the Antenna and Propagation Group of the Communications Elements Research Section.

For the data in Table 1, it was assumed that the reflector surface is aluminum (1.75×10^7 mhos/m electrical conductivity) and is painted with 0.05-mm (0.002-in.)-thick VITA-VAR No. 15966 white thermal diffusion paint. The total electrical conductivity of the painted aluminum surface was reported to be 0.461×10^7 mhos/m (Ref. 5). Porosity, hole size, and plate-thickness data on the perforated surface material are given in Ref. 6. Additional parameters assumed were a reflector surface physical temperature of 283 K; a ground surface air temperature of 10°C (50°F); relative humidity of 60%; and ground electrical dielectric constant and electrical conductivity equal to 3.0 and 0.01 mhos/m, respectively.

Based on the described operating conditions, the total additional noise contributions to antenna temperature due to ohmic and leakage losses of the 64-m reflector surface are computed to be 0.1, 0.3, and 0.6 K at 2.295, 8.448, and 15.3 GHz, respectively. Due to increasing inaccuracies of Eqs. (6) and (7) as d/λ_0 approaches unity, the noise temperature computed for 15.3 GHz could be too low by as much as 0.4 K.

IV. Conclusions

Formulas have been presented for purposes of calculating noise temperature contributions due to RF porosity and metallic surface resistivity. The formulas are approximate but should prove useful for studying the effect of paint on the reflector surface or the effect of using a lossy metal, such as stainless steel, for the reflector surface material.

References

1. Otoshi, T., and Stelzried, C. T., "Antenna Temperature Analysis," in *Supporting Research and Advanced Development*, Space Programs Summary 37-36, Vol. IV, pp. 262–267. Jet Propulsion Laboratory, Pasadena, Calif., Dec. 31, 1965.
2. Ramo, S., and Whinnery, J. R., *Field and Waves in Modern Radio*. John Wiley & Sons, Inc., New York, 1953.
3. Otoshi, T., "Antenna Temperature Analysis," in *Supporting Research and Advanced Development*, Space Programs Summary 37-37, Vol. IV, pp. 207–210. Jet Propulsion Laboratory, Pasadena, Calif., Feb. 28, 1966.
4. Otoshi, T. Y., "A Study of Microwave Transmission Through Perforated Flat Plates," in *The Deep Space Network Progress Report*, Technical Report 32-1526, Vol. II, pp. 80–85. Jet Propulsion Laboratory, Pasadena, Calif., Apr. 15, 1971.

References (contd)

5. Pon, C. Y., "Final Report on Transmission Through Perforated Reflectors and Loss Due to Paint for the AAS/DSIF Program," *Dalmo Victor Report*. Dalmo Victor Company, Belmont, Calif., Dec. 28, 1961.

6. Otoshi, T. Y., and Lyon, R. B., "Improved RF Calibration Techniques: A Study of the RF Properties of the 210-ft-diam Antenna Mesh Material," in *The Deep Space Network*, Space Programs Summary 37-66, Vol. II, pp. 52–57. Jet Propulsion Laboratory, Pasadena, Calif., Nov. 30, 1970.

Table 1. Summary of zenith antenna noise temperature contributions due to ohmic and leakage losses for 64-m antenna

Frequency, GHz	Solid portion,[a] K		Perforated portion,[b] K			Total, K
	Aluminum ohmic loss	Additional paint ohmic loss	Aluminum ohmic loss	Additional paint ohmic loss	Leakage and ground absorption	
2.295	0.033	0.032	0.015	0.014	0.008	0.102
8.448	0.063	0.060	0.029	0.027	0.113	0.292
15.3	0.085	0.080	0.037	0.036	0.374[c]	0.612

[a]Solid portion $0 \leq \psi \leq 34.8°$.

[b]Perforated portion $34.8° < \psi \leq 61.1°$.

[c]Could be factor of 2 too small due to increasing inaccuracy of Eqs. (6) and (7) when hole diameter is not small compared to wavelength.

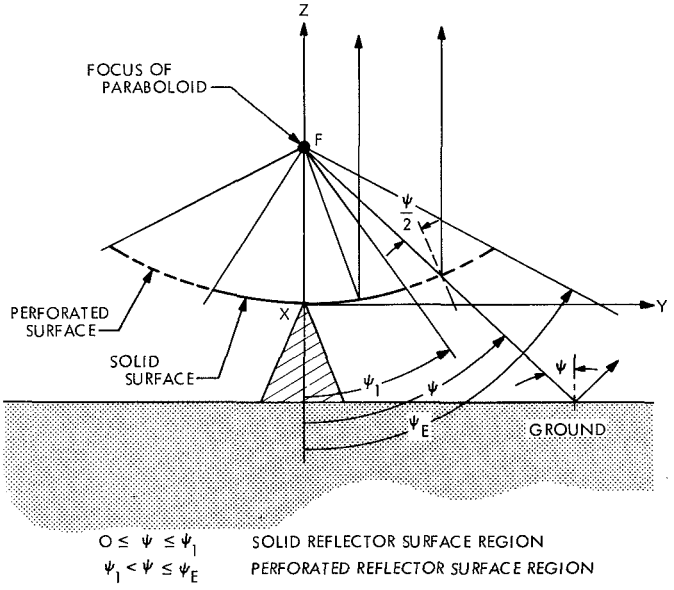

Fig. 1. Two-dimensional geometry of zenith-oriented parabolic antenna with feed (or apparent feed) located at the focal point

DSN Research and Technology Support

E. B. Jackson
R.F. Systems Development Section

The major current activities of the Development Support Group, at both the Venus Deep Space Station and the Microwave Test Facility, are presented and accomplishments and progress for each are described. Activities include pulsar observations, planetary radar (including a general relativity experiment), 100-kW clock synchronization implementation, SDS 930 computer installation into the Mars Deep Space Station, precision antenna gain measurements, very long baseline interferometry, electromagnetic field survey at the Pioneer Deep Space Station, and new phase-lock receiver installation at the Microwave Test Facility.

The Development Support Group, Section 335, is currently engaged in the following activities at DSS 13 and the Microwave Test Facility (MTF) at GDSCC:

I. DSS 13 Activities

A. In Support of Section 331

*1. **Pulsars.*** The twenty pulsars tabulated in Ref. 1 continue to be regularly observed and data on pulse-to-pulse spacing, power density spectra, and pulse arrival time continue to be collected.

*2. **Planetary radar.*** The program continues with the planet Mars being nominally ranged thrice weekly, with an rms range resolution of a few microseconds, and ranging of the planet Venus also. Ranging of the planet Venus is being done in order to obtain data during the period when the signals to and from Venus must pass close by the sun, and thus may be used to further development of the technology of propagation and communications/tracking of signals through the sun's atmosphere. These ranging measurements are being made every third day as schedule time on the 64-m antenna at DSS 14 permits.

*3. **SDS 930 Installation at DSS 14.*** The SDS 930 computer which was installed in the engineering building at the Echo Station was relocated into the alidade control room (the old DSN control room) at the 64-m antenna of DSS 14. Development Support Group personnel effected the relocation, installation, and maintenance required to restore the computer, three magnetic tape units, paper tape reader and punch, and input/output typewriter to service.

B. In Support of Section 332

*1. **100-kW Clock synchronization coolant system.*** The 450-kW heat exchanger and coolant water circulating system were tested for periods of time up to 8 h with power levels reaching 490 kW. The 490-kW test was limited to 4 h due to overload considerations on the DSS 13 electrical power substation. Support was also given to fabrication and installation onto the 9-m antenna of the entire system along with its piping and heat ex-

changers after which full-load testing was again performed. As a result of the first series of tests, the heat exchanger thickness was doubled, and the fan drive motors were increased from 2.24 to 7.46 kW (3 to 10 horsepower) in order to provide lower exit water temperatures as required in the design specifications.

2. Subreflector temperature measurements. In a continuing investigation of the burning of a laminated subreflector on the 26-m antenna last year, the existing subreflector has been stripped of paint and liberally instrumented with thermocouples. After measurements of the subreflector temperature in the unpainted condition while observing the sun, while being radiated with 400-kW RF, and both together, the subreflector was painted in the manner required by JPL Standard 1006D and the temperature measurements were repeated. The data are now in the hands of Section 332 for analysis.

C. In Support of Section 333

1. Precision antenna gain measurement. Data collection by Section 333 personnel with which a precision antenna gain measurement can be made continue, using the Sample and Average (SAVAGE) program. This experiment utilizes the *Apollo* lunar surface experiments package (ALSEP) left on the Moon by *Apollo 12* and the Radio Star Cygnus A as sources of signals for calibration purposes. Data collection was turned over to Development Support Group personnel on August 15, 1971.

2. Weak source observation. Data collection utilizing the noise adding radiometer (NAR) technique continue. Radio sources regularly observed (weekly) by Section 333 personnel include 3C218, 3C270, 3C348, 3C353, Cassiopeia A, the planet Jupiter and the Sun.

D. In Support of Section 335

1. 100-kW Clock synchronization transmitting system. Installation of the coolant circulating system and heat exchangers has been completed, the Cassegrain feed cone has been installed, the high-voltage power supply has been completed and tested, the klystron installed into its mount and tested in conjunction with its control cabinet, and the buffer amplifier has been completed and tested. After complete testing, installation onto the antenna is scheduled to start September 5, 1971.

2. Block IV receiver installation. In preparation for the arrival of the Block IV receiver, twelve semiflexible and one multiconductor cables have been installed between the Operations Building and the 26-m antenna electronics room.

3. Very long baseline interferometry. In cooperation with the National Radio Astronomy Observatory, 37 h were devoted to observation of various radio stars. A total of 144 observations were made, with a new observation being made every 15 min.

II. Microwave Test Facility

A. In Support of Section 335

1. 100-kW Clock synchronization transmitter. The buffer amplifier for the 100-kW clock synchronization transmitter has been completed and tested.

2. Phase-lock receiver installation. A complete phase-lock receiver has been acquired from Section 337 and installed at the MTF. This allows testing and measurements which will be compatible with receivers now installed in the DSIF stations.

3. Electromagnetic field survey at DSS 11. The National Bureau of Standards has developed an electromagnetic field probe using three mutually orthogonal antennas which are electrically short at S-band. Using this probe, a detailed survey of the electromagnetic field strength at DSS 11, using the 20-kW transmitter, has been made and compared with readings made simultaneously using a standard gain horn and power meter detector. The new probe has better response to small diameter "hot spots" while the horn antenna responds properly only to pure plane waves.

Reference

1. Jackson, E. B., "DSN Research and Technology Support," in *The Deep Space Network Progress Report,*" Technical Report 32-1526, Vol. III, p. 158. Jet Propulsion Laboratory, Pasadena, Calif., June 15, 1971.

Load Distribution on the Surface of Paraboloidal Reflector Antennas

M. Kron
DSIF Engineering Section

Wind pressure coefficients have been measured using wind tunnel models of parabolic reflectors. The application of this data and its conversion to useful form for structural deflection analysis within the "NASTRAN" Structural Analysis Computer Program and ultimately Root Mean Square (RMS) program is described in the following article.

I. Introduction

The determination of valid wind pressure distribution data is an important requirement for the design and analysis of large aperture antenna structures. These data can be acquired either from comprehensive full-scale field measurements or from scale-model wind tunnel test studies. The expense of current approaches to field measurement and questions of instrumentation accuracy and interpretations of results tend to make wind tunnel tests appear to be the more practical. Here, the problems of instrumentation and recording are substantially simplified with laboratory procedures and the scaling laws relating model and prototype are well known. Nevertheless, model tests entail questions of uncompensatable differences between wind tunnel and field environments. Therefore, it is necessary to recognize that model testing is an expedient and can reveal the necessity for compromises in the applicability of results.

The following discussion describes a procedure that is used to convert wind tunnel model pressure measurements into surface loading vectors for a prototype reflector of arbitrary size. Because of possible differences in wind tunnel and field environments and also in structural topology, the derived loading vectors are useful primarily for preliminary design and analysis, or to substitute for the absence of more specific data.

II. Data Compilation

Pressures were measured at twenty-two locations on opposite halves of the convex and concave surfaces of the paraboloidal reflector (Fig. 1). The spacing was chosen to roughly represent equal areas per pressure orifice. (Ref. 1).

Table 1 presents tabulations of the resulting pressure coefficients C_p and the difference of the pressure coefficients ΔC_p for corresponding positions on the concave and convex surfaces of the reflector. The tabulations are arranged by position on the surface, while Fig. 2 defines the reflector angular attitudes.

The integral of the pressure coefficient over the reflector paraboloidal surfaces represents the major component of the force or moment on that body. These averaged experimental pressure coefficients were integrated by computer

using mathematical higher order curve fairing between data points.

Data for several surface configurations studied in (Refs. 1–3) using models with direct force–moment measuring devices and the conventional force (axial, normal, side) and moment (pitch, yaw, roll) coefficients were computed for each 5-deg increment of antenna elevation and azimuth orientations (Ref. 4).

III. Nomenclature (Fig. 3)

The position of the dish relative to the wind, is defined by the azimuth and elevation angles. The azimuth angle is the angle between the wind and the centerline of the paraboloidal reflector projected on the ground plane. The elevation angle is the angle between the reflector centerline and the ground plane. When both the azimuth and elevation angles are zero, the concave side of the reflector is directed symmetrically upwind. When the elevation angle is 90 deg, the antenna is pointed at the zenith.

The *body axis system* is a system which always moves with the dish and its axes define the directions of the axial, normal, and side force vectors. The origin is positioned at the reflector vertex and all moments are adjusted to apply at that point.

The forces and moments are in the form of the customary nondimensional aerodynamic coefficients. The force coefficients are defined as

$$\frac{\text{force}}{(\text{dynamic pressure}) \times (\text{reflector frontal area})} \tag{1}$$

and the moment coefficient as

$$\frac{\text{moment}}{(\text{dynamic pressure}) \times (\text{reflector frontal area})} \times \frac{\text{moment}}{(\text{reflector diameter})} \tag{2}$$

The dynamic pressure is defined as

$$\frac{1}{2}\,(\text{ambient static air density}) \times (\text{air velocity})^2$$

The force and moment sign conventions are tabulated as follows (refer to Fig. 3):

Axial force. Along the centerline and positive towards the concave surface at the reflector.

Normal force. Perpendicular to the centerline and positive in a vertical direction upwards when both the azimuth and elevation angles are zero.

Side force. Perpendicular to the centerline and positive to the right (viewed from the convex side) when the azimuth angle is zero and elevation angle is less than 90 deg.

Pitch moment. Positive for a pitch-up moment when azimuth angle is zero.

Yaw moment. Positive for a clockwise moment (viewed from above).

Roll moment. Positive for a clockwise moment when viewed from the convex side of a reflector.

IV. Discussion of Results

The use of an existing computer program used for polar contour plotting affords us the opportunity to input the pressure coefficient differences and allow the program to compute new pressure coefficients at selected points by interpolation from both radial and angular positions of the pressure taps and the topology of the surface panels of a paraboloidal reflector.

A computer program was written to compute the area associated with each node or target point on the reflector surface. In addition the algorithm computes the force from Eq. (1) and normalizes the force at each node according to the equation of the parabola. Components of the force vectors are computed from direction cosines and tabulated for each node, and for each set of input pressure tap data and antenna orientation. The program produces live load data for insertion into the NASTRAN statics program. Normally only loadings for zenith (Z loading) and horizon (Y loading) are used as input to the structural analysis program, since the displacements at any other position can be computed by a linear combination of both loadings. In the case of wind tunnel data, the data available for each position between 0 and 180 deg were treated independently in the NASTRAN program so that correction coefficients can eventually be developed for any other yaw and pitch angle. Since from Ref. 1 the moderately small influence of the ground plane effects can be extended to the pressure coefficients, therefore, force vectors may be computed for any antenna angular attitudes where the spherical sums of the yaw and pitch angles are equal to the pitch angle tested.

Table 2 provides a tabular summation of the forces computed for each case, using the pressure coefficients computed in Ref. 4. Table 3 contains the summation of forces for the same cases as computed using the wind pressure computer program.

Comparing the results of Tables 2 and 3 indicates results of the same order of magnitude. The lack of closer comparison is attributed to the wind tunnel anomalies and the manner in which a balance was used for resolving the force and moments. A correction factor was developed to relate the pressure coefficient readings more closely to the force-moment balance model readings.

Correction factor =

$$\frac{(C^2_{p\,(\text{normal})} + C^2_{p\,(\text{axial})})^{1/2}}{[(\Sigma\,\text{Force}_{(\text{normal/area})})^2 + (\Sigma\,\text{Force}_{(\text{axial/area})})^2]^{1/2}}$$

Table 3 also contains the summation of forces after application of the correction factor.

The output of the program consists of new live loadings of force vectors at surface panel connection points for input to the NASTRAN Structural Program. In all of the above calculations a dynamic pressure of 47.88 N/m² (1 lb/ft²) was used to compute the force vectors, which is equivalent to 32.2-km/h (20 mph) wind velocity. The results of the rms program for each case appear in Table 4, and are best-fit rms with respect to rigid body motion.

The above discussion concludes Phase I of a broad program to investigate methods of attaining realistic wind data for paraboloidal reflectors, and the utilization of these data in present structural design analysis capabilities.

Future phases of the program would include:

(1) Instrumenting an antenna with pressure taps to record pressure coefficients at panel connection points.

(2) Correlating full size model results with wind tunnel data to determine confidence levels for larger antenna designs.

(3) Relating pressure distribution data over reflector surfaces to direct axis forces-moments for use in antenna drive power requirements.

(4) Developing thermal vs wind loading relationships from instrumenting full size models.

(5) Relating various wind yaw angle and pitch angle field measurements to reference data to determine if linearity correction factors can be derived.

References

1. Fox, N. L., *Load Distribution on the Surface of Paraboloidal Reflector Antennas,* CP-4, July 1962 (JPL internal document).
2. Blaylock, R. B., *Aerodynamic Coefficients for a Model of a Paraboloidal Reflector Directional Antenna Proposed for a JPL Advanced Antenna System,* DP-6, May 1, 1964 (JPL internal document).
3. Schlichting, H., *Boundary Layer Theory,* McGraw-Hill, New York, 1960.
4. Levy, R., and Kurtz, D., "Compilation of Wind Tunnel Coefficients for Parabolic Reflectors," in *The Deep Space Network,* Space Programs Summary 37-63, Vol. II, pp. 36–42. Jet Propulsion Laboratory, Pasadena, Calif., May 31, 1970.

Table 1. Pressure coefficients on a thin paraboloidal solid surface

Focal-length-to-diameter ratio, 0.330 solid surface		Diameter Reynolds No., 2.7×10^6 0-deg yaw (azimuth) angle														
		0-deg Pitch angle			60-deg Pitch angle			90-deg Pitch angle			120-deg Pitch angle			180-deg Pitch angle		
R/D[a]	θ,[a] deg	Concave C_p	Convex C_p	ΔC_p	Concave C_p	Convex C_p	ΔC_p	Concave C_p	Convex C_p	ΔC_p	Concave C_p	Convex C_p	ΔC_p	Concave C_p	Convex C_p	ΔC_p
0.468	15	+0.78	−0.55	+1.32	+0.29	−0.58	+0.87	+0.19	−0.36	+0.55	−0.41	−0.43	+0.02	−0.53	+0.42	−0.95
	45	+0.78	−0.52	+1.30	+0.34	−0.63	+0.97	+0.11	−0.14	+0.25	−0.40	−0.42	+0.03	−0.53	+0.21	−0.75
	75	+0.79	−0.55	+1.33	+0.38	−2.00	+2.38	−0.25	−0.27	+0.01	−0.38	−0.37	−0.01	−0.55	+0.08	−0.62
	105	+0.81	−0.58	+1.39	+0.58	−3.76	+4.34	−0.34	−0.20	−0.14	−0.36	−0.10	−0.26	−0.54	+0.07	−0.61
	135	+0.84	−0.60	+1.44	+0.73	−1.60	+2.32	−0.27	+0.29	−0.57	−0.35	+0.46	−0.81	−0.50	+0.06	−0.56
	165	+0.90	−0.63	+1.52	+0.66	−1.14	+1.80	−0.24	+0.75	−0.99	−0.35	+0.93	−1.28	−0.52	+0.07	−0.59
0.408	15	+0.94	−0.54	+1.47	+0.55	−0.60	+1.16	+0.17	−0.36	+0.53	−0.40	−0.49	+0.10	−0.52	+0.60	−1.12
	45	+0.94	−0.55	+1.48	+0.59	−0.66	+1.25	+0.08	−0.22	+0.30	−0.38	−0.54	+0.16	−0.55	+0.47	−1.02
	75	+0.95	−0.56	+1.50	+0.63	−1.39	+2.02	−0.33	−0.36	+0.03	−0.37	−0.44	+0.07	−0.54	+0.37	−0.91
	105	+0.95	−0.59	+1.54	+0.69	−1.84	+2.53	−0.36	−0.28	−0.08	−0.35	−0.05	−0.30	−0.52	+0.33	−0.35
	135	+0.97	−0.63	+1.60	+0.73	−0.73	+1.46	−0.31	+0.15	−0.46	−0.35	+0.54	−0.89	−0.51	+0.31	−0.82
	165	+0.99	−0.66	+1.65	+0.69	−0.51	+1.19	−0.27	+0.50	−0.77	−0.33	+0.93	−1.26	−0.51	+0.32	−0.83
0.326	15	+0.98	−0.55	+1.53	+0.69	−0.64	+1.33	−0.03	−0.34	+0.32	−0.38	−0.53	+0.15	−0.52	+0.77	−1.29
	45	+0.99	−0.53	+1.52	+0.71	−0.69	+1.40	−0.06	−0.30	+0.24	−0.38	−0.61	+0.23	−0.53	+0.72	−1.24
	75	+0.98	−0.57	+1.55	+0.73	−0.97	+1.70	−0.34	−0.40	+0.06	−0.36	−0.48	+0.12	−0.50	+0.63	−1.13
	105	+0.99	−0.60	+1.59	+0.78	−0.88	+1.66	−0.38	−0.31	−0.06	−0.36	−0.07	−0.29	−0.52	+0.58	−1.10
	135	+1.01	−0.64	+1.64	+0.76	−0.63	+1.39	−0.35	−0.01	−0.34	−0.37	+0.44	−0.81	−0.52	+0.58	−1.10
	165	+1.01	−0.66	+1.67	+0.74	−0.43	+1.17	−0.30	+0.60	−0.60	−0.34	+0.80	−1.14	−0.51	+0.56	−1.07
0.206	15	+1.00	−0.54	+1.54	+0.79	−0.73	+1.52	−0.22	−0.34	+0.13	−0.37	−0.61	+0.24	−0.51	+0.84	−1.35
	75	+1.01	−0.56	+1.57	+0.79	−0.83	+1.62	−0.35	−0.42	+0.07	−0.36	−0.48	+0.12	−0.53	+0.82	−1.35
	105	+1.01	−0.60	+1.61	+0.79	−0.73	+1.52	−0.37	−0.34	−0.03	−0.36	−0.18	−0.18	−0.52	+0.79	−1.30
	165	+1.02	−0.63	+1.65	+0.81	−0.29	+1.10	−0.32	+0.00	−0.33	−0.36	+0.59	−0.95	−0.51	+0.82	−1.32

[a]See Fig. 1 for definitions of R/D and θ.

Table 2. Summation of wind forces computed from force-moment balance model

Case No.	Σ Force (side) × 4.448 N	Σ Force (normal) × 4.448 N	Σ Force (axial) × 4.448 N
1	−5.67	−90.79	4315.44
2	−31.21	−221.30	5197.82
3	−19.86	434.10	0.0
4	0	612.84	−1702.34
5	5.67	−85.12	−2726.59

Table 3. Summation of wind forces computed from wind pressure distribution program with corrections

Fig. 2 Case No.	Σ Force (side) × 4.448 N		Σ Force (normal) × 4.448 N		Σ Force (axial) × 4.448 N	
	Computed	Corrected	Computed	Corrected	Computed	Corrected
1	915.82	1027.55	−40.35	−45.27	3851.30	4321.16
2	1064.39	1274.07	−98.39	−117.77	4217.95	5048.87
3	−59.45	−68.72	271.36	−313.69	−259.38	−299.84
4	−135.24	−407.34	249.10	750.29	−593.73	−1788.31
5	−560.71	−604.43	−60.40	−65.11	−2528.74	−2725.98

Table 4. Summation of best-fit rms 26-m az-el wind loading

Case	rms × 2.54 cm
1	0.0057
2	0.0116
3	0.0025
4	0.0094
5	0.0034

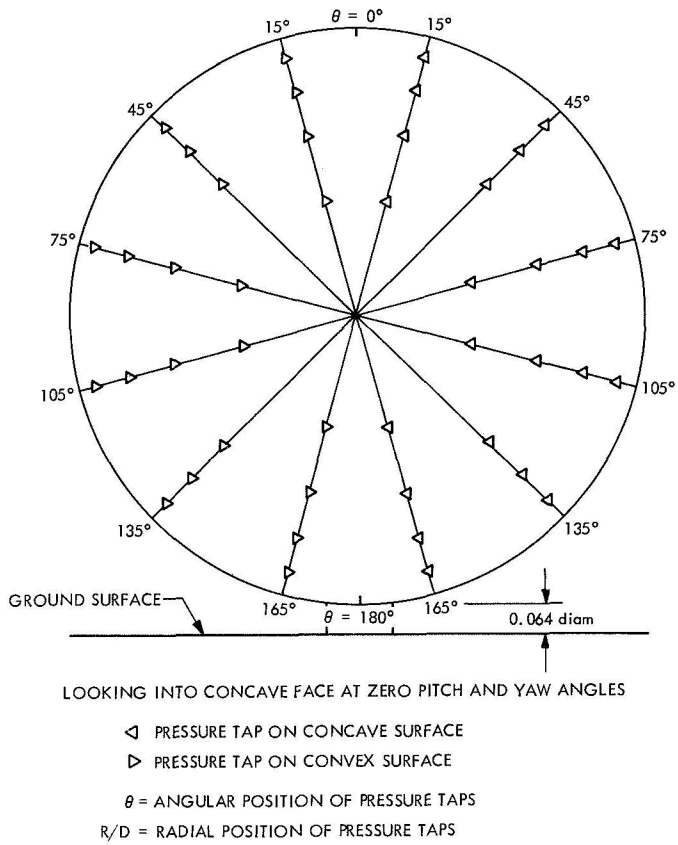

Fig. 1. Pressure tap locations on model

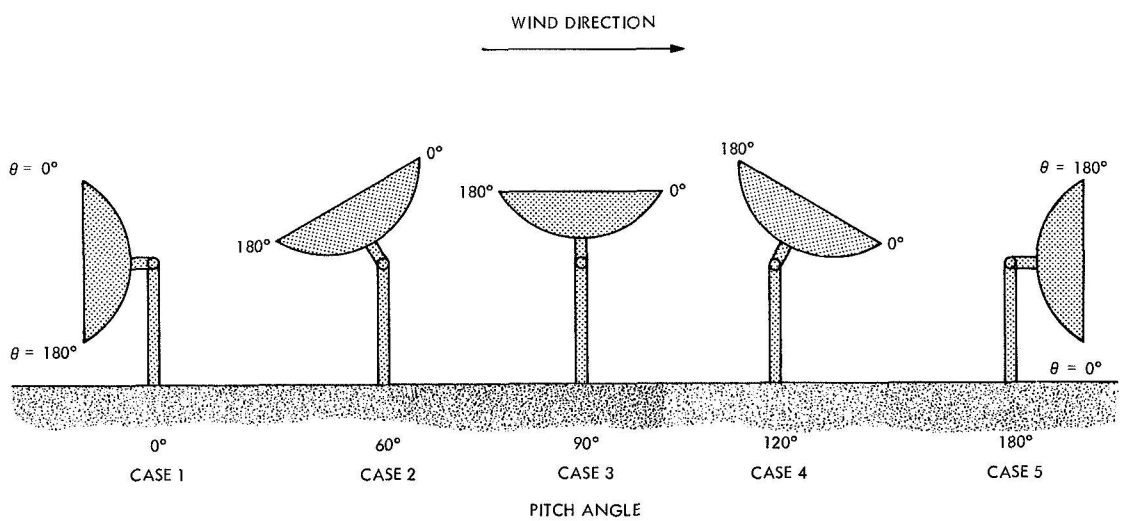

Fig. 2. Paraboloidal reflector antenna model attitudes

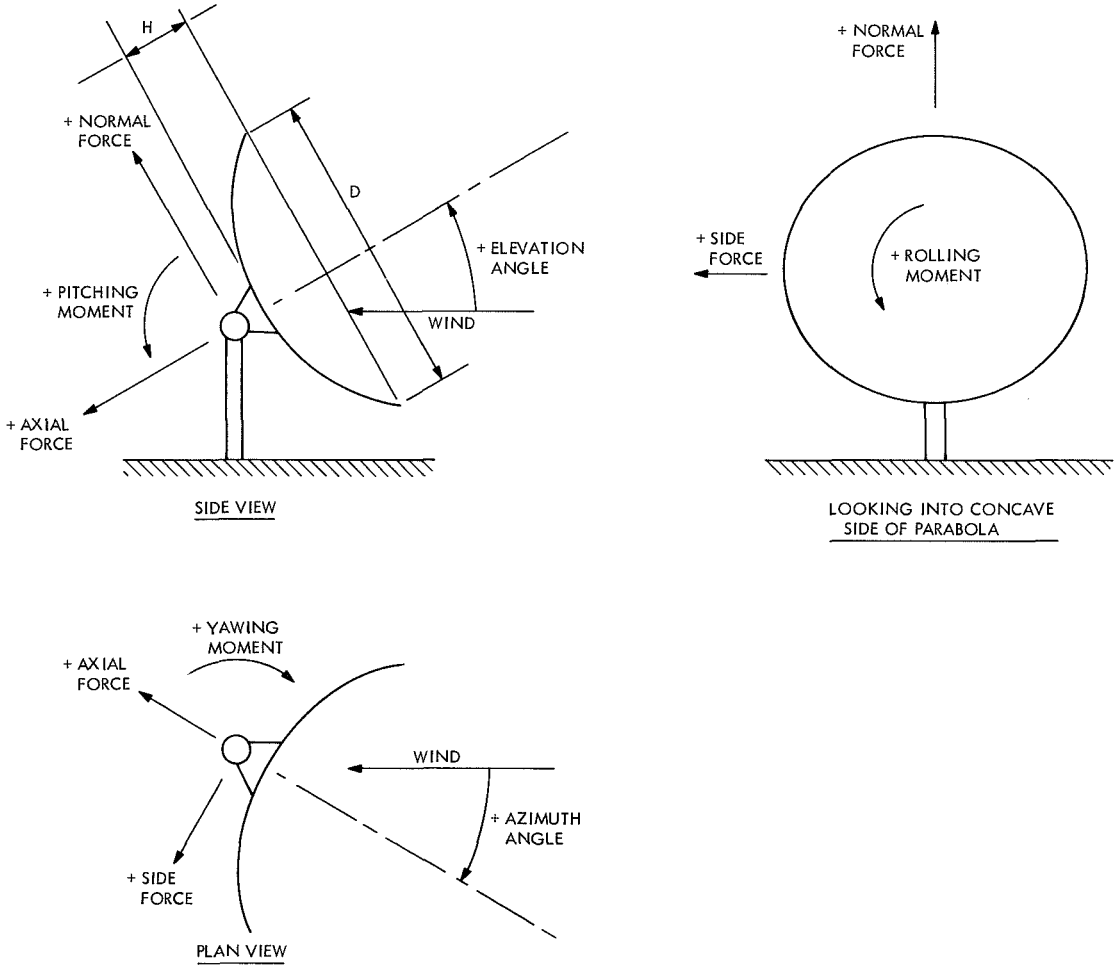

Fig. 3. Nomenclature for force-moment tabular

CPS Sustaining Engineering

C. L. Zandell
SFOF/GCF Development Section

The Sustaining Engineer Program for the Central Processing System (CPS) of the Mark IIIA Space Flight Operations Facility is based on optimizing flight support capabilities. This is being achieved by testing hardware responses during simulated critical conditions, by supporting software development, and by monitoring system performance. This article defines the major hardware/software problem areas and reports the results of studies made to resolve these problem areas.

I. Introduction

The Sustaining Engineer activities are a continuation and refinement of the results of the SFOF Mark IIIA Development. The SFOF Mark IIIA consists of two similar 360/75's (IBM computers), shared interfaces with NASA Communications Network (NASCOM) via the GCF, and extensive user areas (Ref. 1). The required capabilities necessitated the inclusion of many special devices and the use of a special operating system.

Most of the problems with the interaction of special equipment and software were anticipated but solutions were deferred since JPL Operating System (JPLOS) and the Project programs were not solidified. Sustaining Engineer efforts to resolve hardware/software problems have been concentrated in four major areas:

(1) System Recovery Facility studies.

(2) Device switching studies.

(3) Improvement of existing equipment.

(4) System refinement.

In addition, maintenance and operation of the 360/75's are observed to detect possible design and implementation errors.

II. System Recovery Capability Studies

System Recovery Facility (SRF)[1] is a part of JPLOS that attempts to recover from hardware and software errors. With the inclusion of remote devices, it was possible for

[1]System Recovery Facility is IBM's terminology for the software for this function.

a device to lose power while the rest of the system was unaffected. However, the failing device could have interacted with the Central Processing Unit (CPU) if the device was in a signal sequence with the CPU.

Initial studies simulated a power loss in a device and confirmed that the CPU is left in the WAIT state. Investigation revealed that although an interrupt was requested to clear the channel, logic was not ready within the channel to complete the operation. A design change in the logic was installed with IBM concurrence to completely clear the channel once an interrupt has been requested.

Further studies are required to determine if the SRF capabilities can be extended to include more device abnormalities. These activities are currently waiting the resolution of the device switching studies.

III. Device Switching Studies

Since the key to continuous flight support for the Projects is redundant 360/75's, the Mission Support Areas (MSAs) are connected via switches to both 360/75's. The unsynchronized transfer of a device from one 360/75 to the other can cause problems in the same manner as if the device loses power. If the device is in a signal sequence with the CPU and is switched, the CPU ends in the WAIT state.

The design change from the SRF study should also allow the channel and CPU to be cleared after switching. However, the reset initiated by honoring the interrupt request is not complete; some of the latches that should be cleared to fulfill the design of the reset are not affected. An acceptable method of resetting all the latches to clear the channel is being developed.

The incomplete reset of the channel prevents useful testing of the SRF since the problem leaves the hardware in lock, out of software control.

IV. Improvement of Existing Equipment

Existing equipment has been improved by replacing logic elements that experienced an abnormal failure rate and by correcting logic to be consistent with design specifications. A major source of system failures in the 360/75's was the core storage units. The excessive failure rate was confirmed by IBM and treated by replacing most of the logic elements. The failure rate following the replacement is about 30% of the previous rate.

A major Sustaining Engineer effort has been detecting and resolving errors in design implementation. These are usually undetected until software using instruction sequences different from the device diagnostics is executed. Most of these problems have been in the 2909-3 Asynchronous Data Channel (ADC) since it is both a new and special device containing many special subchannels. In addition, the 2909 ADC is being used with standard IBM devices in a manner not previously attempted. The following problems of this nature have been resolved.

(1) *490 input subchannel.* An *end of message* signal was generated on the next to last and last data transfers which allowed only two bytes of the next block to be received.

(2) *490 input subchannel.* The *ready to receive* (RTR) line is propagated by two separate paths but only one was affected by the reset logic. The uncleared RTR would cause an interface control check when clock was received.

(3) *All general purpose input subchannels.* A *no operation* instruction chained to a *store subchannel status* instruction proved to be an illegal sequence not identified in the specification.

V. System Refinement

The operating system, program load, and number of user devices are subject to change but currently there is no measure of system performance to indicate if changes are improving support capabilities. A future Sustaining Engineer function will provide the needed information. All devices, multiple-control unit subchannels, and channels will be monitored to determine usage and conflict as a function of time and machine loading.

VI. Conclusion

The Sustaining Engineer Program is a valuable connection between the development engineer and the system programmer. The foremost concern of the program is implementation of the 360/75's of Mark IIIA consistent with the development design criteria of the Central Processing System (CPS). This has been accomplished to date by

testing hardware responses under critical conditions, by directly supporting software development, and by measuring system performance.

The primary emphasis has been to detect and correct anomalies which could cause interruption to the flight support activity. This effort will continue in support of equipment additions for follow on Mission Support Areas and expanded CPS capability.

Future efforts will concentrate on resolving the problems encountered by unsynchronized device switching and a thorough analysis of equipment performance characteristics. These results will be used to guide configuration and loading modifications in order to optimize system efficiency.

Reference

1. Stiver, R. A., "Mark IIIA IBM 360/75 Computer Configuration," in *The Deep Space Network*, Space Programs Summary 37-66, Vol. II, pp. 71–75. Jet Propulsion Laboratory, Pasadena, Calif., Nov. 30, 1970.

DSS Communications Equipment Subsystem Simulation Center High-Speed Data Assembly

D. S. Bremner
SFOF/GCF Development Section

The 1971–1972 era required expansion of the Simulation Center High-Speed Data Assembly involving extensive modifications. An increase in the number of channels was necessary to provide simultaneous data handling configurations. New data sets were installed to double the data rate as required by the DSN–GCF High-Speed Data System.

I. Introduction

The Mark IIIA requirements for the Simulation Center High-Speed Data Assembly required expansion to three full-duplex data channels as indicated in Ref. 1, which outlines the GCF 1971–1972 requirements. The equipment has been upgraded to accommodate the 4800-bps data rate of the new 203A data set which is used at all stations as mentioned in Refs. 1 and 2 and detailed in Ref. 3. This configuration will support the *Mariner* Mars 1971 and the *Pioneer F* and *G* Projects.

II. Purpose of DCES SIMCEN HSDA

The DSS Communications Equipment Subsystem Simulation Center High-Speed Data Assembly (DCES SIMCEN HSDA) audio interface with the Space Flight Operations Facility (SFOF) is full duplex (FDX) with 4800-bps data rate, which is exactly the same as that used at any Deep Space Station (DSS). The direct current (dc) side of the HSDA is interfaced to the Simulation Center computer. This "long loop" configuration supplies simulation data via the audio interface with the SFOF. The Simulation Center also has a "short loop" dc interface with the six high-speed data channels of the SFOF (Ref. 4).

III. Functional Description

The SIMCEN high-speed data terminal consists of four major full-duplex (FDX) equipment groups as shown in the block diagram of Fig. 1. Each vertical group contains 3 independent full-duplex units which include data sets (DS), error-detection encoders/decoders (EDED), block multiplexers (BMXR), and a BMXR patch and test panel. The horizontal data flow depicts the 3 independent high-speed data channels. Between each group are patch and test jack panels to facilitate rapid electrical substitution by patch cord of any malfunctioning unit.

Figure 1 illustrates the functional block diagram of the SIMCEN HSDA. A brief operational description of this equipment follows. A detailed operational and transmission signal flow description may be found in Ref. 5 and the functional aspect of each piece of equipment is covered in Refs. 3, 4, and 6.

Received data enters the assembly via conditioned telephone lines and is fed to the Western Electric 203A Data Set in the form of a 4-level, amplitude-modulated, suppressed-carrier, vestigial-sideband signal. The data set demodulates, automatically equalizes, and converts analog 4-level (parallel) data to digital (serial) output data.

The decoder has a 1200-bit (one data block) storage register which is used as a delay line to allow a validity check of the data block prior to its output. On the receive side, the BMXR is used only as a 4-port line driver for the received data, feeding it to the data processing equipment through the BMXR patch and test panel.

Data transmission from the data processing equipment through the BMXR patch and test panel and the BMXR does not at present depend on the priority selection capability of the BMXR since only one of the four transmission ports is used at the SIMCEN giving each channel exclusive priority. Block synchronous data transmission is maintained by the automatic insertion of self-generated filler blocks on line between data source transmissions.

The BMXR patch and test panel contains three-channel capability in one unit (Ref. 6). The encoder, as described in Refs. 4 and 5, performs sync word recognition, polynomial division encoding, and error code insertion for each block of data.

The block of serial digital data (4800 bps) is fed to the transmit section of the 203A Data Set where it is converted from serial to parallel and digital to analog by means of a 4-level encoding format. This provides efficient use of available voice channel bandwidth for 4800-bps data rate at a transmission speed of 2400 baud.

IV. Human Engineering Design

Within the physical and electrical constraints of the assembly, the cabinet layout is arranged to provide segregated channel grouping of the EDED–BMXR equipment, which contains the visual status indicators. This may be seen in Fig. 2, where each channel group is outlined for identification. The design also groups all test equipment and patch panels at a convenient operating height.

V. Summary

The DCES SIMCEN HSDA was upgraded to meet the 1971 *Mariner* and *Pioneer F* and *G* Projects as follows:

(1) The data rate was doubled (2400 to 4800 bps) by changing from Western Electric Co. 205B to 203A Data Sets.

(2) Three independent data channels were installed to simultaneously carry FDX simulation data and maintain a hot backup channel.

References

1. McClure, J. P., "Ground Communications Facility Functional Design for 1971–1972," in *The Deep Space Network*, Space Programs Summary 37-66, Vol. II, pp. 99–102. Jet Propulsion Laboratory, Pasadena, Calif., Nov. 30, 1970.
2. Nightingale, D., "High-Speed System Design Mark IIIA," in *The Deep Space Network*, Space Programs Summary 77-66, Vol. II, pp. 103–105. Jet Propulsion Laboratory, Pasadena, Calif., Nov. 30, 1970.
3. Evans, R. H., "GCF High-Speed System Design and Implementation for 1971–1972," in *The Deep Space Network Progress Report*, Technical Report 32-1526, Vol. IV, pp. 133–137. Jet Propulsion Laboratory, Pasadena, Calif., Aug. 15, 1971.
4. Nightingale, D., "High-Speed Data Communications for *Mariner* Mars 1969," in *The Deep Space Network*, Space Programs Summary 37-57, Vol. II, pp. 127–130. Jet Propulsion Laboratory, Pasadena, Calif., May 31, 1969.
5. Yinger, E., "GCF DSS Communications Equipment Subsystem High Speed Data Assembly," in *The Deep Space Network Progress Report*, Technical Report 32-1526, Vol. IV, pp. 138–143. Jet Propulsion Laboratory, Pasadena, Calif., Aug. 15, 1971.
6. Brunder, G. J., "GCF SFOF Communications Terminal Subsystem High-Speed Data Assembly," in *The Deep Space Network Progress Report*, Technical Report 32-1526, Vol. IV, pp. 144–150. Jet Propulsion Laboratory, Pasadena, Calif., Aug. 15, 1971.

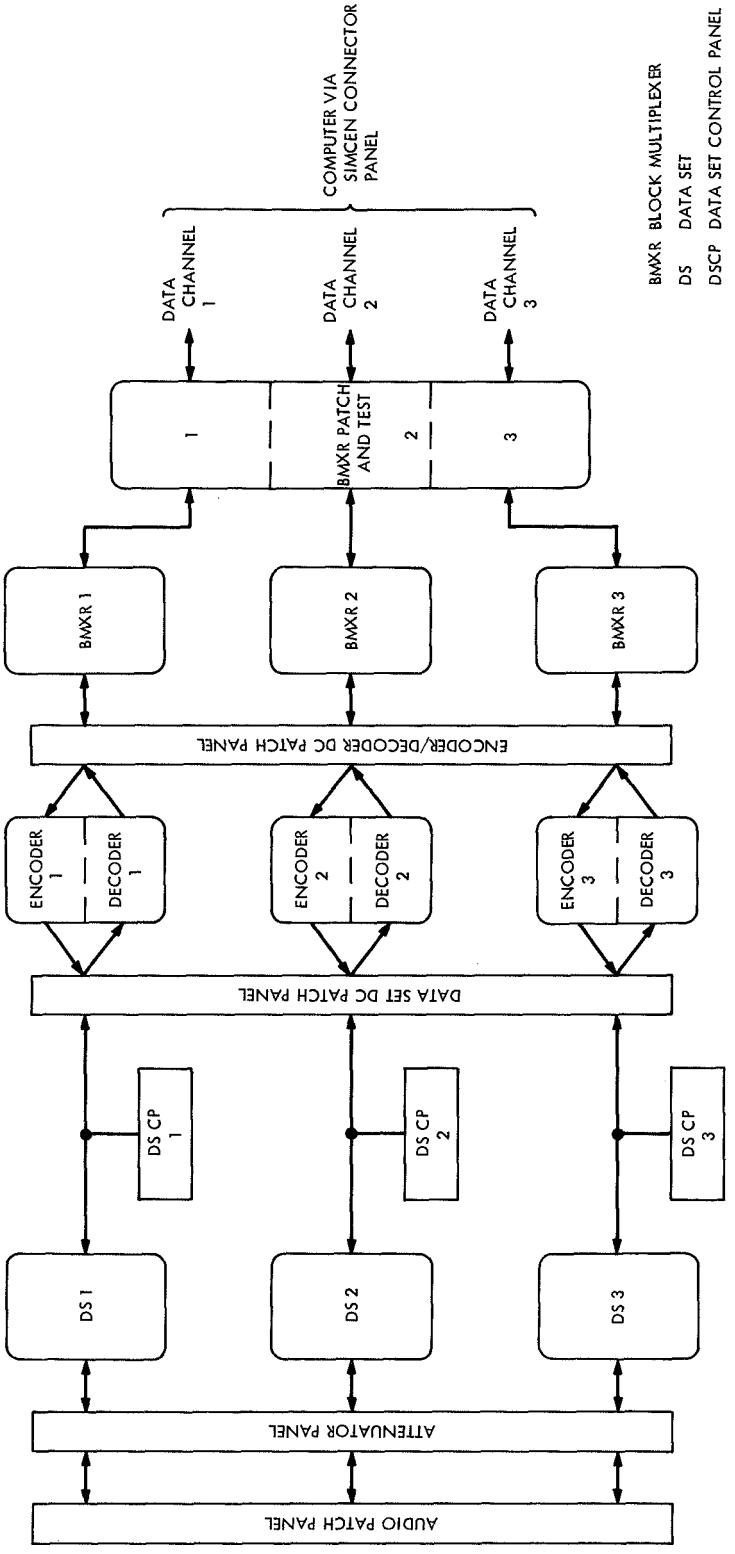

Fig. 1. DCES SIMCEN HSDA block diagram

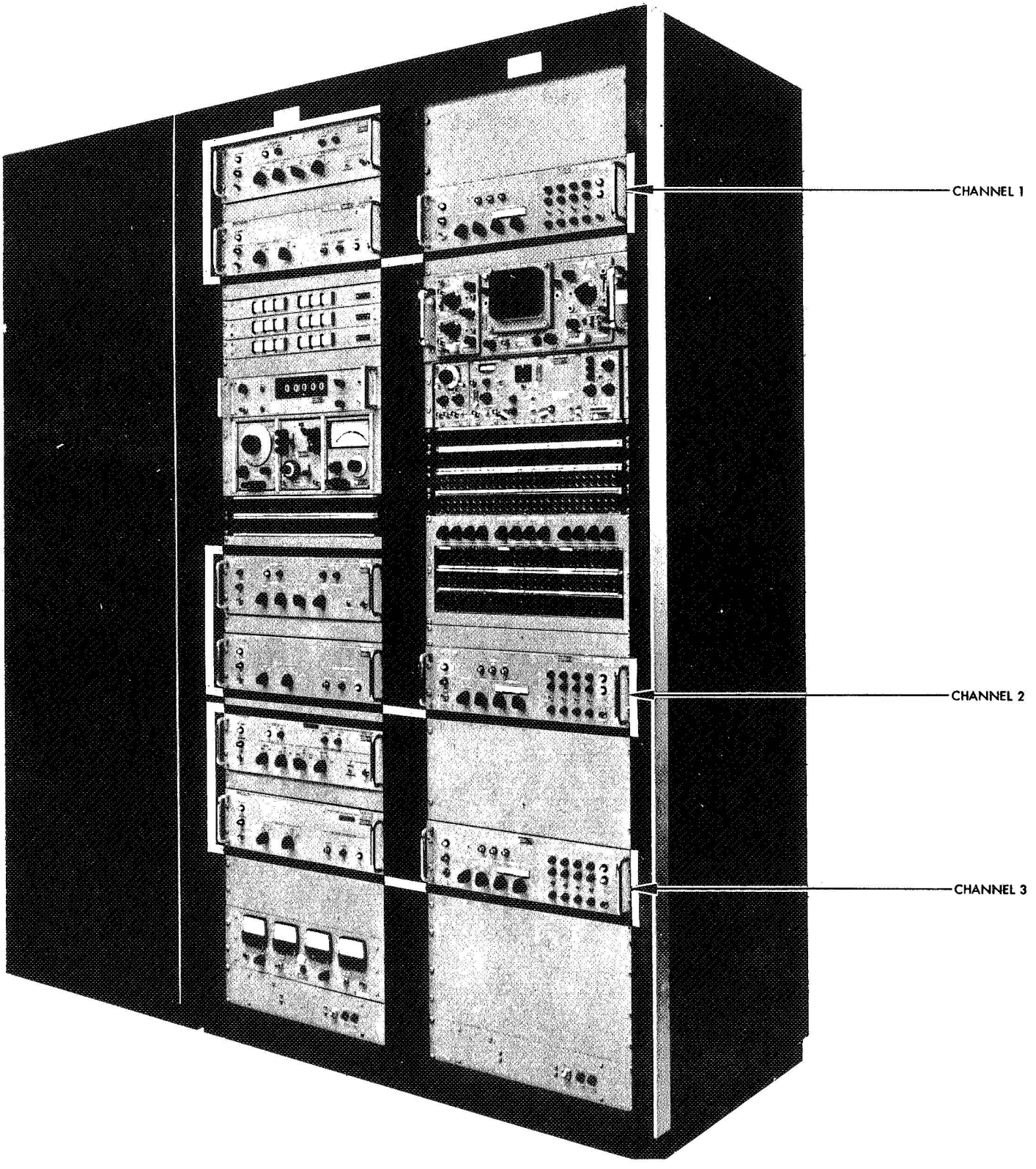

Fig. 2. Simulation Center High-Speed Data Assembly

Pioneer F and *G* Mission Support Area

A. H. Hofmann
SFOF/GCF Operations Section

With the advent of the third-generation computer systems and the increased complexity of interplanetary missions, the area required to support mission operations has exceeded available facilities within the SFOF. Consequently, the Pioneer F Jupiter fly-by mission support area will be located in the new Systems Development Laboratory, Building 264. Following is a description of the mission support area, its relationship with the SFOF and other DSN facilities, and a brief discussion on some anticipated operational problems caused by its remote location from the SFOF.

I. Introduction

The SFOF has provided adequate facilities in support of numerous space missions beginning with the successful *Ranger 7* in 1964. By 1967, deep space missions reached their highest level of activity. At this time the SFOF supported four projects simultaneously, each with a separate mission support area.

The total floor space available for Project operations within the SFOF is 1263 m^2 (13,600 ft^2). This area is arranged in a U-shape around the DSN operations and monitor areas on the first floor. During the second generation computer system it was adequate to provide individual mission support areas for *Mariners 4* and *5*, *Surveyors 1* through *7*, *Lunar Orbiters 1* through *5*, and *Pioneers 6* through *9*. Increased sophistication of spacecraft design has led to the implementation of the Mark III third-generation computer system. More personnel and equipment are required to handle the increased capability of the Mark III system. Accordingly, the size of mission support areas has also increased.

The *Mariner* Mars 1971 mission is the most complex unmanned space mission ever undertaken. Orbital operations will demand the maximum capabilities of the Mark IIIA system. Consequently, a greater number of operational personnel will be required to insure mission success. As a result, the entire SFOF mission support area has been committed to the *Mariner* Mars 1971 Project (Fig. 1).

The *Pioneer F* and *G* Jupiter fly-by missions have also increased in complexity from previous *Pioneer* missions. The *Pioneer F* Support Instrumentation Requirements Document specified a total of 855 m^2 (9200 ft^2). To meet this requirement, the *Pioneer F* and *G* mission support area was located on the second floor of the systems development laboratory (SDL). This building is

linked to the SFOF by an 88-m (290 ft) long communications tunnel to provide all capabilities available in the SFOF.

II. Design and Function of the *Pioneer* F Mission Support Area

The design of the mission support area (MSA) was a joint effort of the SFOF Operations Support Group (Section 916) and the *Pioneer* Project of the NASA Ames Research Center at Moffett Field, California. Original design utilized 855 m^2 (9200 ft^2). However, budget limitations dictated a reduction in user equipment. This resulted in a redesign of the entire MSA. The final design is illustrated in Fig. 2. The total area utilized is just over 557 m^2 (6000 ft^2). One of the guidelines followed in the final design was to utilize mission-independent concepts to prevent extensive modifications for future missions. The MSA is comprised of six major elements. They are:

(1) *Mission Control:* Central control point for overall mission operations. Includes positions for the flight director and the chief of mission operations.

(2) *Command:* One-man position responsible for actuating all spacecraft commands.

(3) *Spacecraft Performance Analysis Team:* This group monitors spacecraft events and health. Positions include the spacecraft team leader, two assistants, and twelve operational positions for six spacecraft subsystems. Also included in this area are five positions for science control and monitoring. The major Science effort will be accomplished at the Remote Information Center at Ames Research Center.

(4) *Software and Data:* This area does all the data processing for the Project. It interfaces directly with the IBM 360/75. It also provides a backup position for command.

(5) *Orientation and Maneuver:* This group is responsible for the attitude control of the spacecraft. It is closely associated with the flight path analysis team.

(6) *Flight Path Analysis Team:* Comprised of Division 39 personnel, but directly responsible to *Pioneer* mission control. This facility analyzes trajectories and ascertains parameters for midcourse trajectory corrections.

Major equipment in the MSA includes:

- 6 IBM 1443 line printers
- 2 IBM 2501 card readers
- 4 IBM 2260 digital input/output devices with keyboard
- 2 IBM 2260 digital output devices without keyboard
- 3 Gould digital television (DTV) hardcopy machines
- 16 Teletypewriter (TTY) character printers
- 1 Univac Data communications terminal (DCT) 500 printer
- 1 Univac Calcomp plotter
- 1 Univac 9300 terminal
- 2 Tektronix 4002 displays
- 44 23 cm (9 in.) TV monitors
- 11 36 cm (14 in.) TV monitors
- 18 58 cm (23 in.) Ceiling TV monitors
- 46 Voice Communications Assembly (VOCA) Stations

An office and conference area is provided for developing operational procedures and contingencies.

III. MSA Interface With the SFOF

Additional equipment was required to extend the SFOF capabilities to the *Pioneer* MSA in the SDL. For support of the VOCA and TV subsystems, complete new terminal and switchgear frames had to be constructed in the SDL. This equipment is located in the northwest quadrant of the second floor. For the IBM devices, special line drivers (IBM 2944) were required to compensate for the distance of the MSA to the SFOF. All of the MSA equipment is linked with the SFOF through the 290-foot-long tunnel. The original tunnel design was meant to serve as a communications link and a personnel route as well. Again, budget limitations eliminated the latter. The tunnel is a hard hat area for installation and maintenance of cabling only. Any other use is not permitted.

IV. Problem Areas Due to Remote Location

Undoubtedly, many operational problems will crop up during the testing and support phases of the *Pioneer F* MSA. It is anticipated that most of them will be minor, more or less an inconvenience rather than a serious problem. A good example is the maintenance of TV, VOCA, and IBM equipment. All maintenance shops, parts, and personnel are located in the SFOF. The carts for moving

items such as TV monitors or IBM 2260's cannot be used on the rough asphalt street. Also, the grade between the SFOF and SDL is fairly steep. These two factors could cause an accident resulting in equipment damage and/or personnel injury. The problem would be compounded by inclement weather. However, two problems exist which could impact *Pioneer* Mission Operations. One is purely from a support standpoint. The SDL building was funded through the NASA Office of Space Science Applications (OSSA) as an institutional facility. The SFOF and other DSN facilities are funded through the Office of Tracking and Data Acquisition (OTDA). SFOF plant maintenance is accomplished through a Tracking and Data Acquisition (TDA) contractor, Philco-Ford. These personnel will not perform plant maintenance in the SDL as it is an institutional facility. Therefore, all maintenance work must go through regular JPL Plant Maintenance channels. This could present a problem if any failures occur during high activity periods where rapid turn-around is required. It is anticipated that procedures can be arranged to minimize this problem. The second problem is more severe. Budget limitations did not permit extension of the uninterruptible power system from the SFOF to the SDL, or provision of any other backup power. If there is a power plant failure, the entire MSA will be without power. At this time it is not known what a sudden power variation would do to the I/O equipment in the MSA, but the DSN is implementing an emergency MSA (Mini-Ops Area) in the SFOF. This facility is located in Room 102C adjacent to the DSN Operations Control Room (Fig. 1). Enough equipment is installed to support the major portions of the *Pioneer F* mission with emphasis on the command function. The *Pioneer* Project and DSN are developing procedures to assure mission success in spite of an SDL power failure.

V. Conclusion

The *Pioneer F* and *G* MSA is designed for operational convenience. The area was designed to be mission independent. It will be used to support the *Helios* mission as presently configured. With minor modifications and addition of the northeast quadrant, the east half of the facility will be used for the *Viking* lander support. Presently, there is no major science support in the *Pioneer F* MSA. All science data will be routed via high speed data line to the Remote Information Center at Ames Research Center. All the principal investigators will be located at that facility.

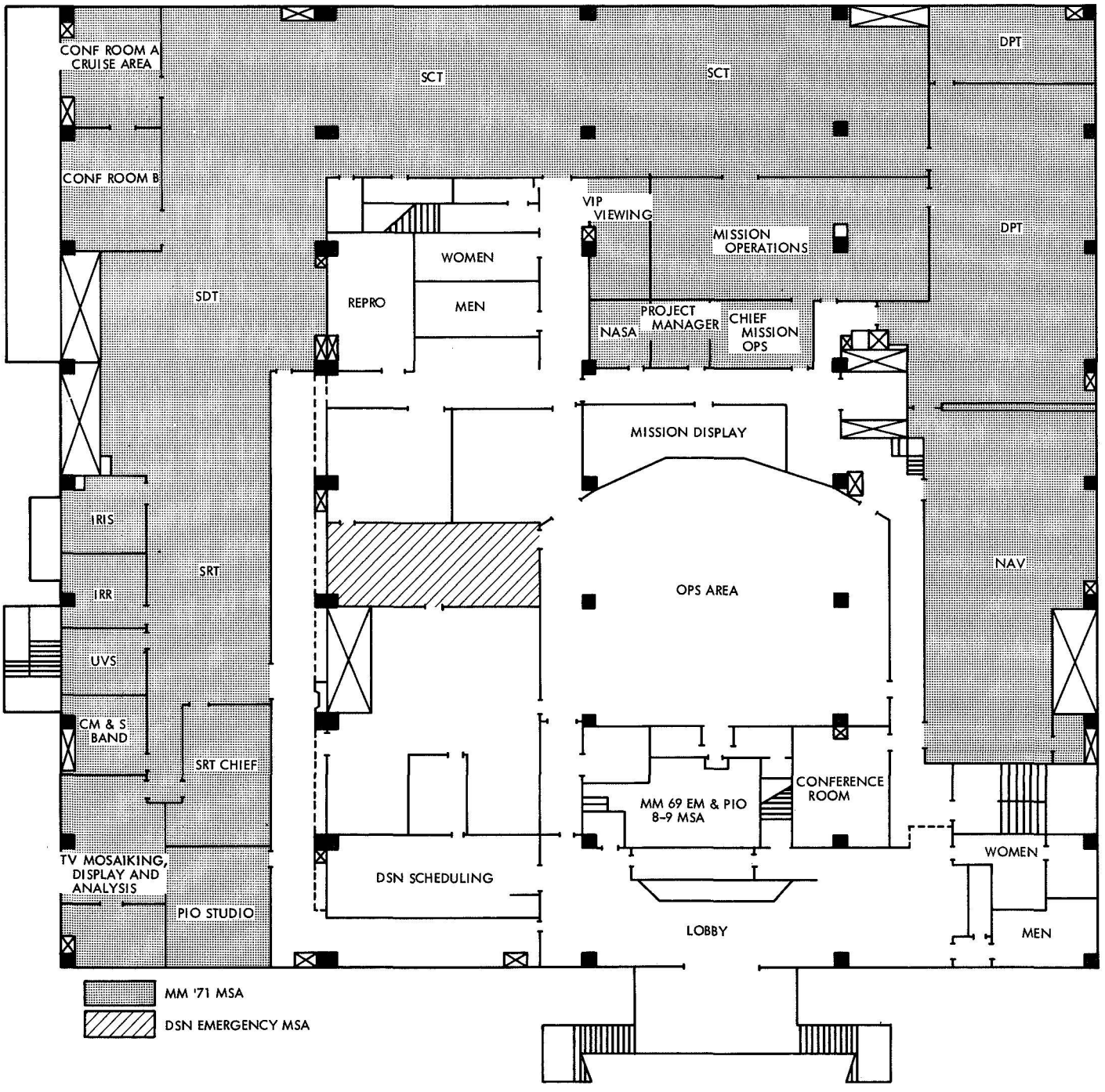

Fig. 1. SFOF first floor

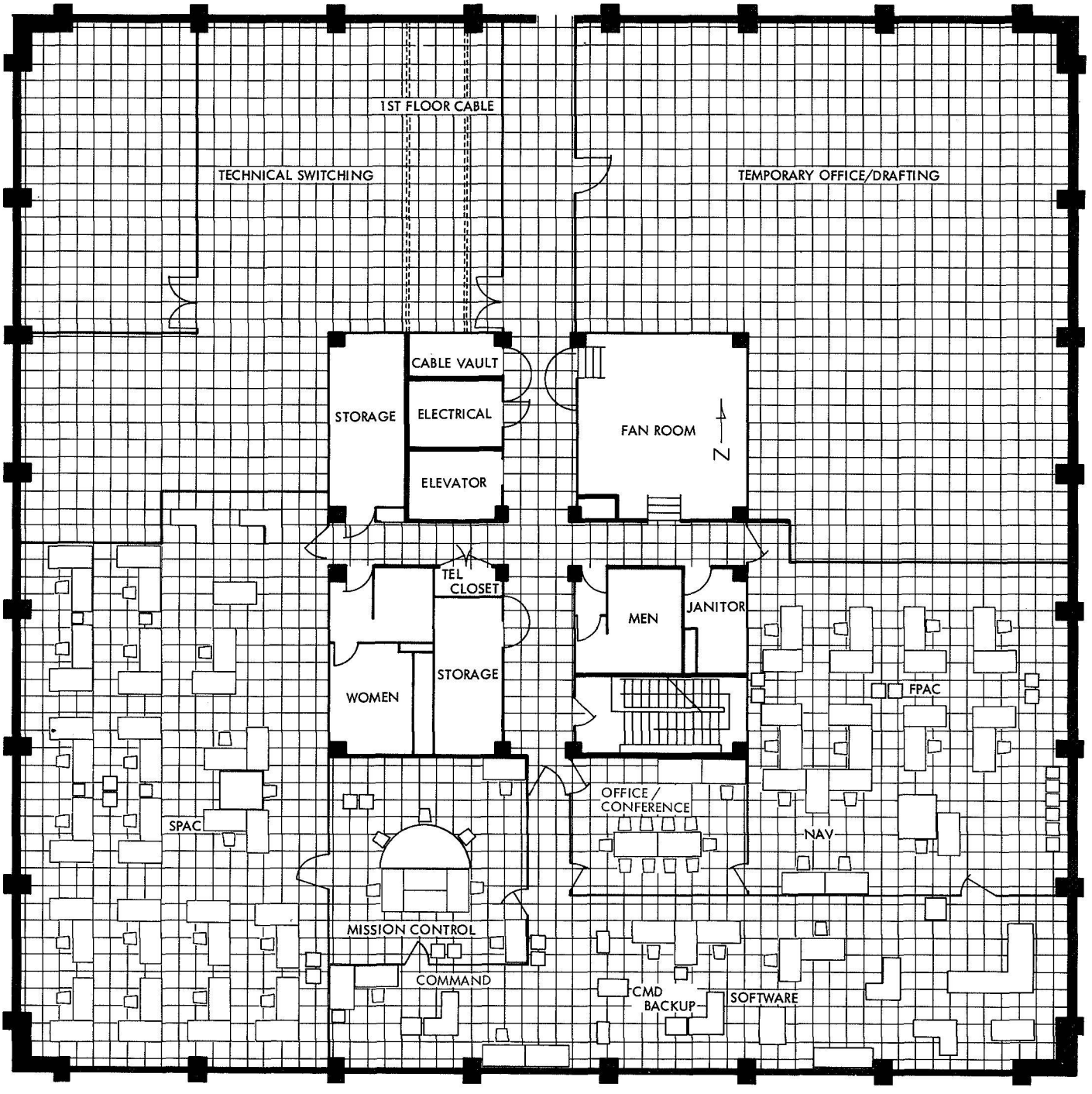

Fig. 2. *Pioneer F* and *G* mission support area

Bibliography

Anderson, J. D., *Determination of the Masses of the Moon and Venus and the Astronomical Unit from Radio Tracking Data of the Mariner II Spacecraft.* Technical Report 32-816. Jet Propulsion Laboratory, Pasadena, Calif., July 1, 1967.

Anderson, J. D., et al., "The Radius of Venus as Determined by Planetary Radar and Mariner V Radio Tracking Data," *J. Atmos. Sci.*, pp. 1171–1174, Sept. 25, 1968.

Berman, A. L., *Tracking System Data Analysis Report, Ranger VII Final Report,* Technical Report 32-719, Jet Propulsion Laboratory, Pasadena, Calif., June 1, 1965.

Berman, A. L., *ABTRAJ—On-Site Tracking Prediction Program for Planetary Spacecraft,* Technical Memorandum 33-391. Jet Propulsion Laboratory, Pasadena, Calif., Aug. 15, 1968.

Cain, D. L., and Hamilton, T. W., *Determination of Tracking Station Locations by Doppler and Range Measurements to an Earth Satellite,* Technical Report 32-534. Jet Propulsion Laboratory, Pasadena, Calif., Feb. 1, 1964.

Carey, C. N., and Sjogren, W. L., "Gravitational Inconsistency, in the Lunar Theory: Confirmation by Radio Tracking," *Science,* Vol. 160, pp. 875, 876, Apr.–June 1968.

Curkendall, D. W., and Stephenson, R. R., "Earthbased Tracking and Orbit Determination—Backbone of the Planetary Navigation System," *Astronaut. Aeronaut.*, Vol. 7, May 1970.

Curkendall, D. W., "Planetary Navigation: The New Challenges," *Astronaut. Aeronaut.*, Vol. 7, May 1970.

Efron, L., and Solloway, C. B., *Proceedings of the Conference on Scientific Applications of Radio and Radar Tracking in the Space Program,* Technical Report 32-1475. Jet Propulsion Laboratory, Pasadena, Calif., July 1970.

Flanagan, F. M., et al., *Deep Space Network Support of the Manned Space Flight Network for Apollo: 1962–1968,* Technical Memorandum 33-452, Vol. I. Jet Propulsion Laboratory, Pasadena, Calif., July 1970.

Flanagan, F. M., et al., *Deep Space Network Support of the Manned Space Flight Network for Apollo: 1969–1970,* Technical Memorandum 33-452, Vol. II. Jet Propulsion Laboratory, Pasadena, Calif., May 1, 1971.

Fjeldbo, G., and Eshleman, V. R., "Radio Occultation Measurements and Interpretations," in *The Atmospheres of Venus and Mars,* p. 225. Gordon and Breach, Science Publishers, Inc., New York, N. Y.

Goldstein, R. M., "Radar Time-of-Flight Measurements to Venus," *Astron. J.*, Vol. 73, No. 9, Aug. 1968.

Goldstein, R. M., and Rumsey, H., Jr., "A Radar Snapshot of Venus," *Science,* Vol. 169, Sept. 1970.

Gordon, H. J., et al., *The Mariner 6 and 7 Flight Paths and Their Determination From Tracking Data,* Technical Memorandum 33-469. Jet Propulsion Laboratory, Pasadena, Calif., Dec. 1, 1970.

Bibliography (contd)

Hamilton, T. W., et al., *The Ranger IV Flight Path and Its Determination From Tracking Data*, Technical Report 32-345. Jet Propulsion Laboratory, Pasadena, Calif., Sept. 15, 1962.

Kellermann, K. I., et al., "High Resolution Observations of Compact Radio Sources at 13 Centimeters," *Astrophys. J.*, Vol. 161, pp. 803–809, Sept. 1970.

Kliore, A., "Radio Occultation Measurements of the Atmospheres of Mars and Venus," in *The Atmospheres of Venus and Mars*, p. 205. Gordon and Breach Science Publishers, Inc., New York, N. Y.

Labrum, R. G., Wong, S. K., and Reynolds, G. W., *The Surveyor V, VI, and VII Flight Paths and Their Determination from Tracking Data*, Technical Report 32-1302. Jet Propulsion Laboratory, Pasadena, Calif., Dec. 1, 1968.

Lieske, J. H., and Null, G. W., "Icarus and the Determination of Astronomical Constants," *Astron. J.*, Vol. 74, No. 2, Mar. 1969.

Lorell, J., and Sjogren, W. L., *Lunar Orbiter Data Analysis*, Technical Report 32-1220. Jet Propulsion Laboratory, Pasadena, Calif., Nov. 15, 1967.

Lorell, J., *Lunar Orbiter Gravity Analysis*, Technical Report 32-1387. Jet Propulsion Laboratory, Pasadena, Calif., June 15, 1969.

Lorell, J., et al., "Celestial Mechanics Experiment for *Mariner*," *Icarus*, Vol. 12, Jan. 1970.

McNeal, C. E., *Ranger V Tracking Systems Data Analysis Final Report*, Technical Report 32-702. Jet Propulsion Laboratory, Pasadena, Calif., Apr. 15, 1965.

Melbourne, W. G., et al., *Constants and Related Information for Astrodynamical Calculations*, Technical Report 32-1306. Jet Propulsion Laboratory, Pasadena, Calif., July 15, 1968.

Melbourne, W. G., "Planetary Ephemerides," *Astronaut. Aeronaut.*, Vol. 7, May 1970.

Miller, L., et al., *The Atlas–Centaur VI Flight Path and Its Determination from Tracking Data*, Technical Report 32-911. Jet Propulsion Laboratory, Pasadena, Calif., Apr. 15, 1966.

Mulhall, B. D., et al., *Tracking System Analytic Calibration Activities for the Mariner Mars 1969 Mission*, Technical Report 32-1499. Jet Propulsion Laboratory, Pasadena, Calif., Nov. 15, 1970.

Mulholland, J. D., and Sjogren, W. L., *Lunar Orbiter Ranging Data*, Technical Report 32-1087. Jet Propulsion Laboratory, Pasadena, Calif., Jan. 6, 1967.

Mulholland, J. D., *Proceedings of the Symposium on Observation, Analysis, and Space Research Applications of the Lunar Motion*, Technical Report 32-1386. Jet Propulsion Laboratory, Pasadena, Calif., Apr. 1969.

Muller, P. M., and Sjogren, W. L., *Consistency of Lunar Orbiter Residuals With Trajectory and Local Gravity Effects*, Technical Report 32-1307. Jet Propulsion Laboratory, Pasadena, Calif., Sept. 1, 1968.

Muller, P. M., and Sjogren, W. L., *Lunar Mass Concentrations*, Technical Report 32-1339. Jet Propulsion Laboratory, Pasadena, Calif., Aug. 16, 1968.

Bibliography (contd)

Null, G. W., Gordon, H. J., and Tito, D. A., *Mariner IV Flight Path and its Determination From Tracking Data,* Technical Report 32-1108. Jet Propulsion Laboratory, Pasadena, Calif., Aug. 1, 1967.

O'Neil, W. J., et al., *The Surveyor III and Surveyor IV Flight Paths and Their Determination From Tracking Data,* Technical Report 32-1292. Jet Propulsion Laboratory, Pasadena, Calif., Aug. 15, 1968.

Pease, G. E., et al., *The Mariner V Flight Path and Its Determination From Tracking Data,* Technical Report 32-1363. Jet Propulsion Laboratory, Pasadena, Calif., July 1, 1969.

Renzetti, N. A., *Tracking and Data Acquisition for Ranger Missions I–V,* Technical Memorandum 33-174. Jet Propulsion Laboratory, Pasadena, Calif., July 1, 1964.

Renzetti, N. A., *Tracking and Data Acquisition for Ranger Missions VI–IX,* Technical Memorandum 33-275. Jet Propulsion Laboratory, Pasadena, Calif., Sept. 15, 1966.

Renzetti, N. A., *Tracking and Data Acquisition Support for the Mariner Venus 1962 Mission,* Technical Memorandum 33-212. Jet Propulsion Laboratory, Pasadena, Calif., July 1, 1965.

Renzetti, N. A., *Tracking and Data Acquisition Report, Mariner Mars 1964 Mission: Near-Earth Trajectory Phase,* Technical Memorandum 33-239, Vol. I. Jet Propulsion Laboratory, Pasadena, Calif., Jan. 1, 1965.

Renzetti, N. A., *Tracking and Data Acquisition Report, Mariner Mars 1964 Mission: Cruise to Post-Encounter Phase,* Technical Memorandum 33-239, Vol. II. Jet Propulsion Laboratory, Pasadena, Calif., Oct. 1, 1967.

Renzetti, N. A., *Tracking and Data Acquisition Report, Mariner Mars 1964 Mission: Extended Mission,* Technical Memorandum 33-239, Vol. III. Jet Propulsion Laboratory, Pasadena, Calif., Dec. 1, 1968.

Renzetti, N. A., *Tracking and Data System Support for Surveyor: Missions I and II,* Technical Memorandum 33-301, Vol. I. Jet Propulsion Laboratory, Pasadena, Calif., July 15, 1969.

Renzetti, N. A., *Tracking and Data System Support for Surveyor: Missions III and IV,* Technical Memorandum 33-301, Vol. II. Jet Propulsion Laboratory, Pasadena, Calif., Sept. 1, 1969.

Renzetti, N. A., *Tracking and Data System Support for Surveyor: Mission V,* Technical Memorandum 33-301, Vol. III. Jet Propulsion Laboratory, Pasadena, Calif., Dec. 1, 1969.

Renzetti, N. A., *Tracking and Data System Support for Surveyor: Mission VI,* Technical Memorandum 33-301, Vol. IV. Jet Propulsion Laboratory, Pasadena, Calif., Dec. 1, 1969.

Renzetti, N. A., *Tracking and Data System Support for Surveyor: Mission VII,* Technical Memorandum 33-301, Vol. V. Jet Propulsion Laboratory, Pasadena, Calif., Dec. 1, 1969.

Bibliography (contd)

Renzetti, N. A., *Tracking and Data System Support for the Mariner Venus 67 Mission: Planning Phase Through Midcourse Maneuver,* Technical Memorandum 33-385, Vol. I. Jet Propulsion Laboratory, Pasadena, Calif., Sept. 1, 1969.

Renzetti, N. A., *Tracking and Data System Support for the Mariner Venus 67 Mission: Midcourse Maneuver Through End of Mission,* Technical Memorandum 33-385, Vol. II. Jet Propulsion Laboratory, Pasadena, Calif., Sept. 1, 1969.

Renzetti, N. A., *Tracking and Data System Support for the Pioneer Project. Pioneer VI. Prelaunch to End of Nominal Mission,* Technical Memorandum 33-426, Vol. I. Jet Propulsion Laboratory, Pasadena, Calif., Feb. 1, 1970.

Renzetti, N. A., *Tracking and Data System Support for the Pioneer Project. Pioneer VII. Prelaunch to End of Nominal Mission,* Technical Memorandum 33-426, Vol. II. Jet Propulsion Laboratory, Pasadena, Calif., Apr. 15, 1970.

Renzetti, N. A., *Tracking and Data System Support for the Pioneer Project. Pioneer VIII. Prelaunch Through May 1968,* Technical Memorandum 33-426, Vol. III. Jet Propulsion Laboratory, Pasadena, Calif., July 15, 1970.

Renzetti, N. A., *Tracking and Data System Support for the Pioneer Project. Pioneer IX. Prelaunch Through June 1969,* Technical Memorandum 33-426, Vol. IV. Jet Propulsion Laboratory, Pasadena, Calif., Nov. 15, 1970.

Renzetti, N. A., *Tracking and Data System Support for the Pioneer Project. Pioneer VI. Extended Mission: July 1, 1966–July 1, 1969,* Technical Memorandum 33-426, Vol. V. Jet Propulsion Laboratory, Pasadena, Calif., Feb. 1, 1971.

Renzetti, N. A., *Tracking and Data System Support for the Pioneer Project. Pioneer VII. Extended Mission: February 24, 1967–July 1, 1968,* Technical Memorandum 33-426, Vol. VI. Jet Propulsion Laboratory, Pasadena, Calif., Apr. 15, 1971.

Renzetti, N. A., *Tracking and Data System Support for the Pioneer Project. Pioneer VII. Extended Mission: July 1, 1968–July 1, 1969,* Technical Memorandum 33-426, Vol. VII. Jet Propulsion Laboratory, Pasadena, Calif., Apr. 15, 1971.

Renzetti, N. A., *Tracking and Data System Support for the Pioneer Project. Pioneer VIII. Extended Mission: June 1, 1968–July 1, 1969,* Technical Memorandum 33-426, Vol. VIII. Jet Propulsion Laboratory, Pasadena, Calif., May 1, 1971.

Renzetti, N. A., *Tracking and Data System Support for the Pioneer Project. Pioneers VI–IX. Extended Missions: July 1, 1969–July 1, 1970,* Technical Memorandum 33-426, Vol. IX. Jet Propulsion Laboratory, Pasadena, Calif., Aug. 15, 1971.

Sjogren, W. L., *The Ranger III Flight Path and Its Determination From Tracking Data,* Technical Report 32-563. Jet Propulsion Laboratory, Pasadena, Calif., Sept. 15, 1965.

Sjogren, W. L., et al., *Physical Constants as Determined From Radio Tracking of the Ranger Lunar Probes,* Technical Report 32-1057. Jet Propulsion Laboratory, Pasadena, Calif., Dec. 30, 1966.

Sjogren, W. L., et al., *The Ranger VI Flight Path and Its Determination From Tracking Data,* Technical Report 32-605. Jet Propulsion Laboratory, Pasadena, Calif., Dec. 15, 1964.

Bibliography (contd)

Sjogren, W. L., et al., *The Ranger V Flight Path and Its Determination From Tracking Data,* Technical Report 32-562. Jet Propulsion Laboratory, Pasadena, Calif., Dec. 6, 1963.

Sjogren, W. L., and Trask, D. W., *Physical Constants as Determined From Radio Tracking of the Ranger Lunar Probes,* Technical Report 32-1057. Jet Propulsion Laboratory, Pasadena, Calif., Dec. 30, 1966.

Sjogren, W. L., *Proceedings of the JPL Seminar on Uncertainties in the Lunar Ephemeris,* Technical Report 32-1247. Jet Propulsion Laboratory, Pasadena, Calif., May 1, 1968.

Stelzried, C. T., *A Faraday Rotation Measurement of a 13-cm Signal in the Solar Corona,* Technical Report 32-1401. Jet Propulsion Laboratory, Pasadena, Calif., July 15, 1970.

Stelzried, C. T., et al., "The Quasi-Stationary Coronal Magnetic Field and Electron Density as Determined From a Faraday Rotation Experiment," *Sol. Phys.,* Vol. 14, No. 2, pp. 440–456, Oct. 1970.

Thornton, J. H., Jr., *The Surveyor I and Surveyor II Flight Paths and Their Determination From Tracking Data,* Technical Report 32-1285. Jet Propulsion Laboratory, Pasadena, Calif., Aug. 1, 1968.

Vegos, C. J., et al., *The Ranger IX Flight Path and Its Determination From Tracking Data,* Technical Report 32-767. Jet Propulsion Laboratory, Pasadena, Calif., Nov. 1, 1968.

Winn, F. B., *Selenographic Location of Surveyor VI, Surveyor VI Mission Report: Part II. Science Results,* Technical Report 32-1262. Jet Propulsion Laboratory, Pasadena, Calif., Jan. 10, 1968.

Winn, F. B., "Post Landing Tracking Data Analysis," in *Surveyor VII Mission Report: Part II. Science Results,* Technical Report 32-1264. Jet Propulsion Laboratory, Pasadena, Calif., Mar. 15, 1968.

Winn, F. B., "Post Lunar Touchdown Tracking Data Analysis," in *Surveyor Project Final Report: Part II. Science Results,* Technical Report 32-1265. Jet Propulsion Laboratory, Pasadena, Calif., June 15, 1968.

Winn, F. B., *Surveyor Posttouchdown Analyses of Tracking Data,* NASA SP-184. National Aeronautics and Space Administration, Washington, D.C., p. 369.

Wollenhaupt, W. R., et al., *The Ranger VII Flight Path and Its Determination From Tracking Data,* Technical Report 32-694. Jet Propulsion Laboratory, Pasadena, Calif., Dec. 15, 1964.

NASA — JPL — Coml., L.A., Calif.

~~06508~~ N71-38564

TECHNICAL REPORT STANDARD TITLE PAGE

1. Report No. 32-1526, Vol. V	2. Government Accession No.	3. Recipient's Catalog No.
4. Title and Subtitle THE DEEP SPACE NETWORK PROGRESS REPORT FOR JULY AND AUGUST 1971		5. Report Date October 15, 1971 6. Performing Organization Code
7. Author(s) JPL Staff		8. Performing Organization Report No.
9. Performing Organization Name and Address JET PROPULSION LABORATORY California Institute of Technology 4800 Oak Grove Drive Pasadena, California 91103		10. Work Unit No. 11. Contract or Grant No. NAS 7-100 13. Type of Report and Period Covered Technical Report
12. Sponsoring Agency Name and Address NATIONAL AERONAUTICS AND SPACE ADMINISTRATION Washington, D.C. 20546		14. Sponsoring Agency Code

15. Supplementary Notes

16. Abstract

This report describes work performed for the JPL/NASA Deep Space Network (DSN). Progress is presented on DSN supporting research and technology, advanced development and engineering, and implementation, and DSN operations which pertain to mission-independent or multiple-mission development as well as to support of flight projects. Each issue contains a description of the functions and facilities of the DSN.

17. Key Words (Selected by Author(s))	18. Distribution Statement
Antennas and Transmission Lines Information Theory Telemetry and Command Tracking	Unclassified -- Unlimited

19. Security Classif. (of this report)	20. Security Classif. (of this page)	21. No. of Pages	22. Price
Unclassified	Unclassified	145	